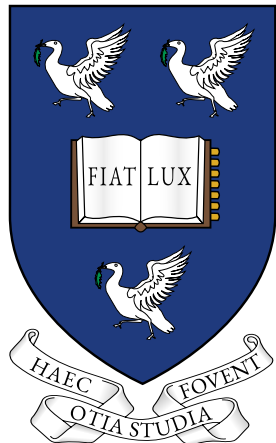


# New Physics Searches with Single Electromagnetic Shower Events at the Fermilab Short Baseline Neutrino Program



Thesis submitted in accordance with the requirements of the  
University of Liverpool for the degree of Doctor in Philosophy by

**Thomas Ham**

March, 2023



# Abstract

The Short Baseline Neutrino (SBN) program is comprised of three Liquid Argon Time Projection Chamber detectors located along the beamline of the Booster Neutrino Beam at Fermilab. The three detectors are SBND, MicroBooNE and ICARUS and are at 110 m, 470 m and 600 m from the beam source respectively. The program was designed with the goal of either confirming or refuting the existence of light sterile neutrinos, which have been hinted at by the LSND and MiniBooNE experiments as well as results from reactor and gallium based neutrino experiments. The observation of sterile neutrinos would provide physics beyond the Standard Model as well as being a vital component in understanding the mass generation mechanism for neutrinos. One of the defining properties of sterile neutrinos is that they do not weakly interact meaning that direct detection is not viable, however, mixing may occur with the active neutrinos which allows for the appearance and disappearance of active neutrinos to be observed.

The development of electromagnetic shower reconstruction algorithms used in SBND are presented which are crucial for calculating the reconstructed neutrino energy from  $\nu_e$  CC interactions. The neutrino energy is one of the variables used to calculate the neutrino oscillation probability which is the other major topic that is discussed in this thesis. Assuming a (3 + 1) neutrino framework, the  $\nu_e$  appearance and disappearance sensitivities are calculated from a  $\nu_e$  CC inclusive sample for the SBN program using Monte Carlo events. The  $\nu_e$  appearance exclusion sensitivities from SBND show a stronger constraint than previous results and the allowed region is compatible with the LSND result. The SBN  $\nu_e$  disappearance exclusion sensitivity excludes much of the allowed region from the ND280 detector whereas the SBN allowed region is still compatible with that from ND280.



# Declaration

I hereby confirm this work is my own, except where other works are referenced. This work has not previously been submitted to any institute, including this one.

Chapter 1 gives an overview of the content in this thesis. Chapter 2 and Chapter 3 give a review of neutrino theory and details of neutrino detection using LArTPCs with a focus on the key features of the SBN program. These chapters cover work done by many members of the wider neutrino community and have been referenced where appropriate.

Chapter 4 builds upon the reconstruction work done by a number of people as part of the LArSoft framework. In particular, the *Shower Num Electrons Energy tool* and the *Shower ESTAR Energy tool* have been newly developed and validated by myself.

Chapter 5 discusses the necessary inputs and analysis choices required for a sterile neutrino oscillation analysis. Again, many people worked on different aspects of the work presented here. Personally, I produced the most recent  $\nu_e$  MC event sample and performed the study investigating the impact of the baseline parametrisation. Chapter 6 goes on to use the inputs from Chapter 5 to perform an oscillation analysis using the VALOR fitting framework. The content shown is essentially all my own and builds upon the work done by current and previous members of the VALOR group.



## Acknowledgements



# Contents

<b>Glossary</b>	<b>xiii</b>
<b>List of Figures</b>	<b>xvii</b>
<b>List of Tables</b>	<b>xxiii</b>
<b>1. Introduction</b>	<b>1</b>
<b>2. Neutrino Physics</b>	<b>5</b>
2.1. A Brief History of Neutrinos . . . . .	5
2.2. Overview of Neutrino Physics . . . . .	8
2.2.1. Neutrinos within the Standard Model . . . . .	9
2.2.1.1. Theory of Weak Interactions . . . . .	9
2.2.1.2. Weak Interaction Processes . . . . .	12
2.2.1.3. CP Violation . . . . .	19
2.2.2. Neutrino Masses . . . . .	21
2.2.2.1. Dirac Mass . . . . .	21
2.2.2.2. Majorana Mass . . . . .	22
2.2.2.3. Seesaw Mechanism . . . . .	23
2.2.2.4. Direct Mass Measurements . . . . .	24
2.2.3. Neutrino Oscillations . . . . .	26
2.2.3.1. 3 Flavour Oscillation Phenomenology . . . . .	26
2.2.3.2. 3 Flavour Oscillation Experimental Results . . .	31
2.2.3.3. Sterile Neutrino Oscillation Phenomenology . . .	40
2.2.3.4. Sterile Neutrino Oscillation Experimental Motivation	42

<b>3. The Short Baseline Neutrino Program</b>	<b>65</b>
3.1. Liquid Argon Time Projection Chambers . . . . .	66
3.1.1. LArTPC Operating Principles . . . . .	67
3.1.2. Physics of Signal Formation . . . . .	69
3.1.2.1. Ionisation and Detector Effects . . . . .	69
3.1.2.2. Scintillation and Cherenkov Light . . . . .	73
3.1.2.3. Wire Signal Processing . . . . .	74
3.2. Booster Neutrino Beam . . . . .	75
3.3. SBN Detectors . . . . .	77
3.3.1. SBND . . . . .	78
3.3.2. MicroBooNE . . . . .	82
3.3.3. ICARUS . . . . .	84
3.4. SBN Physics Capabilities . . . . .	86
<b>4. Electromagnetic Shower Energy Reconstruction in SBND</b>	<b>93</b>
4.1. Event Simulation and Reconstruction . . . . .	93
4.2. Overview of Shower Energy Reconstruction in SBND . . . . .	95
4.2.1. Linear Energy . . . . .	97
4.2.2. Number of Electrons to Energy . . . . .	98
4.2.3. ESTAR Method . . . . .	99
4.3. Shower Energy Reconstruction Performance . . . . .	100
4.3.1. Validation of a BNB Sample . . . . .	101
4.3.2. Performance as a Function of Angle . . . . .	108
4.3.3. Performance as a Function of Energy . . . . .	111
4.4. Summary of EM Shower Reconstruction . . . . .	112
<b>5. Sterile Neutrino Oscillation Inputs Within SBN</b>	<b>113</b>
5.1. Monte Carlo Event Production . . . . .	113
5.2. Event Reconstruction . . . . .	116
5.3. Event Selection . . . . .	117
5.3.1. $\nu_\mu$ Selection . . . . .	117
5.3.2. $\nu_e$ Selection . . . . .	118

5.4.	Systematic Uncertainties . . . . .	120
5.4.1.	Flux Systematics . . . . .	120
5.4.2.	Interaction Systematics . . . . .	125
<b>6.</b>	<b>SBN Oscillation Analysis Within the VALOR Framework</b>	<b>133</b>
6.1.	The VALOR Framework . . . . .	133
6.2.	Oscillation Channels Within SBN . . . . .	136
6.3.	Specifics of SBN Sensitivity Simulation Implementation in VALOR	137
6.3.1.	Baseline and Binning Analysis Choices . . . . .	137
6.3.1.1.	Baseline . . . . .	137
6.3.1.2.	Binning . . . . .	141
6.3.2.	Reaction Modes . . . . .	143
6.3.3.	Implementing and Validating SBN Systematic Uncertainties in VALOR . . . . .	146
6.3.3.1.	Processing Systematic Uncertainties . . . . .	146
6.3.3.2.	Validating Systematic Uncertainties . . . . .	147
6.3.4.	SBN Contour Construction . . . . .	151
6.4.	Event Rate Predictions and the Expected Signal . . . . .	152
6.4.1.	Nominal Event Rate Predictions . . . . .	153
6.4.2.	Expected Oscillation Signal . . . . .	160
6.4.2.1.	$\nu_e$ Appearance Analysis . . . . .	160
6.4.2.2.	$\nu_e$ Disappearance Analysis . . . . .	162
6.5.	Sensitivities Studies . . . . .	165
6.5.1.	Evaluation of SBN Sensitivities for $\nu_e$ Appearance and Dis- appearance . . . . .	165
6.5.2.	Impact of Systematic Uncertainties . . . . .	169
6.5.2.1.	Impact of Systematic Uncertainty Sub-Groups . .	169
6.5.2.2.	Impact of Individual Systematics . . . . .	171
6.5.2.3.	Future Constraints on Systematic Uncertainties .	180
6.5.3.	Evaluation of Impact of Efficiency Uncertainties . . . . .	181
6.5.4.	Evaluation of Impact of Shower Energy Reconstruction Performance . . . . .	193
6.6.	Summary of $\nu_e$ sensitivities within SBN . . . . .	195

<b>7. Conclusion</b>	<b>197</b>
<b>A. Single Parameter Variations</b>	<b>201</b>
<b>B. Detector Volumes</b>	<b>205</b>
<b>C. Reconstruction Performance</b>	<b>207</b>
<b>D. <math>\nu_\mu</math> Disappearance Analysis</b>	<b>209</b>
<b>Bibliography</b>	<b>219</b>

# Glossary

**2p2h** 2 Particles 2 Holes.

**ADC** Analog Digital Converter.

**APA** Andode Plane Assembly.

**ARAPUCA** Argon R&D Advanced Program at UniCAMP.

**ArgoNeuT** Argon Neutrino Test Stand.

**BDT** Boosted Decision Tree.

**BNB** Booster Neutrino Beam.

**BSM** Beyond Standard Model.

**CC** Charged Current.

**CC QE** Charged Current Quasi Elastic.

**CKM matrix** Cabibbo–Kobayashi–Maskawa matrix.

**CNN** Convolutional Neural Network.

**CP** charge-parity.

**CPA** Cathode Plane Assembly.

**CRT** Cosmic Ray Tagger.

**DAR** decay at rest.

**DIF** decay in flight.

**DIS** Deep Inelastic Scattering.

**DONUT** Direct Observation of the Nu Tau.

**DUNE** Deep Underground Neutrino Experiment.

**EM** electromagnetic.

**ES** Elastic Scattering.

**Fermilab** Fermi National Accelerator Laboratory.

**GALLEX** Gallium Experiment.

**GEANT4** GEometry ANd Tracking.

**GENIE** Generates Events for Neutrino Interaction Experiments.

**ICARUS** Imaging Cosmic and Rare Underground Signals.

**KARMEN** Karlsruhe Rutherford Medium Energy Neutrino.

**KATRIN** Karlsruhe Tritium Neutrino Experiment.

**LAr** Liquid Argon.

**LArSoft** Liquid Argon Software.

**LArTPC** Liquid Argon Time Projection Chamber.

**LEP** Large Electron-Positron Collider.

**LSND** Liquid Scintillator Neutrino Detector.

**MC** Monte Carlo.

**MCT** Monte Carlo Template.

**MEC** Meson Exchange Current.

**MicroBooNE** Micro Booster Neutrino Experiment.

**MiniBooNE** Mini Booster Neutrino Experiment.

**MINOS** Main Injector Neutrino Oscillation Search.

**MIP** Minimum Ionising Particle.

**MSW** Mikheyev–Smirnov–Wolfenstein.

**NC** Neutral Current.

**NIST** National Institute of Standards and Technology.

**NuMI** Neutrinos at the Main Injector.

**P** Parity.

**PDG** Particle Data Group.

**PDS** Photon Detection System.

**PMNS** Pontecorvo-Maki-Nakagawa-Sakata.

**PMT** Photo Multiplier Tube.

**POT** Protons-On-Target.

**RENO** Reactor Experiment for Neutrino Oscillation.

**SAGE** Soviet-American Gallium Experiment.

**SBN** Short Baseline Neutrino.

**SBND** Short Baseline Near Detector.

**SCE** Space Charge Effect.

**SciBooNE** SciBar Booster Neutrino Experiment.

**SiPM** Silicon Photomultiplier.

**SK** Super Kamiokande.

**SM** Standard Model.

**SNO** Sudbury Neutrino Observatory.

**SP** Space Point.

**STEREO** Sterile Reactor Neutrino Oscillations.

**T2K** Tokai to Kamioka.

**TPB** Tetraphenyl Butadiene.

**TPC** Time Projection Chamber.

**VUV** Vacuum Ultra Violet.

# List of Figures

2.1.	Elementary particle classifications within the SM. . . . .	9
2.2.	Feynman diagrams of possible 2p2h interactions. . . . .	15
2.3.	Feynman diagrams of the CC processes most commonly expected in SBN. . . . .	18
2.4.	Feynman diagrams of the NC processes most commonly expected in SBN. . . . .	19
2.5.	Schematic of the KATRIN detector. . . . .	25
2.6.	Neutrino hierarchy. . . . .	34
2.7.	A global fit of the allowed region in $\sin^2 \theta_{12} - \Delta m_{21}^2$ space from solar experiments and the KamLAND experiment. . . . .	36
2.8.	Allowed regions in $\sin^2 \theta_{13} - \Delta m_{31}^2$ space from the RENO and Daya Bay experiments. . . . .	37
2.9.	Allowed regions in $\sin^2 \theta_{23} - \Delta m_{31}^2$ space from the SK and IceCube DeepCore experiments. . . . .	38
2.10.	Allowed regions in $\sin^2 \theta_{23} - \Delta m_{31}^2$ space from the T2K, NO $\nu$ A, MINOS and K2K experiments. . . . .	39
2.11.	Allowed regions in $\sin^2 \theta_{13} - \delta_{CP}$ space from the T2K and NO $\nu$ A experiments. . . . .	40
2.12.	LSND excess. . . . .	43
2.13.	MiniBooNE excess and the $\nu_\mu$ disappearance sensitivites from a simultaneous fit of MiniBooNE and SciBooNE data. . . . .	45
2.14.	Exclusion contour from KARMEN for $\nu_e$ and $\bar{\nu}_e$ appearance. . . .	49
2.15.	Ratio of energy spectra in the far and near detector of MINOS plus exclusion contours ( $\sin^2 \theta_{24}, \Delta m_{41}^2$ ) space. . . . .	51

2.16.	$\beta$ -decay spectrum from tritium decay with the inclusion of the presence of a sterile neutrino. . . . .	52
2.17.	$\nu_e$ disappearance exclusion contours from the KATRIN experiment. . . . .	53
2.18.	$\nu_e$ disappearance limits from ND280. . . . .	54
2.19.	$\nu_e$ disappearance limits from the IceCube experiment. . . . .	55
2.20.	Reconstructed shower energy spectra for the MicroBooNE $1\gamma 1p$ (left) and $1\gamma 0p$ (right) analyses. . . . .	57
2.21.	Reconstructed neutrino energy from MicroBooNE data using a CC QE $1e^- 1p(0\pi)$ final state topology for a $\nu_e$ analysis. . . . .	58
2.22.	Reconstructed neutrino energy from MicroBooNE data using pionless final state topology for a $\nu_e$ analysis. . . . .	59
2.23.	Reconstructed neutrino energy from MicroBooNE data using an inclusive final state topology for a $\nu_e$ analysis. . . . .	60
2.24.	$\nu_e$ appearance exclusion contours from MicroBooNE compared with the results from MiniBooNE. . . . .	61
2.25.	STEREO exclusion sensitivity at the 95% confidence level. . . . .	63
2.26.	Global analysis showing the allowed region from appearance experiments and the excluded region from disappearance experiments. . . . .	64
3.1.	SBN map. . . . .	65
3.2.	Schematic of LArTPC detector. . . . .	68
3.3.	Schematic of the BNB layout. . . . .	75
3.4.	Neutrino fluxes in SBN. . . . .	77
3.5.	Schematic of the SBN detector. . . . .	79
3.6.	CRT positioning in SBND. . . . .	80
3.7.	ARAPUCA operating principle. . . . .	82
3.8.	Image of PDS box. . . . .	83
3.9.	MicroBooNE detector. . . . .	84
3.10.	ICARUS detector. . . . .	85
3.11.	SBN oscillation probability. . . . .	88
3.12.	$\nu_e$ appearance SBN proposal sensitivity. . . . .	89
3.13.	Feynman diagrams of BSM processes. . . . .	91
4.1.	Example of a well and poorly fitted waveform. . . . .	95

4.2.	The linear relationship between deposited charge and energy. Produced from a sample of muons used for calibrating the <i>Shower Linear Energy tool</i> . . . . .	98
4.3.	ESTAR lookup curve. . . . .	100
4.4.	True vs reconstructed energy from a showering electron. The true energy has been evaluated from the hits of each shower. . . . .	102
4.5.	True vs reconstructed energy from a showering electron. The true energy is the energy of the showering electron. . . . .	103
4.6.	Comparison of the fractional shower energy separation. . . . .	104
4.7.	Fractional energy separation using the true energy of the hits with a Gaussian fitted to the distribution. . . . .	105
4.8.	Fractional energy separation using the true energy of the showering electron with a Gaussian fitted to the distribution. . . . .	106
4.9.	True vs reconstructed energy from a showering electron for the two induction planes using the ESTAR method. The true energy has been evaluated from the hits of each shower. . . . .	107
4.10.	True vs reconstructed energy from a showering photon using the ESTAR method. The true energy has been evaluated from the hits of each shower. . . . .	108
4.11.	The SBND coordinate system. . . . .	109
4.12.	The fractional energy separation as a function of $\theta_{xz}$ . . . . .	110
4.13.	Profile histograms of the fractional energy separation as a function of $\theta_{xz}$ . . . . .	110
4.14.	The fractional energy separations as a function of true energy. . . . .	111
4.15.	Profile histograms of the fractional energy separation as a function of true energy. . . . .	112
5.1.	SBN Oscillation analysis paradigm. . . . .	114
6.1.	The baseline distribution of events in the $\nu_\mu$ sample for each of the SBN detectors. . . . .	138
6.2.	Oscillation probability for different baseline parametrisations. . . . .	139
6.3.	The baseline distribution of events in the intrinsic $\nu_e$ sample for each of the SBN detectors. . . . .	140

6.4. The baseline distribution of events in the oscillated $\nu_\mu \rightarrow \nu_e$ sample for each of the SBN detectors. . . . .	140
6.5. The overall $\nu_e$ baseline distributions. . . . .	141
6.6. $+1\sigma$ variation comparison for the $f_{HornCurrent}$ , $f_{M_A^{CCRes}}$ and $f_{\Delta \rightarrow N\gamma}$ parameters. . . . .	149
6.7. The ratio between the $\pm 1\sigma$ variation from VALOR and the universes for the flux, proposal interaction and modern interaction set of systematics. . . . .	150
6.8. $\nu_e$ appearance contours overlaid on the $\chi^2$ surface. . . . .	152
6.9. SBN $\nu_e$ CC inclusive reconstructed neutrino energy spectra. . . . .	157
6.10. SBN $\nu_e$ CC inclusive reconstructed neutrino energy spectra with a $1\sigma$ prefit envelopes. . . . .	158
6.11. ICARUS $\nu_e$ CC inclusive neutrino energy spectra with a $1\sigma$ prefit and postfit envelope. . . . .	159
6.12. SBN $\nu_e$ appearance CC inclusive reconstructed neutrino energy spectra with oscillated spectrum overlaid. . . . .	161
6.13. Ratio of $\nu_e$ appearance spectra with the oscillation parameters shown on the statistical only contour. . . . .	162
6.14. SBN $\nu_e$ disappearance CC inclusive reconstructed neutrino energy spectra with oscillated spectrum overlaid. . . . .	163
6.15. Ratio of $\nu_e$ disappearance spectra with the oscillation parameters shown on the statistical only contour. . . . .	164
6.16. $\nu_e$ appearance contours with external limits. . . . .	166
6.17. $\nu_e$ disappearance contours with external limits. . . . .	167
6.18. $\nu_e$ appearance sensitivities from different detector combinations. .	168
6.19. $\nu_e$ disappearance sensitivities from different detector combinations.	169
6.20. Impact of the different systematic parameter groups on the $\nu_e$ appearance sensitivity. . . . .	170
6.21. $\nu_e$ app sensitivity reduction from different systematic groups. . .	171
6.22. $\nu_e$ appearance oscillation parameter pulls due to varying a single systematic parameter by $\pm 1\sigma$ . . . . .	173
6.23. $\nu_e$ disappearance oscillation parameter pulls due to varying a single systematic parameter by $\pm 1\sigma$ . . . . .	174

6.24. $\nu_e$ appearance exclusion contours with the inclusion of a single systematic parameter at a time. . . . .	175
6.25. $\nu_e$ disappearance exclusion contours with the inclusion of a single systematic parameter at a time. . . . .	176
6.26. $\nu_e$ appearance and disappearance allowed regions with the inclusion of a single systematic parameter at a time. . . . .	177
6.27. The $\nu_e$ appearance allowed regions with the inclusion of single systematic parameters compared to the region with the inclusion of all parameters in the associated set. . . . .	178
6.28. The $\nu_e$ disappearance allowed regions with the inclusion of single systematic parameters compared to the region with the inclusion of all parameters in the associated set. . . . .	179
6.29. Example efficiency uncertainty covariance matrices. . . . .	183
6.30. $\nu_e$ app sensitivity reduction from different systematic groups with a (2+2)% efficiency uncertainty. . . . .	185
6.31. Impact of correlated and uncorrelated efficiency systematics on the $\nu_e$ appearance sensitivity. . . . .	186
6.32. $\nu_e$ app with a 2% uncorrelated efficiency systematic for one detector only. . . . .	187
6.33. $\nu_e$ appearance with poorly constrained efficiency systematic for a set of bins. . . . .	188
6.34. $\nu_e$ disappearance sensitivity reduction from different systematic groups with a (2+2)% efficiency uncertainty. . . . .	189
6.35. Impact of correlated and uncorrelated efficiency systematics on the $\nu_e$ disappearance sensitivity. . . . .	190
6.36. $\nu_e$ disapp with a 2% uncorrelated efficiency systematic for one detector only. . . . .	191
6.37. $\nu_e$ disapp with poorly constrained efficiency systematic for a set of bins. . . . .	192
6.38. $\nu_e$ appearance exclusion contours using events from the selection motivated by EM shower reconstruction. . . . .	194
6.39. $\nu_e$ disappearance exclusion contours using events from the selection motivated by EM shower reconstruction. . . . .	195

A.1. Flux systematic parameter validation. . . . .	202
A.2. Proposal interaction systematic parameter validation. . . . .	203
A.3. Modern interaction systematic parameter validation. . . . .	204
C.1. True vs reconstructed energy from the ESTAR method without using Pandora in cheating mode. . . . .	208
C.2. Fractional separation of the shower energy with Pandora being run not in cheating mode. . . . .	208
D.1. SBN $\nu_\mu$ CC inclusive reconstructed neutrino energy spectra with oscillated spectrum overlayed. . . . .	210
D.2. $\nu_\mu$ disappearance contours with external limits. . . . .	211
D.3. Impact of correlated and uncorrelated efficiency systematics on the $\nu_\mu$ disappearance channel. . . . .	212
D.4. Impact of a 2% uncorrelated efficiency systematic on the $\nu_\mu$ disap- pearance channel for each individual detector. . . . .	213
D.5. Impact of a 2% uncorrelated efficiency systematic for one detector and 0.5% for the other two on the $\nu_\mu$ disappearance channel. . . .	214
D.6. $\nu_\mu$ disappearance with poorly constrained efficiency systematic for a set of bins. . . . .	215

# List of Tables

2.1.	3-flavour neutrino best fit values. . . . .	35
2.2.	Best fit value for sterile oscillation parameters. . . . .	41
3.1.	Hadron decay mode in the BNB. . . . .	76
3.2.	BNB flavour composition. . . . .	76
4.1.	The $\sigma$ value used in the Gaussian fit to the fractional energy separation distributions of each algorithm. . . . .	106
5.1.	Events generated and selected as part of the $\nu_e$ sample. . . . .	115
5.2.	Optical, beam focusing flux systematic parameters. . . . .	121
5.3.	Hadronic secondary interaction flux systematic parameters. . . . .	123
5.4.	Hadronic neutrino production flux systematic parameters. . . . .	124
5.5.	SBN proposal interaction cross-section systematic parameters. . .	129
5.6.	Modern interaction cross-section systematic parameters. . . . .	130
5.7.	Intranuclear hadron transport systematic parameters. . . . .	131
6.1.	Fine Reaction Modes. . . . .	144
6.2.	Coarse Reaction Modes. . . . .	145
6.3.	The phase space considered for each of the SBN analyses. . . . .	151
6.4.	$\chi^2_{critical}$ values for various confidence levels. . . . .	152
6.5.	Nominal $\nu_e$ event rate breakdown in SBND. . . . .	154
6.6.	Nominal $\nu_e$ event rate breakdown in MicroBooNE. . . . .	155
6.7.	Nominal $\nu_e$ event rate breakdown in ICARUS. . . . .	156
6.8.	Binning scheme for the efficiency uncertainties. . . . .	182
6.9.	The variable bias and resolution used to emulate reconstructed energy. . . . .	193

B.1. The active and fiducial volumes of the SBN detectors. . . . .	205
--	-----



# Chapter 1.

## Introduction

Neutrinos are a class of neutral leptonic particle that, within the Standard Model (SM), only interact via the weak interaction and gravity [1]. The idea of a neutrino was first proposed in 1930 by Pauli and was not experimentally confirmed until 1956 by Cowan and Reines [2] [3]. Two further types (or flavours) of neutrinos were discovered in 1962 and 2000 by the Alternating Gradient Synchrotron and the Direct Observation of the Nu Tau (DONUT) experiment respectively [4] [5].

Neutrinos were long thought to be massless, but results from the Super Kamiokande (SK) collaboration in 1988 showed that the flavour of a neutrino may oscillate which disabused this idea [6]. Confirmation of neutrino oscillations required non-zero neutrino masses and also helped resolve the long-standing *Solar Neutrino Problem* and the *Atmospheric Neutrino Anomaly* [7] [8]. There are, however, still a number of open questions which are of interest to particle physics that are linked to neutrinos, such as;

- The amount, if any, of charge-parity (CP) violation in the lepton sector.
- The absolute mass of the neutrinos.
- The neutrino mass hierarchy.
- The Dirac or Majorana nature of neutrinos. Since neutrinos are neutral particles, it is possible that they may be their own antiparticles (a Majorana particle), a property that would be unique to neutrinos.

- The possible existence of sterile neutrinos which are additional flavours of neutrinos that would only interact via gravity.

The Majorana nature of neutrinos would allow for neutrinoless double beta decay, a process which does not conserve lepton number [9]. Sterile neutrinos have been hinted at by a number of experiments and are expected to have right-handed helicities which is in contrast to the active neutrinos which have all been observed to have left-handed helicities [10]. The confirmation of either of these would give direct evidence of physics beyond the SM. All of these questions are under active investigation by current and future neutrino experiments.

The focus of this thesis will be on the Short Baseline Neutrino (SBN) program which is currently under development with the main goal being to either confirm or refute the existence of light sterile neutrinos. The SBN program is located at Fermilab and consists of three distinct Liquid Argon Time Projection Chamber (LArTPC) type detectors located along the Booster Neutrino Beam (BNB) beamline [11]. The Short Baseline Near Detector (SBND) will be the nearest detector to the beam source at a distance of a 110 m and is currently under construction with the expectation that data taking will begin in early 2024 [12]. The two other detectors which are part of the SBN program are the Micro Booster Neutrino Experiment (MicroBooNE) detector at 470 m and the Imaging Cosmic and Rare Underground Signals (ICARUS) detector at 600 m from the beam source, both of which are currently taking data. As mentioned, the main goal of the program will be to search for eV scale sterile neutrinos, but there are numerous other aims which include, measuring neutrino-argon interactions (due to the close proximity of SBND to the beam source, the observed statistics will far exceed that of any current dataset), developing large scale LArTPC technology and the search for possible Beyond Standard Model (BSM) processes [13]. All of these will be crucial in the development and physics analysis of future Liquid Argon (LAr) neutrino detectors such as the Deep Underground Neutrino Experiment (DUNE).

The remaining content of this thesis begins with Chapter 2, which gives a brief overview of the ideas and experiments which have led to the discovery of the three active neutrino flavours. This is then followed by a discussion of the key

physics principles describing neutrino behaviour. Finally, the experimental results which are at odds with a 3-flavour paradigm and point towards the presence of sterile neutrinos are considered along with the theory that underpins their possible existence.

Chapter 3 then gives an overview of the SBN program along with the general operating principles of a LArTPC and the BNB. The individual detector specifics and the key components of SBND, MicroBooNE and ICARUS are discussed as well as the expected physics capabilities of the program as a whole.

The different algorithms for calculating the reconstructed electromagnetic (EM) shower energy in SBND that have been developed are presented in Chapter 4. EM shower energy is an important quantity that is used in a number of areas, including calculating the reconstructed neutrino energy. The method that each of the three EM shower reconstruction algorithms that are available as part of the *LArPandoraShower* suite of tools, the *Shower Linear Energy tool*, the *Shower Num Electrons Energy tool* and the *Shower ESTAR Energy tool* use is outlined as well as comparing the reconstruction performance with truth information. The reconstruction performance is validated for showers arising from both electrons and photons as well as evaluating the performance as a function of true shower energy and the direction of a shower within the Time Projection Chamber (TPC).

The necessary inputs, choices, method and results for an oscillation analysis are outlined in Chapter 5 and Chapter 6. First the Monte Carlo (MC) event production and selection are described followed by the systematic uncertainties that are considered. The VALOR framework is used to perform the oscillation analysis with an emphasis on the  $\nu_e$  appearance and  $\nu_e$  disappearance channels. Each oscillation channel is considered as an independent analysis and sensitivities are presented from various combinations of detectors and systematic uncertainties. These include exclusion contours and allowed regions for the statistical-only case and the case where flux and interaction uncertainties have been included plus an investigation into the possible impact of additional efficiency uncertainties on the exclusion sensitivity.



# Chapter 2.

## Neutrino Physics

This chapter begins with a historical overview of neutrino discoveries in Section 2.1. Some of the key properties of neutrino physics are then discussed in Section 2.2 along with the associated experiments. These include the weak interaction, CP violation, possible mass generation mechanisms and neutrino oscillations. Finally, neutrino physics in the context of sterile neutrinos is considered with a discussion of experimental results that are either in favour of the possible existence of light sterile neutrinos and those that disfavour their existence.

### 2.1. A Brief History of Neutrinos

The neutrino was first postulated in 1930 by Pauli in an attempt to explain the continuous energy spectrum observed for the electrons from beta decay experiments [2]. At the time it was assumed that along with the nucleus, an electron was the only other product from beta decay. That is, beta decay was thought to be a two-body decay of the form,

$${}^A_Z X \longrightarrow {}^{A-1}_{Z+1} Y + e^-, \quad (2.1)$$

where  $X$  and  $Y$  are the elements undergoing the decay and the resultant element respectively. The continuous energy spectrum of the electron was puzzling as it was expected that the electron would always have a fixed kinetic energy and observing

electrons with a range of energies appeared to violate energy conservation. Pauli theorised that in addition to the electron, a neutral particle was also emitted in beta decay and that the sum of the energy of the electron and this neutral particle would be constant [2].

The (electron) neutrino was not experimentally confirmed until 1956 by Cowan and Reines who used a nuclear reactor as their neutrino source [3]. Their detector consisted of two tanks of water in which cadmium chloride had been dissolved, interlaced between three tanks of liquid scintillator. When the electron antineutrinos would interact with protons in one of the water tanks via inverse beta decay, a neutron and positron would be produced. The positron would then quickly annihilate with an electron producing two gamma rays. The cadmium would absorb the neutron and then emit a single gamma ray. The liquid scintillator was surrounded by Photo Multiplier Tubes (PMTs) and the signal for the experiment was two gamma rays from the electron-positron annihilation shortly followed by another gamma ray from the absorption of the neutron [3].

The second type of neutrino to be discovered was the muon neutrino by the Alternating Gradient Synchrotron at Brookhaven National Laboratory in 1962. The neutrinos were predominantly produced from charged pion decays which in turn were produced by firing a beam of protons at a beryllium target. The pions were directed in the direction of an iron wall during which they had the chance to decay. The iron wall was designed to absorb muons and other interacting particles. The resulting particles from neutrino interactions were then detected by an aluminium spark chamber located behind the shield. Of the selected events, the majority showed muon-like signatures (e.g. long tracks), with only a small number of events showing shower-like objects. The large disparity between the number of muon-like and electron-like events confirmed that at least two types of neutrino exist. That is the muon neutrino is distinct from the already discovered electron neutrino [4].

Following the discovery of the tau lepton in 1975 by the SLAC National Accelerator Laboratory, the tau neutrino was predicted in order to mirror the structure of the electron and muon lepton both of which have an associated neutrino [14]. The

existence of the tau neutrino was eventually confirmed by the DONUT experiment in 2000. The DONUT experiment used a neutrino beam created from the decay of charmed mesons produced by protons from the Tevatron accelerator at Fermi National Accelerator Laboratory (Fermilab). Most of the tau neutrinos were produced from the decay of the  $D_s$  meson and the decay from the resulting tau lepton [5].

It was understood that electromagnetic and strong interactions conserved parity, however, there was no sign that this was also true for weak interactions. In 1957 it was demonstrated by Wu that the weak interaction did indeed violate parity. The experiment that determined this used a sample of cobalt-60 that was placed in a solenoid and cooled to 0.01 K which meant that the nuclear spins would align parallel to the magnetic field. The cobalt would then decay via,



Under the assumption that parity was conserved, it was expected that the number of electrons emitted in the *forward* hemisphere would be equal to the number emitted in the *backwards* hemisphere with respect to the spin of the decaying cobalt because parity reverses particle momenta whilst the spin angular momentum remains unchanged. It was, however, observed that the majority of the electrons decayed in the direction opposite to the nuclear spin. This asymmetry lead the confirmation of parity violation in weak interactions [15] [16]. It has also been observed that neutrinos and antineutrinos appear to only exist as having left and right handed helicity respectively. This was demonstrated by the Goldhaber experiment (which is discussed in Section 2.2.1.1) and shows that weakly interacting neutrinos violate parity since the parity operator converts left handed neutrinos to their right handed counterpart. Additionally, charge invariance is violated since it requires identical weak interactions for both neutrinos and antineutrinos, however, charge-parity conjugation is still conserved [17] [18].

The three confirmed flavours of neutrinos ( $\nu_e, \nu_\mu, \nu_\tau$ ) are consistent with predictions from the SM. The number of active neutrinos may be determined from the decay of the Z boson since its lifetime is dependent on the number of flavours. This was

shown by the Large Electron-Positron Collider (LEP) experiment, which found the lifetime of the Z boson to be consistent with a three neutrino model [19] [20]. There have, however, been results from experiments which are inconsistent with the 3 neutrino framework. Namely the excess of events observed by the Liquid Scintillator Neutrino Detector (LSND) and Mini Booster Neutrino Experiment (MiniBooNE) experiments, the deficit of events observed by the Soviet-American Gallium Experiment (SAGE) and Gallium Experiment (GALLEX) detectors (dubbed the *Gallium Anomaly*) and the deficit of events observed from nuclear reactors (dubbed the *Reactor Anomaly*) [21] [22] [23] [24] [25] [26]. Additional neutrino flavours may exist and not contradict the statement on the lifetime of the Z boson if they have a mass greater than half that of the Z boson and/or they do not weakly interact and hence do not contribute to the decay rate of the Z boson [19]. The hypothetical neutrinos which do not weakly interact are known as *sterile* neutrinos in order to distinguish them from the *active* ones that do. Sterile neutrinos will be discussed in greater detail in Section 2.2.3.

## 2.2. Overview of Neutrino Physics

Elementary particles are classified as either fermions or bosons depending on their spin. Fermions have odd half-integer spin whereas bosons have integer spin. Fermions are then subdivided between leptons and quarks, with one of the defining differences being that quarks experience the strong force along with the other three fundamental forces whereas the leptons only experience gravity, the weak and the electromagnetic forces. Within the SM, bosons are subdivided into vector bosons which have a spin of one and scalar bosons which have a spin of zero [1]. The classification of elementary particles is shown in the flow chart in Figure 2.1.

Since neutrinos are neutral fermions, it is possible that neutrinos are their own antiparticle (a Majorana Particle). This idea was first proposed in 1937 by Majorana [17]. Within the SM, all fermions with the possible exception of neutrinos behave as Dirac fermions, that is, the particle and antiparticle are distinct [27]. With the possibility that neutrinos are Majorana in nature, it has led to the search for neutrinoless double beta decay [28]. This is a variation on ordinary double

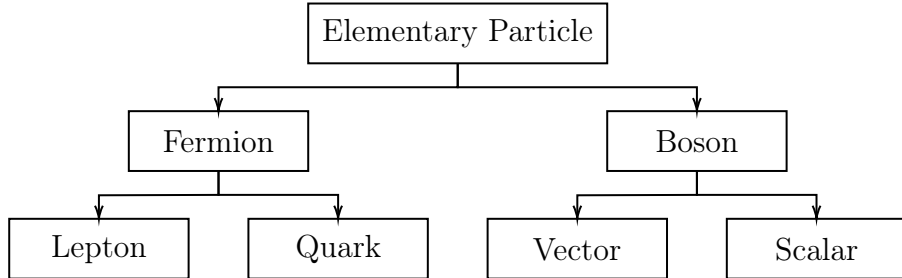


**Figure 2.1.:** Elementary particle classifications within the SM.

beta decay in which a nucleus decays by emitting two electrons simultaneously. In ordinary double beta decay, there would also be two (anti)neutrinos in the final state, however, if neutrinos are Majorana particles, it can be thought of as one nucleon emitting a neutrino and the other absorbing it hence there are no neutrinos in the final state. Observation of such a decay would confirm the Majorana nature of neutrinos and give direct evidence for physics beyond the SM since the lepton number would not be conserved. Furthermore, neutrino oscillations (which is discussed in Section 2.2.3) are at odds with the SM assumption that neutrinos are massless. With the requirement that neutrinos are indeed massive, the Dirac or Majorana nature of neutrinos is again discussed in Section 2.2.2 within the context of mass generation mechanisms [29].

### 2.2.1. Neutrinos within the Standard Model

Neutrinos are a class of leptonic particle that only interact via the weak interaction and are considered massless within the SM. It has been shown that CP violation is allowed and exists within the SM, however, the amount observed so far is insufficient to explain the matter-antimatter asymmetry. The amount of CP violation associated with neutrinos, if any, is currently unknown, but may help explain the observed asymmetry.

#### 2.2.1.1. Theory of Weak Interactions

The weak force is mediated by the charged  $W^\pm$  and neutral  $Z^0$  bosons. It is dubbed *weak* because if the strong or EM forces are also present the weak force is

usually subdominant. The active neutrinos only interact via the weak force (and gravity) which is one of the reasons they have been historically difficult to detect.

One of the key components of the weak interaction relies on the concept of helicity of particles. The helicity of a particle is defined as the projection of its spin along the propagation direction. If the spin is aligned with the direction of motion, the particle is said to be *right-handed* and has an eigenvalue equal to +1 whereas if the spin is aligned in the opposite direction a particle is said to be *left-handed* and has an eigenvalue equal to -1 [15]. It was observed by Goldhaber and others that neutrinos appear to exclusively have left-handed helicities (and right-handed helicities for antineutrinos). The experiment they used to determine this was as follows; consider the decay of an isomer of europium via electron capture to an excited state of samarium. The samarium nucleus then decays to its ground state by emitting a photon.



To conserve momentum, the excited samarium nucleus must recoil in a direction opposite to the emitted neutrino. To conserve angular momentum the spin of the neutrino and the recoiling nucleus must be in opposite directions which means that they both have the same handedness. Finally, the photon emitted will have a spin in the opposite direction to the neutrino and if the photon is emitted in a direction opposite to the neutrino direction, both will have the same helicity. The photons emitted in the direction opposite to the neutrino were identified, their helicity determined and it was found that they were all left-handed [18].

Helicity does commute with the Hamiltonian, however, it is not Lorentz invariant (for massive particles) [30]. Since massive particles travel at speeds less than  $c$ , it is always possible to boost to a frame such that the direction of motion is reversed. Spin is not affected by this which means that it is possible for the sign of the helicity to change. In contrast to helicity, chirality is a Lorentz invariant quantity that does not commute with the Hamiltonian. The chirality operator is  $\gamma^5$  and it is defined as  $i\gamma^0\gamma^1\gamma^2\gamma^3$  (i.e.  $i$  times the product of the gamma matrices). Similarly to helicity, when the chirality operator acts on the eigenfunctions  $\psi_R$  and  $\psi_L$  it

results in an eigenvalue of +1 and -1 respectively. It is commonly expressed in term of projection operators  $P_{(L,R)}$  such that,

$$\begin{aligned}\psi_L &= P_L \psi \equiv \frac{1 - \gamma^5}{2} \psi \\ \psi_R &= P_R \psi \equiv \frac{1 + \gamma^5}{2} \psi,\end{aligned}\tag{2.4}$$

where  $\psi$  is a spinor which can be written in terms of left and right chiral components,  $\psi = \psi_L + \psi_R$ . By defining  $\bar{\psi} \equiv \psi^\dagger \gamma^0$  and noting that  $P_{(L,R)}^\dagger = P_{(L,R)}$  and  $P_{(L,R)} \gamma^0 = \gamma^0 P_{(R,L)}$ , it follows that

$$\overline{\psi}_L \psi_L = \overline{\psi}_R \psi_R = 0.\tag{2.5}$$

It should be noted that for massless particles, helicity is Lorentz invariant and becomes identical to chirality [31].

The weak force has two associated types of interaction: Charged Current (CC) interactions which are mediated by the charged W boson and Neutral Current (NC) interactions which are mediated by the neutral Z boson. The defining difference is that for CC interactions current flows between the interacting fermions (i.e. charge is exchanged), whereas for NC interactions, the total flow of charge between the interacting fermions is zero. The weak component of the SM Lagrangian is therefore comprised of two terms, one representing CC and one representing NC. The CC current,  $j_{weak}^{CC}$ , and NC current,  $j_{weak}^{NC}$ , components of each of these terms may be expressed as,

$$\begin{aligned}j_{weak}^{CC} &= \frac{g}{\sqrt{2}} \overline{\psi} \gamma^\mu P_L \psi, \\ j_{weak}^{NC} &= \frac{g}{2 \cos \theta_W} \sum_{i=\nu,l} \overline{\psi}_i \gamma^\mu (g_V^i - g_A^i \gamma^5) \psi_i,\end{aligned}\tag{2.6}$$

where  $g$  is the weak coupling factor,  $\theta_W$  is the Weinberg angle,  $g_V$  is the vector coupling and  $g_A$  is the axial coupling [1] [31] [32]. The weak coupling is related to

the Fermi Constant,  $G_F$ , and the boson masses such that,

$$\begin{aligned}\frac{g^2}{8m_W^2} &= \frac{G_F}{\sqrt{2}}, \\ \frac{g^2}{8m_Z^2 \cos^2 \theta_W} &= \frac{G_F}{\sqrt{2}},\end{aligned}\tag{2.7}$$

where  $m_W$  is the mass of the W boson and  $m_Z$  is the mass of the Z boson [31].

$j_{weak}^{CC}$  has the form of a vector-axial (V–A) interaction, where the vector current is given by  $\bar{\psi}\gamma^\mu\psi$  and the axial current is given by  $\bar{\psi}\gamma^\mu\gamma^5\psi$ . The axial component remains unchanged under a parity transformation, whereas the sign of the vector component changes. Usually, the square of the amplitude is of interest, which in short means taking the square of the weak current. This results in a squared vector and axial component plus a cross-term. Since the axial and vector components behave differently under a parity transformation, this cross term leads to parity violation [1] [31].  $j_{weak}^{NC}$  does not have the form of a V–A interaction, but does again have both vector and axial components which lead to parity violation [1].

The SM is constructed such that only the left components of the field couple to the W and Z bosons so it follows that only left-handed particles (and right-handed antiparticles) can weakly interact. Neutrinos only interact via the weak force which means they are therefore produced with a left-handed chirality and since they are ultra-relativistic, for all intents and purposes they also have a left-handed helicity. Additionally, a neutrino that is present in a weak interaction is always in a definite flavour state which corresponds to the associated charged lepton (therefore conserving lepton number) [33].

### 2.2.1.2. Weak Interaction Processes

The following section outlines some of the most common CC and NC interaction processes. The associated CC and NC Feynman diagrams for these processes are shown in Figure 2.3 and Figure 2.4 respectively (the possible 2 Particles 2 Holes (2p2h) interactions are shown separately in Figure 2.2). Only examples of neutrino interactions are shown, however, these may be easily adapted to the antineutrino

case. Additionally, interaction flavours are kept general with  $l$  representing the lepton flavour.

### Elastic and Quasi-Elastic

When particles interact via elastic scattering, the initial particles do not change. Since neutrinos are neutral particles that weakly interact, NC elastic scattering being mediated by the  $Z^0$  boson may occur with a neutrino scattering off a proton via

$$\nu_l + p \rightarrow \nu_l + p. \quad (2.8)$$

Quasi-elastic scattering is similar to elastic scattering, however, charge is exchanged and therefore the interaction is mediated by the  $W^+$  boson. Charged Current Quasi Elastic (CC QE) interactions are defined by the production of a charged lepton plus a (semi-) stable baryon. The dominant form of these interactions occur when the incoming neutrino scatters off a neutron and is converted to its charged lepton counterpart whilst the neutron changes to a proton via

$$\nu_l + n \rightarrow l^- + p. \quad (2.9)$$

CC QE interactions are the most abundant in the GeV range, which is the energy range of the BNB [34].

### Resonant

At higher energies, the neutrino-nucleon interaction may cause the nucleon to be excited into a baryon resonance. The resonance will then decay back into a nucleon plus a pion. Using the Delta resonance (Delta baryon) as an example, CC interaction occur via

$$\nu_l + N \rightarrow l^- + \Delta \rightarrow l^- + N + \pi, \quad (2.10)$$

whereas NC interactions occur via,

$$\nu_l + N \rightarrow \nu_l + \Delta \rightarrow \nu_l + N + \pi. \quad (2.11)$$

In both cases,  $N$  represents some nucleon with  $\Delta$  and  $\pi$  being one of the possible Delta resonances and pions appropriate for a given interaction [34] [35].

## 2 Particles 2 Holes

Within the nuclear environment, there is a correlation between the distribution of nucleons. Therefore, some of the nucleons are bounded in pairs and these bound nucleon pairs may be thought of as being bound due to the exchange of virtual mesons.<sup>1</sup> In this type of interaction, multiple nucleons are excited in a quasi-elastic fashion. The boson may couple to either a nucleon or the meson that is being exchanged. This leads to a number of possibilities such as; 1) the boson couples to the exchanged meson (pion-in-flight diagram), 2) the boson couples at the vertex between the nucleon and exchanged meson (seagull diagram), 3) the meson exchange occurs with a virtual intermediate nucleon to which the boson couples, 4) as in case 3), but the intermediate particle is a Delta resonance instead of a nucleon. Feynman diagrams of these 4 possibilities are shown in Figure 2.2 [34] [36] [37].

---

<sup>1</sup>This exchange of mesons is sometimes also known as a Meson Exchange Current (MEC). MECs are a subset of 2p2h interaction where the W boson couples directly to the exchanged meson, however, these terms are sometimes used interchangeably.

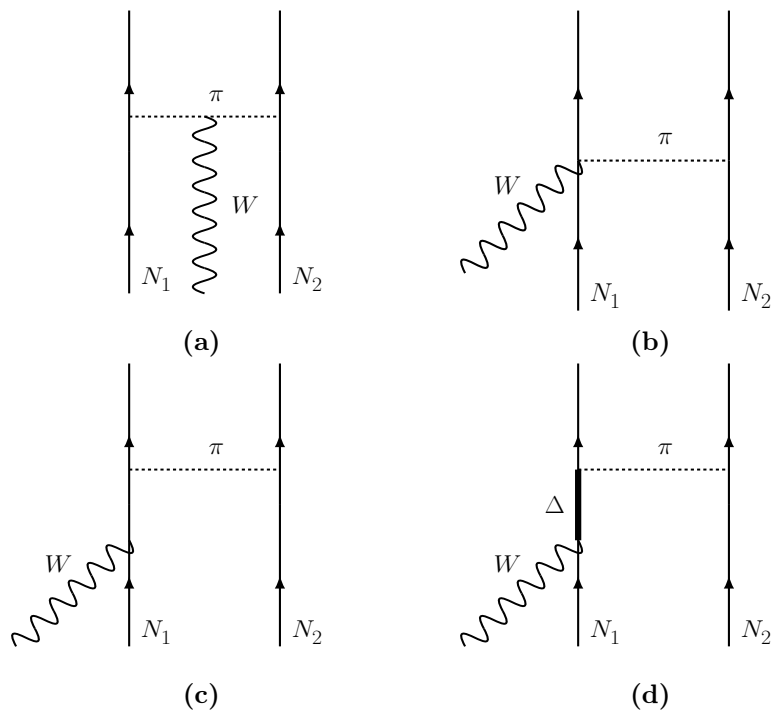


**Figure 2.2.:** Feynman diagrams of possible 2p2h interactions. The boson may couple to (a) the pion-in-flight, (b) the 2p2h vertex (seagull diagram), (c) an intermediate nucleon, (d) an intermediate Delta resonance [34].

## Deep Inelastic Scattering

At even higher energies than those for resonant interactions ( $> \mathcal{O}(5 \text{ GeV})$ ), Deep Inelastic Scattering (DIS) interactions become dominant. In DIS interactions, the neutrino scatters off individual quarks rather than the nucleon as a whole. This results in the breakup of the nucleon, but since the strong force prevents single quarks from existing, a hadronic shower  $X$  is produced [31] [34]. A CC DIS interaction occurs via

$$\nu_l + N \rightarrow l^- + X, \quad (2.12)$$

whereas the NC interaction occurs via

$$\nu_l + N \rightarrow \nu_l + X. \quad (2.13)$$

## Coherent Production

Coherent interactions occur when the neutrino scatters off the whole nucleus with a negligible momentum transfer. This results in final state particles such as pions, rho mesons or photons being produced, but leaves the target nucleus unaltered. Coherent scattering may occur for both CC and NC interactions (with pions in the final state being used as an example) via

$$\nu_l + A \rightarrow l^- + A + \pi^+ \quad (2.14)$$

and

$$\nu_l + A \rightarrow \nu_l + A + \pi^0 \quad (2.15)$$

respectively [35] [36].

## Neutrino Electron Scattering

Instead of scattering off the nucleus, neutrinos may also scatter off the electrons in an atom via,

$$\nu_l + e^- \rightarrow \nu_l + e^-. \quad (2.16)$$

This is an elastic process that has indistinguishable CC and NC components for  $\nu_e$  interactions, whereas only a NC component is allowed for  $\nu_\mu$  and  $\nu_\tau$  [31].

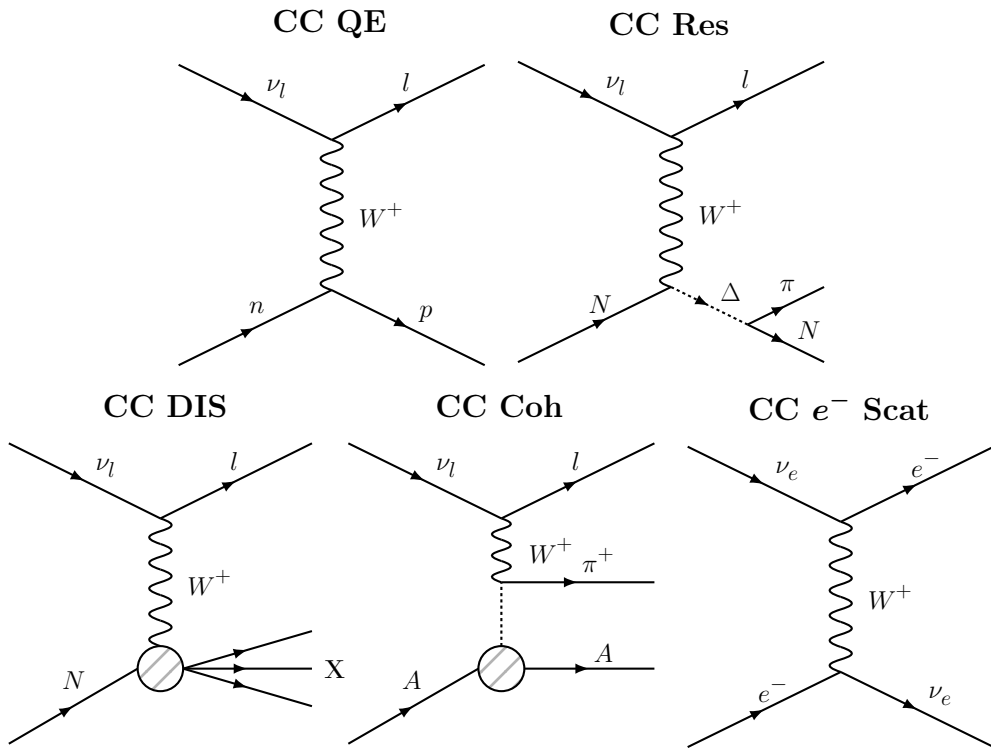


**Figure 2.3.:** Feynman diagrams of the CC processes most commonly expected in SBN.  $\nu_l$  corresponds to the neutrino with leptonic flavour  $l$ , with  $l$  typically being either an electron or a muon.  $\Delta$  denotes one of the possible Delta resonances,  $N$  denotes a nucleon,  $X$  denotes some set of final hadrons and  $A$  denotes a nucleus.

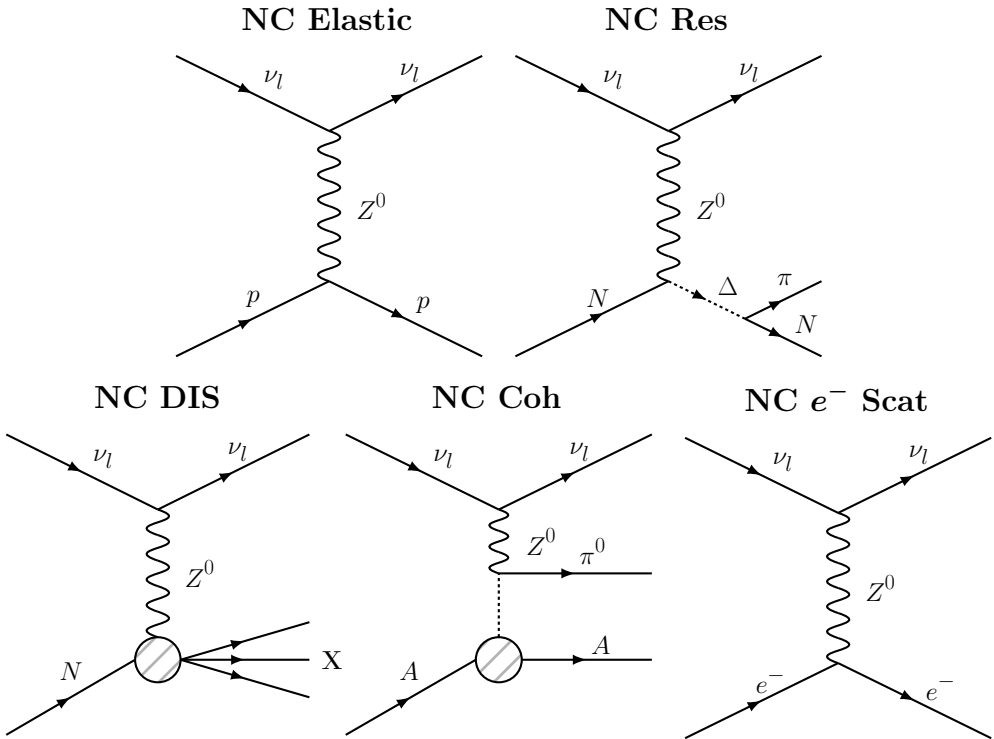


**Figure 2.4.:** Feynman diagrams of the NC processes most commonly expected in SBN.  $\nu_l$  corresponds to the neutrino with leptonic flavour  $l$ , with  $l$  typically being either an electron or a muon.  $\Delta$  denotes one of the possible Delta resonances,  $N$  denotes a nucleon,  $X$  denotes some set of final hadrons and  $A$  denotes a nucleus.

### 2.2.1.3. CP Violation

It was shown experimentally by Wu that Parity (P) conservation is violated and later by Cronin and Fitch that CP conservation is also violated [16] [38]. CP violation is one of the Sakharov conditions required to have a matter-antimatter asymmetry in the universe, however, the amount of CP violation that has currently been observed is seemingly insufficient to explain the matter-dominated universe that is observed [39].

Currently, essentially all the CP violation that has been experimentally confirmed arises from the Cabibbo–Kobayashi–Maskawa matrix (CKM matrix) in the quark sector. The CKM matrix is a unitary matrix that gives a measure of the strength of flavour changes for quarks in weak interactions. Before the discovery of the

third generation of quarks, the "CKM matrix", was simply a  $2 \times 2$  rotation matrix known as the Cabibbo matrix defined in terms of the Cabibbo angle. For a  $N \times N$  unitary matrix, there are  $(N - 1)^2$  free parameters.  $\frac{1}{2}N(N - 1)$  parameters are rotation angles (mixing angles) and the remaining  $\frac{1}{2}(N - 1)(N - 2)$  parameters (assuming Dirac particles) are complex phases resulting in CP violation. For the case of the Cabibbo matrix there is only one mixing angle, which is the Cabibbo angle and no complex phase [31] [40].

CP violation had been observed in Kaon decays as early as 1964, which was before the discovery of the bottom quark [38]. Kobayashi and Maskawa proposed the existence of a third-generation of quarks in order to explain CP violation since a  $3 \times 3$  matrix is required to generate a CP violating term [41]. The bottom quark was then experimentally discovered in 1977 later followed by the top quark to complete the quark pairs of each generation [42].

The strong interaction appears not to violate CP, despite seemingly having the possibility to do so. As there is currently no explanation for why the strong force does not violate CP, it has been dubbed the *Strong CP Problem* and is an example of fine-tuning. An experimental example of the strong force conserving CP is the case of no electric dipole moment being observed in neutrons. The electric dipole moment predicted by the strong interaction if CP were to be violated far exceeds the upper bound that has been experimentally found [43].

Since the strong interaction appears to conserve CP and the CP violation in the quark sector is insufficient to explain the matter-antimatter asymmetry observed, an additional source is required. Similar to how the CKM matrix matrix gives a measure of flavour changes in quarks, the Pontecorvo-Maki-Nakagawa-Sakata (PMNS) matrix gives a measure of mixing in neutrinos and may provide a source of CP violation in the lepton sector. The confirmation of the 3 generations of neutrinos again gives rise to a complex CP violating Dirac phase. The amount of CP violation in the neutrino sector is largely unconstrained with the current best fit value for  $\delta_{CP}/^\circ$  being  $197^{+0.21}_{-0.2}$  for the normal hierarchy and  $286^{+27}_{-32}$  for the inverted hierarchy [44]. One of the primary aims of future long baseline neutrino experiments such as Hyper-Kamiokande and DUNE will be to measure

CP violation from the Dirac phase [45] [46]. If the Majorana nature of neutrinos is confirmed, additional sources of CP violation may be present. Unlike Dirac particles, the number of phases associated with Majorana particles is given by  $\frac{1}{2}N(N - 1)$ , meaning for a three neutrino model, there are two additional CP violating terms [47].

### 2.2.2. Neutrino Masses

Assuming that the mass generation of neutrinos follows similar rules to that of other Dirac mass terms, there is motivation to try and attempt to include sterile neutrinos into theoretical models since right-handed fields are required. Some of the potential options for neutrino mass generation are discussed below. The initial mass scale for sterile neutrinos is unconstrained, however, one of the more well-motivated models is the "Type 1" *seesaw model* which attempts to explain the relative size of neutrino masses and points towards very heavy sterile neutrino masses ( $\gg 1$  eV). Variations of the Seesaw model have also been proposed that incorporate light sterile neutrinos [10].

The SM Lagrangian,  $\mathcal{L}$ , for a fermion is given by

$$\mathcal{L} = \bar{\psi}(i\gamma^\mu\partial_\mu - m)\psi \quad (2.17)$$

with the associated Euler-Lagrange equation being the Dirac equation which is given by [31]

$$(i\gamma^\mu\partial_\mu - m)\psi = 0. \quad (2.18)$$

#### 2.2.2.1. Dirac Mass

Within the SM Lagrangian, the Dirac mass term is given by  $m_D\bar{\psi}\psi$  where  $\psi$  is the Dirac spinor. By dividing this into left and right components it follows that

$$\begin{aligned} m_D\bar{\psi}\psi &= m_D(\overline{\psi_L + \psi_R})(\psi_L + \psi_R) \\ &= m_D(\overline{\psi_L}\psi_R + \overline{\psi_R}\psi_L), \end{aligned} \quad (2.19)$$

where the second step follows from Equation 2.5. Naturally, to have a non-zero Dirac mass term, particles require a left and right-handed chiral state. This is the mass generation method that all particles in the SM follow and hence why neutrinos are massless in the SM. To give the neutrino mass in this way, a field associated with a right-handed neutrino could be introduced. This would usually correspond to the left-handed neutrinos being the *active* ones, whilst the right-handed neutrinos would be considered *sterile*. Yukawa coupling can be introduced between the lepton doublets and the Higgs doublet include right handed neutrinos. After spontaneous symmetry breaking, this gives rise to a Dirac mass term which is given by,

$$m_{Di} = \frac{y_i v}{\sqrt{2}}, \quad (2.20)$$

where  $y$  is the Yukawa coupling and  $v$  gives the vacuum expectation value from the Higgs field ( $v \simeq 246$  GeV) [48]. A concern with generating neutrino masses in this way is the required size of the Yukawa coupling. To generate a mass of say 0.1 eV, the Yukawa coupling would need to be very small ( $\sim 6$  orders of magnitude less than that of the electron). This small number is sometimes considered unnatural and provides motivation to search for alternative mass mechanisms to explain the neutrino masses [31].

#### 2.2.2.2. Majorana Mass

To generate mass without the requirement of a right-handed field, it is required that the neutrino be a Majorana particle. It may be shown that

$$P_R C \overline{\psi}_L^T = C \overline{\psi}_L^T, \quad (2.21)$$

which means that  $C \overline{\psi}_L^T$  is a right handed object, where the superscript  $T$  indicates the transpose and  $C = i\gamma^2\gamma^0$  which is the charge conjugation operator. By defining  $\psi_L^C = C \overline{\psi}_L^T$ , the Majorana field mass term in the Lagrangian can be written as

$$\frac{m_L}{2} (\overline{\psi}_L^C \psi_L + \overline{\psi}_L \psi_L^C), \quad (2.22)$$

where the factor of  $1/2$  arises due to double counting. As is the case for the Dirac mass, the SM requires the introduction of additional fields to allow for spontaneous symmetry breaking [31].

### 2.2.2.3. Seesaw Mechanism

If both Dirac and Majorana mass terms are present, the mass component of the Lagrangian,  $\mathcal{L}_{mass}$ , may be written as a matrix equation. For one active and one sterile neutrino, this has the form

$$\mathcal{L}_{mass} = \frac{1}{2} \begin{pmatrix} \overline{\psi}_L^C & \overline{\psi}_R \end{pmatrix} \begin{pmatrix} m_L & m_D \\ m_D & m_R \end{pmatrix} \begin{pmatrix} \psi_L \\ \psi_R^C \end{pmatrix} + h.c. \quad (2.23)$$

where the central  $4 \times 4$  matrix is known as the mass matrix,  $\mathcal{M}$  [10]. By diagonalising  $\mathcal{M}$  into mass eigenstates,  $m_1, m_2$ , and assuming  $m_L = 0$  (since it is not allowed in the SM) and that  $m_R \gg m_D$ , the mass eigenvalues may be expressed as

$$m_1 \simeq \frac{m_D^2}{m_R} \quad (2.24)$$

$$m_2 \simeq m_R.$$

Since  $m_R \gg m_D$ ,  $m_2$  is also large and  $m_1$  is small since the value of  $m_D^2$  is suppressed by the large value of  $m_R$  in the denominator. Furthermore, the larger the value of  $m_2$ , the smaller the value of  $m_1$ . This linked relationship gives rise to the so-called Type I <sup>2</sup> *seesaw mechanism*.  $m_1$  would give the mass scale of the active neutrinos whereas  $m_2$  would be a heavy sterile neutrino. This mechanism requires neutrinos to be Majorana particles, but can be extended to include three active neutrinos and an arbitrary number of sterile neutrinos and does provide an explanation of the relative smallness of the neutrino masses compared with other SM particles [31].

---

<sup>2</sup>A number of other seesaw mechanisms exist which typically involve the exchange of a particle such as a heavy Majorana neutrino as is the case in the Type I mechanism [10].

#### 2.2.2.4. Direct Mass Measurements

The absolute neutrino mass scale is currently unknown, with only upper limits on the (effective) mass having been set.

#### Beta Decay

In  $\beta$ -decays, an electron and electron antineutrino are emitted (along with the associated nuclide). By knowing the decay energy (i.e. the difference in mass between the parent and daughter nuclide), the combined energy of the electron and neutrino are also known. If the neutrino were to be massless, the electron energy spectrum would extend to the decay energy, however, for massive neutrinos, the electron energy spectrum would have a lower maximum that is given by the decay energy minus the rest mass energy of the neutrino. By measuring the maximum possible electron energy from  $\beta$ -decays, it is possible to therefore infer the mass of electron neutrino.

This is the idea that underpins the Karlsruhe Tritium Neutrino Experiment (KATRIN) which uses tritium as the nucleus that undergoes  $\beta$ -decay. Tritium is chosen due to it having one of the lowest endpoint energies meaning the contribution from the neutrino mass will be relatively large. When tritium  $\beta$ -decays, the neutrino escapes whilst the electron is guided towards a spectrometer by magnetic fields. Within the spectrometer a retarding electric potential is applied meaning only electrons with a sufficient energy may pass through the spectrometer to the detector where they are counted. A schematic of the KATRIN detector is shown in Figure 2.5. The applied electric potential may be varied which allows the number of detected electrons to be counted as a function of energy. By combining the two physics runs, KATRIN has set an upper limit of 0.8 eV on the effective electron antineutrino mass at a 90% confidence limit [49].

#### Neutrinoless Double Beta Decay

Assuming that neutrinos are Majorana in nature, neutrinoless double beta decay ( $0\nu\beta\beta$ ) should be an observable process in certain nuclei. The half-life,  $T^{0\nu}$ , of nuclei undergoing  $0\nu\beta\beta$  is given by,

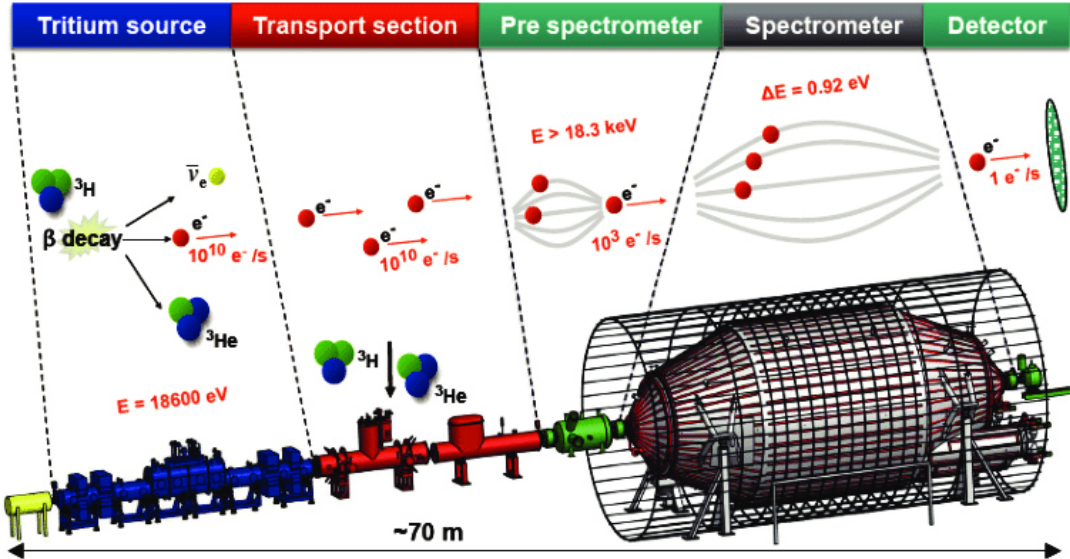


**Figure 2.5.:** Schematic of the KATRIN detector [50].

$$[T^{0\nu}]^{-1} = G^{0\nu} \cdot |M^{0\nu}|^2 \cdot \langle m_{\beta\beta} \rangle^2, \quad (2.25)$$

where,  $G^{0\nu}$ , is the phase space factor,  $M^{0\nu}$ , is the matrix element and  $\langle m_{\beta\beta} \rangle = \sum_i U_{ei}^2 m_i$ , which is the effective Majorana neutrino mass. Both  $G^{0\nu}$  and  $M^{0\nu}$  depend on the nucleus that undergoes the decay. Therefore, measuring the half-life of a  $0\nu\beta\beta$  decay process gives a measure of the effective neutrino mass.

Some of the most stringent limits on the effective neutrino mass are provided by the KamLAND-Zen experiment. As of yet no  $0\nu\beta\beta$  has been observed and a lower bound on the half-life of  $2.3 \times 10^{26}$  years at a 90% confidence level which equates to an upper limit on the effective Majorana neutrino mass of 36 – 156 meV, depending on the model of the nuclear matrix element [51].

## Cosmological Constraints

A number of cosmological observations have put upper bounds on the neutrino mass. Some of the most stringent constraints come from the *Planck* collaboration which measured temperature anisotropies in the cosmic microwave background [32] [52].

By combining *Planck* data with that from baryon acoustic oscillations (BAO) and Type Ia supernovae the total neutrino mass,  $\sum m_\nu = m_1 + m_2 + m_3$ , may be constrained to have an upper mass limit as low as 0.11 eV at the 95% confidence level [32] [52].

### 2.2.3. Neutrino Oscillations

Another unique property of neutrinos are their ability to oscillate. That is, the neutrino flavour may change as it propagates. This phenomenon was first proposed by Pontecorvo in 1957 [53]. In the following years, this work was built upon by Maki, Nakagawa, Sakata and Pontecorvo himself [54].

#### 2.2.3.1. 3 Flavour Oscillation Phenomenology

Neutrino oscillations is one of the key topics in the field and this thesis. The remainder of this section will discuss the theory of neutrino oscillations in both vacuum and in matter. The three flavour states ( $\nu_e$ ,  $\nu_\mu$ ,  $\nu_\tau$ ) have already been established, but it is expected that the neutrino mass states ( $\nu_1$ ,  $\nu_2$ ,  $\nu_3$ ) are distinct in order to explain neutrino oscillations. The flavour eigenstate of a neutrino is what is observed, however, each flavour state is a superposition of the three mass states. As a neutrino propagates, the relative phase between the mass states is continuously changing. When a neutrino then interacts, the mass states may have a relative phase that is different to that when the neutrino was created. At the point of interaction, the flavour superposition will then collapse into a single flavour and this is what is then detected. This is the mechanism which allows neutrino flavours to oscillate.

## Oscillations in Vacuum

The transformation between the flavour and mass states is expressed as

$$|\nu_\alpha\rangle = \sum_k U_{\alpha k}^* |\nu_k\rangle, \quad (2.26)$$

where  $\alpha \in (e, \mu, \tau)$ ,  $k \in (1, 2, 3)$  and  $U$  is a unitary matrix. In the case of three flavour neutrino oscillations,  $U$ , is known as the PMNS mixing matrix which is a  $3 \times 3$  matrix representing the three different states [31]. The PMNS matrix is parameterised in terms of three mixing angles ( $\theta_{12}, \theta_{13}, \theta_{23}$ ) and a single physical CP violating phase,  $\delta_{cp}$ <sup>3</sup>, as

$$\begin{aligned} U &= \begin{pmatrix} U_{e1} & U_{e2} & U_{e3} \\ U_{\mu 1} & U_{\mu 2} & U_{\mu 3} \\ U_{\tau 1} & U_{\tau 2} & U_{\tau 3} \end{pmatrix} \\ &= \begin{pmatrix} 1 & 0 & 0 \\ 0 & c_{23} & s_{23} \\ 0 & -s_{23} & c_{23} \end{pmatrix} \begin{pmatrix} c_{13} & 0 & s_{13} e^{-i\delta_{cp}} \\ 0 & 1 & 0 \\ -s_{13} e^{i\delta_{cp}} & 0 & c_{13} \end{pmatrix} \begin{pmatrix} c_{12} & s_{12} & 0 \\ -s_{12} & c_{12} & 0 \\ 0 & 0 & 1 \end{pmatrix} \end{aligned} \quad (2.27)$$

where  $c_{kj} = \cos \theta_{kj}$ ,  $s_{kj} = \sin \theta_{kj}$  and the other 5 phases of the unitary matrix have been absorbed by rephasing the lepton fields.

The time-dependent Schrödinger equation is given by

$$i \frac{d}{dt} |\nu_k(t)\rangle = H |\nu_k(t)\rangle, \quad (2.28)$$

and since neutrino mass states are eigenstates of the Hamiltonian,  $H$ , it follows that the solution to Equation 2.28 is given by a plane wave solution

$$|\nu_k(t)\rangle = e^{-iE_k t} |\nu_k\rangle. \quad (2.29)$$

---

<sup>3</sup>Here we are assuming that neutrinos are Dirac particles. If they are Majorana particles the PMNS matrix would have two additional phases as described in Section 2.2.1.3.

The amplitude of a transition,  $A_{\nu_\alpha \rightarrow \nu_\beta}(t)$ , is defined as the projection of the final state onto the initial state, so for flavour oscillations, the amplitude is given by

$$A_{\nu_\alpha \rightarrow \nu_\beta}(t) \equiv \langle \nu_\beta | \nu_\alpha(t) \rangle. \quad (2.30)$$

The probability of transition,  $P_{\nu_\alpha \rightarrow \nu_\beta}(t)$ , is then given by the absolute square of the amplitude

$$P_{\nu_\alpha \rightarrow \nu_\beta}(t) = |A_{\nu_\alpha \rightarrow \nu_\beta}(t)|^2. \quad (2.31)$$

It follows from Equation 2.26 and Equation 2.29 that

$$|\nu_\alpha(t)\rangle = \sum_k U_{\alpha k}^* e^{-iE_k t} |\nu_k\rangle \quad (2.32)$$

and that the transition amplitude is given by

$$A_{\nu_\alpha \rightarrow \nu_\beta}(t) = \sum_k U_{\alpha k}^* U_{\beta k} e^{-iE_k t} \quad (2.33)$$

where the fact that  $\langle \nu_j | \nu_k \rangle = \delta_{jk}$  has been used since the mass eigenstates are orthonormal. It then follows that the oscillation probability is given by

$$P_{\nu_\alpha \rightarrow \nu_\beta}(t) = \sum_{k,j} U_{\alpha k}^* U_{\beta k} U_{\alpha j} U_{\beta j}^* e^{-i(E_k - E_j)t}. \quad (2.34)$$

Under the assumption that neutrinos are relativistic, the mass state energy,  $E_k$ , may be expressed in terms of the neutrino energy,  $E$ ,

$$E_k = \sqrt{|\vec{p}|^2 + m_k^2} \simeq E + \frac{m_k^2}{2E}. \quad (2.35)$$

By noting that the mass splitting,  $\Delta m_{kj}^2$ , is defined as

$$\Delta m_{kj}^2 = m_k^2 - m_j^2 \quad (2.36)$$

and that for highly relativistic particles  $t \approx L$ , where  $L$  is known as the baseline (i.e. the distance the neutrino has travelled), the oscillation probability may be

written as

$$P_{\nu_\alpha \rightarrow \nu_\beta}(L, E) = \sum_{k,j} U_{\alpha k}^* U_{\beta k} U_{\alpha j} U_{\beta j}^* e^{-i \frac{\Delta m_{kj}^2 L}{2E}}. \quad (2.37)$$

It should be noted that what neutrino experiments probe is the mass splitting and not the absolute neutrino masses. Finally, for the special case where only two neutrinos contribute to mixing in a non-negligible way, the oscillation probability may be simplified to

$$P_{\nu_\alpha \rightarrow \nu_\beta} = \begin{cases} \sin^2(2\theta) \sin^2(\frac{\Delta m^2 L}{4E}), & \nu_\alpha \neq \nu_\beta \\ 1 - \sin^2(2\theta) \sin^2(\frac{\Delta m^2 L}{4E}), & \nu_\alpha = \nu_\beta, \end{cases} \quad (2.38)$$

where the mixing matrix has been reduced to a rotation matrix [31].

## Oscillations in Matter

The neutrino oscillations discussed so far have assumed that the neutrinos are propagating in a vacuum. It was shown by Wolfenstein that neutrinos propagating in matter experience a potential due to coherent forward scattering with the electrons and nucleons [55]. This potential may be thought of as an effect similar to the index of refraction in a material [31]. Both CC and NC scattering may occur, however, CC scattering may only occur for electron neutrinos whereas NC scattering may occur for all active neutrino flavours equally. The total Hamiltonian for neutrinos propagating in matter,  $H_T$ , is, therefore, the vacuum Hamiltonian as seen in Equation 2.28 plus the Hamiltonian due to the additional potential from matter effects,  $H_m$ . That is

$$H_T = H + H_m \quad \text{with, } \begin{aligned} H|\nu_k\rangle &= E_k |\nu_k\rangle \\ H_m|\nu_k\rangle &= V_m |\nu_k\rangle, \end{aligned} \quad (2.39)$$

where  $V_m$  is the effective potential the neutrinos are subjected to [31]. In the three neutrino mass basis,

$$H_T = \frac{1}{2E} \begin{pmatrix} m_1^2 & 0 & 0 \\ 0 & m_2^2 & 0 \\ 0 & 0 & m_3^2 \end{pmatrix} + U^\dagger \begin{pmatrix} V_e & 0 & 0 \\ 0 & 0 & 0 \\ 0 & 0 & 0 \end{pmatrix} U, \quad (2.40)$$

where  $V_e$  is the effective potential due to CC scattering. It may be shown that

$$V_e = \pm \sqrt{2}G_F n_e, \quad (2.41)$$

where the positive value is used for neutrinos and the negative value for antineutrinos,  $G_F$  is the Fermi constant and  $n_e$  is the electron density in the medium. The NC component is omitted since it contributes equally to all neutrino flavours and therefore has no impact on the oscillation probability [32].

If only two neutrino species are considered, the mass splitting in matter,  $\Delta m_m^2$ , is given by

$$\Delta m_m^2 = m_{2m}^2 - m_{1m}^2 = \Delta m^2 \sqrt{(\cos 2\theta - A/\Delta m^2)^2 + \sin^2 2\theta}, \quad (2.42)$$

and the mixing angle in matter,  $\theta_m$ , is given by

$$\tan 2\theta_m = \frac{\sin 2\theta}{\cos 2\theta - A/\Delta m^2}, \quad (2.43)$$

where  $\Delta m^2$  and  $\theta$  are the vacuum mass splitting and vacuum mixing angle respectively and  $A \equiv 2EV_e$ . The oscillation probability is the same as is shown in Equation 2.38, but substituting in the relevant matter mixing angle and mass splitting instead of the vacuum values. It should be noted that if  $\theta = 0$ , then  $\theta_m = 0$ , which means that oscillations in matter can only occur if oscillations in a vacuum are possible. Furthermore, if  $A = \Delta m^2 \cos 2\theta$ , Equation 2.43 diverges. This critical value of  $A$  is known as the Mikheyev–Smirnov–Wolfenstein (MSW) resonance and corresponds to  $\theta_m = \pi/4$ , which means that the oscillation probability is maximal.

Therefore, for any non-zero vacuum oscillation probability, there exists a value of  $A$  where the matter oscillation probability is a 100% [32].

### 2.2.3.2. 3 Flavour Oscillation Experimental Results

One of the first experimental results to eventually be explained by neutrino oscillations was the Homestake experiment. This was an experiment in the 1960s that was designed to count the number of solar neutrinos. The crux of the experiment was to fill an underground tank with dry-cleaning fluid (perchloroethylene) since it contains chlorine. The solar neutrinos would be detected by inverse beta decay via



where the argon would be extracted and counted as it decayed. From this, the number of interacting electron neutrinos was determined, however, this number was consistently about a third of the number expected by solar predictions. This inconsistency was later dubbed the *Solar Neutrino Problem* [7].

The ratio of muon to electron neutrinos produced in the atmosphere from the decay of pions and muons was also studied. The predicted rate of neutrinos in the atmosphere was thought to be well understood, however a number of experiments, the most notable of which, SK, all observed ratios significantly below the expected value. This indicated a deficit in the observed muon neutrinos or an excess in electron neutrinos (or both). Mirroring the solar neutrino problem, these observations were dubbed the *Atmospheric Neutrino Anomaly* [8].

The SK detector consists of a tank of 50,000 tons of pure water. Neutrino interactions with either electrons or nuclei from the water may result in Cherenkov light that is detected by PMTs surrounding the detector. In addition to measuring the ratio of atmospheric neutrinos, SK was also able to measure the zenith angle of the incoming neutrinos. This allowed the observed and predicted number of neutrinos to be compared as a function of the zenith angle. It was noted that the number of electron neutrinos agreed reasonably well with the expected value across all angles whereas for low-energy muon neutrinos there was a deficit of

events for all angles and for high-energy muons, there was a deficit of events for zenith angles corresponding to large distances travelled (e.g. neutrinos which travelled through the earth and into the detector from below). The observed rate of high energy muons at angles corresponding to travelling directly down from the atmosphere to the detector agreed with predicted values [6].

The results published by SK in 1998 allowed the atmospheric neutrino anomaly to be reconciled with neutrino oscillations and was the first time neutrino oscillations were confirmed to have been observed [6]. Shortly after, in 2001, the Sudbury Neutrino Observatory (SNO) resolved the solar neutrino problem by again explaining the deficit in observed electron neutrinos as a result of neutrino oscillations. The SNO detector was designed with the intention of being able to measure the total neutrino flux (the sum of all three flavours) and the electron neutrino flux in isolation. The detector consisted of a tank of heavy water. Solar neutrinos have sufficient energy to interact via NC interactions with the deuterium in the heavy water regardless of neutrino flavour,

$$\nu + d \longrightarrow \nu + p + n. \quad (2.45)$$

Neutrinos of any flavour may also interact via Elastic Scattering (ES),

$$\nu + e^- \longrightarrow \nu + e^-. \quad (2.46)$$

ES interactions are subdivided into CC and NC components, but since only  $\nu_e$ 's are above the threshold energy for CC interactions, there is no CC component for  $\nu_\mu$  or  $\nu_\tau$ . Therefore, all active neutrino flavours contribute equally to the NC ES flux, but the flux of  $\nu_e$ 's is enhanced due to also having a CC component [56]. Finally, only electron neutrinos may interact via CC,

$$\nu_e + d \longrightarrow p + p + e^-, \quad (2.47)$$

therefore this channel only measured the flux of  $\nu_e$ . Confirmation that the flux of  $\nu_e$  was less than the flux from the NC or ES channels coupled with the fact

that the  $\nu_e$  flux was in agreement with previous solar neutrino experiments was sufficient to resolve the solar neutrino problem [57].

It is understood from oscillation experiments that  $\Delta m_{21}^2$ , known as the solar mass splitting, is equal to  $\sim 7.5 \times 10^{-5}$  eV<sup>2</sup> and that  $|\Delta m_{31}^2|$ , known as the atmospheric mass splitting, is equal to  $\sim 2.4 \times 10^{-3}$  eV<sup>2</sup>. The sign of the atmospheric mass splitting is, however, unknown i.e. it is an open question whether  $m_3$  is the heaviest or the lightest neutrino mass state. This leads to two possibilities, the so-called *normal hierarchy* where the neutrino mass states increase from  $m_{1 \rightarrow 2 \rightarrow 3}$  or the *inverted hierarchy* where the mass states increase from  $m_{3 \rightarrow 1 \rightarrow 2}$ . This is shown graphically in Figure 2.6.

A key feature of Equation 2.43 is that the matter mixing angle depends on the sign of  $\Delta m^2$ . This is not the case for vacuum oscillations. The sign of  $\Delta m_{21}^2$  was determined using the matter effect by comparing day and night solar neutrino interactions in SK. An asymmetry in the day/night flux of  $\nu_e$ 's was observed because during the night, neutrinos travel through the earth and thus the matter effect becomes relevant whereas during the day, the matter that neutrinos traverse is negligible. Therefore, unlike vacuum oscillations, matter oscillations may be used to determine the neutrino mass hierarchy within a 2-flavour approximation.

The nature of the neutrino hierarchy has major impacts on several areas. Within the inverted hierarchy, there is a lower bound on the Majorana mass of the electron neutrino mass. If neutrinoless double beta decay experiments can put bounds on the neutrino mass below this, the inverted hierarchy may be ruled out (under the assumption that neutrinos are Majorana in nature). Alternatively, if the inverted hierarchy is realised, neutrinoless double beta decay experiments are promising ways to determine whether neutrinos are Majorana particles or not. There are also a number of theories which predict either the normal or inverted hierarchy, so determining the hierarchy will be a strong motivator in determining the credibility of a given theory [58].

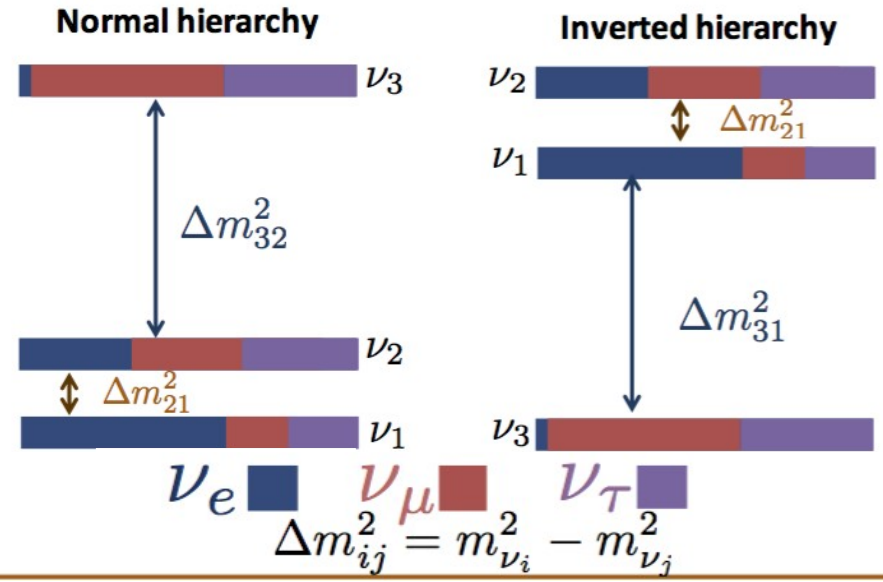


**Figure 2.6.:** Diagrammatic representation of the normal hierarchy (left) and the inverted hierarchy (right). The flavour contributions to each mass state are illustrated by the different colours [59].

The best fit values for oscillation parameters and the CP violating phase from a 3-flavour neutrino framework are shown in Table 2.1 for both the normal and inverted hierarchy<sup>4</sup>. The numbers have been provided by the 2020 edition of the Particle Data Group (PDG) collaboration [60]. Some of the experiments that have determined the oscillation parameters are discussed below.

---

<sup>4</sup>The factor of 2 in the argument of  $\sin^2 2\theta$  is sometimes absorbed into the mixing angle as is the case for example in Figures 2.7–2.11.

Parameter	Best Fit	
	Normal Hierarchy	Inverted Hierarchy
$\sin^2 2\theta_{12}$	$0.307 \pm 0.013$	$0.307 \pm 0.013$
$\sin^2 2\theta_{13}$	$(2.20 \pm 0.07) \times 10^{-2}$	$(2.20 \pm 0.07) \times 10^{-2}$
$\sin^2 2\theta_{23}$	$0.546 \pm 0.021$	$0.539 \pm 0.022$
$\Delta m_{21}^2$	$(7.53 \pm 0.18) \times 10^{-5} \text{ eV}^2$	$(7.53 \pm 0.18) \times 10^{-5} \text{ eV}^2$
$\Delta m_{32}^2$	$(2.453 \pm 0.033) \times 10^{-3} \text{ eV}^2$	$(-2.536 \pm 0.034) \times 10^{-3} \text{ eV}^2$
$\delta_{CP}$	$1.36^{+0.20}_{-0.16}\pi \text{ rad}$	$1.36^{+0.20}_{-0.16}\pi \text{ rad}$

**Table 2.1.:** The best fit values for 3-flavour neutrino oscillation parameters from the 2020 PDG [60].

### $\Delta m_{21}^2$ and $\sin^2 2\theta_{12}$

The  $\Delta m_{21}^2$  and  $\sin^2 2\theta_{12}$  parameter values are determined from the solar neutrino experiments, Homestake, GALLEX/GNO, SAGE, Borexino, phases I-IV of SK and the three phases of SNO [61] [24] [62] [63] [64] [65] [66] [67] [68] [69]. The relevant standard solar model used in the combined analysis is AGSS09 [70]. In addition to the solar experiments, the KamLAND experiment, which detected neutrinos from a number of nuclear reactors over a long baseline ( $\sim 180$  km), also measured the solar mass splitting and mixing angles. [71] [72] [73] A global fit of the solar experiments and the KamLand results are shown in Figure 2.7 along with a combined fit of the two [74]. The best fit point from the allowed region of the solar experiments is highly disfavoured by the KamLAND experiment, however, the 99% confidence level allowed regions do overlap.

### $\Delta m_{31}^2$ and $\sin^2 2\theta_{13}$

Parameters  $\Delta m_{31}^2$  and  $\sin^2 2\theta_{13}$  may again be determined from reactor neutrino experiments, but with baselines considerably shorter than that of KamLAND. The Reactor Experiment for Neutrino Oscillation (RENO) experiment consists of two identical detectors which detect electron antineutrinos from 6 reactors. The 6 reactors are part of a linear 1.3 km array with equal spacing between each reactor and the two RENO detectors are 294 m and 1383 m either side of the centre of the reactor array. The  $\bar{\nu}_e$ 's are detected in a liquid scintillator doped with gadolinium

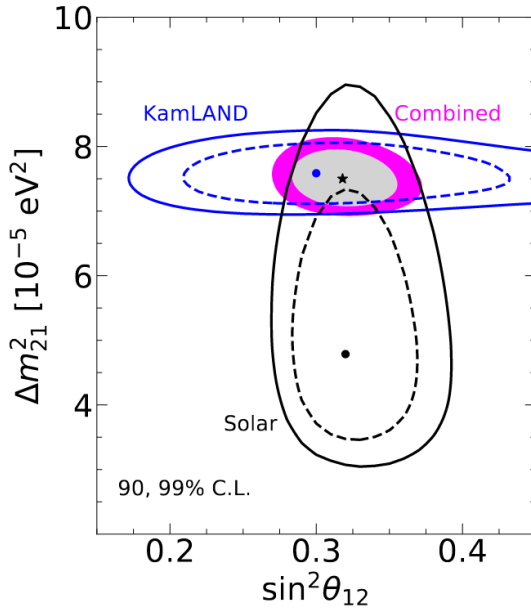


**Figure 2.7.:** A global fit of the allowed region in  $\sin^2 \theta_{12}$  –  $\Delta m_{21}^2$  space from solar experiments, the KamLAND experiment and a combination of the two. The relevant best fit points are also shown [74].

via inverse beta decay [75]. After a 2900 day data taking period, RENO determined that the mixing angle,  $\sin^2 2\theta_{13} = 0.0892 \pm 0.0063$  and that the mass splitting,  $|\Delta m_{ee}^2| = (2.74 \pm 0.12) \times 10^{-3} \text{ eV}^2$ , where  $|\Delta m_{ee}^2| = \cos^2 \theta_{12} \Delta m_{31}^2 + \sin^2 \theta_{12} \Delta m_{32}^2$  [76].

The Daya Bay experiment consists of eight antineutrino detectors which measure the oscillation probability from the antineutrinos produced from the Daya Bay nuclear plant. There are two associated near experimental halls each of which houses two of the detectors and one far experimental hall which houses the other four detectors. The near detectors have a baseline of  $\sim 0.3\text{--}1.3$  km whereas the far detectors have a baseline of  $\sim 1.5\text{--}1.9$  km [74]. The detectors consist of a cylindrical gadolinium-doped liquid scintillator target which is surrounded by undoped liquid scintillator which is in turn surrounded by PMTs. After 1958 days of data taking, Daya Bay determined that the mixing angle,  $\sin^2 2\theta_{13} = 0.0856 \pm 0.0029$  and that the mass splitting,  $|\Delta m_{ee}^2| = (2.522^{+0.068}_{-0.070}) \times 10^{-3} \text{ eV}^2$  [77].

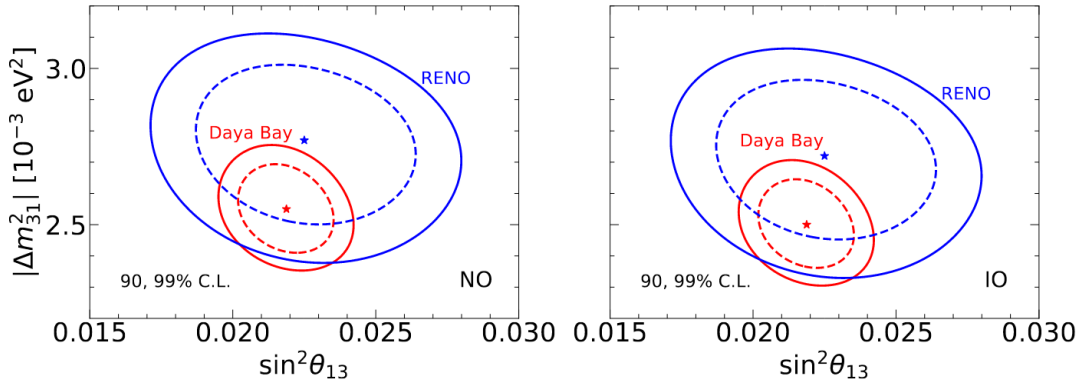


**Figure 2.8.:** Allowed regions from a global analysis in  $\sin^2 \theta_{13} - \Delta m^2_{31}$  space from the RENO and Daya Bay experiments for the normal hierarchy (left) and the inverted hierarchy (right). The associated best fit points are also shown [74].

The allowed regions and best fit points from both RENO and Daya Bay are shown in Figure 2.8 for both the normal and inverted hierarchy, but since neither experiment is sensitive to the mass ordering the results are essentially the same. Much of the allowed parameters space is consistent between the two experiments [74].

### $\Delta m^2_{31}$ , $\sin^2 2\theta_{23}$ and $\delta_{CP}$

Both atmospheric neutrino experiments and accelerator neutrino experiments may be used to measure  $\Delta m^2_{31}$  and  $\sin^2 2\theta_{23}$ . Atmospheric experiments detect neutrinos resulting from cosmic rays interacting in the atmosphere which result in particle showers that produce a neutrino flux that is comprised mainly of  $\nu_\mu^{(-)}$ 's. Long baseline accelerator experiments typically utilise a semi-pure  $\nu_\mu^{(-)}$  beam and measure  $\nu_\mu^{(-)}$  disappearance as well as  $\nu_e^{(-)}$  appearance. In addition to  $\Delta m^2_{31}$  and  $\theta_{23}$ , accelerator experiments are sensitive to  $\theta_{13}$  and  $\delta_{CP}$  [74].

The SK experiment measured both the  $\nu_\mu$  disappearance and  $\nu_e$  appearance channels using atmospheric neutrinos with the former providing most of the sensitivity to  $\Delta m^2_{31}$  and  $\theta_{23}$ . It was determined that  $\Delta m^2_{31} = 2.63^{+0.10}_{-0.21} \times 10^{-3} \text{ eV}^2$  for the normal hierarchy and that  $\Delta m^2_{31} = 2.53^{+0.14}_{-0.08} \times 10^{-3} \text{ eV}^2$  for the inverted hierarchy. Within the normal hierarchy, it was determined that  $\sin^2 2\theta_{23} = 0.425^{+0.051}_{-0.034}$  in the first octant and  $\sin^2 2\theta_{23} = 0.588^{+0.030}_{-0.062}$  in the second octant and

within the inverted hierarchy, it was determined that  $\sin^2 2\theta_{23} = 0.425^{+0.075}_{-0.027}$  in the first octant and  $\sin^2 2\theta_{23} = 0.575^{+0.034}_{-0.075}$  in the second octant [78].

The IceCube Deep Core experiment, which consists of 5160 PMTs located  $\sim 2$  km below the geographic South Pole recorded over  $10^5$  atmospheric neutrinos per year via Cherenkov radiation in the ice. Following 3 years of data taking where both track and shower like events were observed, it was determined that the mixing angle,  $\sin^2 2\theta_{23} = 0.53^{+0.09}_{-0.12}$  and that the mass splitting,  $|\Delta m_{31}^2| = 2.72^{+0.19}_{-0.20} \times 10^{-3}$  eV $^2$  [79]. The allowed region from the global analysis of SK and IceCube DeepCore are shown in Figure 2.9 for both the normal and inverted hierarchy [74].

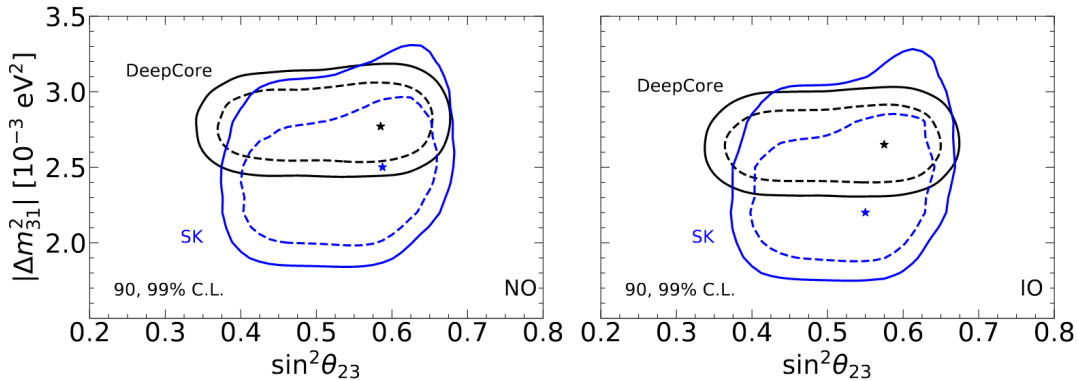


**Figure 2.9.:** Allowed regions from a global analysis in  $\sin^2 \theta_{23} - \Delta m_{31}^2$  space from the SK and IceCube experiments for the normal hierarchy (left) and the inverted hierarchy (right). The associated best fit points are also shown [74].

The Tokai to Kamioka (T2K) experiment observed events from a beam exposure of  $1.97 \times 10^{21}$  Protons-On-Target (POT) in neutrino mode and  $1.63 \times 10^{21}$  POT in antineutrino mode. The neutrino beam is produced at the J-PARC facility and then travels 295 km to the SK detector. There are also two near detectors as part of the T2K experiment located at 280 m from the beam source, INGRID and ND280, which monitor the beam direction and stability and measure the flux of neutrinos respectively. 318 muon events and 137 antimuon events were observed as well as 94 electron events and 16 antielectron events. Additionally 14 electron events along with an electron from pion decays were observed [80]. Similarly, the NO $\nu$ A experiment consists of a near detector and far detector located 1 km and 810 km from the beam source respectively and utilises the Fermilab NuMI

neutrino beam. Both detectors are comprised of PVC cells containing liquid scintillator with the near detector having a mass of 290 tons whereas the far detector has a mass of 14,000 tons. NO $\nu$ A observed 212 muon and 82 electron events from a beam exposure of  $1.3.6 \times 10^{20}$  POT whilst running in neutrino mode and 137 antimuon and 16 antielectron events from a beam exposure of  $12.5 \times 10^{20}$  POT whilst running in antineutrino mode [81] [82]. The global analysis for the allowed region in  $\sin^2 \theta_{23} - \Delta m_{31}^2$  space (which assumes no prior on  $\theta_{13}$ ) are shown in Figure 2.10 using data from T2K and NO $\nu$ A experiments as well as Main Injector Neutrino Oscillation Search (MINOS) and the K2K experiment for both the normal and inverted hierarchy [83] [84] [85]. Figure 2.11 shows the allowed region in  $\sin^2 \theta_{13} - \delta_{CP}$  space from the global analysis using data from T2K and NO $\nu$ A. Results from the MINOS and K2K experiments are not included as they are not sensitive to  $\theta_{13}$  or  $\delta_{CP}$  [74].

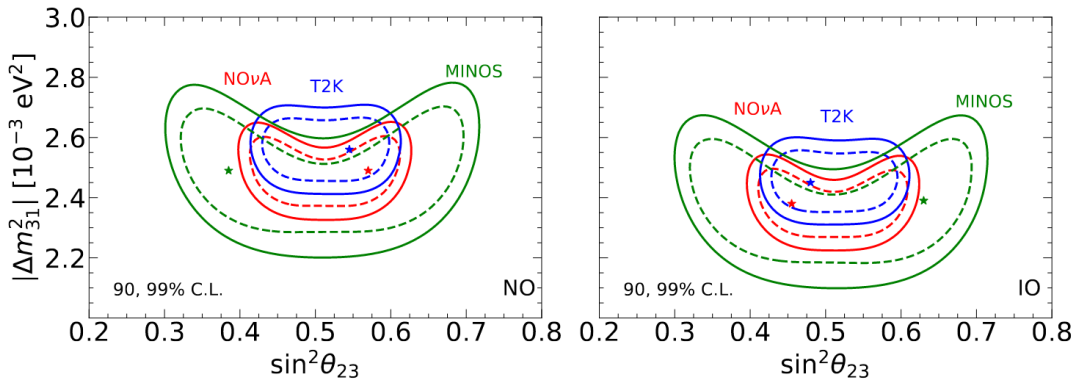


**Figure 2.10.:** Allowed regions from a global analysis in  $\sin^2 \theta_{23} - \Delta m_{31}^2$  space from the T2K, NO $\nu$ A, MINOS and K2K experiments for the normal hierarchy (left) and the inverted hierarchy (right). The associated best fit points are also shown [74].

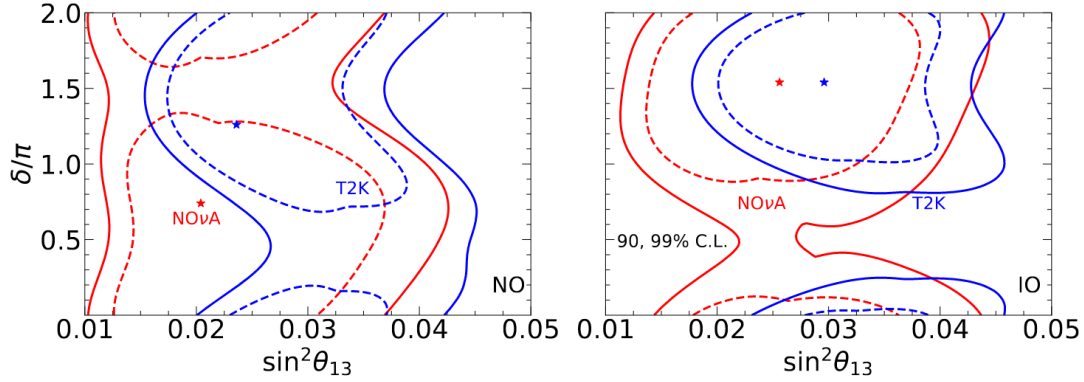


**Figure 2.11.:** Allowed regions from a global analysis in  $\sin^2 \theta_{13} - \delta_{CP}$  space from the T2K and NO $\nu$ A experiments for the normal hierarchy (left) and the inverted hierarchy (right). The associated best fit points are also shown [74].

### 2.2.3.3. Sterile Neutrino Oscillation Phenomenology

An overview of the physics describing neutrino oscillations within the active sector was presented in Section 2.2.3. This approach may be extended to include an arbitrary number of additional neutrino states by expanding the PMNS matrix to include the desired number of sterile neutrinos

$$U_{\text{sterile}} = \begin{pmatrix} U_{e1} & U_{e2} & U_{e3} & U_{e4} & \dots \\ U_{\mu 1} & U_{\mu 2} & U_{\mu 3} & U_{\mu 4} & \dots \\ U_{\tau 1} & U_{\tau 2} & U_{\tau 3} & U_{\tau 4} & \dots \\ U_{s1} & U_{s2} & U_{s3} & U_{s4} & \dots \\ \vdots & \vdots & \vdots & \vdots & \ddots \end{pmatrix}. \quad (2.48)$$

For simplicity, often only the special case with one sterile neutrino that is heavier than the three active neutrinos is considered. This is known as the (3 + 1) neutrino framework which takes into account the three usual active neutrinos with the addition of one sterile neutrino. Within a (3 + 1) framework and assuming that  $\Delta m_{41}^2 \gg |\Delta m_{31}^2|, \Delta m_{21}^2$ , short baseline oscillation are well represented by the two flavour oscillation probability,

$$P_{\nu_\alpha \rightarrow \nu_\beta} = \delta_{\alpha\beta} - 4|U_{\alpha\beta}|^2(\delta_{\alpha\beta} - |U_{\alpha\beta}|^2) \sin^2 \left( \frac{\Delta m_{41}^2 L}{4E} \right), \quad (2.49)$$

where  $\delta_{\alpha\beta}$  is the Kronecker delta between states  $\alpha$  and  $\beta$ ,  $U_{\alpha\beta}$  are the relevant entries from the PMNS matrix and  $\Delta m_{41}^2$  is the mass splitting involving the sterile neutrino state [13].

When performing a search for sterile neutrinos, typically there are three channels, one or more of which may be probed (plus their corresponding antineutrino variants). For each of these channels, the relevant PMNS matrix elements are parameterised in terms of mixing angles such that,

$$\nu_\mu \text{ disappearance } (\nu_\mu \rightarrow \nu_\mu) : \sin^2 2\theta_{\mu\mu} \equiv 4|U_{\mu 4}|^2(1 - |U_{\mu 4}|^2) \quad (2.50)$$

$$\nu_e \text{ appearance } (\nu_\mu \rightarrow \nu_e) : \sin^2 2\theta_{\mu e} \equiv 4|U_{\mu 4}|^2|U_{e 4}|^2 \quad (2.51)$$

$$\nu_e \text{ disappearance } (\nu_e \rightarrow \nu_e) : \sin^2 2\theta_{ee} \equiv 4|U_{e 4}|^2(1 - |U_{e 4}|^2). \quad (2.52)$$

It should be noted that  $\nu_e$  appearance depends on  $U_{\mu 4}$  and  $U_{e 4}$ , which  $\nu_\mu$  and  $\nu_e$  disappearance depend on respectively. The observation of  $\nu_e$  appearance would therefore automatically imply that  $\nu_\mu$  and  $\nu_e$  disappearance is also present. Additionally, this allows these parameters to be over-constrained [13]. The current global best fit values for the three mixing angles and the mass splitting term,  $\Delta m_{41}^2$  are outlined in Table 2.2.3.3.

Oscillation Parameter	Best Fit Value
$\sin^2 2\theta_{\mu\mu}$	0.07157
$\sin^2 2\theta_{\mu e}$	0.0009809
$\sin^2 2\theta_{ee}$	0.05310
$\Delta m_{41}^2$	1.32 eV <sup>2</sup>

**Table 2.2.:** The global best fit values for the (3 + 1) sterile neutrino oscillation parameters [86].

#### 2.2.3.4. Sterile Neutrino Oscillation Experimental Motivation

There have been a number of experimental results which are not consistent with oscillations in a three-neutrino model. Most of these anomalous results can be explained by oscillations with one or more eV scale neutrinos pointing towards the existence of at least one light sterile neutrino. Experiments reporting these anomalous results include, LSND and MiniBooNE as well as data from reactor and gallium based experiments all of which are in tension with the null results reported from other experiments [86]. These results which are seemingly in favour of eV scale sterile neutrinos are discussed below along with the null results from Karlsruhe Rutherford Medium Energy Neutrino (KARMEN), MINOS, KATRIN, T2K, IceCube, MicroBooNE, Sterile Reactor Neutrino Oscillations (STEREO).

#### LSND

The LSND experiment involved a close to 800 MeV proton beam which produced mainly  $\pi^+$  and was designed to focus on the search for  $\bar{\nu}_\mu \rightarrow \bar{\nu}_e$  appearance where the  $\bar{\nu}_\mu$ 's were a result from the decay of antimuons which in turn were produced from the decay at rest (DAR)  $\pi^+$ .  $\nu_\mu \rightarrow \nu_e$  oscillations were also studied resulting from decay in flight (DIF) modes. The detector consisted of a tank filled with 167 tons of liquid scintillator (mineral oil) positioned 30 m from the neutrino beam source. An array of 1220 PMTs were located on the inside of the tank and were used to detect both Cerenkov and scintillation light. Data was taken over a period of 6 years between 1993 and 1998.

The electron selection was designed to minimise backgrounds from cosmic rays whilst still being able to identify electron events from neutrino interactions. For the  $\bar{\nu}_\mu \rightarrow \bar{\nu}_e$  oscillations, the energy range considered is 20–60 MeV, whereas for the  $\nu_\mu \rightarrow \nu_e$  oscillations an energy range of 60–200 MeV was used. The minimum energy of 20 MeV was chosen because the  $\beta$ -decay of  $^{12}\text{B}$  resulting from the capture of  $\mu^-$  on  $^{12}\text{C}$  in the target would lead to a significant background. The maximum energy of 200 MeV was chosen as above this there would be a significant background from  $\pi^+ \rightarrow e^+ + \nu_e$  decays compared to the oscillation signals.

The  $\bar{\nu}_e$  appearance signal was identified from the  $\bar{\nu}_e + p \rightarrow e^+ + n$  reaction with the signature of the reaction being the energy of the  $e^+$  and the energy of a gamma as a result of neutron capture on a free proton. The LSND experiment observed an excess of  $87.96 \pm 22.46_{(stat)} \pm 6.0_{(syst)}$  events from  $\bar{\nu}_e + p \rightarrow e^+ + n$  reactions which corresponds to a  $3.8\sigma$  excess which is shown in Figure 2.12. The  $\nu_\mu \rightarrow \nu_e$  did not show a clear excess in events, but was still consistent with the  $\bar{\nu}_\mu \rightarrow \bar{\nu}_e$  signal [21]. This was the first experiment to point towards the existence of an eV-scale neutrino.

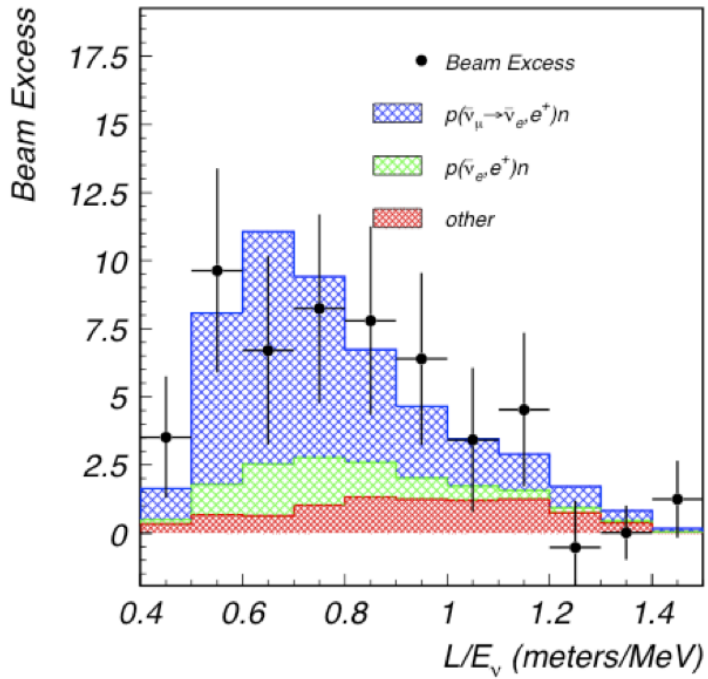


**Figure 2.12.:** The LSND excess as a function of the neutrino  $L/E$  value. Events require a positron in the energy range  $20 < E < 60$  MeV and a likelihood ratio of  $> 10$  that the associated gamma was correlated (i.e.  $\frac{\mathcal{L}_\gamma(\text{correlated})}{\mathcal{L}_\gamma(\text{accidental})} > 10$ ) [21].

## MiniBooNE

MiniBooNE collected data from the BNB operating in both neutrino and antineutrino mode from 2002–2017. The BNB is described in detail in Section 3.2. The detector was a sphere 12.2 m in diameter containing 818 tonnes of mineral oil. Charged particles in the oil would result in both Cherenkov and scintillation light that would be detected by 1520 PMTs that surrounded the detector. The baseline from the BNB source to MiniBooNE was 541 m.

Similar to LSND, MiniBooNE was searching for  $\nu_e^{(-)}$  appearance from a predominantly  $\nu_\mu^{(-)}$  beam. In neutrino mode, MiniBooNE observed an excess of  $381.2 \pm 85.2$  CC QE events from an exposure of  $12.84 \times 10^{20}$  POT which corresponds to a  $4.5\sigma$  excess. This is shown in Figure 2.13. Combining this with the antineutrino data from an exposure of  $11.27 \times 10^{20}$  POT, an excess of  $460.5 \pm 99.0$  CC QE events ( $4.7\sigma$ ) were observed. The excess of (anti)neutrinos considered were in the energy range of  $200 < E_\nu < 1250$  MeV. The minimum energy of 200 MeV was chosen due to requiring a visible Cherenkov ring from a muon as a result of  $\nu_\mu$  CC QE interactions which were used to constrain  $\nu_e$  events, whereas the maximum value of 1250 MeV was chosen to give a small value of L/E. Some of the most substantial backgrounds are due to  $\nu_e^{(-)}$  events resulting from muon and kaon decays as well as NC  $\pi^0$  and NC  $\gamma$  events which mimic signal events. The intrinsic  $\nu_e^{(-)}$ 's are constrained by a joint fit of  $\nu_\mu^{(-)}$  and  $\nu_e^{(-)}$  assuming that  $\nu_\mu^{(-)}$  disappearance is negligible, whilst the  $\nu_e^{(-)}$ 's from kaon decays are constrained by results from SciBar Booster Neutrino Experiment (SciBooNE) and fits to kaon production data. Events from NC interactions are constrained using MiniBooNE data.

A two neutrino model was assumed so that a comparison with LSND data can be made, however, this results in the appearance and disappearance data not being compatible with one another. This may be resolved by assuming a different model to the 3+1 neutrino framework. The results are consistent with those seen by LSND and again point to the existence of additional neutrino flavours beyond the three predicted by the SM [22].

The combined sensitivity results for a  $\nu_\mu$  disappearance search at the 90% confidence limit from the MiniBooNE and SciBooNE collaborations and a MiniBooNE

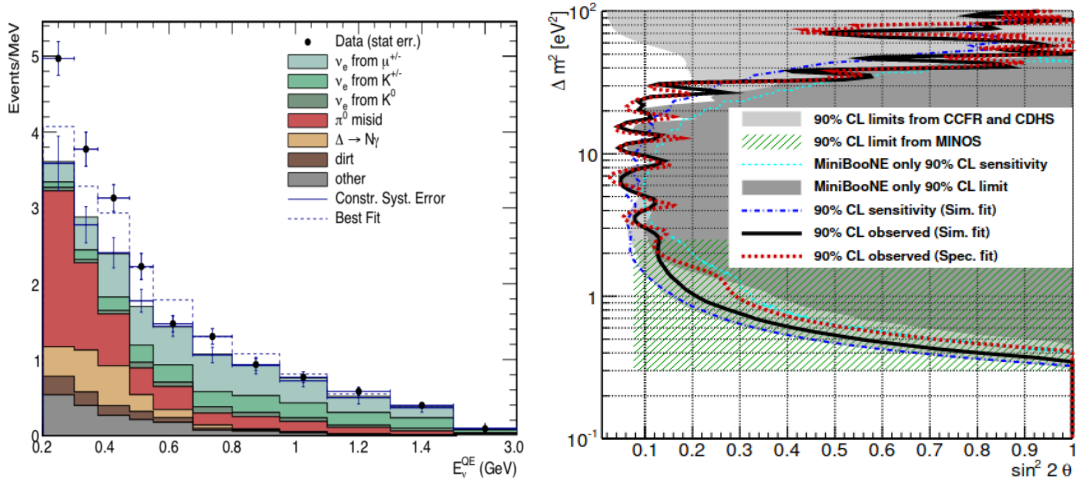


**Figure 2.13.:** Left: The MiniBooNE excess from  $\nu_e$  CC QE events. The best fit line assumed two neutrino oscillations [22]. Right:  $\nu_\mu$  disappearance exclusion contours obtained from the simultaneous fit of MiniBooNE and SciBooNE data along with other experimental results [87].

only analysis (along with other experimental results) are shown on the right of Figure 2.13 [87].

## Gallium Anomaly

The *Gallium Anomaly* refers to the apparent deficit of electron neutrinos observed by placing radioactive sources which decay via electron capture in the solar neutrino experiments, SAGE and GALLEX. The GALLEX experiment utilised two separate  $^{51}\text{Cr}$  neutrino sources. The key measured quantity was the production of  $^{71}\text{Ge}$  due to the transformation of  $^{71}\text{Ga}$  via inverse beta decay. The strength of the  $^{51}\text{Cr}$  neutrino sources was measured directly and via the production of  $^{71}\text{Ge}$ . The combined ratio of the strength of the two sources was found to be  $0.93 \pm 0.08$  [23]. A later reanalysis of the results from GALLEX with new technical data gave a ratio of  $0.902 \pm 0.078$  [24]. Similar to the GALLEX experiment, the SAGE experiment also compared the strength of a neutrino source from direct measurements and the production of  $^{71}\text{Ge}$ . SAGE used both a  $^{51}\text{Cr}$  and a  $^{37}\text{Ar}$  source. SAGE observed a ratio  $0.95 \pm 0.12$  for the  $^{51}\text{Cr}$  source and a ratio of  $0.79_{-0.10}^{+0.09}$  for the  $^{37}\text{Ar}$  source. The weighted average from the results from the two sources from SAGE and the reevaluated values from the two GALLEX sources is  $0.88 \pm 0.05$  [25]. This is consistent with a  $2.3\sigma$  significance and is consistent with  $\bar{\nu}_e$  disappearance due to mixing with a sterile neutrino [88].

## Reactor Anomaly

The *Reactor Anomaly* refers to the apparent deficit of electron antineutrinos produced from neutron-rich fission products such as  $^{235}\text{U}$ ,  $^{238}\text{U}$ ,  $^{239}\text{Pu}$  and  $^{241}\text{Pu}$  undergoing  $\beta$ -decay. For most cases, this involves placing a detector within a 100m of a reactor and measuring the ratio of observed to predicted event rates. The predicted event rates rely on antineutrinos produced from many isotopes with some of decay pathways not being well understood, thus accurately modelling them becomes difficult. The two principle antineutrino flux modelling methods are the *summation* method and the *beta conversion* method [26] [89].

The *summation* method relies on  $\beta$ -decay information from nuclear databases. Antineutrino contributions from individual  $\beta$ -decay branches are first calculated followed by a weighted sum from all the fissioning isotopes. A clear source of

uncertainty with this method is the reliance on nuclear databases which are sometimes incomplete or inaccurate [89].

The *beta conversion* method uses virtual decay branches that sum up to experimentally found beta spectrum for each fissioning isotope. The individual beta spectrum from each branch is converted to a antineutrino spectrum and then summed together to produce an antineutrino spectrum for each fissioning isotope.  $\beta$ -decay measurements have been performed for  $^{235}\text{U}$ ,  $^{239}\text{Pu}$  and  $^{241}\text{Pu}$  [89].

Flux data from experiments in the 1980's to the 2000's was generally in agreement with the best predictions of the time. In 2011, new antineutrino flux predictions were performed using the *summation* method for  $^{238}\text{U}$  and the *beta conversion* method for  $^{235}\text{U}$ ,  $^{239}\text{Pu}$  and  $^{241}\text{Pu}$  by Mueller *et al.* and Huber. These new predictions were sufficiently different from previous estimations to lead to a  $\sim 5\%$  discrepancy between predictions and measurements which has been dubbed the reactor anomaly [89].

The average ratio of observed to predicted events is  $0.943 \pm 0.023$ . It is acknowledged that the reactor fluxes may not be perfectly understood which could be the cause for such a deficit, however, it should be noted that other experiments have observed similar deficits for comparable L/E ranges [26].

## KARMEN

The KARMEN experiment is associated with the ISIS neutron source which produced  $\nu_\mu$ 's,  $\bar{\nu}_\mu$ 's and  $\nu_e$ 's with a mean baseline of 17.7 m from source to detector. The  $\nu_\mu$ 's are produced mono-energetically at 30 MeV from decay at rest  $\pi^+$ 's whereas the  $\bar{\nu}_\mu$ 's and  $\nu_e$ 's have a continuous energy spectrum up to 52.8 MeV from decay at rest  $\mu^+$ . The lifetime of pions is much shorter than muons, meaning  $\nu_\mu$ 's are easily distinguished from  $\bar{\nu}_\mu$ 's and  $\nu_e$ 's since there is a significant time difference between the detection of the two. The KARMEN detector consists of 65 tons of liquid scintillator used to detect neutrinos. 7000 tons of steel along with a two layer veto counter provides shielding against cosmic and beam related backgrounds [90].

KARMEN investigated both the  $\nu_\mu \rightarrow \nu_e$  and  $\bar{\nu}_\mu \rightarrow \bar{\nu}_e$  oscillation channels with the latter being the more sensitive channel due to no  $\bar{\nu}_e$ 's being produced by ISIS (other than by contamination) meaning that any  $\bar{\nu}_e$ 's detected would be from oscillations. The  $\bar{\nu}_e$ 's would be detected via inverse beta decay with protons in the scintillator with the signal being a prompt  $e^+$  followed by a delayed  $\gamma$  as a result of neutron capture [90].

After applying the selection criteria, to the data collected between February 1997 to March 2001, 15  $\bar{\nu}_e$  candidate events were observed with the total background expectation being  $(15.8 \pm 0.5)$  events. Assuming that mixing is maximal and that  $\Delta m^2 \geq 100$  eV<sup>2</sup> an oscillation signal of  $(2913 \pm 269)$  events would be expected. The selection criteria include considering the timing information of the ISIS beam meaning the  $e^+$  must be detected within 0.6 and 10.6  $\mu s$  of the beam window, the neutron capture must occur with a time delay between 5 and 300  $\mu s$ , the  $e^+$  must deposit a minimum of 16 MeV of visible energy which removes neutral current contributions and the neutron capture event must have an energy below 8 MeV [90].

$\nu_e$ 's are detected by CC interactions with carbon-12 via



with the requirement that the  $\nu_e$ 's are detected within the  $\nu_\mu$  beam time window. The signature for a  $\nu_e$  interaction is a prompt monoenergetic  $e^-$  with 12.5 MeV kinetic energy (which is calculated from the initial energy of  $\nu_\mu$  and the mass difference between  ${}^{12}\text{C}$  and  ${}^{12}\text{N}$ ) and a delayed  $e^+$  with energies up to 16.3 MeV (which is the  $\beta$ -decay end-point energy). In order to distinguish the  $\nu_e$ 's from oscillations and those due to the decay of  $\mu^+$ , oscillated  $\nu_e$ 's were only considered between 0–110 ns and 330–440 ns after the beam-on-target. Additionally, the  $e^+$  was required to have an energy between 3.5 and 16.5 MeV during a time window of 0.5–36.5 ms after the beam time. From the data collected between June 1990 and May 1994, 3 candidate events were found. With an oscillation signal, 158.4 events are to be expected [91].

No evidence of oscillations was found from either channel, with the number of events observed being consistent with background predictions. 90% confidence limit contours for both  $\nu_\mu \rightarrow \nu_e$  and  $\bar{\nu}_\mu \rightarrow \bar{\nu}_e$  are shown on the left of Figure 2.14 from four years of data collected between 1990 and 1994. An updated  $\bar{\nu}_\mu \rightarrow \bar{\nu}_e$  90% confidence level exclusion contour is shown on the right of Figure 2.14 from the data collected between 1997 and 2001 as well as external results from LSND, Bugey and CCFR [21] [92] [93] [90] [91].

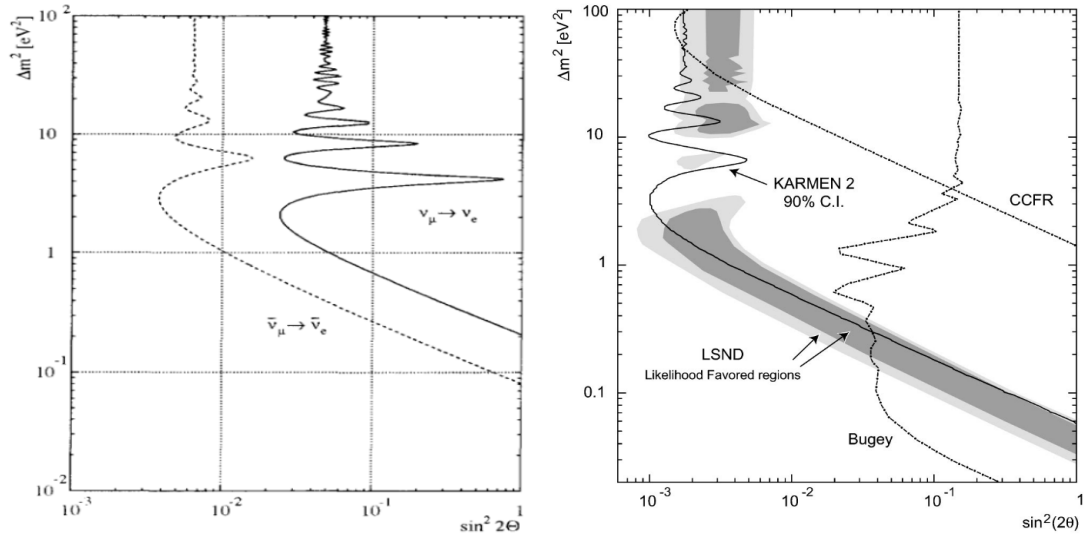


**Figure 2.14.:** Left: Exclusion contours for  $\nu_\mu \rightarrow \nu_e$  and  $\bar{\nu}_\mu \rightarrow \bar{\nu}_e$  oscillations from data taken between 1990 and 1994 [91]. Right: Updated Exclusion contours for  $\bar{\nu}_\mu \rightarrow \bar{\nu}_e$  oscillations from data taken between 1997 and 2001. External limits from LSND, Bugey and CCFR are also shown [90].

## MINOS

The MINOS experiment consisted of a near detector at a baseline of 1.04 km and a far detector at a baseline of 735 km and utilised the Neutrinos at the Main Injector (NuMI) beam. The NuMI beam is muon-neutrino dominated and has a peak energy of 3 GeV. Therefore, MINOS focused on measuring  $\nu_\mu$  CC and NC interactions from an exposure of  $10.56 \times 10^{20}$  POT. Both detectors consist of steel scintillator calorimeters that measure the charge and momentum of muons by the use of magnetic field.

The NC sample is selected by requiring that activity from interactions is contained on fewer than 47 steel scintillator planes as well as requiring the reconstructed track (if present) to not extend more than 5 planes beyond the hadronic shower. Additional criteria are applied to account for the reconstruction not being able to resolve coincident events. Only events that are rejected by the NC selection are considered for the CC selection. The CC sample requires a contained interaction with a single outgoing muon track and the possible presence of hadronic shower.

For the oscillation analysis, MINOS assumed a (3+1) framework and used the full oscillation probabilities in vacuum (it was determined that including the matter effect had a negligible effect). Based on global data,  $\sin^2 \theta_{12}$  and  $\Delta m_{41}^2$  were set to 0.307 and  $7.54 \times 10^{-5}$  eV<sup>2</sup> respectively.  $\sin^2 \theta_{13}$  was set to 0.022 which was based on data from reactor experiments and  $\theta_{13}$  was set to 0 since it had negligible impact on the analysis. The analysis also has negligible sensitivity to  $\delta_{13,14,24}$ , so all three were also set to 0. Parameters  $\theta_{23}$ ,  $\theta_{24}$ ,  $\theta_{34}$ ,  $\Delta m_{32}^2$  and  $\Delta m_{41}^2$  are what are fit for in the analysis.

Since MINOS is sensitive to  $10^{-3} \lesssim \Delta m^2 \lesssim 10^2$  eV<sup>2</sup>, sterile oscillations may occur in both detectors. Due to this, the ratio of the energy spectrum in the far detector to the near detector are considered instead of using the near detector to predict the spectrum of the far detector. Both the CC and NC spectra are shown on the left of Figure 2.15 and show good agreement with a three neutrino model. Three flavour oscillations are consistent with the data at the 54.7% confidence level with no indication of the presence of sterile neutrinos [94].

Following the results from MINOS, it's successor, MINOS+, was exposed to  $5.80 \times 10^{20}$  POT with a peak  $\nu_\mu$  energy of 7 GeV. MINOS+ used the same detectors as MINOS, but the analysis used a two detector fit instead of the ratio of energy spectra to obtain the sensitivity contours. The exclusion contours are produced in  $(\sin^2 \theta_{24}, \Delta m_{41}^2)$  space where parameters  $\theta_{23}$ ,  $\theta_{34}$  and  $\Delta m_{31}^2$  are varied to minimise the fit statistic with the results from the combined data from MINOS and MINOS+ being shown on the right of Figure 2.15 [95].

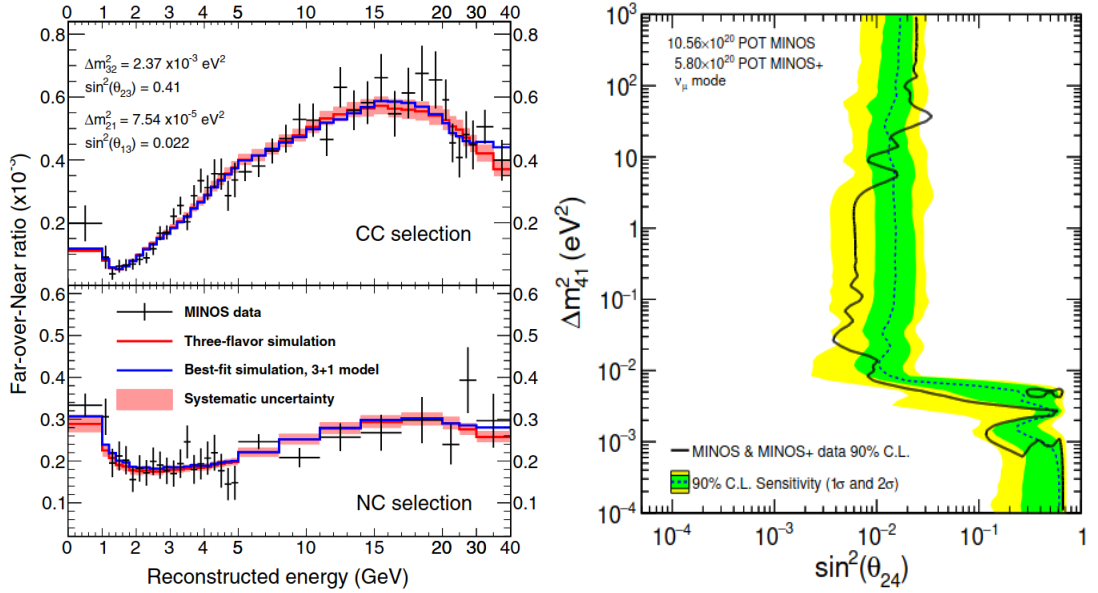


**Figure 2.15.:** Left: The ratio of energy spectra from the far detector to the near detector of MINOS for both CC and NC samples [94]. Right: Exclusion contours from MINOS at the 90% and 95% confidence level along with external limits [95].

## KATRIN

In addition to measuring the neutrino mass scale, the KATRIN experiment has also produced exclusion contours for the possible existence of light sterile neutrinos from a (3+1) model. The experimental setup is essentially the same as that described in Section 2.2.2.4. The  $\beta$ -decay spectrum produced from tritium decay depends on the mass of the emitted electron neutrino which is a superposition of the relevant mass states. Due to the active mass states,  $m_{1,2,3}$ , having relatively similar masses their superposition can not be probed by KATRIN, however, if a sterile neutrino with mass significantly greater than  $m_{1,2,3}$  is present this would be observable. The total differential  $\beta$ -decay spectrum,  $\frac{d\Gamma}{dE}$ , would be given by the superposition of the standard spectrum from just the three active neutrinos with  $m_\beta$  being the corresponding effective electron neutrino mass and the spectrum from a sterile neutrino with mass  $m_s$  as,

$$\frac{d\Gamma}{dE} = \cos^2 \theta \frac{d\Gamma}{dE}(m_\beta^2) + \sin^2 \theta \frac{d\Gamma}{dE}(m_s^2), \quad (2.55)$$

where  $\theta$  is the active-sterile mixing angle. The signature for the presence of a light sterile neutrino would be a *kink* like feature in the  $\beta$ -decay spectrum as is shown in Figure 2.16. Due to the large mass of the  $m_s$  it can be seen that the endpoint energy from the sterile neutrino is much less than that of the active neutrinos. Therefore, the spectrum would also be distorted at energies below the active neutrino endpoint energy minus  $m_s$ . [96].

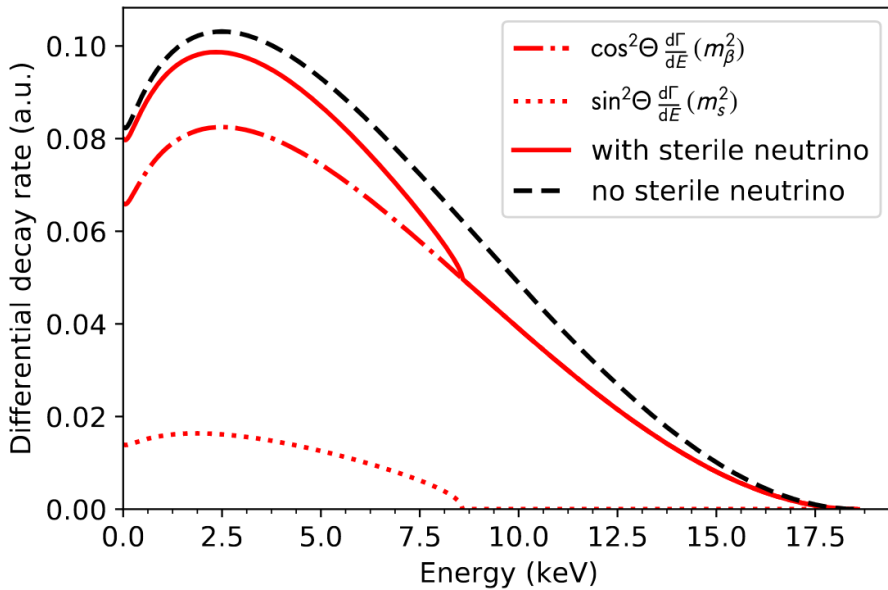


**Figure 2.16.:** The  $\beta$ -decay spectrum from the decay of tritium showing the change in shape from due to the presence of 10 keV sterile neutrino and mixing angle of  $\sin^2 \theta = 0.2$  [96].

From its second data collection period, KATRIN has analysed  $3.76 \times 10^6$   $\beta$ -electrons from tritium decays and was sensitive to  $m_4^2 \lesssim 1600$  eV $^2$  and  $|U_{e4}|^2 \gtrsim 6 \times 10^{-3}$ . No signal indicating the presence of light sterile neutrinos was observed and exclusion contours were produced at the 95% confidence level. Two separate analyses were performed: one where the effective electron neutrino mass,  $m_\nu^2$ , was fixed to zero (which is justified since  $m_4 \gg m_{1,2,3}$ ) and one where  $m_\nu^2$  is an unconstrained nuisance parameter. The exclusion contours from both cases are shown in Figure 2.17 for data from the first and second campaign as well as both campaigns combined [97].

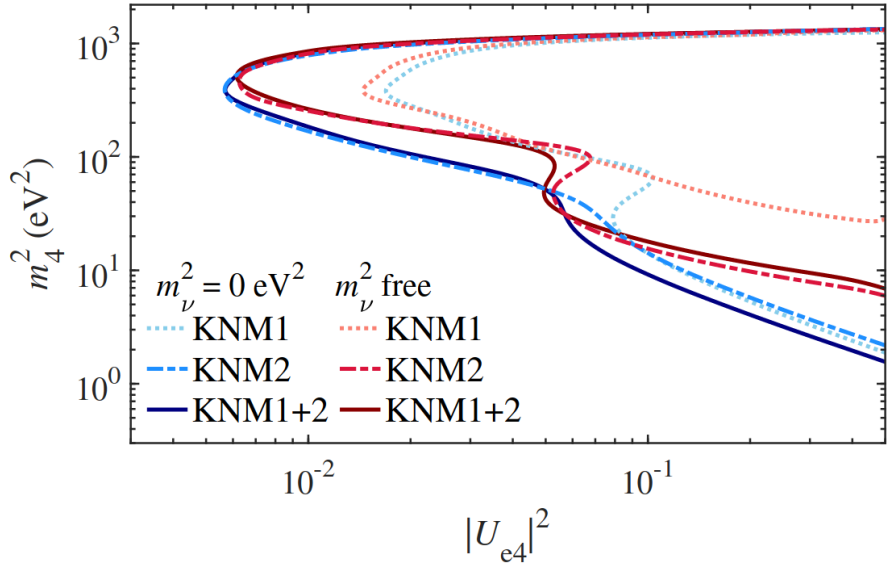


**Figure 2.17.:**  $\nu_e$  disappearance exclusion contours from both data campaigns from the KATRIN experiment as well as the combined data set. Both the case where the effective electron neutrino mass is fixed to  $0 \text{ eV}^2$  and where it is a free parameter are considered [97].

## T2K

The near detector of the T2K experiment, ND280, is located at 280 m from the neutrino beam source produced at J-PARC. Neutrino interactions occur with either a polystyrene scintillator or with water inside two fine grain detectors. Adjacent to the fine grain detectors are three TPCs which are used to identify the particle type and momentum. Electromagnetic calorimeters which surround the detectors and TPCs are used to distinguish showers and tracks [98].

A  $\nu_e$  CC event sample was selected by identifying electron candidates by use of both the TPCs and the electromagnetic calorimeters. Backgrounds due to  $\pi^0$  were reduced by rejecting events where a positive electron like track was observed within 10 cm of the electron and the  $e^+ e^-$  invariant mass is less than  $100 \text{ MeV}/c^2$ . The selection efficiency of  $\nu_e$  CC interactions was 26% with a purity of 63% [98].

ND280 analysed data taken between January 2010 and May 2013 which corresponds to  $5.9 \times 10^{20}$  POT with the horn running in neutrino mode. A total of 614  $\nu_e$  candidate events were observed with an expected number of  $665 \pm 51_{(syst)}$

events assuming no oscillations. The reconstructed neutrino energy range considered is 0.2 - 10 GeV and sensitivities are produced in  $(\sin^2 2\theta_{ee}, \Delta m_{eff}^2)$  parameters space using the Feldman-Cousins approach. The allowed regions at the 68% and 90% confidence level are shown alongside the exclusion region at the 95% confidence level in Figure 2.18. The best fit point oscillation point is at  $\sin^2 2\theta_{ee} = 1$  and  $\Delta m_{eff}^2 = 2.05 \text{ eV}^2/\text{c}^4$ . The  $p$ -value of the no oscillation hypothesis was determined to be 0.085 [98].

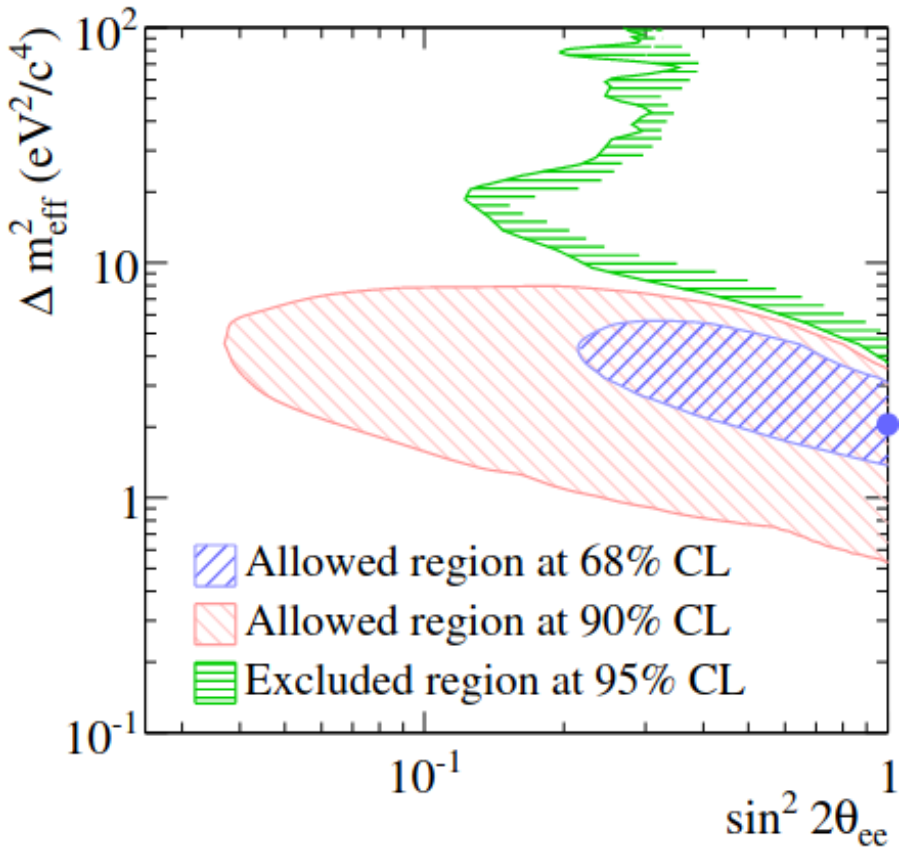


**Figure 2.18.:**  $\nu_e$  disappearance exclusion and allowed regions from the near detector of the T2K experiment, ND280 [98].

## IceCube

Located close to the South Pole, the IceCube observatory is an ice-Cherenkov detector that is comprised of 5160 modules with each housing a number of PMTs.

The modules are located between 1450 and 2450 m below the ice surface. The majority of the detected neutrinos are produced from cosmic ray showers and have an energy ranging from 10 GeV to 1 PeV. To avoid backgrounds from high energy muons that may penetrate the ice sheet, the neutrino events selected are required to be upward going (i.e. originating from below the horizon) [99].

A total of 305,735  $\nu_\mu$  and  $\bar{\nu}_\mu$  events were analysed from 8 years of IceCube data under a (3+1) neutrino hypothesis. The results depend on both  $\theta_{24}$  and  $\theta_{34}$ , but the contours have been produced under the assumption that  $\theta_{34}$  and the CP phases are set to zero. The results are shown in Figure 2.19 along with other experimental results. The left plot is the 90% C.L. allowed region, whereas the right plot is the 99% C.L. exclusion contour. The star in each plot represents the best-fit point. The best fit likelihood is found to be consistent with the no sterile neutrino oscillation with a  $p$ -value of 8% [99].

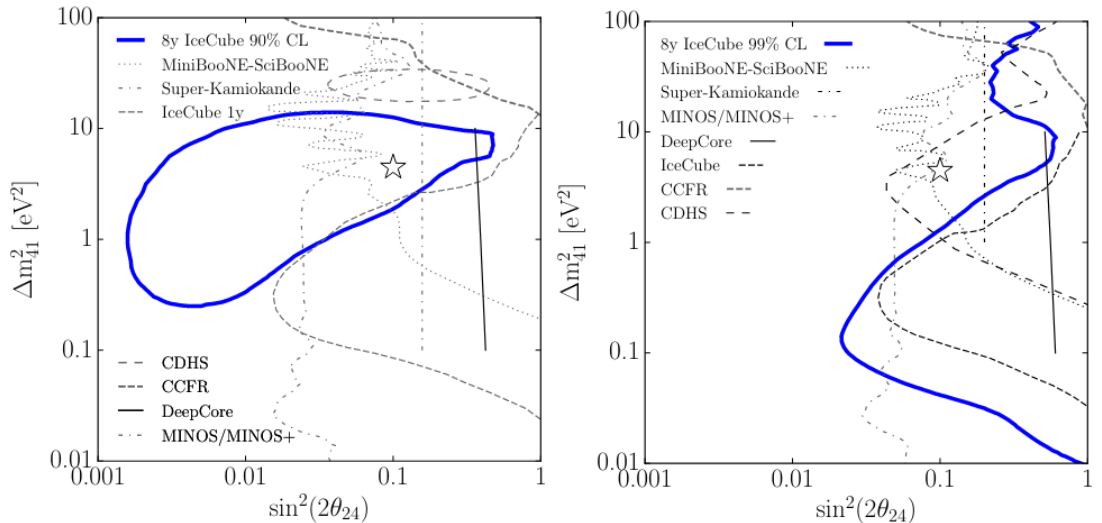


**Figure 2.19.:**  $\nu_\mu$  disappearance results from the 8 years of IceCube data. The 90% allowed region (Left) and the 99% exclusion region (right) are shown under the assumption that  $\theta_{34} = 0$  [99].

## MicroBooNE

The MicroBooNE experiment was designed to investigate the low energy excess of events observed by the MiniBooNE collaboration. A detailed description of the MicroBooNE detector can be found in Section 3.3.2. MicroBooNE analysed data from the BNB running in neutrino mode between February 2016 and July 2018 which corresponds to an exposure  $\sim 7 \times 10^{20}$  POT. A single  $\gamma$  analysis along with three separate single  $e^-$  from  $\nu_e$  interaction analyses were performed, each classified by the event topology and reconstruction method namely,

- $1\gamma 0p, 1\gamma 1p$  (0 lepton) final state from a  $\Delta$  baryon decay with Pandora being used for reconstruction.
- $1e^- 1p(0\pi)$  two-body CC QE scattering final state using a deep learning approach to perform the reconstruction.
- $1e^- Np0\pi, 1e^- 0p0\pi$  (pionless) final state using Pandora to perform the reconstruction.
- $1e^- X$  inclusive scattering final state using Wire-Cell to perform the reconstruction.

The production of single photon events (with no charged leptons or pions in the final state) at BNB energies is dominated by the neutrino induced NC  $\Delta(1232) \rightarrow N\gamma$  decay, where  $N$  represents either a proton or neutron. The analysis searches for a single photon shower with either a single visible proton or no other visible activity which are labelled  $1\gamma 1p$  and  $1\gamma 0p$  respectively. The Pandora reconstruction framework is used to classify events as either track or shower like events, followed by identifying topologies with one shower and either zero or one associated track which define the two  $1\gamma$  selections. The analysis requires that candidate events are fully contained in the fiducial volume as well as applying cuts on the shower energy, properties of the track and shower opening angle which ensures sufficient reconstruction performance as well as rejecting some backgrounds. A number of Boosted Decision Trees (BDTs) are then used on the remaining events to further reduce backgrounds from cosmic muons,  $\pi^0$  decays,  $\nu_e$  CC events and  $\nu_\mu$  CC events [100].

The dominant background in this search is due to  $\Delta \rightarrow N\pi^0$  where the pion decays into two photons. If one of the photons is not reconstructed the event may mimic a single photon event. Possible reasons a photon may not be reconstructed include: the pion decay being very asymmetric leading to one low energy  $\gamma$  that is not reconstructed, the emission of the two photons is highly co-linear meaning the two photons are reconstructed as a single shower, one of the photons exits the TPC before interacting or one of the photons may be poorly reconstructed (due to unresponsive wires). In order to constrain this background, a  $2\gamma 1p$  and  $2\gamma 0p$  sample are also selected [100].

For the  $1\gamma 1p$  sample, 16 events were observed with a background prediction of  $20.5 \pm 3.6_{(syst)}$ , whereas for the  $1\gamma 0p$  sample, 153 events were observed with a background prediction of  $145.1 \pm 13.8_{(syst)}$ . This is shown in Figure 2.20 where the  $1\gamma 1p$  and  $1\gamma 0p$  analyses are shown in the left and right plots respectively. This analysis disfavours the single photon interpretation of the MiniBooNE low energy excess and instead favours the nominal prediction at the 94.8% confidence level [100].

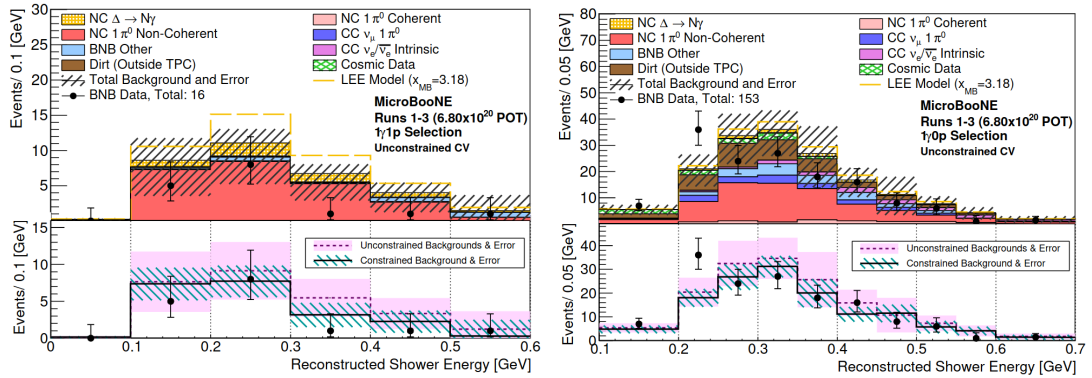


**Figure 2.20.:** The reconstructed shower energy spectra for the MicroBooNE  $1\gamma 1p$  (left) and  $1\gamma 0p$  (right) analyses. In each case the top section shows the breakdown of the unconstrained background prediction whereas the bottom section shows the total unconstrained background as well as the background after the  $2\gamma$  constraint has been applied [100].

The  $1e^- 1p$  CC QE topology is expected to dominate at energies below 500 MeV. The analysis only considers fully contained  $\nu_e$  or  $\nu_\mu$  interactions with a lepton and proton in the final state. Convolutional Neural Networks (CNNs) are used to

distinguish track and shower like images as well as determining particle species. A BDT uses kinematic and topological variables to produce a CC QE event sample followed by a CNN to select the final candidates. The reconstructed neutrino energy range considered is 200–1200 MeV. 25  $\nu_e$  candidate events were selected in this energy range which is in agreement with the background prediction of  $29.0 \pm 1.9_{(sys)} \pm 5.4_{(stat)}$  events which is shown in Figure 2.21. By mapping the low energy excess observed by MiniBooNE to MicroBooNE, 11.6  $\nu_e$  events are expected in addition to the background prediction which is not observed in this analysis [101] [102].

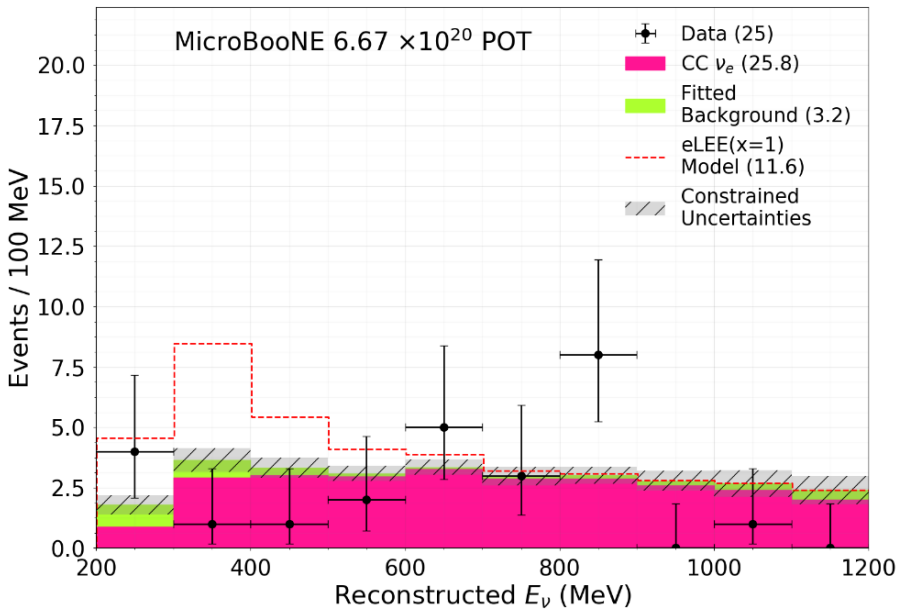


**Figure 2.21.:** The reconstructed neutrino energy from a  $1e^- 1p(0\pi)$  CC QE final state topology using a deep learning approach to analyse MicroBooNE data. Background events include cosmic and  $\nu_\mu$  interactions [101].

The pionless final state analysis considers two sub-topologies: one with a single electron plus one or more visible protons and one with a single electron and no visible protons. Pandora is used in conjunction with other tools to reconstruct events and remove cosmic ray background events. Combining these two topologies is the exact signal event signature that MiniBooNE used. The reconstructed neutrino energy range considered is 10–2390 MeV. 64  $\nu_e$  events were observed from the  $1e^- Np0\pi$  channel which had a background prediction of  $86.8 \pm 8.8_{(stat)} \pm 11.5_{(syst)}$

events. The  $1e^-0p0\pi$  channel instead observed 34  $\nu_e$  events with a background prediction of  $30.2 \pm 5.6_{(stat)} \pm 4.3_{(syst)}$  events which are shown in Figure 2.22. The  $1e^-Np0\pi$  result rejects the MiniBooNE low energy excess at a 97.9% confidence level. The  $1e^-0p0\pi$  channel has an excess of events in the lowest energy region and does not fully exclude the hypothesis that  $\nu_e$  CC interactions caused the low energy excess, however, it is the least sensitive channel to the MiniBooNE excess [101] [103].

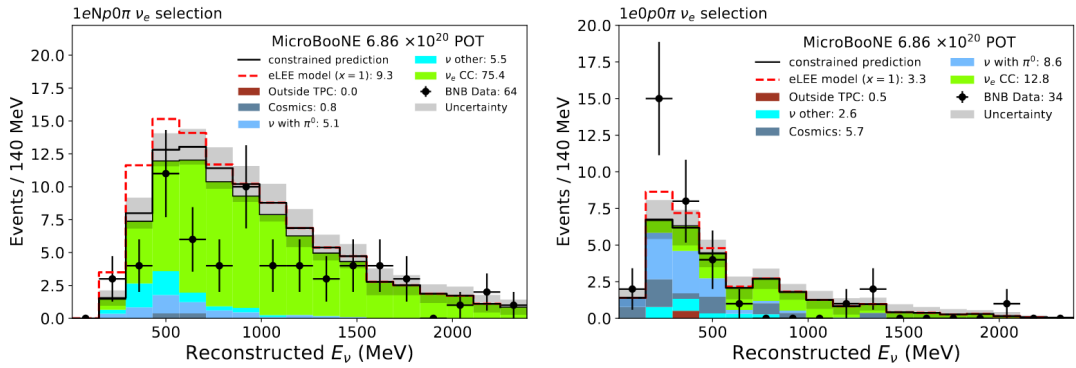


**Figure 2.22.:** The reconstructed neutrino energy from a pionless final state topology (Left:  $1e^-Np0\pi$ , Right  $1e^-0p0\pi$ ) using Pandora for event reconstruction to analyse MicroBooNE data [101].

The inclusive topology considers all hadronic final states and therefore has the largest statistics. Wire-Cell, which creates 3D images from 1D wire position tomography is used for the reconstruction. Clustering algorithms and rejection tools are used on the images along with a deep neural network to identify the neutrino vertex and characterise the event. The analysis considers events in the 0 – 2500 MeV neutrino energy range. Constraints coming from selected  $\nu_\mu$  CC events and both CC and NC events with a reconstructed  $\pi^0$  are used to improve the sensitivity and reduce systematic uncertainties. Following the  $\nu_e$  analysis and applying these constraints, 338 candidate  $\nu_e$  CC events were observed which is a slight deficit with the predicted number of  $(384.9 \pm 19.2_{(stat)} \pm 15.9_{(syst)})$  nominal events which is shown in Figure 2.23. An additional 37 events are predicted by applying the low energy excess observed by MiniBooNE.

Interpreting the most recent MicroBooNE results in terms of the allowed regions preferred by MicroBooNE, it is found that MicroBooNE excludes a significant

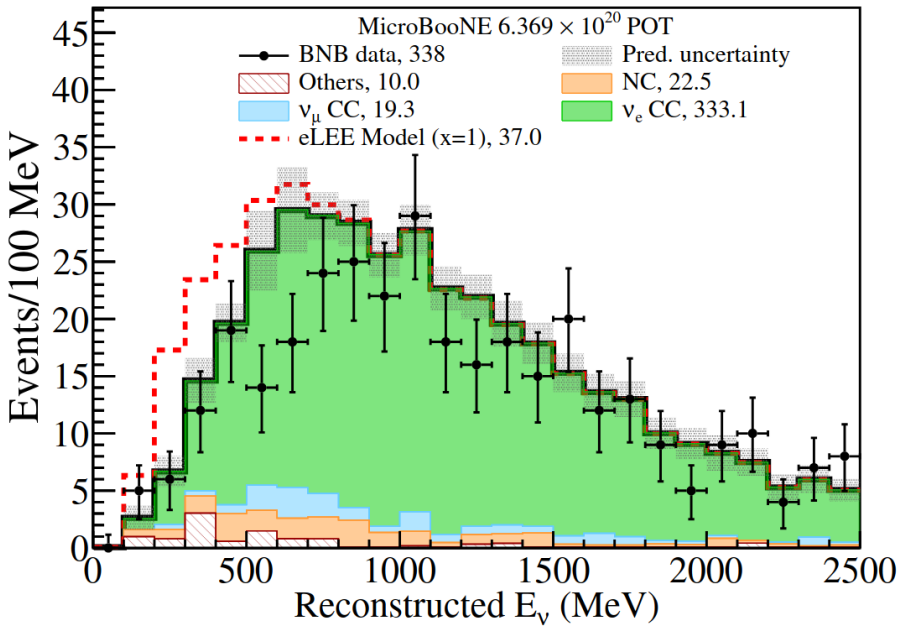


**Figure 2.23.:** The reconstructed neutrino energy from an inclusive final state topology using Wire-Cell for event reconstruction to analyse MicroBooNE data [101].

portion of the parameter space, but not the entire region. Both the inclusive and CC QE channels from MicroBooNE are shown alongside the MiniBooNE results at the  $3\sigma$  confidence level in Figure 2.24. The detection efficiency of CC QE events decreases at higher energies for both MicroBooNE and MiniBooNE which is not the case for the inclusive channel, hence the latter provides a significantly stronger constraint. While the above analyses have only considered about half of the MicroBooNE data, it is not expected that using the full data set will significantly change the results. This is due to the number of observed events in the inclusive data showing a deficit when compared to the background events leading to a stronger constraint [104].

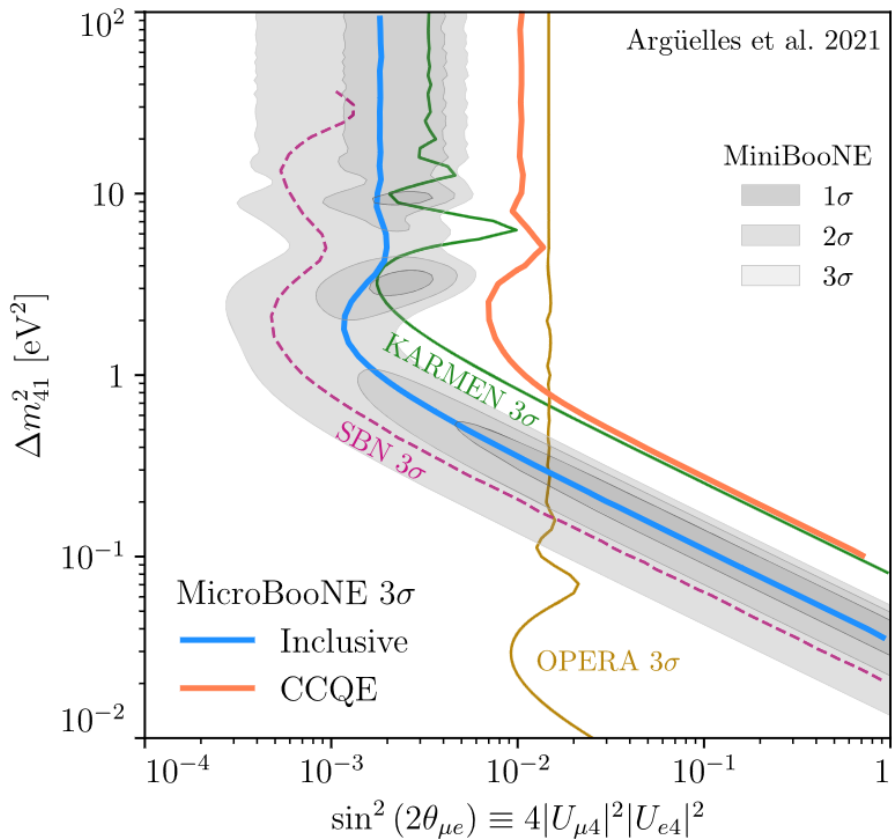


**Figure 2.24.:**  $\nu_e$  appearance exclusion contours from MicroBooNE data for both inclusive and CC QE channels at the  $3\sigma$  confidence level. The allowed regions from MiniBooNE are shown for comparison. MicroBooNE excludes much of the region favoured by MiniBooNE but not the entire parameter space [104].

## STEREO

The STEREO experiment is situated a few metres from the Institut Laue–Langevin research reactor in Grenoble. The detector consists of 6 cells filled with  $1.8 \text{ m}^3$  of gadolinium doped liquid scintillator which acts as the target and measures the antineutrino energy spectrum as a result of the fission of uranium-235. PMTs located at the top of each cell are used to detect the scintillation light. A water Cherenkov detector surrounds the cells which is used to identify cosmic muons which are passing through the detector. The 6 cells are positioned in a line along the axis of the reactor meaning each cell is at a slightly different baseline from the reactor (the baseline ranges from around 9 to 11 metres).

The antineutrinos produced by the reactor are detected via inverse beta decay with the signature being a prompt signal from the positron a delayed signal when the neutron is captured by the gadolinium followed by photon cascade due to the de-excitation of the gadolinium. After selection cuts, STEREO detected an average of 394 antineutrinos per day and a total of 107,588 antineutrinos from two data taking periods over 3 years.

The independent spectra from each of the 6 cells was compared with a given hypothesis where all parameters other than  $\sin^2 2\theta_{ee}$  and  $\Delta m_{41}^2$  were allowed to float in the fit. Exclusion contours at the 95% confidence level produced from STEREO data following a Feldman Cousins' and Gaussian confidence level approach are shown in Figure 2.25. Additionally, the allowed region and best fit point from reactor antineutrino anomaly data is shown. STEREO data is compatible with a no oscillation hypothesis, excludes much of the reactor antineutrino anomaly allowed region up to  $\Delta m_{41}^2 = \sim 5 \text{ eV}^2$  as well as excluding the best fit points from Neutrino-4 and the NEOS-RENO collaborations at a  $\sim 3\sigma$  level [105].

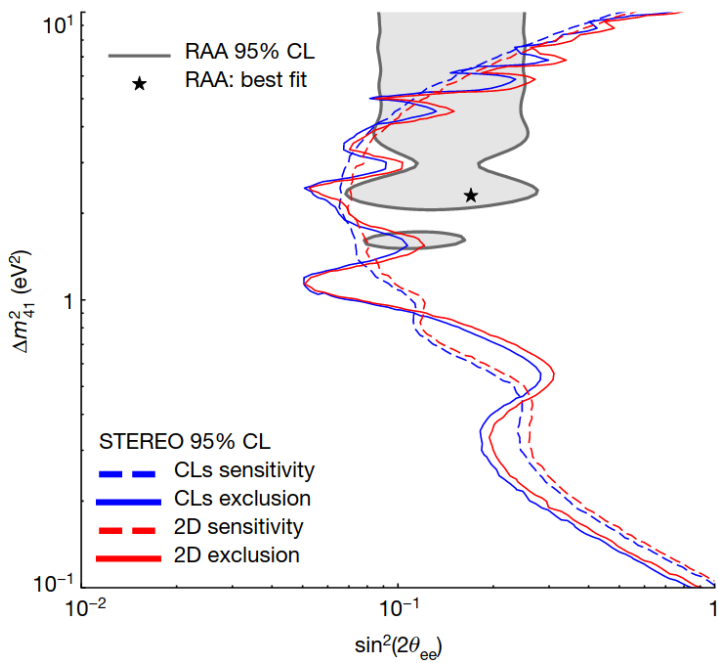


**Figure 2.25.**: The exclusion contour and exclusion sensitivity at the 95% confidence level using both the Feldman-Cousins approach and the Gaussian Confidence Level method. The reactor antineutrino anomaly allowed region and best fit point are also shown [105].

## Global Analysis

A global analysis may be performed to encompass experimental data from a number of experiments into a single result. The LSND and MiniBooNE experiments push the results away from the SM and towards a (3+1) model, however, the mixing angles required to explain the LSND and MiniBooNE excess are in tension with  $\nu_\mu$  disappearance data. The different allowed regions from a (3+1) model as well the combined region are shown on the left of Figure 2.26 with large portions of the allowed regions not being excluded by appearance data. The combined allowed region along with the exclusion region from disappearance experiments are shown on the right of Figure 2.26 with the entire allowed region being excluded by the disappearance contour. The level of tension between the allowed region and disappearance data has been quantified in terms of a  $p$ -value of  $3.7 \times 10^{-7}$ , which strongly disfavours the (3+1) model. A caveat in the calculation of the

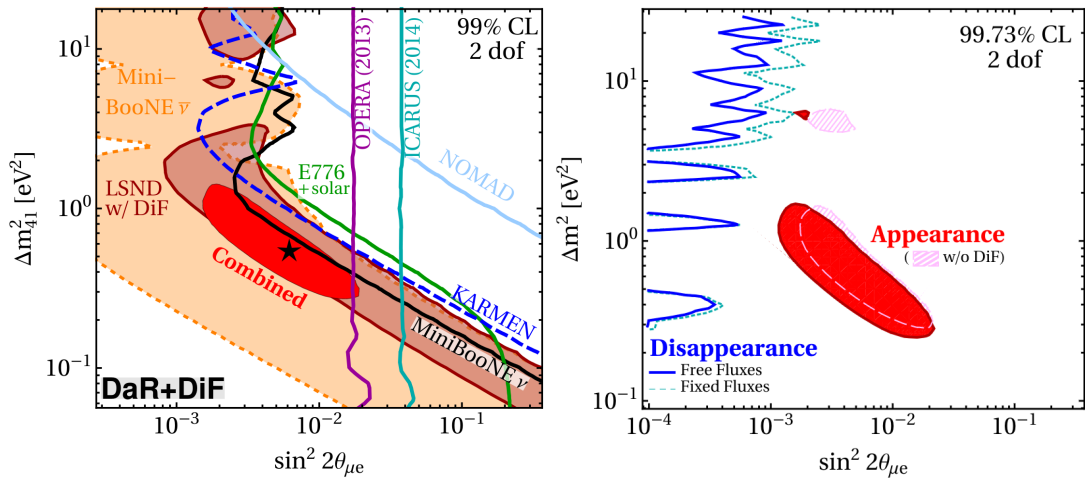


**Figure 2.26.:** Left: The allowed regions from LSND and MiniBooNE appearance signals as well as the combined region all at the 90% confidence limit. Right: The preferred allowed region from appearance experiments as well as the excluded region from disappearance experiments at the 99.73% confidence limit [107].

*p*-value is that the global fits have assumed that Wilks' theorem applies, however, it is not entirely clear if this is true for neutrino experiments [106] [89].

## Chapter 3.

# The Short Baseline Neutrino Program

The SBN program is comprised of three distinct LArTPC type detectors located at Fermilab. The three detectors are SBND, MicroBooNE, and ICARUS, and all three lie along the axis of the BNB. In order to minimise systematic uncertainties, the three detectors share many of the same technologies. The general operating principles of a LArTPC are described in Section 3.1 and the specific details of each detector are discussed in Section 3.3.1 (SBND), Section 3.3.2 (MicroBooNE) and Section 3.3.3 (ICARUS). The BNB consists predominantly of muon neutrinos with energies of the order 1 GeV and is discussed in detail in Section 3.2. The

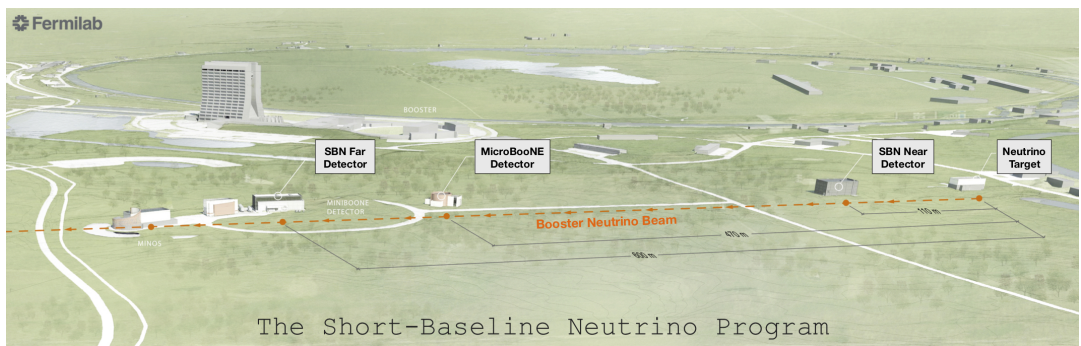


**Figure 3.1.:** A view of the Fermilab complex highlighting the position of the SBN detectors [13].

three detectors are positioned at 110m, 470m and 600m from the neutrino beam source respectively [13].

One of the primary aims of the SBN program is to provide a definitive test to either confirm or refute the existence of light sterile neutrinos which have been hinted at by a number of experiments discussed in Section 2.2.3. Other major aims of the SBN program include investigating neutrino argon cross-sections and developing large-scale LArTPC technologies. The close proximity of SBND to the BNB source means that SBND will observe neutrino argon interactions with high statistics allowing statistical uncertainties to be minimised and will allow for the exploration of rare channels such as neutrino-electron scattering. Both the development of LArTPC technology and an improved understanding of neutrino interaction cross-sections will be invaluable for future neutrino experiments such as DUNE [13].

### 3.1. Liquid Argon Time Projection Chambers

The idea of a LArTPC was first proposed in 1977 by Rubbia in an attempt to consolidate the high-resolution but low number of interactions obtained from 'bubble chamber' style detectors and the high rate but low-resolution interactions obtained from 'counter' experiments. This would be achieved by propagating the complete image of an event through a noble element and then electronically reconstructing the 3D event by combining the 2D information collected and the drift time [108].

Liquid argon was identified as the most suitable medium to use for such a detector due to the following properties [108];

- High density ( $1.4 \text{ gcm}^{-3}$ ) with a sufficiently high atomic mass to allow for a reasonable probability of neutrino interactions.
- Argon is a noble element, meaning the electrons will not combine with the argon resulting in long drift times, assuming a sufficient purity is obtained.

- Argon is a noble element, meaning that any energy absorbed by the argon atom can only be used to ionise the atom or is again released in the form of scintillation light. The energy cannot be consumed by actions such as vibrations or rotations.
- A high electron mobility, meaning the electrons may drift quickly across the detector.
- Argon is relatively cheap and easy to purify.
- Argon may be liquefied easily using liquid nitrogen.

### 3.1.1. LArTPC Operating Principles

The general design of a single chamber LArTPC is shown in Figure 3.2. Most LAr detectors consist of one or more TPCs with a cathode and anode plane at either end inducing an electric field across the TPC. The resulting particles from a neutrino interaction will ionise argon atoms as they traverse through the TPC. The electric field causes the ionisation electrons to drift towards the anode where they will induce a current on a series of wire planes. The rearmost wire plane (the one furthest away from the cathode) is known as the collection plane and the one or more wire planes in front of the collection plane are known as induction plane(s). There is a further potential difference between the induction and collection planes which ensures that the electrons will also reach the collection plane. The wire planes are orientated so that the wire angles between the planes are different which allows for 2D position reconstruction. A series of PMTs surround the detector which collects scintillation light. The specific designs of the three LArTPCs used in the SBN program are discussed in Section 3.3.1 (SBND), Section 3.3.2 (MicroBooNE) and Section 3.3.3 (ICARUS).

Along with the global volume of a detector which is defined by its dimensions, there are usually two other volumes associated with LArTPCs: the *active* volume and the *fiducial* volume. The active volume is defined as the volume which is enclosed within the TPC and is the volume of the detector which allows for event detection. The fiducial volume is not directly defined by the physical design

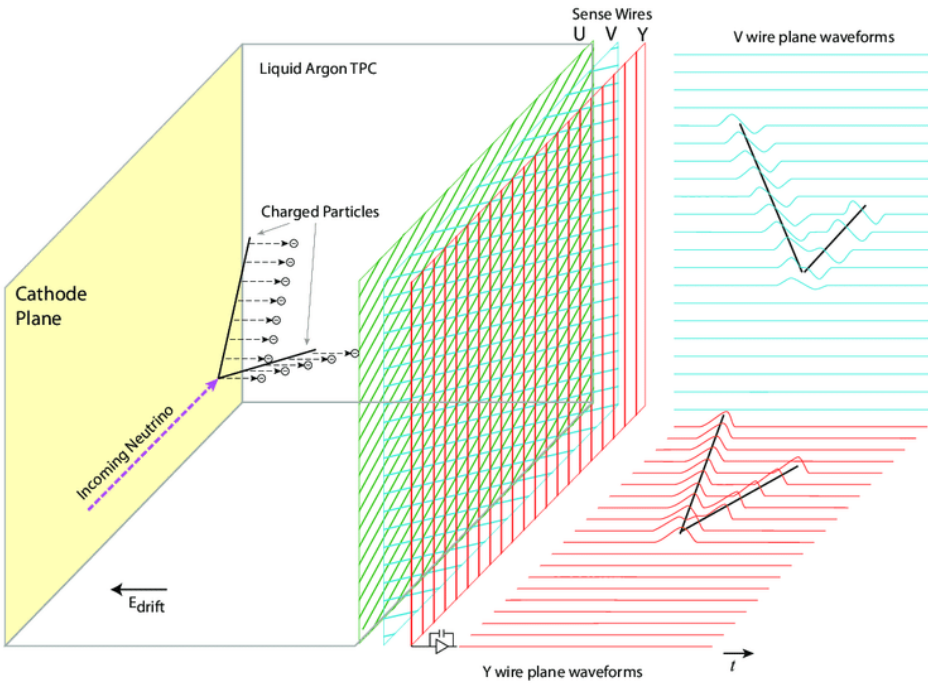


**Figure 3.2.:** A schematic of the operating principle of a LArTPC detector. A neutrino interacts in the argon producing secondary particles which ionise the argon atoms as they travel across the TPC. The electric field causes the ionisation electrons to drift towards the wire planes where their energy deposits are recorded. [109]

of the detector but is instead the region within the active volume where event reconstruction is thought to be well understood. Events occurring right at the edge of the TPC may be difficult to reconstruct and are therefore poorly understood. Additionally, background events tend to occur close to the edge of the TPC, so by only considering events within the fiducial volume, the percentage of well-understood signal events is maximised [32]. The active and fiducial volumes used in each of the SBN detectors are defined in Appendix B.

### 3.1.2. Physics of Signal Formation

Despite the many desirable properties of liquid argon, there are still a number of effects which have to be considered when performing event reconstruction.

#### 3.1.2.1. Ionisation and Detector Effects

If sufficient energy is imparted to an argon atom, an electron-ion pair will be produced due to ionisation. The energy required to ionise an atom of liquid argon is  $\sim 23.6$  eV. Following ionisation, the electron-ion pair may drift in opposite directions across the detector. The drifting electrons are key to event reconstruction and for an electric field of 500 V/cm, the electron drift velocity is  $\sim 1.6$  mm/ $\mu$ s [110]. Several different processes effect the number of drifting electrons and describe how they drift, each of which are detailed below.

#### Diffusion

Diffusion is the process in which the drifting electrons do not drift in such a way that they will continue to perfectly represent the initial image of an event. That is to say that the electrons will disperse as they drift in the detector. This happens in both the transverse and longitudinal directions with respect to the direction of the electric field and impacts the spatial resolution of the detector [111].

For the case of a zero electric field and with the electrons in thermal equilibrium, the diffusion is isotropic and the diffusion coefficient,  $D$ , is given by the Einstein relation such that

$$D = \frac{kT}{e}\mu_0, \quad (3.1)$$

where  $k$  is Boltzmann's constant,  $T$  is the temperature,  $e$  is the elementary charge and  $\mu_0$  is the electron mobility (for the case of no electric field) [111].

In the presence of an electric field, the electron mobility is no longer given by  $\mu_0$ , but instead by  $\mu$  and the electrons are no longer in thermal equilibrium. The diffusion also becomes anisotropic, leading to distinct diffusion coefficients for the

longitudinal and transverse directions,  $D_L$  and  $D_T$  respectively which are given by

$$\begin{aligned} D_L &= \frac{kT}{e}(\mu + E\frac{\partial\mu}{\partial E}) \\ D_T &= \frac{kT}{e}\mu. \end{aligned} \quad (3.2)$$

In general, the diffusion in the transverse direction is greater than the diffusion in the longitudinal direction [111] [112].

### Electron Lifetime

Electron lifetime is a measure of the free electrons lost due to attachment to impurities in the liquid argon whilst drifting across the detector [113]. It is also the quantity that drives the width to which a TPC is constructed. Naturally, the electron lifetime,  $\tau_e$ , is coupled to the purity of the argon such that

$$\tau_e \propto 1/k_e, \quad (3.3)$$

where  $k_e$  is the impurity concentration. The rate of charge loss is then given by

$$Q = Q_0 e^{-t/\tau_e}, \quad (3.4)$$

where  $Q$  is the charge remaining after correcting for electron lifetime,  $Q_0$  is the initial charge and  $t$  is the drift time [113]. The lowest electron lifetime (during a period where the purity was considered stable) that MicroBooNE has observed is 18.0 ms [114]. Currently, the SBND simulation uses a default value of 10.0 ms for the electron lifetime, whereas the ICARUS simulation uses a value of 15.0 ms. By requiring that the maximum charge loss is only of the order 10%, this results in a maximum drift distance (TPC width) of  $\sim 1.5$  m.

### Recombination

When argon atoms are ionised, the resulting ionised electron may immediately recombine with a nearby argon ion instead of being separated by the electric field in the detector. This is known as the recombination effect and the magnitude of

the effect is largely determined by the local electric field. A number of different approaches to model the recombination effect exist, however, for liquid argon detectors, a form of the box model or Jaffé model are usually used [111].

The Jaffé model is based on the idea that recombination depends on the charge density of both nearby electrons and ions. The model assumes a cylinder surrounding the ionisation track and recombination may occur between any of the ionised electrons and ions, not just the electron with its associated parent ion which is where the Jaffé model largely differs from earlier models [115]. The recombination effect from the Jaffé model is given by

$$Q = \frac{Q_0}{1 + q_0 F(E \sin \phi)}, \quad (3.5)$$

where  $Q_0$  is the initial charge,  $Q$  is the charge after recombination,  $q_0$  is the initial density of electron-ion pairs and  $F$  is a function depending on the electric field  $E$ , the angle between the field and the ionisation track,  $\phi$  and other quantities which describe the diffusion. Equation 3.5 is commonly approximated by Birks' law with a normalisation parameter to help fit the model to the experimental data [111].

In their development of the box model, Thomas and Imel assumed the diffusion and ion mobility to be zero and instead of the cylindrical column used in the Jaffé model, they considered a box with a uniform charge distribution such that,

$$Q = Q_0 \frac{1}{\xi} \ln(1 + \xi), \quad (3.6)$$

where  $\xi = \alpha Q_0 / E$ .  $\alpha$  is a free parameter and  $Q$  and  $Q_0$  are defined as in Equation 3.5 [111] [116].

In addition to being model-dependent, the exact recombination value is often presented as a function of  $dE/dx$ . For an electric field of 0.5 kV/cm, the recombination value has a maximum of  $\sim 0.7$  at a  $dE/dx$  value of  $\sim 1$  MeV/cm and falls to a minimum of  $\sim 0.1$  as the  $dE/dx$  value increases to  $\sim 30$  MeV/cm [111].

## Space Charge

The electric field in a TPC is usually designed to be uniform between the cathode and the anode, however, particularly for surface-level detectors this often does not end up being the case. Cosmic muons may enter the detector ionising the argon atoms. The ionised electrons and argon ions then drift towards the anode and cathode respectively, however, the drift time for the ions is much greater than the electron drift time. If the flux of cosmic muons entering the detector is sufficiently large, this results in a significant positive charge build-up towards the cathode. This effect is known as *space charge* and directly impacts the recombination effect since it is linked to the magnitude of the local electric field as well as affecting the drifting electrons [117].

The ion drift velocity,  $\vec{v}$ , is given by

$$\vec{v} = \mu \vec{E}, \quad (3.7)$$

where  $\mu$  is the ion mobility and  $\vec{E}$  is the electric field. The build up of charge density,  $\rho$ , is given by the continuity equation,

$$\vec{\nabla} \cdot \vec{J} + \frac{\partial \rho}{\partial t} = K, \quad (3.8)$$

where  $\vec{J} = \rho \vec{v}$  and  $K$  is the volume rate at which ion pairs are created ( $[K] = \text{ion pairs/volume/second}$ ) [118].

With the simplified assumption that the build-up of charge is constant (time-independent) and that the drift direction is only in the x-direction which is the same as the electric field, Equation 3.8 may be reduced to

$$\frac{d\rho v}{dx} = K. \quad (3.9)$$

Gauss's law states that,

$$\nabla \cdot \vec{E} = \frac{\rho}{\epsilon}, \quad (3.10)$$

where  $\epsilon$  is the dielectric constant of the medium. By combining Equation 3.9 and Equation 3.10 it follows that

$$\frac{dE}{dx} = \frac{Kx}{\mu E \epsilon}. \quad (3.11)$$

By defining the coordinates of the system such that the anode is at  $x = 0$  and  $0 \leq x \leq D$  where  $D$  is the position of the cathode, Equation 3.11 may be integrated via,

$$\int_{E_A}^E E' dE' = \int_0^x \frac{Kx'}{\mu \epsilon} dx', \quad (3.12)$$

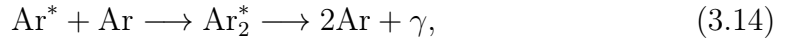
where  $E_A$  is the electric field at the anode and both  $E'$  and  $x'$  are dummy variables. This gives an x-dependent electric field solution,

$$E(x) = \sqrt{E_A^2 + \frac{Kx^2}{\mu \epsilon}} = E_0 \sqrt{\left(\frac{E_A}{E_0}\right)^2 + \alpha^2 \frac{x^2}{D^2}}, \quad (3.13)$$

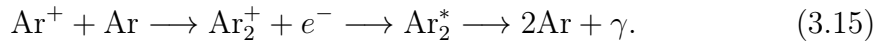
where  $E_0 = V/D$  is the nominal electric field,  $V$  is the difference in the voltage between the anode and cathode and  $\alpha = \frac{D}{E_0} \sqrt{\frac{K}{\epsilon \mu}}$  which is a dimensionless parameter [118].

### 3.1.2.2. Scintillation and Cherenkov Light

Scintillation light in liquid argon is produced via the de-excitation of an argon excimer,  $\text{Ar}_2^*$ . The scintillation light has two components, *fast* and *slow*, which are due to two distinct scintillation mechanisms. An excimer may be produced by direct excitation via,



or by recombination via,



The excimer may be in one of two states each with a different decay time which gives rise to the fast and slow scintillation mechanisms. Around 23% of all scintillation light is produced via the fast mechanism with remainder produced via the slow mechanism [119]. The time period to detect the fast component is  $\sim 6$  ns, whereas for the slow component it is  $\sim 1.6 \mu\text{s}$  [11]. Since the scintillation light is detected almost instantaneously when compared to the time taken for the electrons to drift to the wire planes, the horizontal drift distance may be determined. Combining this with the 2D information from the wire planes allows for 3D event reconstruction.

Cherenkov light may also be emitted in liquid argon by charged particles crossing the TPC (the refractive index of liquid argon is  $\sim 1.22$ ). For highly relativistic particles, this results in a Cherenkov angle of  $\sim 34^\circ$ . The number of photons produced by Cherenkov light is significantly less than scintillation light, however, Cherenkov light has the advantage of having an associated direction [120].

The light detection methods of each of the SBN detectors is described in the relevant subsection of Section 3.3 with the general design consisting of a series of PMTs and light traps.

### 3.1.2.3. Wire Signal Processing

In order to extract the original charge signal on the wire planes from the measured signal, a technique known as deconvolution is used. A convolutional integral of the detector response and the original signal is used to model the measured signal. The detector response encompasses both the wire and electronics responses and may be estimated using data from a calibration sample or from simulations. In order to obtain the original signal, the integral is solved by the use of a Fourier transform. An additional filter may be applied to account for noise contributions [121].

The induced current on the wire planes is interpreted in terms of signal waveforms. If the waveforms are above some threshold value such that they can be distinguished from noise, *hits* are constructed which encapsulate the signal. Each hit contains information such as the associated wire plane, wire number and charge and it

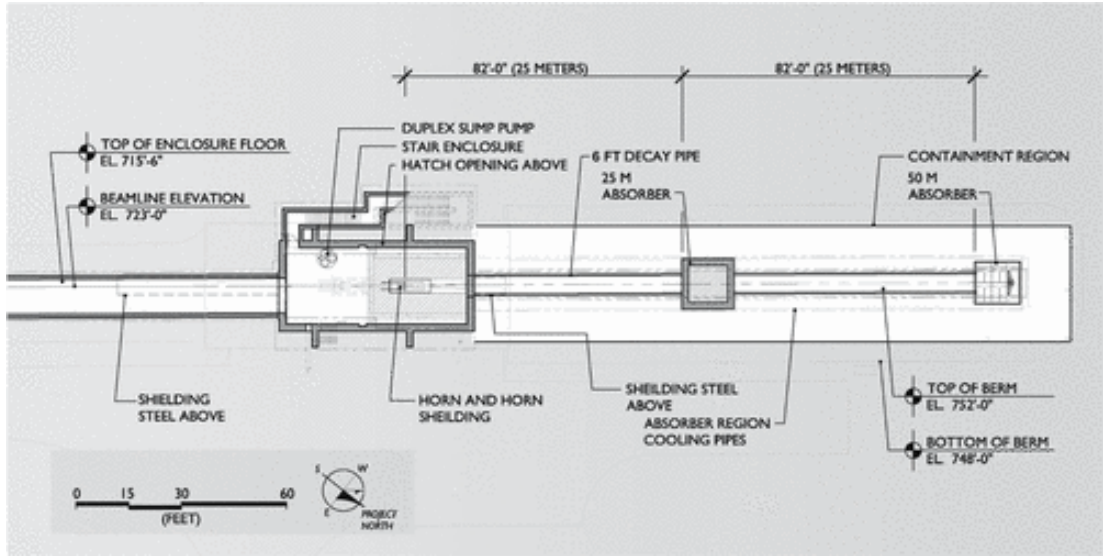


**Figure 3.3.:** A schematic of the layout of the BNB [124].

is this information which is used to obtain reconstructed information about an event [109].

The details of hit construction and the basics of reconstruction are discussed in Chapter 4.

## 3.2. Booster Neutrino Beam

The BNB is produced by firing 8 GeV protons onto a beryllium target resulting in a secondary beam of hadrons [122]. A toroidal focusing horn surrounds the target and focuses or defocuses charged particles depending on the sign of their charge. The focused hadrons then travel down a 50 m tunnel where most of them will decay producing muon neutrinos and a small fraction of electron neutrinos. At the end of the 50 m decay region is a concrete and steel absorber designed to absorb any non-neutrino particles [123]. A schematic of the BNB layout is shown in Figure 3.3. The decay modes of the hadrons resulting in a neutrino and the corresponding branching ratios are listed in Table 3.1.

Particle	Decay Mode	Branching Ratio (%)
$\pi^+$	$\mu^+ + \nu_\mu$	99.9877
	$e^+ + \nu_e$	0.0123
$K^+$	$\mu^+ + \nu_\mu$	63.44
	$\pi^0 + e^+ + \nu_e$	4.98
	$\pi^0 + \mu^+ \nu_\mu$	3.32
$K^0$	$\pi^- + e^+ + \nu_e$	20.333
	$\pi^+ + e^- + \bar{\nu}_e$	20.197
	$\pi^- + \mu^+ + \nu_\mu$	13.551
	$\pi^+ + \mu^- + \bar{\nu}_\mu$	13.469
$\mu^+$	$e^+ + \nu_e + \bar{\nu}_\mu$	100

**Table 3.1.:** The decay modes of the hadrons produced by the BNB when running in neutrino mode. The branching ratio of each of the decay modes is also given [124].

A current of 174 kA is supplied to the magnetic horn in 143  $\mu$ s pulses which corresponds to the frequency of the incident protons. The direction of the current may be reversed allowing for the focusing of positively or negatively charged particles. Since the charge of the decaying hadrons is linked to the type of neutrino produced, the ability to focus both positively and negatively charged particles allows the BNB to run in neutrino or antineutrino mode [124]. Pions are the primary particle produced from the incident protons hence the BNB is muon (anti)neutrino dominated. The percentage neutrino flavour composition of the BNB is given in Table 3.2 for both neutrino and antineutrino mode.

Neutrino Flavour	% in Neutrino Mode	% in Antineutrino Mode
$\nu_\mu$	93.6	15.71
$\bar{\nu}_\mu$	5.86	83.73
$\nu_e$	0.52	0.2
$\bar{\nu}_e$	0.05	0.4

**Table 3.2.:** The neutrino flavour composition of the BNB when it is running in either neutrino or antineutrino mode [124].

The neutrino flux of the BNB was simulated by the MiniBooNE collaboration for both neutrino and antineutrino mode [124]. The flux of the electron and muon (anti)neutrinos in each of the three SBN detectors is shown in Figure 3.4. The

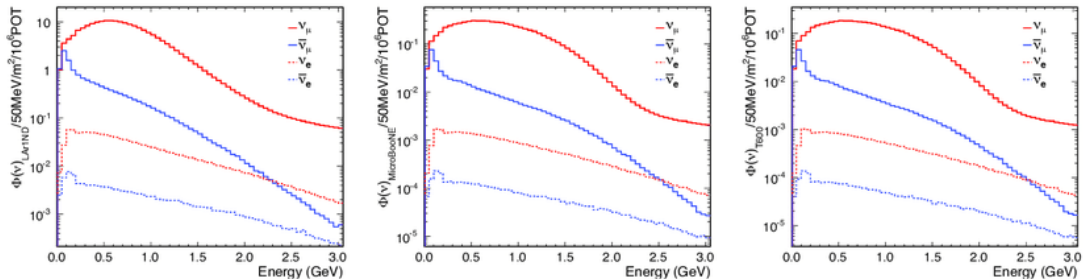


**Figure 3.4.:** The predicted flux of the BNB at SBND (left), MicroBooNE (middle) and ICARUS (right) for both electron and muon neutrinos and antineutrinos [11].

systematic uncertainties associated with the BNB account for an error of  $\sim 9\%$  at the peak of the  $\nu_\mu$  flux with a larger error for energies either side of the peak. The systematic uncertainties are mainly due to determining the rate and spectrum of neutrinos for each proton on target, determining the rate and spectrum of secondary particles produced from protons interacting with the beryllium target, the rate of hadronic interactions, the focusing properties of the magnetic horn and the beamline geometry [124].

### 3.3. SBN Detectors

The SBN program is a multi-phase program. The first phase consisted only of the MicroBooNE detector which began operating 2015. The main goal was to investigate the low energy excess of events observed by the MiniBooNE collaboration hence it is purposely located close to the same position as MiniBooNE was.

The second phase of the program focuses on the SBND and ICARUS detectors which act as the near and far detector respectively. The ICARUS detector began data taking in 2021, whilst SBND is still under construction. It is expected that liquid argon filling may begin in SBND by early summer of 2023 and that data taking can start at the beginning of 2024. The BNB is expected to operate until

a long shutdown period which is due to start at the beginning of 2027. From 2024 to 2027, the BNB anticipates an exposure of  $(10 - 18) \times 10^{20}$  POT, which is up to  $\sim 3$  times the predicted POT used in the SBN proposal [125].

The close proximity of SBND to the BNB means an unprecedented number of neutrino-argon events will be observed which is expected to be of the order 2 million events a year, with 50,000 of them being  $\nu_e$  CC events which is sufficient to investigate multiple exclusive channels in addition to the inclusive ones [125]. Joint fits between SBND and ICARUS will be performed in order to exploit the best sensitivity of the SBN program. MicroBooNE data may also be included to produce a three detector fit as is shown in Chapter 6.

### 3.3.1. SBND

SBND was purposely designed to be the near detector of the SBN program and has a total active volume with dimensions (4, 4, 5) m containing 112 tons of liquid argon. It consists of two TPCs and therefore two distinct active volumes. A central shared cathode sits in the middle of the detector with an anode on either side as is shown in Figure 3.5 with the detector orientated such that the z-direction is along the neutrino beam line. Each of the Andode Plane Assemblies (APAs) consists of three wire planes where the first and second induction plane are orientated at  $\pm 60^\circ$  to the vertical and the collection plane is vertical. In all cases, the wire plane spacing and the wire pitch are 3 mm. The nominal electric field in each of the TPCs is 500 V/m [11].

#### Cosmic Ray Tagger

SBND is considered to be a surface-level detector with no overburden. Consequently, the cosmic ray flux will be significant with an average of 3 cosmic rays seen in each neutrino event [11]. This will be the most abundant background in SBND and therefore it will be crucial to be able to identify the cosmic ray muons. In order to do this, SBND will use a Cosmic Ray Tagger (CRT) system which consists of a total of 7 panels, one for each side of the detector plus an additional one for the top face as this is where most of the cosmic rays will be entering the

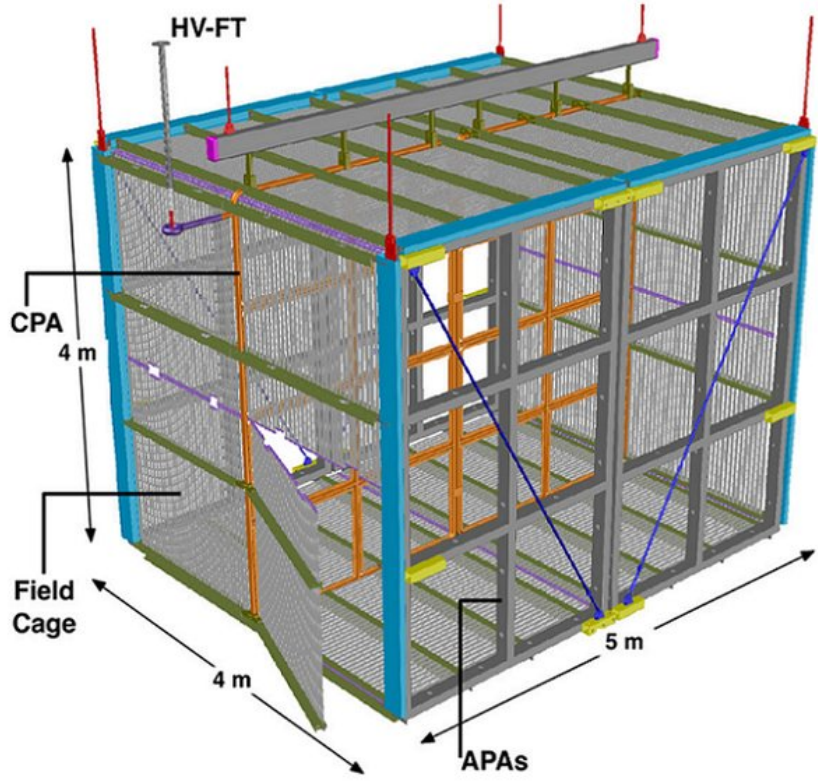


**Figure 3.5.:** Schematic showing the dimensions of the SBND detector. The Cathode Plane Assembly (CPA), APAs (only one is labelled) and field cage are shown. The Photon Detection System (PDS) is not shown, but the 12 squares on the near APA represent the location where the PDS boxes will be positioned. [126]

detector from. Figure 3.6 shows how the CRT panels will be positioned. Each CRT plane consists of two layers, where one layer is comprised of  $2 \times 5$  X-oriented modules and the other layer is comprised of  $2 \times 4$  Y-oriented modules. Each of these modules is comprised of 16 scintillator strips. Two fibres are attached to each strip which are in turn attached to Silicon Photomultipliers (SiPMs). The orthogonal two-layer setup coupled with the SiPM readout allows the location of an interaction in the CRT to be determined [127]. The CRT system monitors the crossing time and coordinates of the particles and compares them with the information from the light detection system and the beam time rejecting the events that are identified as cosmic muons. [128].

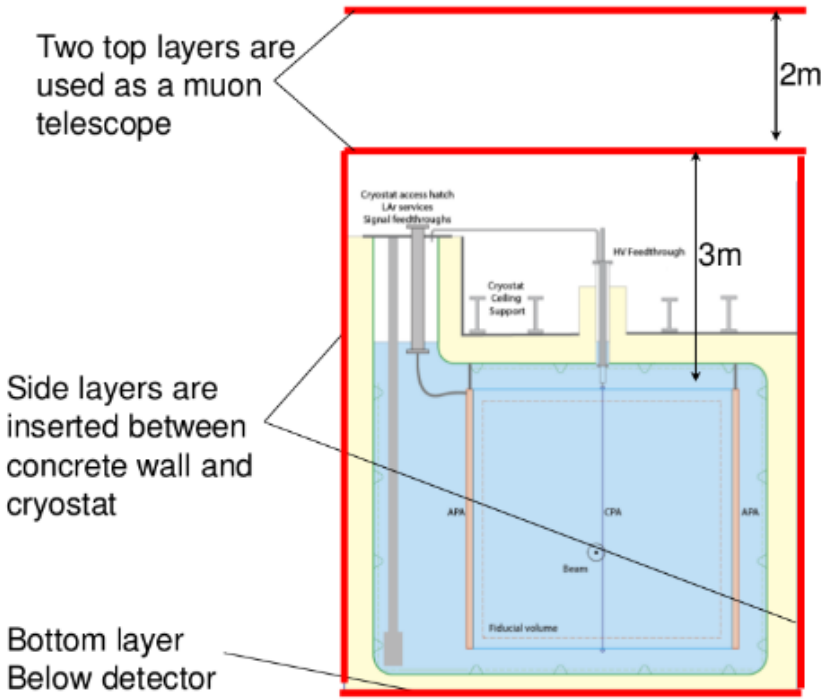


**Figure 3.6.:** Diagram showing how the CRT will surround SBND on all sides with an additional panel above the top surface [11].

## Photon Detection System

The PDS consists of a total of 24 *boxes*, 12 of which will be mounted behind each APA. Each box houses 5 PMTs and 8 Argon R&D Advanced Program at UniCamps (ARAPUCAs) (specifically, X-ARAPUCA's are used which are an advancement over the initial ARAPUCA design) as shown in Figure 3.8. The 4 outer PMTs of each box are coated with Tetraphenyl Butadiene (TPB) whilst the central one remains uncoated. The scintillation light produced by argon has wavelengths in the Vacuum Ultra Violet (VUV) region, however, the PMTs are only able to detect visible light. The TPB coating shifts the wavelength of the VUV light into the visible region allowing it to be detected. Therefore, the coated PMTs are sensitive to both visible and VUV light whilst the uncoated PMTs are only sensitive to visible light [126].

ARAPUCAs are a novel light trap which consists of a box where the internal surfaces are highly reflective. The surface of the ARAPUCA which faces the incoming light consists of a dichroic filter with a wavelength shifter on either side of the filter. The wavelength of the light which is incident on the outermost shifter is shifted such that it may pass through the dichroic filter and after passing through the filter the light is again wavelength shifted so that it may no longer pass through the filter and thus remains trapped in the ARAPUCA. A schematic of the ARAPUCA design is shown on the left of Figure 3.7. The inside of the ARAPUCA module contains a SiPM photo-sensor in order to detect the light. Due to the highly reflective nature of the inside of the ARAPUCA, only a small region needs to be exposed to a photo-sensor in order to detect the trapped photons [129]. The X-ARAPUCA improves on the initial design by replacing the inner wavelength shifter with an acrylic slab with the wavelength shifter implanted in the slab and the photo-sensor being directly attached to the slab. Light entering the X-ARAPUCA may be detected in the same way as was done in the original ARAPUCA (Figure 3.7: Left), however, the photons may also become trapped in the slab by total internal reflection and travel within the slab to the photo-sensor (Figure 3.7: Middle) or if the light enters at a large angle, the photons may become trapped between the surface of the slab and the filter and will travel to the photo-sensor without ever entering the slab (Figure 3.7: Right). The middle scenario of Figure 3.7 represents a direct improvement over the original ARAPUCA design because the number of reflections on the internal sides of the X-ARAPUCA module is reduced which in turn increases the photon detection efficiency [130].

Another component of the PDS is covering each side of the CPA with a  $19\text{ m}^2$  of TPB coated reflective covering. This means that VUV light directed towards the CPA will be wavelength shifted into the visible spectrum and reflected back to towards the PMTs where it may be detected. Since one of the PMTs in each of the boxes remains uncoated, it will allow SBND to distinguish between light that is initially directed towards the PMTs and the reflected light because the reflected light will be visible in all PMTs whereas only the four outer PMTs will be able to detect direct light [126].

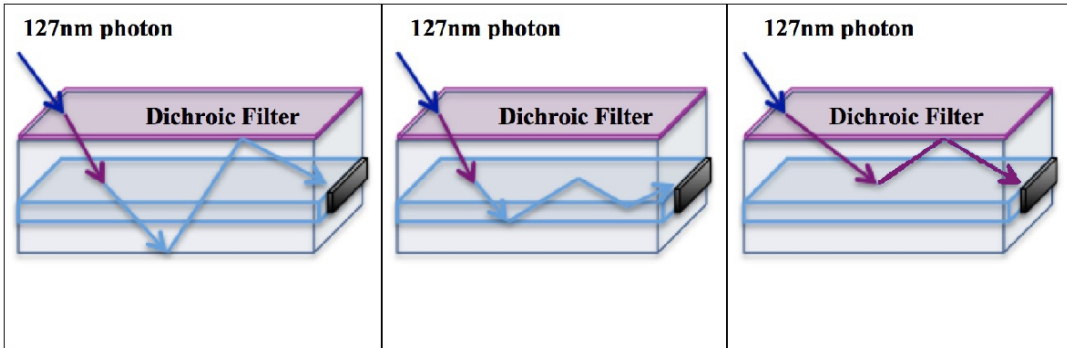


**Figure 3.7.:** The three possibilities for trapping light in an X-ARAPUCA. Left: The standard ARAPUCA design. Light is wavelength shifted in order to pass through the dichroic filter. Once passed the filter, it is wavelength shifted again so that may not exit through the filter again. The photons are reflected within the ARAPUCA until they are detected by the photo-sensor. Middle: an acrylic slab containing the inner wavelength shifter is placed in the X-ARAPUCA and the photo-sensor is attached to the slab. Light may become trapped within the slab by total internal reflection. Right: Incident light at a large angle may become trapped between the surface of the slab and the filter [130].

### 3.3.2. MicroBooNE

The MicroBooNE detector is located slightly upstream of its predecessor, Mini-BooNE. The detectors are at 470 m and 541 m from the BNB source respectively. The principal design goal of MicroBooNE is to investigate the low energy excess of events observed by MiniBooNE and it began its operations in 2015 where it was initially used as a stand-alone detector before becoming part of the larger SBN program [131].

The MicroBooNE detector consists of a single TPC enclosed within a cryostat as is shown in Figure 3.9. The TPC has dimensions of (2.560, 2.325, 10.368) m and is orientated such that the z-direction is along the neutrino beam line with the cathode to the left of the beam and the anode to the right. The active volume is defined as the volume enclosed by the LArTPC field cage which has a liquid argon mass of 90 tonnes out of a total 170 tonnes. The APA consists of three wire planes with the wires on the two induction planes orientated at  $\pm 60^\circ$  to the vertical and the wires of the collection plane orientated vertically. Both the wire plane spacing and the wire pitch of each plane is 3 mm. Unlike SBND and ICARUS, the nominal electric field in MicroBooNE is 273 V/cm. The light collection system



**Figure 3.8.:** Image of a PDS box showing the position of the 5 PMTs and the 4 pairs of X-ARAPUCA'S. The central PMT is left uncoated, whilst the 4 outer PMTs are coated with TPB.

consists of a series of 32 PMTs and 4 lightguide paddles which are located directly behind the anode planes. The lightguides have a large collection area and their purpose is to guide light to the PMTs (the lightguide paddles were disfavoured once the ARAPUCA technology was developed.) [131].

MicroBooNE is also considered a surface level detector being only  $\sim 6$  m underground and as there is no overburden present, a large flux of cosmic rays are observed. A CRT system similar to the one described in Section 3.3.1 for SBND was implemented. The CRT system consists of 73 scintillating modules,

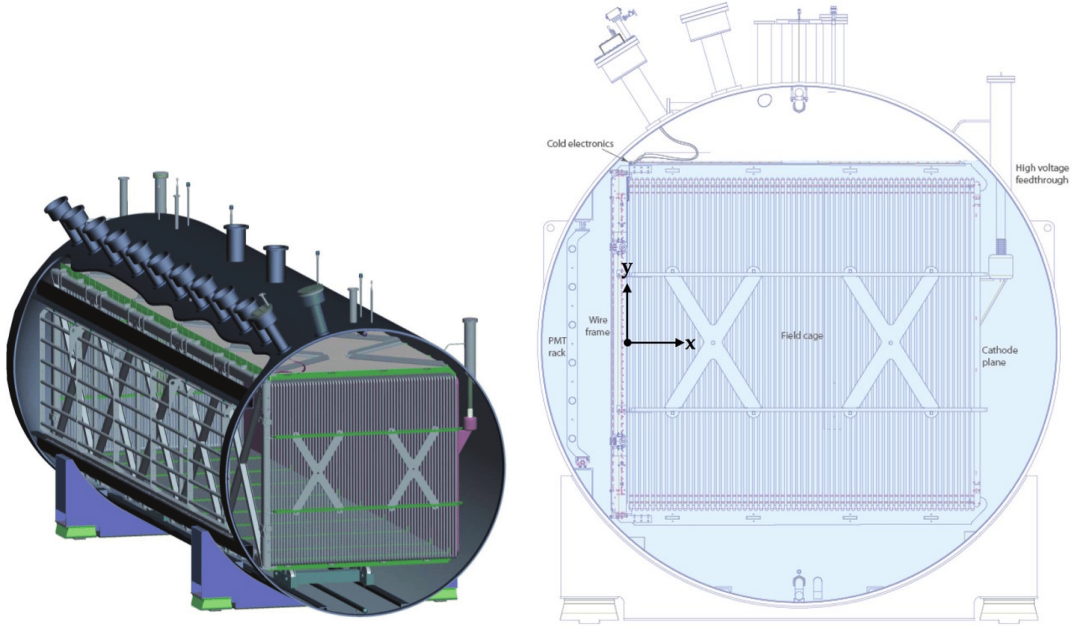


**Figure 3.9.:** Diagram of the MicroBooNE LArTPC inside the cryostat with the open front and left side showing the field cage and anode planes respectively (Left). Cross-section schematic of the MicroBooNE detector orientated such that the beam direction (z-direction) is orientated out of the page [131].

however, it is only sensitive to the four sides of the X and Y coordinates of the detector [128].

### 3.3.3. ICARUS

The ICARUS detector was first operated in 2010 and located at the Gran Sasso National Laboratory in Italy where it was used to detect events from cosmic rays and from the neutrino beam which is directed from CERN to Gran Sasso. In 2013 the decommissioning process began and the detector was taken to CERN for refurbishment before making its way to Fermilab and becoming part of the SBN program [11].

The ICARUS detector consists of two *modules* within a single cryostat with each module containing two TPCs. A schematic of this design is shown in Figure 3.10. Similar to SBND, the two TPCs within each module share a common cathode.

The dimensions of each module are (3.6, 3.9, 19.6) m and the cryostat contains 760 tonnes of liquid argon with an active volume of 476 tonnes. Again, the APAs consists of three wire planes with a wire plane spacing and wire pitch of 3 mm. In contrast to SBND and MicroBooNE however, the wire planes are orientated horizontally for the first induction plane and at  $\pm 60^\circ$  for the second induction plane and the collection plane. The choice of having a horizontal wire plane is due to ICARUS being initially designed to detect cosmic rays which would predominantly enter the detector from above and therefore be travelling perpendicular to the horizontal. The nominal electric field in each of the TPCs is 500 V/m [11].

The light collection system for ICARUS is comprised of a series of 74 PMTs positioned behind the wire planes. The layout of the PMTs is, however, asymmetric with the east module having a  $3 \times 9$  array of PMTs for each TPC whereas the two TPCs in the west module have a single row of 9 PMTs plus two additional PMTs located centrally above and below the main row in the right chamber. Since the light is again produced with wavelengths in the VUV region, the PMTs are coated with TPB in order to shift the wavelength into the visible region [11].

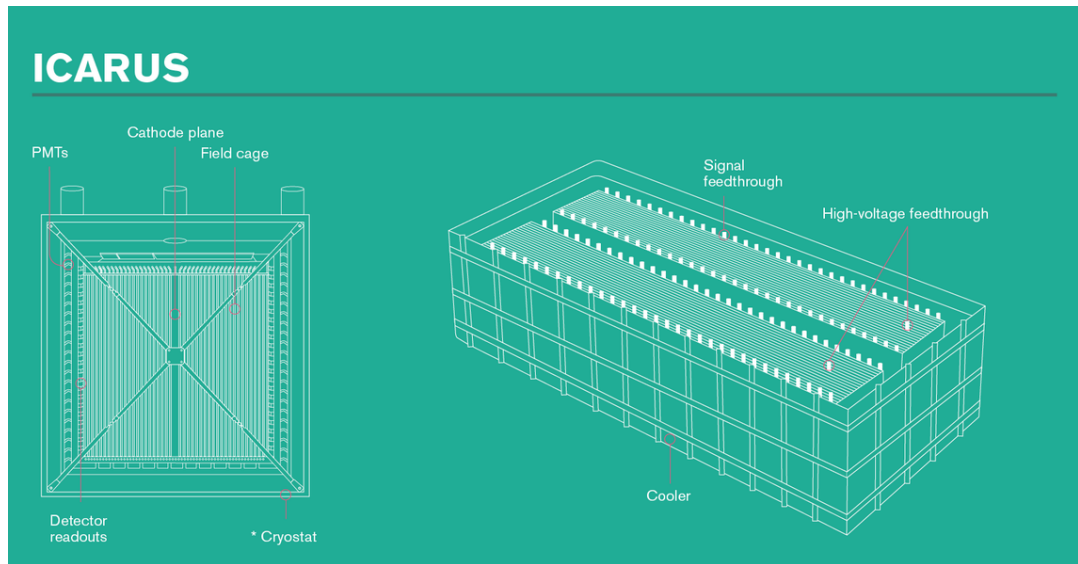


**Figure 3.10.:** Schematic of the ICARUS detector. The left image shows a cross-section of one of the two modules whereas the right image shows the whole detector with the two modules side by side [132].

The ICARUS CRT system surrounds the detector on all sides however the actual position is not always the same due to design choices. The CRT on the topmost side which experiences the highest flux of cosmic rays, is located outside the TPC, about 3m from the top face above the readout electronics. It consists of two planes of scintillating modules with the readout coming from the same electronics board as is used by SBND. The CRT for the vertical sides are again outside the TPC and behind the PMT arrays and close to the cryostat walls. The scintillator modules from the MINOS experiment are being reused for this purpose. The CRT for the bottom face are the repurposed spare modules from the veto shield from the Double Chooz experiment and are located within the cryostat. Only about 50% of the bottom face is covered by the CRT because of limited space due to the supporting structure of the cryostat [11] [133].

### 3.4. SBN Physics Capabilities

The SBN program was designed with the aim of resolving the contentious results observed by a number of experiments as was discussed in Section 2.2.3. Since it was purposely planned with this in mind, the SBN program has a number of advantages over previous experiments in the hopes of detecting eV scale sterile neutrinos: it has a multi-detector design, the near and far detectors are positioned such that the oscillation signal is close to maximal for an expected set of oscillation parameters, the detectors use the same technology and have the same target medium [13].

The top two plots of Figure 3.11 show the expected oscillation probability for the  $\nu_e$  appearance channel as a function of the baseline for two sets of oscillation parameters,  $(\sin^2 2\theta_{\mu e}, \Delta m_{41}^2) = (0.015, 0.3 \text{ eV}^2), (0.002, 1.5 \text{ eV}^2)$  and a neutrino energy of 700 MeV. The neutrino energy corresponds to the peak energy of the BNB and the oscillation points are chosen as the upper and lower limits of the global  $\nu_e$  appearance data. In both cases, there is a clear difference in the oscillation probability between the near and far detector showing that the SBN program is sensitive to oscillations within this parameter range [13]. The bottom two plots show the oscillation probability for the same two oscillation points as a function of neutrino energy for baselines of 110 m and 600 m. The ratio of the

oscillation probability at 600 m to that at 110 m is also shown. Again, there is a clear difference in the oscillation probability for most energies showing that the SBN program is sensitive to a wide range of neutrino energies [13]. The  $\nu_e$  appearance oscillation sensitivity constructed at the time of the proposal is shown in Figure 3.12. These contours include the relevant backgrounds and systematic uncertainties with the exception of detector systematics.

As Figure 3.11 shows, SBND will observe no or very few oscillated events and will give a measure of the absolute flux and interaction cross-section whereas both MicroBooNE and ICARUS are able to detect oscillated events with significant probability. Typically the BNB flux uncertainties and interaction cross-section uncertainties are fairly large, however, since SBND, MicroBooNE and ICARUS use the same interaction medium and the same technology to detect interactions, the uncertainties may be constrained [13].

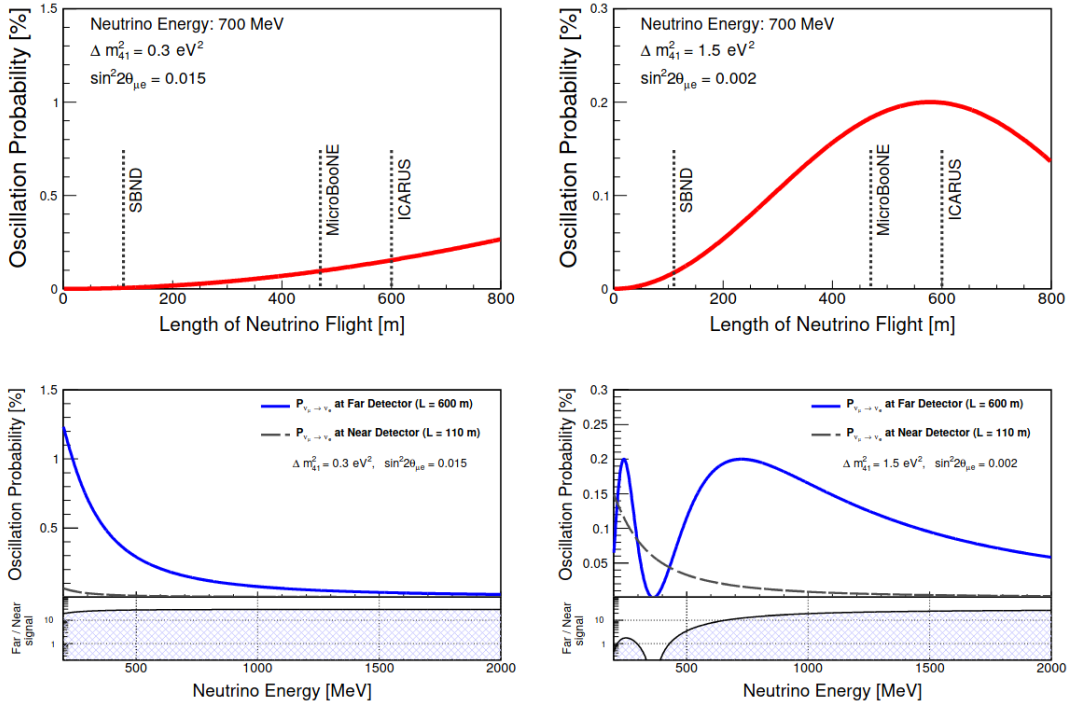


**Figure 3.11.:** The oscillation parameters used in the two left and right plots are  $(\sin^2 2\theta_{\mu e}, \Delta m_{41}^2) = (0.015, 0.3 \text{ eV}^2), (0.002, 1.5 \text{ eV}^2)$  respectively. Top: The oscillation probability as a function of the baseline for the  $\nu_e$  appearance channel. A neutrino energy of 700 MeV is used in both cases. Bottom: The oscillation probability is shown as a function of neutrino energy in both the near and far detectors. Additionally, the ratio of the oscillation probabilities between the two detectors is also shown. [13]

This main goal of the SBN program revolves around sterile neutrino oscillation analyses, however, the close proximity of the SBN detectors and in particular SBND to the neutrino beam source will allow for a high statistics study of neutrino argon interactions. This will provide valuable information for future liquid argon-based experiments such as DUNE. SBND is expected to observe on the order of 2 million neutrino CC interactions a year which is sufficient to be able to minimise the associated uncertainty to a point such that systematic uncertainties become dominant. As the BNB consists predominantly of  $\nu_\mu$ 's, most events will also be  $\nu_\mu$  based, however the  $\nu_e$  fraction of the BNB is sufficient to expect 50,000  $\nu_e$  events a year in SBND which is enough to perform both inclusive and exclusive analyses. There is also the opportunity to measure rare channels with a big increase in

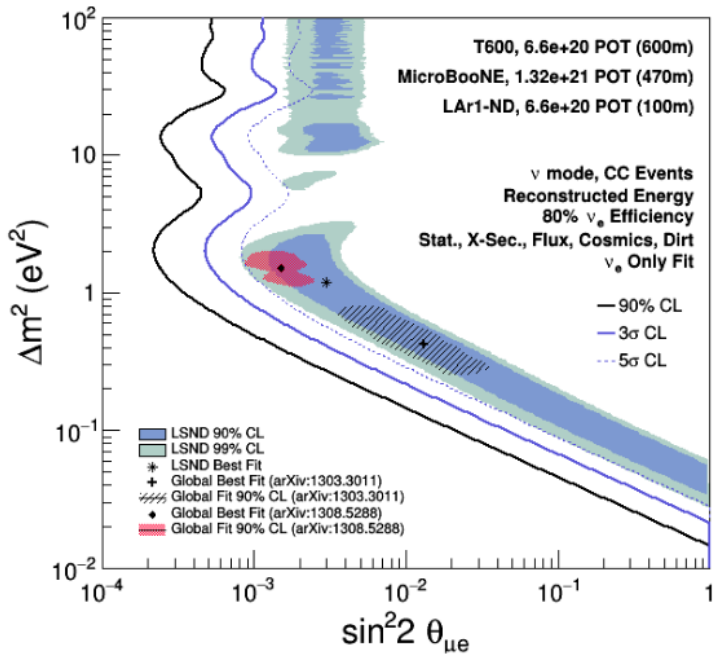


**Figure 3.12.:** The expected  $\nu_e$  appearance sensitivity from the SBN program using inputs constructed at the time of the SBN proposal. Limits from LSND and global best fit results are also shown [11].

statistics or possibly even for the first time such as final states involving hyperons or  $\nu - e^-$  elastic scattering [13] [134].

The large event rate and the high-resolution event reconstruction provided may allow the SBN program to be sensitive to BSM physics other than sterile neutrino oscillations [13]. The potential areas include, but are not limited to,

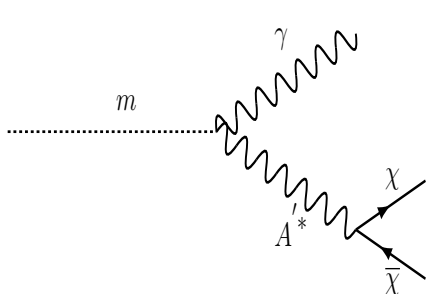
- Light Dark Matter - Assuming a dark matter particle has an associated light mediator particle which interacts with quarks, the high-intensity proton beam will produce a dark matter beam alongside neutrinos. The dark matter particles will propagate to the detectors alongside the neutrinos where they may scatter off the argon nuclei. Neutrinos will however represent a large background in such a search [13].
- Large Extra Dimensions - The neutrino mass scale could be explained by the presence of additional dimensions. The right-handed neutrinos would be

able to propagate in the extra dimensions whilst the active neutrinos would be confined to the standard dimensions [13].

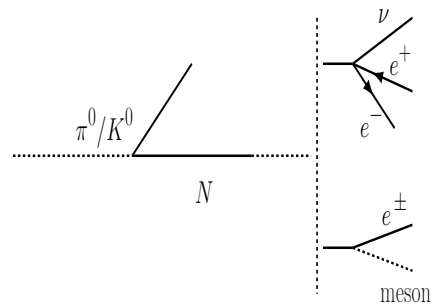
- Heavy Sterile Neutrinos - If heavy sterile neutrinos (heavy neutral leptons) such as those present in the seesaw-mechanism discussed in Section 2.2.2.3 are of an MeV mass scale, they may be produced in the BNB via meson decay. They would then propagate along the beamline and their decay products may be observed in the detectors [13] [135].
- Dark Neutrinos - A beam neutrino interacts with an argon nucleus and scatters to a dark neutrino. The dark neutrino decays to a dark boson (and neutrino) and in turn, the dark boson decays to an  $e^+ e^-$  pair. This mechanism could provide an explanation for the MiniBooNE low energy excess [13] [136].
- Millicharged Particles - Extensions to the SM may lead to particles with a very small charge relative the electron (i.e. the observed quantised charge would no longer hold). Millicharged particles may be produced via the decay of mesons meaning SBN has the ability to detect them. Two possible signatures for millicharged particles would be the observation of multiple low energy deposits which are aligned with the beam target or the elastic scattering of millicharged particles with electrons with the sensitivity being enhanced for the detection of low energy electrons.

Feynman diagrams of possible light dark matter, heavy sterile neutrino, dark neutrino and millicharged particle interactions are shown in Figure 3.13.

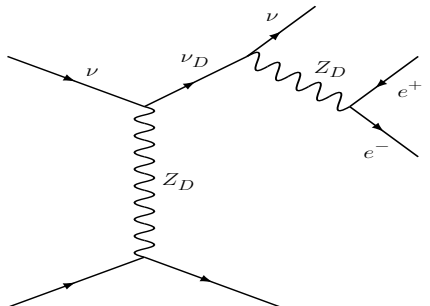
**Light Dark Matter**



**Heavy Sterile Neutrino**



**Dark Neutrinos**



**Millicharged Particles**

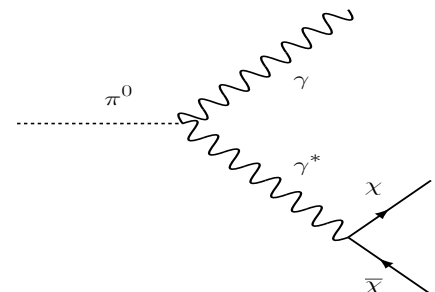


**Figure 3.13.:** Feynman diagrams of BSM processes. Top right: Light dark matter. Top Left: Heavy sterile neutrinos. Bottom Left: Dark neutrinos. Bottom Right: Millicharged particles.



# Chapter 4.

## Electromagnetic Shower Energy Reconstruction in SBND

The EM shower energy is an important quantity that is used in a number of areas, especially in the context of a  $\nu_e$  analysis. One of the primary uses is in calculating the reconstructed electron neutrino energy, which is a key component of neutrino oscillations since the oscillation probability depends on  $\frac{L}{E}$ . The neutrino energy is usually found by summing up the energy of all the outgoing products of a neutrino interaction to which (for  $\nu_e$  CC QE interactions) the shower energy is expected to make the dominant contribution [137].

This chapter covers the basics of event simulation and reconstruction and then goes on to discuss the three currently available EM shower reconstruction algorithms available for use in SBND. The performance of each algorithm is assessed by comparing with truth information. The reconstruction is validated for both electron and photon showers as well investigating the impact of the shower energy and angle on the reconstruction performance.

### 4.1. Event Simulation and Reconstruction

Event simulation and analysis are performed using the Liquid Argon Software (LArSoft) framework which interfaces with a number of other frameworks such

as Generates Events for Neutrino Interaction Experiments (GENIE) for neutrino interaction generation, GEometry ANd Tracking (GEANT4) for simulated particle tracking and Pandora for pattern recognition and 3D reconstruction [138] [139] [140] [141]. LArSoft has been designed to work for many liquid argon-based neutrino experiments, including the SBN program, with many of the underlying algorithms being common to all experiments [142] [143].

Reconstructed quantities are the main focus of this chapter and these are typically derived from the reconstructed charge which is obtained in the following steps;

1. Drifting electrons induce current on a wire at the anode.
2. Apply signal processing techniques to remove the effects of the E-field, electronics and some frequency-dependent noise.
3. A hit finding algorithm identifies any significant waveforms and classifies these as hits across a certain time window (number of ticks).
4. The Pandora pattern recognition software clusters the hits together such that they represent an individual particle. This is initially done in 2D, followed by matching the clusters between the wire planes in order to produce 3D clusters.
5. The lineage of the particles is identified and the particles are classified as either track- or shower-like.

A number of different hit-finding algorithms exist, but the default one used by LArSoft is the *GausHitFinder*. Once the algorithm has identified a waveform that peaks above some threshold (the threshold in SBND is 10 Analog Digital Converter (ADC) counts), it attempts to fit one or more Gaussians to the waveform. For each peak, the centre and width are identified and these values are used to produce the associated Gaussian fit. For most cases, the *GausHitFinder* works well, but two areas where it can struggle are resolving hits which are closely spaced and fitting a Gaussian to waveforms that are not well represented by a Gaussian. The latter tends to occur when charge is directed towards the wire planes (e.g. from a shower that was produced at a large angle to the beam line instead of being mostly forward going) which causes a long pulse train on but a few wires. This

results in waveforms where the ADC count is above threshold for many ticks and is without a clear central peak. In such cases, the signal above threshold may be better represented by a series of N-Gaussians, however, this is still far from perfect and fitting a large number of peaks can appreciably increase computing time [144]. Figure 4.1 shows examples of some waveforms in blue along with the attempted Gaussian fit in red. The top plot shows an example waveform that is well represented by a Gaussian, whereas in the bottom plot there is a waveform that is above threshold for many ticks with a number of different peaks to which the *GausHitFinder* has attempted to fit a single Gaussian. This waveform is not representative of a single Gaussian and therefore the associated reconstructed charge will deviate significantly from the true value.

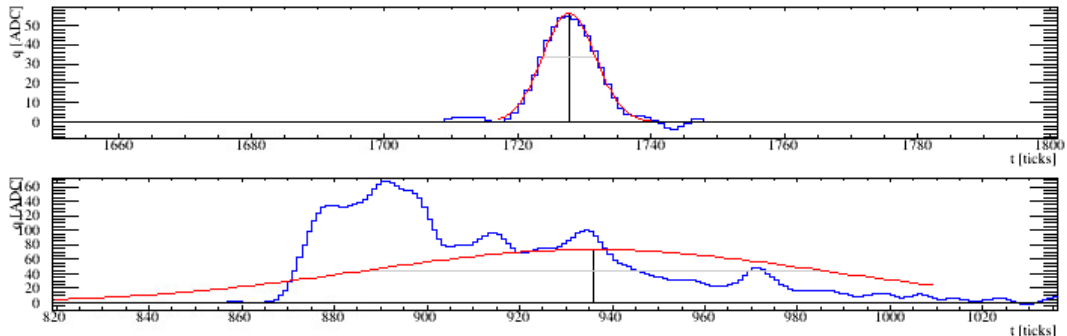


**Figure 4.1.:** Waveforms (blue) that have been fitted with a Gaussian (red) from the *GausHitFinder*. Top: an example of a waveform that is well represented by a Gaussian. Bottom: an example of a waveform that is not well represented by a Gaussian.

## 4.2. Overview of Shower Energy Reconstruction in SBND

Currently, there are three algorithms available for reconstructing EM shower energy within SBND as part of the *LArPandoraShower* suite of tools, each of which is described below. Regardless of the algorithm used, the initial approach is the same for all three methods which is as follows,

1. Identify the hits associated with a given wire plane.

2. Integrate the hits to obtain the associated charge in ADC units whilst correcting for electron lifetime.
3. Convert the charge in ADC units to a conventional charge (number of electrons) using the calibration constant which is part of the calorimetry algorithm (this step was not performed in the case of the *Linear Energy tool*).

Once the charge of a hit has been determined, the final steps which involve converting the charge to energy become method dependent. The other major detector effect that still needs to be considered is recombination, which is modelled by the Modified Box Recombination Model and given by

$$\frac{dE}{dx} = \frac{\exp\left(\frac{\beta}{\rho\mathcal{E}}W_{ion}\cdot\frac{dQ}{dx}\right) - \alpha}{\frac{\beta}{\rho\mathcal{E}}}, \quad (4.1)$$

where  $\frac{dE}{dx}$  is the deposited energy per unit length,  $\frac{dQ}{dx}$  is the deposited charge per unit length,  $\mathcal{E}$  is the electric field in the detector,  $\rho$  is the density of liquid argon,  $W_{ion} = 23.6 \text{ eV}/e^-$  which is the energy required to ionise an argon atom,  $\alpha = 0.93 \pm 0.02$  and  $\beta = 0.212 \pm 0.002 \text{ (kV/cm)(g/cm}^2\text{)/MeV}$ . The values for parameters  $\alpha$  and  $\beta$  are results from the Argon Neutrino Test Stand (ArgoNeuT) experiment [145]. The recombination correction,  $R$ , is given by  $\frac{\frac{dQ}{dx}\cdot W_{ion}}{\frac{dE}{dx}}$ .

Since the recombination model is  $\frac{dE}{dx}$  dependent, an accurate path length,  $dx$ , is needed which requires 3D reconstruction of the direction. Because a shower is treated as a single object, which means the trajectory of constituent components are not tracked, it is therefore not straightforward to directly correct for the recombination effect [146]. Two different approaches have been considered and are discussed in the relevant energy reconstruction methods below: 1) assume a nominal recombination value for all hits and 2) use a lookup curve which relates the collected charge to energy which circumvents the need to evaluate a recombination correction directly because it already gets accounted for in the curve.

In the analysis and validation of the shower reconstruction, a number of *true* and *reconstructed* quantities are considered. Care must be taken that it is clear what each value relates to. For clarity, the following quantities are explicitly described;

- Collected charge (or energy): This is the charge that is seen by the wire planes.
- Deposited charge (or energy): This is the charge that is initially deposited in the detector. Typically this would be obtained from the collected charge by correcting for the electron lifetime and the recombination effect.
- Hit energy: This is the energy associated with each individual hit. Both true and reconstructed values may be obtained.
- Energy of showering particle: This is the energy of the particle which results in the shower which is being investigated.

#### 4.2.1. Linear Energy

The first shower energy reconstruction method developed was the *Shower Linear Energy tool*. This tool relies on the linear relationship between the true energy deposited in the detector and the reconstructed charge from Minimum Ionising Particle (MIP) muons. A sample of simulated muons are used as calibration because the  $\frac{dE}{dx}$  value for electrons and MIP muons are not dissimilar. The relationship between the charge obtained from the hits due to the muons and the energy deposited by the muons is shown in Figure 4.2. A linear relationship such as this is comparable to assuming a constant recombination factor.

To estimate the reconstructed shower energy, the charge found to be associated with a shower would be used to directly read off the associated energy from the linear calibration. A further recombination correction is not required as it has already been accounted for in the charge-to-energy conversion. It should be noted that along with the recombination correction, hit reconstruction and pattern recognition inefficiencies are also corrected for in the calibration curve. The *Shower Linear Energy tool* has been largely disfavoured since the development of the two other reconstruction tools.

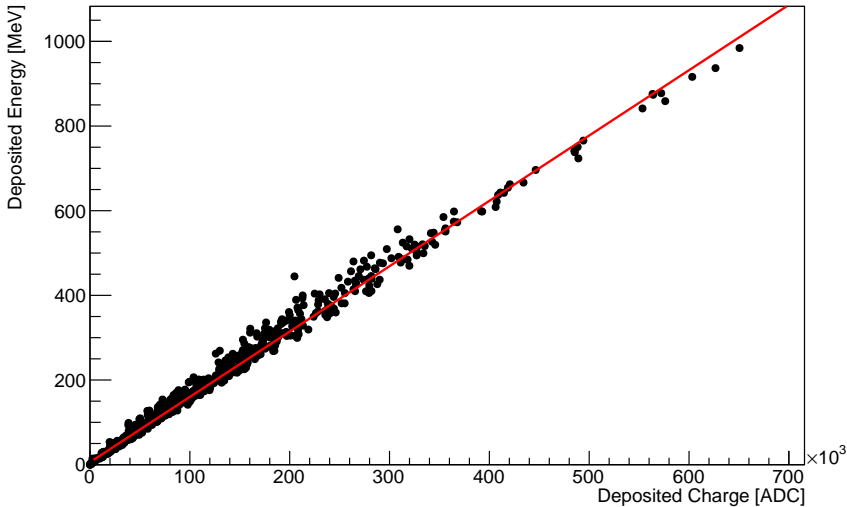


**Figure 4.2.:** The linear relationship between deposited charge and energy. Produced from a sample of muons used for calibrating the *Shower Linear Energy tool*.

#### 4.2.2. Number of Electrons to Energy

The *Shower Num Electrons Energy tool* was developed to move away from being reliant on in-house calibration curves and instead use the pre-existing calibration available in the SBND portion of the LArSoft framework. This has the advantage of being much more flexible to physics changes. For example, a change in the recombination correction could be investigated by changing a single number, whereas, for the *Shower Linear Energy tool*, the calibration curves would have to be regenerated. The number of electrons are found from the ADC charge and are then directly converted to energy using a scale factor which is the inverse of the energy required to ionise an argon atom. A nominal recombination value of 0.64 is assumed which is applied to all hits.

The nominal recombination value was calculated by simulating electrons whilst using a large (effectively infinite) value for the electron lifetime and setting both the transverse and longitudinal diffusion coefficients to zero. The only detector effect remaining that may impact the collected energy is the recombination effect and therefore taking the ratio between the collected and deposited energy will give a value for the recombination effect. For electrons, it was found that the

recombination effect was fairly constant at a value of 0.64 across a broad range of energies [147].

### 4.2.3. ESTAR Method

The *Shower ESTAR Energy tool* combines the ESTAR database provided by the National Institute of Standards and Technology (NIST) along with the Modified Box recombination model in an approach that was first used by the ArgoNeuT experiment [148]. The ESTAR database provides the track length of electrons in various materials, including liquid argon, for energies ranging from 0.01 MeV to 1000 MeV [149].

$\frac{dE}{dx}$  values may be calculated by dividing the energy by the track length for each entry in the ESTAR database. The deposited charge,  $Q$ , can then be found by using Equation 4.1 to find  $\frac{dQ}{dx}$  and multiplying by the track length,  $dx$ . This now allows the collected charge and energy to be related. If  $\mathcal{E}$  in Equation 4.1 is taken to be a variable, the above process may be repeated whilst iterating over a set value of  $\mathcal{E}$ . This results in a 3D curve relating both the deposited charge and electric field to energy as is shown in Figure 4.3. The energy may then be interpolated from the collected charge and the appropriate electric field. As with the *Shower Linear Energy tool*, a direct correction for recombination is not needed as it is again accounted for in the lookup curve.

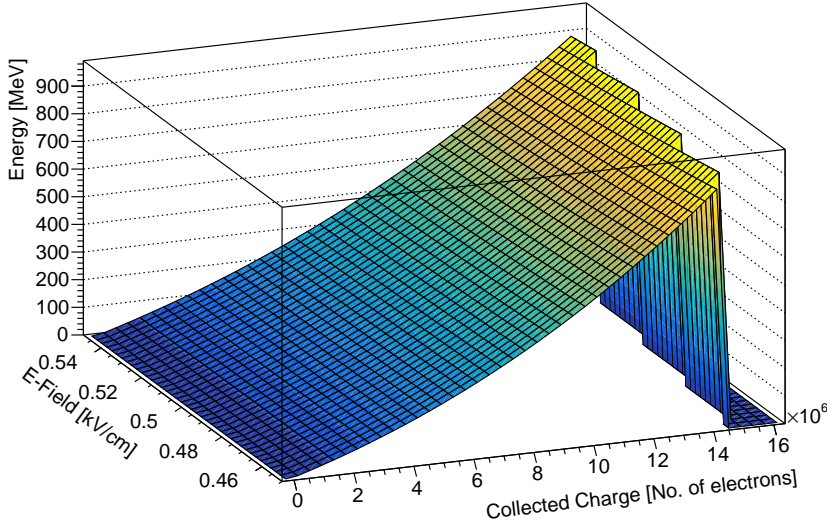


**Figure 4.3.:** ESTAR lookup curve generated from the ESTAR database and the Modified Box Recombination Model.

### 4.3. Shower Energy Reconstruction Performance

In order to assess the performance of the different reconstruction methods, a comparison with *truth* information is performed. Depending on the approach, a few other inefficiencies should be considered, namely that the hit reconstruction and Pandora pattern recognition are not perfect [141]. This results in hits missing due to not being reconstructed plus the addition of the clusters that Pandora produces being incomplete. Therefore, there are typically fewer hits than there would be if the shower in question were to be perfectly reconstructed. Reconstructing the energy of the showering particle, is desirable for a number of analyses, however, due to these issues, it is not realistic to expect agreement to be within a few per cent. Improving the hit reconstruction or the pattern recognition within Pandora would clearly help, but it is likely that a non-negligible bias would remain. Work on Pandora, the hit reconstruction and addressing any remaining bias is however beyond the scope of this chapter. To circumvent the inefficiencies in Pandora's pattern recognition, Pandora is run in *cheating* mode, which means that truth information is used to perform the clustering. This decouples the reconstruction

methods from any effects due to Pandora’s pattern recognition. For comparison, a number of figures showing the reconstruction performance without using Pandora in cheating mode are shown in Appendix C.

To purely gauge the performance of a given reconstruction method, it is probably best to compare the truth and reconstructed energy of a shower by only considering the available hits. This way, the reconstruction method is only validated from the available information and is additionally decoupled from hit reconstruction inefficiencies. However, additional care must be taken when using the true energy of the hits. What is considered a hit is user defined in that the width that defines a hit is a parameter that may be changed. Therefore, the true energy associated with a hit is dependent on the chosen width. Within LArSoft, the default width of a hit is  $1\sigma$  which is chosen to try and find a balance between covering a sufficient amount of charge whilst still being able to resolve multiple hits which are closely spaced. The hit width considered here has been left at the default value of  $1\sigma$ .

Generally, the validation is performed on a shower-hit level. This means that for a given shower, the energy of each hit is reconstructed and then summed together to obtain the energy of the shower. The exception to this is in the case of the *Linear Energy tool*. During its development, it was customary to sum up the charge of all the hits and then convert to energy. This is why the calibration curve in Figure 4.2 has energies on the order of a shower level and not a hit level (individual hit energies are usually  $\lesssim 5$  MeV) and also why it is possible to evaluate shower energies above 1000 MeV using the ESTAR method.

#### 4.3.1. Validation of a BNB Sample

In order to validate the reconstruction methods, an  $e^- + \pi^+$  vertex sample with BNB-like properties was produced where the electron is the showering particle. The pattern recognition is comprised of a number of steps some of which rely on the reconstructed vertex. It is therefore important to correctly reconstruct the vertex to avoid inaccuracies in the pattern recognition and it is usually easier to accurately reconstruct the vertex of an event if two particles are emanating

from a single point rather than just one particle. Unless otherwise stated, all the validation has been performed using the collection plane.

The true vs reconstructed energy is shown in Figure 4.4 for all three methods where the true energy has been calculated from the shower hits. The results from the *Shower Linear Energy tool* and the *Shower ESTAR Energy tool* are similar and show good agreement between true and reconstructed energies across the whole energy range whereas the *Shower Num Electrons Energy tool* tends to overestimate the hit energies. Figure 4.5 is similar, but instead, the true energy is the energy of the showering electron. This gives a measure of the bias each method can expect due to the inefficiencies mentioned above. Both the *Shower Linear Energy tool* and the *Shower ESTAR Energy tool* underestimate the true energy of the showering electron as is expected. The *Shower Num Electrons Energy tool* shows better agreement due to systematically applying a higher energy to individual hits which compensates for other inefficiencies.

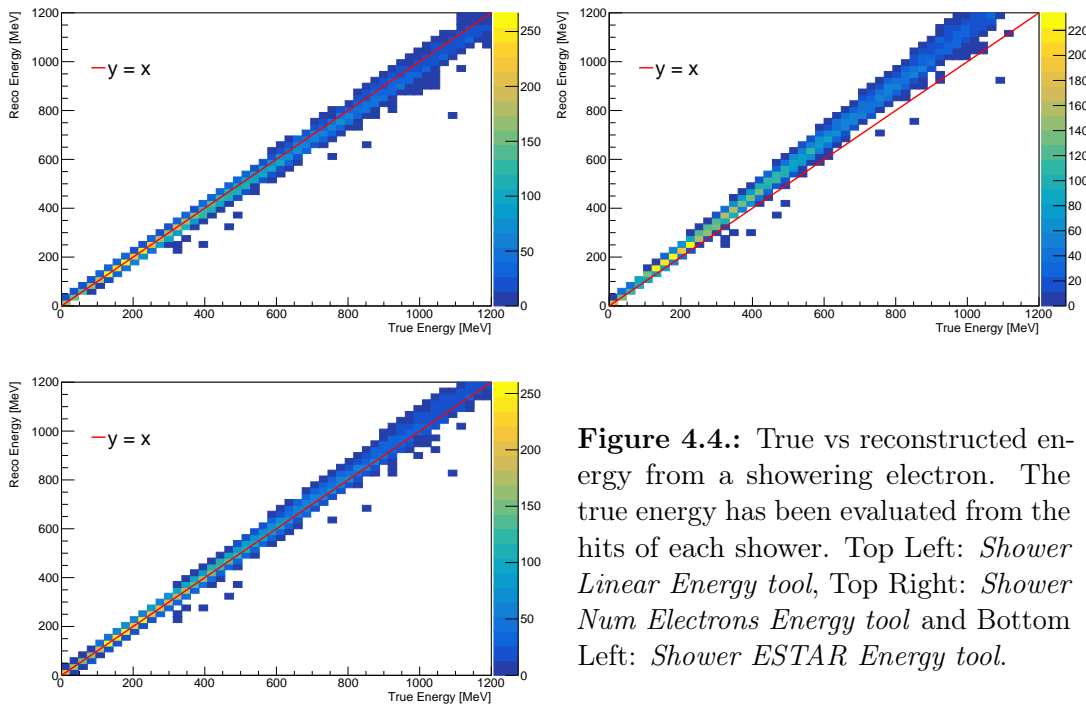


**Figure 4.4.:** True vs reconstructed energy from a showering electron. The true energy has been evaluated from the hits of each shower. Top Left: *Shower Linear Energy tool*, Top Right: *Shower Num Electrons Energy tool* and Bottom Left: *Shower ESTAR Energy tool*.

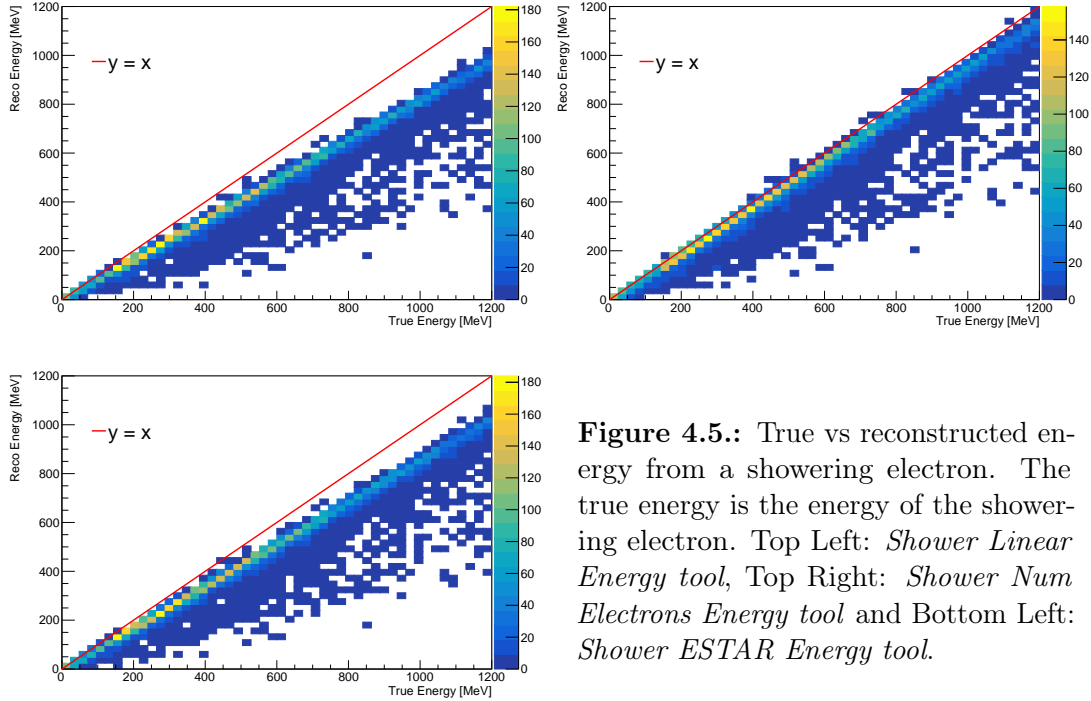


**Figure 4.5.:** True vs reconstructed energy from a showering electron. The true energy is the energy of the showering electron. Top Left: *Shower Linear Energy tool*, Top Right: *Shower Num Electrons Energy tool* and Bottom Left: *Shower ESTAR Energy tool*.

A comparison of the fractional energy separation, which is defined as  $\frac{\text{Reco} - \text{True}}{\text{True}}$ , is shown in Figure 4.6 for both true energies. When comparing with the true energy of the hits, the *Shower ESTAR Energy tool* peaks quite tightly around zero as does the *Shower Linear Energy tool*. The *Shower Num Electron Energy tool* peaks to the right of the zero line again indicating that the reconstructed quantity is an overestimate. All three distributions peak to the left of the zero line when compared with the true energy of the showering particle with the *Shower Num Electrons Energy tool* giving the closest result.

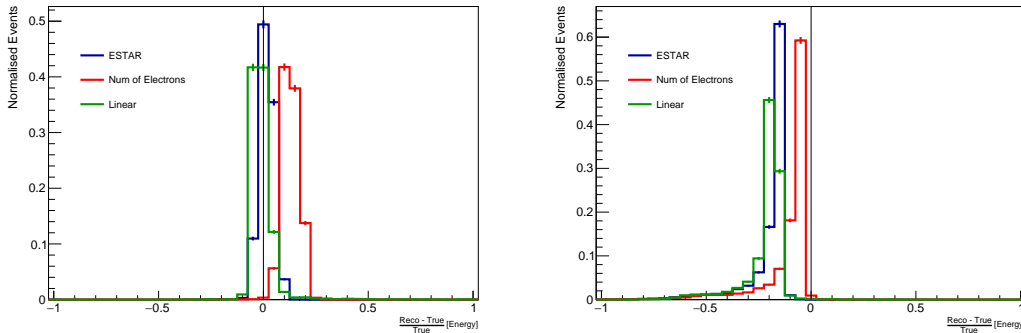


**Figure 4.6.:** Comparison of the fractional shower energy separation for the *Shower Linear Energy tool*, the *Shower Num Electrons Energy tool* and the *Shower ESTAR Energy tool*. Left: Using the true energy of the hits. Right: Using the true energy of the showering particle.

To get a measure of the resolution, which is defined as the width of the distribution, a Gaussian of the form

$$A \exp \left( -0.5 \left( \frac{x - \mu}{\sigma} \right)^2 \right), \quad (4.2)$$

is fitted to each distribution, where  $A$  is a constant that defines the peak of the Gaussian,  $\mu$  is the mean value and  $\sigma^2$  is the variance.  $\sigma$  is the quantity that defines the width of the Gaussian fit and will therefore also give a measure of the resolution of the associated distribution. For the distributions which use the true energy of the hits (the left plot of Figure 4.6), Gaussians are fitted to the entire distribution, whereas for the distributions using the true energy of the showering electron (the right plot of Figure 4.6), Gaussians are only fitted to the central region which encompasses the peak of the distribution. The reason for not fitting a Gaussian to the entire distribution in the second case is in order to avoid having the fit be influenced by the non-Gaussian tail which is usually caused by issues in the reconstruction. Since the tail in the first case is minimal, this is not a concern and therefore a fit to the whole distribution is suitable.

The Gaussian fits to the fractional energy separation distributions of each of the three reconstruction algorithms are shown in Figure 4.7 and Figure 4.8 for the comparison with the true energy of the hits and the true energy of the showering

electron respectively. In order for the resolution comparisons to remain valid, the Gaussian fits in Figure 4.8 are produced by considering the same x-axis range size. Additionally, the binning range has been chosen such that the distribution shapes are comparable in order to minimise binning effects on the fit width whilst maintaining the same bin width for each method. The corresponding  $\sigma$  values for each of the Gaussian fits are shown in Table 4.1.

The Gaussian fits in Figure 4.7 for the *Shower Linear Energy tool* and the *Shower ESTAR Energy tool* are fairly similar with *Shower Num Electrons Energy tool* having a slightly broader fit. This is likely due to the *Shower Num Electrons Energy tool* systematically assigning higher energy values to each of the hits which makes event migration across bins more likely. It should be noted that the Gaussian fits will be influenced by binning artefacts in the distributions which are then mapped to the resolution. The Gaussian fits for all three methods have a similar width in Figure 4.8. The effect from event migration across bins is likely to be reduced due to the larger difference in energy between the sum of the hits and the showering electron.

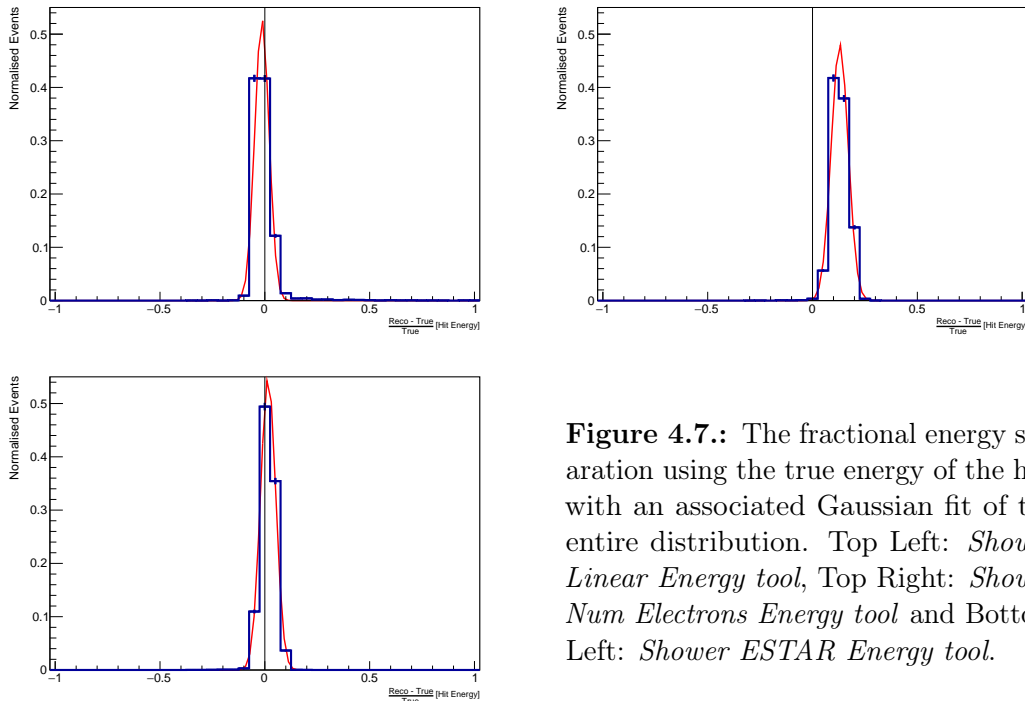


**Figure 4.7.:** The fractional energy separation using the true energy of the hits with an associated Gaussian fit of the entire distribution. Top Left: *Shower Linear Energy tool*, Top Right: *Shower Num Electrons Energy tool* and Bottom Left: *Shower ESTAR Energy tool*.

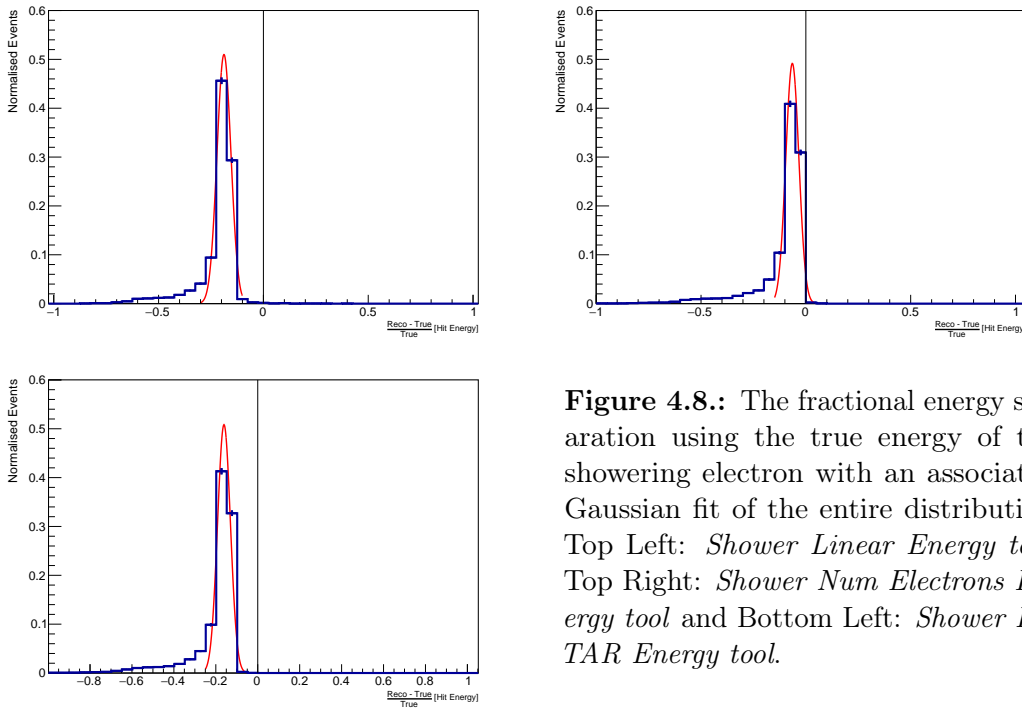


**Figure 4.8.:** The fractional energy separation using the true energy of the showering electron with an associated Gaussian fit of the entire distribution. Top Left: *Shower Linear Energy tool*, Top Right: *Shower Num Electrons Energy tool* and Bottom Left: *Shower ESTAR Energy tool*.

Algorithm	Hits	$\sigma$ of the Gaussian Fit Showering Electron
Linear	0.034	0.033
Num of Electrons	0.040	0.031
ESTAR	0.036	0.031

**Table 4.1.:** The  $\sigma$  value used in the Gaussian fit to the fractional energy separation distributions of each algorithm. Both the distributions which use the true energy of the hits (Figure 4.7) and the true energy of the showering electron (Figure 4.8) are shown.

To confirm that the reconstruction performance is comparable across all wire planes, the true vs reconstructed energy was also plotted for the two induction planes using the ESTAR method. This is shown in Figure 4.9 where the comparison has been made with the true energy of the hits.

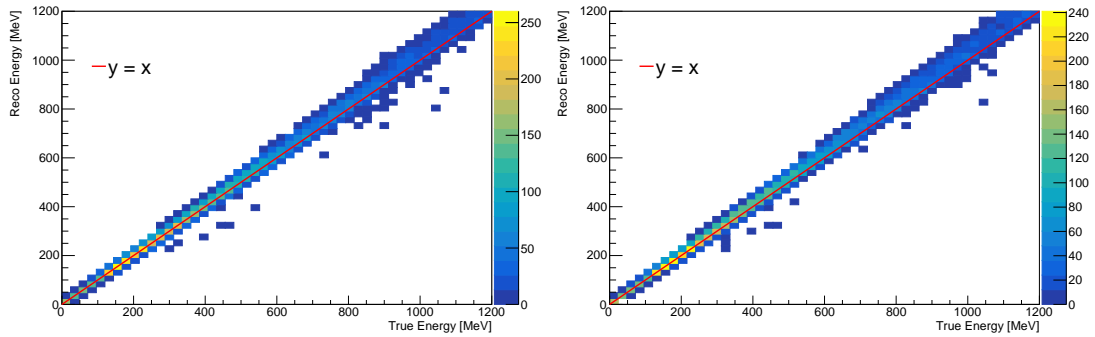


**Figure 4.9.:** True vs reconstructed energy from a showering electron for the first induction plane (Left) and the second induction plane (Right) using the ESTAR method. The true energy has been evaluated from the hits of each shower.

Since photons also produce EM showers, a BNB-like  $\gamma + \pi^+$  sample was produced to verify that the reconstruction works equally well in this case. Figure 4.10 shows this using the ESTAR method with the hits from the collection plane.

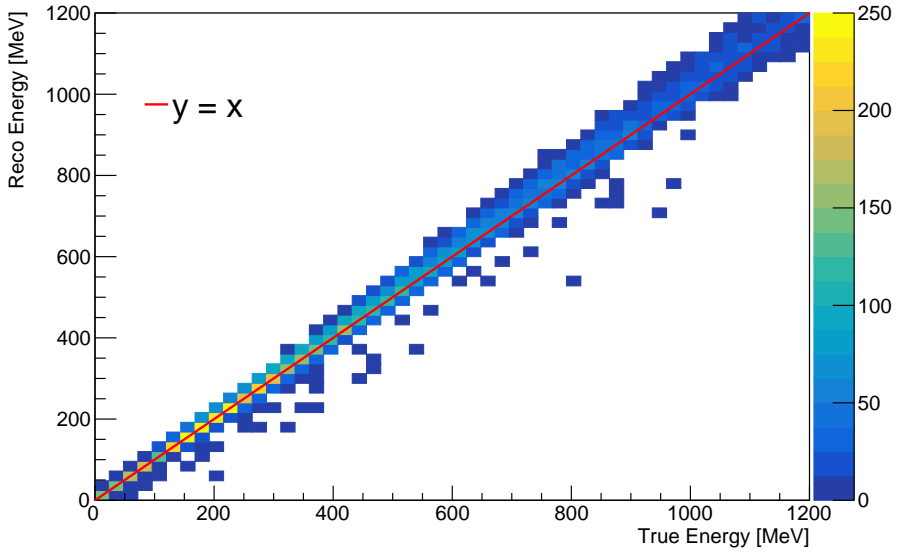


**Figure 4.10.:** True vs reconstructed energy from a showering photon using the ESTAR method with the hits from the collection plane. The true energy has been evaluated from the hits of each shower.

### 4.3.2. Performance as a Function of Angle

From a BNB neutrino sample, most of the showers are expected to be predominantly forward-going. A fraction of showers will however be directed at large angles to the beamline. As was mentioned in Section 4.1, showers directed towards the wire planes tend to produce waveforms which are not well represented by Gaussians. Since the *GausHitFinder* has trouble applying a suitable fit to these cases, a degradation in the reconstruction performance is expected as a function of angle.

In order to verify this, an  $e^- + \pi^+$  sample was produced with the electron being directed in all  $\theta_{xz}$  angles. Otherwise, this sample is also BNB-like.  $\theta_{xz}$  is the angle between the beamline and the positive x-direction and is defined in terms of the SBND coordinate system which is shown in Figure 4.11. The reconstruction performance is shown in Figure 4.12 using the ESTAR method for both definitions of true energy. Profiles of the histograms in Figure 4.12 are shown in Figure 4.13 where the y-axis error bars are the standard deviations. As

is expected, a degradation in the reconstruction performance is observed in both cases as  $\theta_{xz}$  tends away from  $0^\circ$ . It should be noted that the degradations are in opposite directions which may be explained by the fact that at large angles, the reconstruction method tends to overestimate the energy of the available hits, but the hit reconstruction also suffers, so the overall fraction of hits representing the shower is reduced. Both the *Shower Linear Energy tool* and *Shower Num Electrons Energy tool* have a constant recombination correction and therefore the conversion from charge to energy is linear. The *Shower ESTAR Energy tool* is not perfectly linear but it is close, especially in the region up to  $\mathcal{O}(10)$  MeV. Therefore, there is essentially no angular variation among the three methods so results akin to Figure 4.12 for the *Shower Linear Energy tool* and the *Shower Num of Electrons Energy tool* would look almost identical only with the y-axis scaled appropriately.

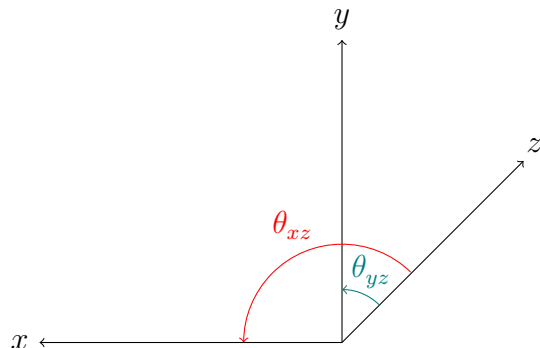


**Figure 4.11.:** The SBND coordinate system. The origin is located at the centre of the upstream face of the detector which is defined to be at  $(0, 200, 0)$  cm with the *z* direction being along the beamline.

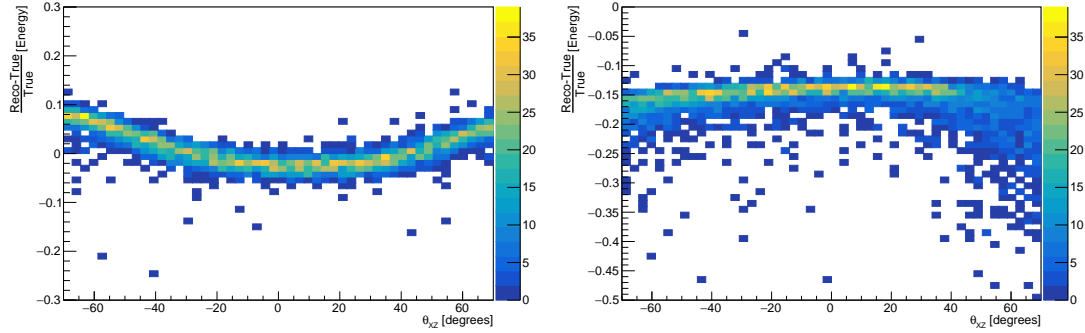


**Figure 4.12.:** The fractional energy separations as a function of  $\theta_{xz}$  using the ESTAR method. Left: true energy is calculated from the hits. Right: true energy is the energy of the showering electron.

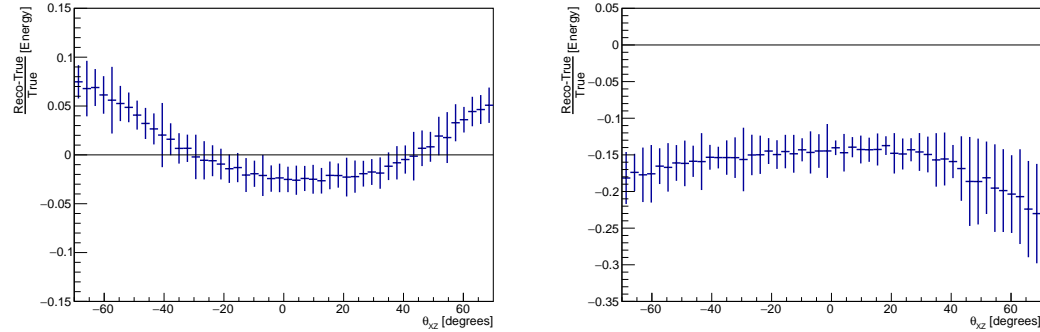


**Figure 4.13.:** Profile histograms of the fractional energy separation as a function of  $\theta_{xz}$  using the ESTAR method. The profile histograms are constructed from Figure 4.12 and the y-axis error bars are the standard deviations. Left: true energy is calculated from the hits. Right: true energy is the energy of the showering electron.

### 4.3.3. Performance as a Function of Energy

The EM showers produced in SBND from the BNB are expected to have energies up to around a GeV. Since the energy range is relatively broad, the reconstruction performance is evaluated as a function of the energy in order to confirm that the reconstruction methods work sufficiently well for all energies. As was the case for the angular dependence, the performance as a function of true energy is expected to not be method dependent. The only difference would be a y-axis scaling due to the different reconstruction performances.

On the whole, the fractional separation is observed to be fairly constant across all energies when comparing with both the true energy of the hits and the true energy of the showering particle as can be seen in Figure 4.14. The fractional energy separation is slightly lower at the lowest energies, especially when compared with the true energy of the showering particle. This is highlighted in Figure 4.15 which shows the profiles of the histograms of the fractional energy separation as a function of true energy and can likely be explained by a greater fraction of the hits not passing the threshold cut.

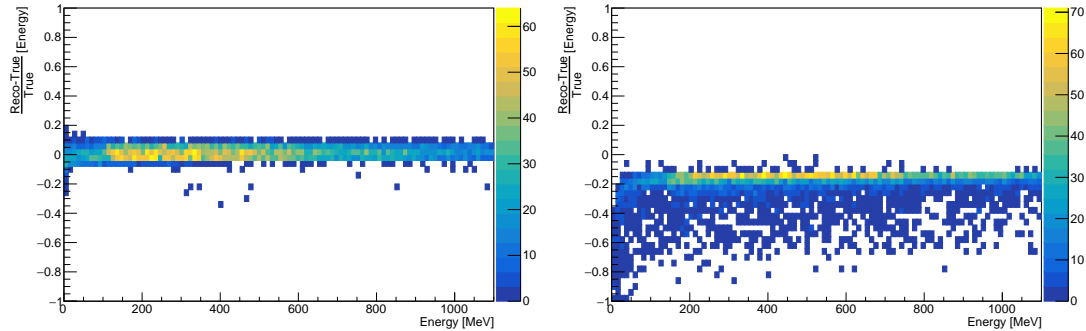


**Figure 4.14.:** The fractional energy separations as a function of true energy using the ESTAR method. Left: true energy is calculated from the hits. Right: true energy is the energy of the showering electron.

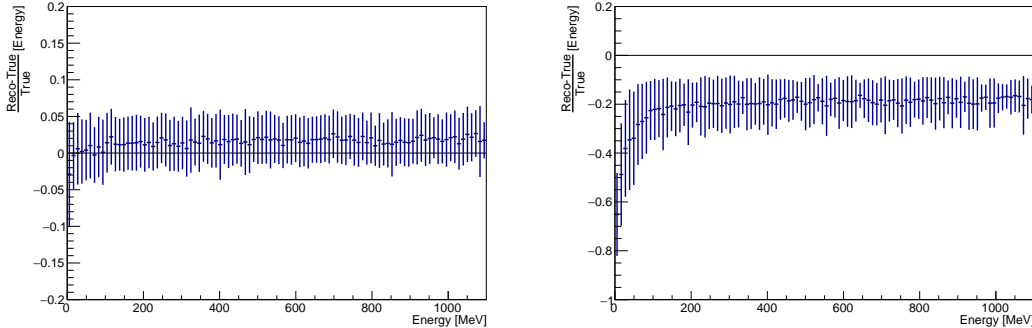


**Figure 4.15.:** Profile histograms of the fractional energy separation as a function of true energy using the ESTAR method. The profile histograms are constructed from Figure 4.14 and the y-axis error bars are the standard deviations. Left: true energy is calculated from the hits. Right: true energy is the energy of the showering electron.

## 4.4. Summary of EM Shower Reconstruction

The EM shower reconstruction algorithms have been demonstrated to work consistently across all three wire planes in SBND for showers originating from both electrons and photons. The reconstructed energy obtained from the *Shower Linear Energy tool* and the *Shower ESTAR Energy tool* show good agreement with the true energy of  $1\sigma$  width hits with the *Shower ESTAR Energy tool* performing slightly better. The *Shower Num Electrons Energy tool* systematically assigns a slightly higher energy to each of the hits. All three methods underestimate the true energy of the showering particle due to inefficiencies in the hit reconstruction plus the expected presence of an overall bias. The *Shower Num Electrons Energy tool* has the closest agreement with the true energy of the showering particle due to assigning higher energies to the individual hits.

The reconstruction performance is fairly consistent across all shower energies that are expected to be seen by the BNB. There is however a slight dip in performance at the lowest energies when compared with the true energy of the showering particle. This is due to a greater percentage of hits having energies below the threshold value. The reconstruction performance also degrades as the angle at which showers are produced to the beamline increases. This is not expected to be much of a concern as the majority of showers will be forward-going.

# Chapter 5.

## Sterile Neutrino Oscillation Inputs Within SBN

In order to perform an oscillation analysis, a number of inputs and analysis choices are required. Typically this involves generating some event sample in each detector for a given analysis, applying a physics hypothesis and some set of systematic uncertainties. A fit comparing the observed and predicted event rate is then performed giving the confidence level of the applied physics hypothesis. This is summarised in Figure 5.1 which shows the generic overview of the procedure coupled with the different components. Many of these items are common to all oscillation analyses and are agnostic to the fitting framework. The remainder of this chapter highlights some of the key inputs to the oscillation analysis along with some of the decisions that were made. The actual analysis results are detailed in Section 6 in addition to explaining how the VALOR framework processes or consumes these inputs where appropriate.

### 5.1. Monte Carlo Event Production

The events used in this oscillation analysis are truth based with a *pseudo reconstruction* applied. Work on the reconstruction is still in progress and at the time of writing has not been sufficiently completed for it to be possible to generate a fully reconstructed event sample. The pseudo-reconstruction involves applying

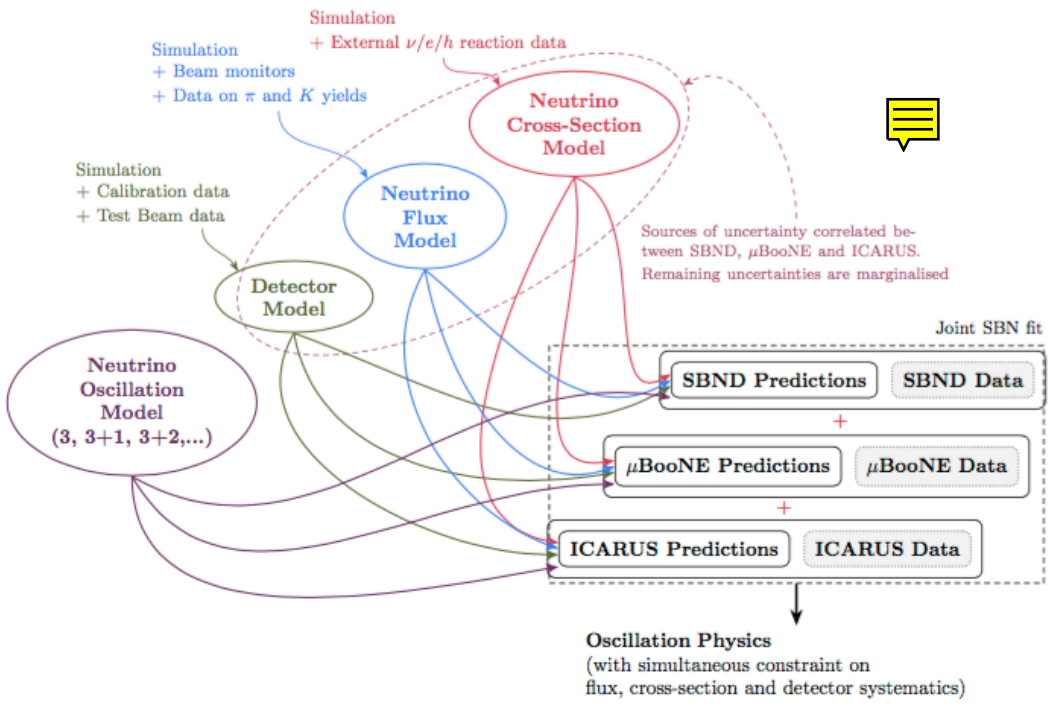


**Figure 5.1.:** Overview of the SBN oscillation analysis paradigm. A given model for the neutrino oscillation, detector, neutrino flux and neutrino cross-section are combined with the appropriate data to give the prediction for the respective detector. Individual detector predictions may be combined to give an overall SBN prediction.

energy smearing and a series of cuts to try and emulate a fully reconstructed sample. The details of the cuts and smearing that were applied to each of the analyses are discussed in Section 5.2.

Both the events for the  $\nu_\mu$  and  $\nu_e$  sample were generated using GENIEv3 (specifically the G18\_10a\_02\_11a tune) and then propagated through GEANT4 using the LArSoft framework [138] [150] [151] [139] [142]. For the  $\nu_\mu$  sample, this involved generating  $\sim 1,000,000$  intrinsic  $\nu_\mu$  events in each detector. The  $\nu_e$  sample is a little more involved since in addition to generating an intrinsic sample, an oscillated  $\nu_\mu \rightarrow \nu_e$  sample, a dirt sample and a cosmic sample also needed to be produced. The oscillated sample is used to mimic the  $\nu_e$  appearance signal whereas the dirt and cosmic samples are backgrounds. The other major background associated with a  $\nu_e$  analysis involves  $\nu_\mu$ . A dedicated sample was not produced to emulate this, but instead, the events from the  $\nu_\mu$  production were also

run through the  $\nu_e$  selection. Table 5.1 outlines the number of events produced for the  $\nu_e$  sample for each sub-sample for each detector. Additionally, the number of events that were selected from each sample are shown for all three detectors. The dirt events were produced with an additional filter at the generation stage which discarded any events where a shower above 10 MeV in the active volume was not present. This filter was used in order to remove any delta rays. Only about 1% of dirt events would pass this filter so the number of dirt events used in the  $\nu_e$  selection was  $\sim 100,000$ .

Sample	Produced	Selected		
		SBND	MicroBooNE	ICARUS
Intrinsic $\nu_e$	$\sim 1,000,000$	$\sim 150,000$	$\sim 140,000$	$\sim 130,000$
Oscillated $\nu$	$\sim 1,000,000$	$\sim 180,000$	$\sim 150,000$	$\sim 140,000$
$\nu_\mu$	Used $\nu_\mu$ sample	$\sim 2,000$	$\sim 3,000$	$\sim 3,000$
Dirt	$\sim 10,000,000$	$\sim 80$	$\sim 100$	$\sim 300$
Cosmic	$\sim 100,000$	$\sim 1$	0	$\sim 30$

**Table 5.1.:** The number of events produced and selected for each sub-sample of the  $\nu_e$  analysis. The same number of events were produced in each of the three SBN detectors.

The actual number of real  $\nu_\mu$  events expected in SBND is well over 5 million for about 3 years of data taking [125]. Generating this many events is not feasible as part of a MC production, hence the above number of events were generated. The MC events produced have an associated POT so the number of events may be scaled to the nominal POT of each experiment. For SBND and ICARUS the nominal POT is  $6.6 \times 10^{20}$  which corresponds to around 3 years of data taking. Since MicroBooNE has already been collecting data for some time, the nominal POT is  $1.32 \times 10^{21}$ . Due to scaling the generated event rate to the nominal POT this results in a non-integer number of events.

## 5.2. Event Reconstruction

To emulate reconstructed energies, the true energy of particles are smeared. For the  $\nu_\mu$  sample, the following conditions are applied. Primary tracks (which is the leading muon in the final state) contained in the active volume, have their true energy smeared by scaling the energy with a Gaussian which has a standard deviation of 0.02. If the primary track is not contained, the energy is instead smeared by a Gaussian with a standard deviation that is given by  $-A \ln(BL)$ , where  $L$  is the track length and  $A = 0.102$  and  $B = 0.000612 \text{ cm}^{-1}$  [11]. This emulates the multiple scatterings of the track, but in order for the track to have sufficient resolution, a minimum track length of 100 cm is required. Parameters  $A$  and  $B$  were chosen based on the work of [152]. Non-primary tracks with a true energy of less than 21 MeV are removed (21 MeV is the kinetic energy threshold for reconstructing tracks [11]) and any remaining tracks are smeared with a Gaussian which has a standard deviation of 0.05 [11]. An additional condition that the minimum smeared energy is 0 MeV is applied which ensures that negative energies do not occur.

The values used to determine the degree of energy smearing for the  $\nu_e$  sample are different to the  $\nu_\mu$  sample. The energy of electron and photon showers are smeared with a Gaussian that has a standard deviation of  $0.15/\sqrt{E_{true}}$ . Contained muons are smeared with a Gaussian that has a standard deviation of 0.15 whereas the smearing of non-contained muons is not considered. Finally, the hadrons are smeared with a Gaussian that has a standard deviation of 0.05. The same condition ensuring that negative energies are not allowed is again applied. A check is also performed to see if there is more than 50 MeV of hadronic activity at the vertex, which is the threshold for the vertex to be considered visible [11]. Additionally, the reconstruction is assumed to only be sufficiently accurate for showers above 200 MeV, therefore any events with showers that do not exceed this energy threshold are removed.

When reconstructed quantities are considered, background events may mimic the key signature of signal events, resulting in events being misidentified. Some of the most common backgrounds to a CC inclusive sample in SBN will be due to:

- $\nu_\mu$  sample: Charged pions which may be produced by NC interactions will result in a track that can resemble a muon. Most of the tracks produced by pions will be relatively short at less than 50 cm.
- $\nu_e$  sample: Final state neutral pions which are a result of NC interactions decay into two photon showers.
- $\nu_e$  sample: If the track length is short ( $< 1$  m) and has a single associated EM shower,  $\nu_\mu$  CC events with a  $\mu + \gamma$  in the final state may be mistaken for  $\nu_e$  CC events with a  $\pi + e$  in the final state.
- $\nu_e$  sample: Cosmic photons may produce electrons in the TPC via pair production or Compton scattering. The cosmic photons may be produced in the atmospheric shower or by cosmic muons passing through the detector [11].



## 5.3. Event Selection

The event selections are performed in order to first identify  $\nu_\mu$  or  $\nu_e$ -like interactions which form a  $\nu_\mu$  or  $\nu_e$  CC inclusive sample. The selection steps are designed to produce as pure as possible CC inclusive sample by rejecting contributions from other samples such as NC or cosmics, the details of which are outlined below.

### 5.3.1. $\nu_\mu$ Selection

The selection criteria for the  $\nu_\mu$  sample are as follows:

1. Remove any events whose interaction vertex is not located in the fiducial volume. The fiducial volume used is outlined in Table B.1.
2. If no muon or charged pion track are produced, remove the event.
3. If the primary track has a length less than 50 cm and is fully contained in the detector, remove the event.
4. If the primary track exits the detector and has a length less than 100 cm, remove the event.

5. A weight of 0.8 is applied to all selected events to account for an assumed 80% reconstruction efficiency [11].

### 5.3.2. $\nu_e$ Selection

The  $\nu_e$  selection follows a similar basis to the  $\nu_\mu$  selection described in section 5.3.1, however, different criteria for the selection were applied to beam-induced TPC events, dirt events and cosmic events, each of which are outlined below.

#### Beam-induced active volume events

1. Remove any events whose interaction vertex is not located in the fiducial volume. The fiducial volume used is outlined in Table B.1.
2. If more than one shower arising from the vertex has an energy above a 100 MeV, the event is removed.
3. If there is only one photon candidate in the event, a conversion gap cut is applied rejecting any event where the photon shower occurs more than 3 cm from the vertex.
4. A weight of 0.06 is applied to the remaining photons which undergo a  $dE/dx$  cut resulting in a 94% background rejection.
5. If a misidentified photon originates from a resonant  $\nu_\mu$  CC interaction, the muon lepton is identified. Events where a muon travels greater than 1 m are assumed to be from  $\nu_\mu$  CC interactions and the event is removed.
6. A weight of 0.8 is applied to all selected events to account for an assumed 80% reconstruction efficiency [153].

#### Dirt Events

The selection procedure for dirt events is similar to that of beam-induced events outlined above. However, since the vertex for dirt events occurs outside the detector volume, the conversion gap and muon track length cuts are not undertaken [153].

## Cosmic Events

A largely separate analysis is applied for cosmic events which is as follows:

1. If a cosmic photon initially interacts outside the fiducial volume the event is removed.
2. Cosmic events which occur outside the beam spill time window are removed if there is no other activity in the TPC during the beam spill time.
3. 95% of cosmic events occurring within the beam spill window are removed by use of the PDS and CRT systems and taking advantage of the bucket structure of the beam.
4. Same dE/dx cut as described above.
5. A topological cosmic cylinder cut is applied to cosmic photons which originate from cosmic muons that pass through the TPC. These can be removed by a fiducial volume cut corresponding to a cylinder of radius 15 cm around the cosmic muon [153].

## 5.4. Systematic Uncertainties

A number of uncertainties associated with the neutrino flux, neutrino interactions and detector effects have to be considered. Within the simulation, predictions on the event rate and the properties of an event are required to reflect changes in these uncertainty parameters.

The majority of flux and interaction systematic parameters considered are implemented using well-validated reweighting schemes provided by MicroBooNE and GENIE respectively (the two exceptions are the POT normalisation and 2p2h uncertainty) [124] [154]. For each MC event and systematic parameter included in the reweight schemes, *universes* are simulated where the given parameter is randomly varied within its limits. Each universe will therefore have a single parameter which is tweaked from its nominal value and for each parameter, 500 universes are simulated each with a different tweaked value for the parameter. This allows changes in event rate spectra to be related to systematic parameter variations. The systematic parameters considered are described below along with a table quoting their estimated uncertainty.

Currently, uncertainties due to detector effects remain largely unconstrained and therefore a dedicated package describing their effects does not exist. They are instead handled internally and are described in Section 6.5.3.

### 5.4.1. Flux Systematics

The flux systematics are grouped into 3 distinct sets with different origins as part of the MicroBooNE reweight scheme which are detailed below plus the additional POT normalisation.

#### Optical Flux Systematics

The optical flux systematics are comprised of two parameters: the *skin effect* and the *horn current*. The horn current parameter is simply the uncertainty of the supplied current to the focusing horn. Since the current is linked to the focusing properties of the horn, uncertainty on the current leads to an uncertainty in the

neutrino flux. The focusing horn is surrounded by a conductor where currents travel on the surface of the conductor. The skin effect is a measure of how much these surface currents penetrate into the conductor which in turn affects the internal fields of the conductor. Therefore, due to the skin effect, the strength of the magnetic field that particles propagating through the horn experience may vary [124].

Parameter	Description	Uncertainty
$f_{SkinEffect}$	Depth that the current penetrates the horn conductor	< 18%
$f_{HornCurrent}$	Current running in the horn conductor	$\pm 0.6\%$

**Table 5.2.:** Optical systematic flux uncertainties associated with the current in the horn [124].

## Secondary Hadron Interaction Cross-Sections

The proton interaction rate in the BNB target is largely dependent on the hadronic cross-sections with the beryllium target and aluminium horn. The total cross-section,  $\sigma_{TOT}$ , is defined as the sum of the elastic,  $\sigma_{EL}$  and inelastic,  $\sigma_{INEL}$ , cross-sections, with the quasi-elastic cross-section,  $\sigma_{QE}$ , being a subset of the  $\sigma_{INEL}$  cross-section. The  $\sigma_{TOT}$  variations are based on comparing calculations with neutron-nucleus measurements. The model describing  $\sigma_{TOT}$  is assumed to work sufficiently well for  $\pi^\pm$ -nucleus interactions and is extended to include these interactions in addition to all nucleon-nucleus interactions.  $\sigma_{INEL}$  is estimated directly from the available data and the deviations are therefore noticeably smaller than for  $\sigma_{TOT}$ .  $\sigma_{QE}$  variations are again estimated from a combination of the available data and models [124].

The above approach is applied for both beryllium and aluminium nuclei and the uncertainty associated with the total, quasi-elastic and inelastic cross-sections for both nucleons and pions for the two nuclei are shown in Table 5.3.

Parameter	Description	Uncertainty	
		Be	Al
$f_{\sigma_{INEL}^N}$	Secondary inelastic nucleon cross-section in the target (Be) and horn (Al)	$\pm 5\%$	$\pm 10\%$
$f_{\sigma_{QE}^N}$	Secondary quasi-elastic nucleon cross-section in the target (Be) and horn (Al)	$\pm 20\%$	$\pm 45\%$
$f_{\sigma_{TOT}^N}$	Secondary total nucleon cross-section in the target (Be) and horn (Al)	$\pm 15\%$	$\pm 25\%$
$f_{\sigma_{INEL}^\pi}$	Secondary inelastic pion cross-section in the target (Be) and horn (Al)	$\pm 10\%$	$\pm 20\%$
$f_{\sigma_{QE}^\pi}$	Secondary quasi-elastic pion cross-section in the target (Be) and horn (Al)	$\pm 11.2\%$	$\pm 25.9\%$
$f_{\sigma_{TOT}^\pi}$	Secondary total pion cross-section in the target (Be) and horn (Al)	$\pm 11.9\%$	$\pm 28.7\%$

**Table 5.3.:** The systematic uncertainties associated with secondary hadron interaction cross-sections in both the horn (Aluminium) and the target (Beryllium) [11].

### Hadronic Neutrino Production Flux Uncertainties

The neutrinos in the BNB are due to decaying particles which are a result of protons interacting with the beryllium target. Understanding the neutrino flux, therefore, relies on understanding the production of the particles decaying to neutrinos, which are predominately pions for  $\nu_\mu$  and kaons for  $\nu_e$  (plus the decay of muons which in turn are produced in the meson decays).

The Sanford-Wang parameterisation is used to estimate the  $\pi^\pm$  production. It depends on the meson momentum,  $p$ , and angle relative to the incident proton,  $\theta$ , and also the proton momentum,  $p_B$ . The parametrisation is given by

$$\frac{d^2\sigma}{dpd\theta} = c_1 p^{c_2} \left(1 - \frac{p}{p_B - c_9}\right) \exp\left(-c_3 \frac{p^{c_4}}{p_B^{c_5}} - c_6 \theta(p - p_B c_7 \cos^{c_8} \theta)\right), \quad (5.1)$$

where parameters  $c_{1 \rightarrow 9}$  are determined from the HARP (8.89 GeV/c), BNL E910 (6.4 GeV/c) and BNL E910 (12.3 GeV/c) experiments. The uncertainties associated with the parametrisation are one of the driving factors in the uncertainty on the meson production [124].

No  $K^+$  production rates exist for proton-beryllium interactions at 8.89 GeV/c which is the primary BNB operating momentum. To estimate the  $K^+$  production rate at the BNB momentum, Feynman scaling is used to extrapolate the rate from production rates at nearby energies [124].

The major contribution that the  $K^0$  makes to the BNB flux is from the decay of the  $K_L^0$ . The  $K^0$  that are produced via strong interactions have equal contents of  $K_L^0$  and  $K_s^0$ , therefore the production rate of  $K_L^0$  can be inferred from knowing the production rate of  $K_s^0$ . The Sanford-Wang parametrisation is again used to estimate the production cross-section by combining data from the BNL E910 experiment at 12.3 GeV/c and 17.5 GeV/c and the KEK experiment at 12.3 GeV/c.

For the  $K^-$ , there is minimal production data available, therefore, simulations are used exclusively. The rate and spectrum of the  $K^-$  are estimated by simulating 8.89 GeV/c proton-beryllium interactions [124].

Parameter	$\nu$ production	Uncertainty			
		$\nu_\mu$	$\bar{\nu}_\mu$	$\nu_e$	$\bar{\nu}_e$
$f_{\pi^+}$	Mechanism: $\pi^+$	$\pm 11.7\%$	$\pm 1.0\%$	$\pm 10.7\%$	$\pm 0.03\%$
$f_{\pi^-}$	Mechanism: $\pi^-$	$\pm 0.0\%$	$\pm 11.6\%$	$\pm 0.0\%$	$\pm 3.0\%$
$f_{K^+}$	Mechanism: $K^+$	$\pm 0.2\%$	$\pm 0.1\%$	$\pm 2.0\%$	$\pm 0.1\%$
$f_{K^-}$	Mechanism: $K^-$	$\pm 0.0\%$	$\pm 0.4\%$	$\pm 0.0\%$	$\pm 3.0\%$
$f_{K^0}$	Mechanism: $K^0$	$\pm 0.0\%$	$\pm 0.3\%$	$\pm 2.3\%$	$\pm 21.4\%$

**Table 5.4.:** Hadronic neutrino production systematic flux uncertainties [155].

## BNB POT Normalisation

The intensity of the proton beam is monitored by two toroids and it has been found that the two toroids agree with one another to within 2% [124]. An additional 2% normalisation uncertainty is applied in order to account for this POT accounting uncertainty. This uncertainty is set so that it is fully correlated between all analysis bins.

### 5.4.2. Interaction Systematics

The uncertainties associated with neutrino interactions are provided by GENIE and are implemented using the GENIE ReWeight package. This is the case for all the interaction systematics considered here except for the 2p2h systematic which is described below. The GENIE reweighting scheme works as follows; for each quantity,  $P$ , which has an associated uncertainty, a systematic parameter,  $x_P$  is introduced. Varying  $x_P$  will modify,  $P$  such that

$$P \rightarrow P' = P(1 + x_P \cdot \frac{\delta P}{P}), \quad (5.2)$$

where  $\delta P$  represents the standard deviation of  $P$ . It follows from Equation 5.2 that for a  $x_P = 0$ ,  $P' = P$  and for  $x_P = \pm 1$ ,  $P' = P \pm \delta P$ .

The two main types of interaction systematics considered in this analysis are cross-section and intranuclear hadron transport model uncertainties, however, within an SBN analysis, the interaction systematics are generally grouped into two categories: the *proposal* and *modern* set of parameters. The proposal systematics are those that were included as part of the analysis done at the time of the SBN proposal, whereas the modern systematics represent the additional systematics which have been deemed relevant for SBN in the period following the proposal [11]. The details of how GENIE handles cross-section and intranuclear hadron transport parameters are detailed below, followed by outlining which parameters are included as part of the proposal and modern set of parameters.

The cross-section uncertainties are based on GENIE tunes which utilise data from hydrogen and deuterium bubble chamber experiments, namely ANL 12FT, BNL

7FT, BEBC and FNAL 15FT. The data corresponds to  $\nu_\mu$  and  $\bar{\nu}_\mu$  CC inclusive scattering, CC quasi-elastic scattering, CC single pion production and  $\nu_\mu$  CC two pion production. In total, a 169 data points were used in the fit obtained from the most recent datasets from a given experiment. Therefore, not all available data was used since older datasets which have been superseded have not been considered. Additionally, data points with a neutrino energy below 0.5 GeV are omitted due to smearing of the energy and absence of unfolding in the measurements [151].

The intranuclear uncertainties are informed by use of the GENIE *INTRANUKE hA* empirical model. The model is data-driven and considers the total cross-section of nuclear processes for pions and nucleons with energies up to 1.2 GeV. Typically the data is obtained by firing hadron beams onto a nuclear target [154] [156] [157].

### Neutrino Cross-Section uncertainties

The neutrino cross-section gives a measure of the neutrino interaction probability. The event weight,  $w_\sigma^{evt}$ , associated with a given parameter for a neutrino cross-section is calculated via

$$w_\sigma^{evt} = \left( \frac{d^n \sigma'_\nu}{dK^n} \right) \Bigg/ \left( \frac{d^n \sigma_\nu}{dK^n} \right), \quad (5.3)$$

where  $\frac{d^n \sigma'_\nu}{dK^n}$  is the differential cross-section with varied physics parameters and  $\frac{d^n \sigma_\nu}{dK^n}$  is the nominal differential cross-section with  $K^n$  being the kinematical phase space in both cases [154].

### Intranuclear hadron transport uncertainties

When hadrons are produced in the nucleus they may interact as they propagate out of the nucleus. The reinteraction in the nucleus may significantly alter the observed final state particles. There are two primary uncertainties considered with this effect: the uncertainty in the overall probability of rescattering and the uncertainty corresponding to the probability of each rescattering mode once it has been determined that rescattering will occur for a given hadron [154].

For a hadron propagating in the nucleus, the survival probability,  $P_{surv}^h$ , is calculated as

$$P_{surv}^h = \int e^{-r/\lambda^h(\vec{r}, h, E_h)} dr, \quad (5.4)$$

where the integral is evaluated along the path the hadron takes in the nucleus and  $\lambda^h$  is the mean free path. The probability of rescattering,  $P_{rescat}^h$ , is then defined as

$$P_{rescat}^h = 1 - P_{surv}^h. \quad (5.5)$$

The mean free path is a function of the hadron type,  $h$ , the hadron energy,  $E_h$  and position,  $\vec{r}$  and is given by

$$\lambda^h = \frac{1}{\rho_{nucl}(r) \cdot \sigma^{hN}(E_h)}, \quad (5.6)$$

where  $\rho_{nucl}(r)$  is the density profile of the nucleus and  $\sigma^{hN}(E_h)$  is the total cross-section of the hadron-nucleon [154].

In terms of reweighting, for a given systematic parameter,  $x_{mfp}^h$ , with an uncertainty,  $\delta\lambda^h$ , the mean free path may be tweaked such that

$$\lambda^h \rightarrow \lambda^{h'} = \lambda^h \left( 1 + x_{mfp}^h \frac{\delta\lambda^h}{\lambda^h} \right), \quad (5.7)$$

where  $\lambda^{h'}$  is the tweaked mean free path. The modified survival probability,  $P_{surv}^{h'}$ , is then found by substituting  $\lambda^{h'}$  into Equation 5.4. The weight,  $w_{mfp}^h$ , associated with a given change in the mean free path is calculated as [154]

$$w_{mfp}^h = \begin{cases} \frac{1-P_{surv}^{h'}}{1-P_{surv}^h}, & \text{if } h \text{ reinteracts} \\ \frac{P_{surv}^{h'}}{P_{surv}^h}, & \text{if } h \text{ escapes.} \end{cases} \quad (5.8)$$

Once it has been determined that a hadron will rescatter, the following scattering modes are considered: elastic, inelastic, charge exchange, absorption and pion

production. The probability of a given mode,  $P_f^h$ , occurring is given by

$$P_f^h = \frac{\sigma_f^{hA}}{\sigma_{total}^{hA}}, \quad (5.9)$$

where  $\sigma_f^{hA}$  is the cross-section for the given hadron-nucleus mode and  $\sigma_{total}^{hA}$  is the total hadron-nucleus cross-section. Similarly to the mean free path, the hadron-nucleus cross-section of a mode may be tweaked such that

$$\sigma_f^{hA} \rightarrow \sigma_f^{hA'} = \sigma_f^{hA} \left( 1 + x_f^h \frac{\delta\sigma_f^{hA}}{\sigma_f^{hA}} \right), \quad (5.10)$$

where  $\sigma_f^{hA'}$  is the tweaked cross-section,  $x_f^h$  is a systematic parameter and  $\delta\sigma_f^{hA}$  is the associated uncertainty. The weight of a mode,  $w_{mode}^h$ , is given by

$$w_{mode}^h = \sum_f \delta_{ff'} \cdot x_f^h \cdot \frac{\delta\sigma_f^{hA}}{\sigma_f^{hA}}, \quad (5.11)$$

where the sum is over the possible rescattering modes,  $f'$  is the actual mode for the given hadron, and  $\delta_{ff'}$  is the Kronecker delta between  $f$  and  $f'$  [154].

The total weight of a single hadron,  $w^h$ , is then given by the product of the two weights such that,

$$w^h = w_{mfp}^h \cdot w_{mode}^h. \quad (5.12)$$

For a single neutrino event, there may be multiple hadrons present, therefore the total weight,  $w_{HT}^{evt}$ , for a neutrino event is given by the product of individual hadron weights,

$$w_{HT}^{evt} = \prod_j w_j^h, \quad (5.13)$$

where the index  $j$  corresponds to all the primary hadrons [154].

## Proposal Interaction Systematics

The proposal systematics only included a set of cross-section parameters which are listed in Table 5.5 along with their uncertainty.

Parameter	Description	$\delta P/P$
$f_{M_A^{CCQE}}$	Axial mass for CC quasi-elastic	-15% +25%
$f_{M_A^{CCRes}}$	Axial mass for CC resonance neutrino production	$\pm 20\%$
$f_{M_A^{NCRes}}$	Axial mass for NC resonance neutrino production	$\pm 20\%$
$f_{NC}$	Additional error on NC/CC ratio	$\pm 25\%$
$f_{nR_{\nu n}^{CC1\pi}}$	Non-Res bkg normalisation in $\nu n$ CC1 $\pi$ reactions	$\pm 50\%$
$f_{nR_{\nu p}^{CC1\pi}}$	Non-Res bkg normalisation in $\nu p$ CC1 $\pi$ reactions	$\pm 50\%$
$f_{nR_{\nu n}^{CC2\pi}}$	Non-Res bkg normalisation in $\nu n$ CC2 $\pi$ reactions	$\pm 50\%$
$f_{nR_{\nu p}^{CC2\pi}}$	Non-Res bkg normalisation in $\nu p$ CC2 $\pi$ reactions	$\pm 50\%$
$f_{nR_{\bar{\nu} n}^{CC1\pi}}$	Non-Res bkg normalisation in $\bar{\nu} n$ CC1 $\pi$ reactions	$\pm 50\%$
$f_{nR_{\bar{\nu} p}^{CC1\pi}}$	Non-Res bkg normalisation in $\bar{\nu} p$ CC1 $\pi$ reactions	$\pm 50\%$
$f_{nR_{\bar{\nu} n}^{CC2\pi}}$	Non-Res bkg normalisation in $\bar{\nu} n$ CC2 $\pi$ reactions	$\pm 50\%$
$f_{nR_{\bar{\nu} p}^{CC2\pi}}$	Non-Res bkg normalisation in $\bar{\nu} p$ CC2 $\pi$ reactions	$\pm 50\%$
$f_{nR_{\nu n}^{NC1\pi}}$	Non-Res bkg normalisation in $\nu n$ NC1 $\pi$ reactions	$\pm 50\%$
$f_{nR_{\nu p}^{NC1\pi}}$	Non-Res bkg normalisation in $\nu p$ NC1 $\pi$ reactions	$\pm 50\%$
$f_{nR_{\nu n}^{NC2\pi}}$	Non-Res bkg normalisation in $\nu n$ NC2 $\pi$ reactions	$\pm 50\%$
$f_{nR_{\nu p}^{NC2\pi}}$	Non-Res bkg normalisation in $\nu p$ NC2 $\pi$ reactions	$\pm 50\%$
$f_{nR_{\bar{\nu} n}^{NC1\pi}}$	Non-Res bkg normalisation in $\bar{\nu} n$ NC1 $\pi$ reactions	$\pm 50\%$
$f_{nR_{\bar{\nu} p}^{NC1\pi}}$	Non-Res bkg normalisation in $\bar{\nu} p$ NC1 $\pi$ reactions	$\pm 50\%$
$f_{nR_{\bar{\nu} n}^{NC2\pi}}$	Non-Res bkg normalisation in $\bar{\nu} n$ NC2 $\pi$ reactions	$\pm 50\%$
$f_{nR_{\bar{\nu} p}^{NC2\pi}}$	Non-Res bkg normalisation in $\bar{\nu} p$ NC2 $\pi$ reactions	$\pm 50\%$

**Table 5.5.:** GENIE interaction cross-section systematics considered in SBN as part of the proposal set of systematics. [154].

## Modern Interaction Systematics

The modern systematics include an additional set of cross-section parameters which are listed in Table 5.6 in addition to a set of intranuclear hadron transport parameters which are listed in Table 5.7. Again, both tables also show the associated uncertainty of each parameter. The 2p2h uncertainty mentioned is also considered as part of the modern systematic parameters and is detailed below.

Parameter	Description	$\delta P/P$
$f_{M_A^{NCEl}}$	Axial mass for NC elastic	$\pm 25\%$
$f_{\eta}^{NCEl}$	Strange axial form factor for NC elastic	$\pm 30\%$
$f_{M_V^{CCRes}}$	Vector mass for CC resonance neutrino production	$\pm 10\%$
$f_{M_V^{NCRes}}$	Vector mass for NC resonance neutrino production	$\pm 10\%$
$f_{A_{HT}}$	Higher-twist parameter A for NC and CC DIS events	$\pm 25\%$
$f_{B_{HT}}$	Higher-twist parameter B for NC and CC DIS events	$\pm 25\%$
$f_{C_{v1u}}$	Valence p.d.f. correction factor $C_{v1u}$ for DIS events	$\pm 30\%$
$f_{C_{v2u}}$	Valence p.d.f. correction factor $C_{v2u}$ for DIS events	$\pm 40\%$
$f_{M_A^{Coh}}$	Axial mass for NC and CC coherent pion production	$\pm 50\%$
$f_{R_0^{Coh}}$	Nuclear size parameter controlling $\pi$ absorption	$\pm 20\%$
$f_{\Delta \rightarrow N\gamma}$	Branching ratio for $\Delta$ radiative decay	$\pm 50\%$

**Table 5.6.:** GENIE interaction cross-section systematics considered in SBN as part of the modern set of systematics [154].

Parameter	Description	$\delta P/P$
$f_{\lambda_\pi}$	Mean free path for pions	$\pm 20\%$
$f_{R_\pi^{CEx}}$	Charge exchange rescattering fraction for pions	$\pm 50\%$
$f_{R_\pi^{Inel}}$	Inelastic rescattering fraction for pions	$\pm 40\%$
$f_{R_\pi^\pi}$	Pion-production rescattering fraction for pions	$\pm 20\%$
$f_{R_\pi^{Abs}}$	Absorption fraction for pions	$\pm 20\%$
$f_{\lambda_N}$	Mean free path for nucleons	$\pm 20\%$
$f_{R_N^{CEx}}$	Charge exchange rescattering fraction for nucleons	$\pm 50\%$
$f_{R_N^{Inel}}$	Inelastic rescattering fraction for nucleons	$\pm 40\%$
$f_{R_N^\pi}$	Pion-production rescattering fraction for nucleons	$\pm 20\%$
$f_{R_N^{Abs}}$	Absorption fraction for nucleons	$\pm 20\%$

**Table 5.7.:** Intranuclear hadron transport systematic parameters considered in SBN as part of the modern set of systematics [154].

## 2p2h uncertainty

A 2p2h uncertainty parameter which specifically affects 2p2h events is not included from the GENIE event generator since it was decided that the parameter was not sufficiently validated. Instead, a 100% normalisation uncertainty is applied to all 2p2h events. The value of the uncertainty was chosen to be a 100% (maximal) to ensure the effect of the 2p2h parameter would not be an underestimate.



# Chapter 6.

## SBN Oscillation Analysis Within the VALOR Framework

The VALOR framework is a neutrino fitting framework that was first developed for the T2K experiment but has since been adapted to also cover Hyper-Kamiokande, DUNE and the SBN program [158].

Performing an analysis within VALOR involves a number of physics parameters that define a physics hypothesis (e.g. neutrino oscillations) and the relevant systematic uncertainties. Event rate predictions are constructed for the associated detector, beam and event sample. These predictions are constructed as a function of a kinematical variable for either a nominal scenario or with variations due to a physics hypothesis and/or systematic uncertainties. This approach allows for joint oscillation and systematic fits to be constructed from a binned likelihood fitting approach for a given event topology. Fits may be performed for individual detectors or for a combination of multiple detectors and may include any number of systematic uncertainties.

### 6.1. The VALOR Framework

The data inputs used for an oscillation analysis are mainly provided in the form of Monte Carlo Templates (MCTs), which provide a mapping between true and

reconstructed variables. They are constructed following the full event processing chain which includes event simulation, reconstruction and selection. Since the MCTs include the effects from reconstruction and selection, it is not feasible to directly recreate them using only information on the flux, cross-section and efficiency. These MCTs,  $T$ , encapsulate a number of quantities describing a given event and are listed below,

- b – Beam configuration e.g. neutrino or anti-neutrino mode,
- d – Detector e.g. SBND, MicroBooNE or ICARUS,
- s – Topological event selection e.g.  $\nu_e$  CC-inclusive,  $\nu_\mu$  CC-inclusive,
- m – True Reaction Mode e.g.  $\nu_\mu$  CC QE,  $\nu_e$  CC  $1\pi^\pm$ ,
- r – A bin in multi-dimensional reconstructed kinematic space e.g.  $E_{\nu, \text{reco}}$ ,
- t – A bin in multi-dimensional true kinematic space e.g.  $E_{\nu, \text{true}}$ ,

with  $T = T_{d;b;s;m}(r, t)$ . By combining  $T$  with the necessary physics parameters,  $\vec{\theta}$ , and systematic parameters,  $\vec{f}$ , the predicted event rate,  $n_{d;b;s}^{\text{pred}}$ , may be expressed as

$$n_{d;b;s}^{\text{pred}}(r; \vec{\theta}; \vec{f}) = \sum_m \sum_t P_{d;b;m}(t; \vec{\theta}) \cdot R_{d;b;s;m}(r, t; \vec{f}) \cdot T_{d;b;s;m}(r, t) \cdot N^{MC}, \quad (6.1)$$

where  $P_{d;b;m}(t; \vec{\theta})$  represents the effect due to a physics hypothesis,  $R_{d;b;s;m}(r, t; \vec{f})$  represents the response of a MCT bin to the systematic variations and  $N^{MC} = \text{POT}_{b;d}^{\text{data}} / \text{POT}_{b;d}^{MC}$ , which is the normalisation by which to scale the event rate to account for the POT which was used to construct the sample of neutrino events with respect to the nominal POT in the analysis. The variation due to systematic parameters is applied separately to each combination of beam, detector, topological selection and reaction mode in true-reconstructed space and is, therefore, dependant on,  $b$ ,  $d$ ,  $s$  and  $m$ . The dependence of  $P_{d;b;m}(t; \vec{\theta})$  on  $d$  and  $b$  is due to  $d$  and  $b$  encapsulating the baseline information which is a component of the oscillation probability. The unoscillated CC MCTs are weighted by the appropriate oscillation probability,  $P_{\nu_\alpha \rightarrow \nu_\beta}$ , to reflect the change in event rate due to neutrino oscillations. The NC MCTs are left unweighted since they remain

unchanged due to flavour oscillations. This distinction between CC and NC is encapsulated by  $m$ , hence,  $P_{d;b;m}(t; \vec{\theta})$  is required to also be dependent on  $m$ .

For  $n_{d;b;s}^{obs}(r)$  observed events, the log likelihood,  $\ln \lambda_{d;b;s}(\vec{\theta}, \vec{f})$ , is given by

$$\ln \lambda_{d;b;s}(\vec{\theta}, \vec{f}) = - \sum_{b,d,s,r} \left\{ \left( n_{d;b;s}^{pred}(r, \vec{\theta}, \vec{f}) - n_{d;b;s}^{obs}(r) \right) + n_{d;b;s}^{obs}(r) \cdot \ln \frac{n_{d;b;s}^{obs}(r)}{n_{d;b;s}^{pred}(r, \vec{\theta}, \vec{f})} \right\}. \quad (6.2)$$

An additional term is applied to penalise deviations from the nominal values of systematic parameters which is defined as,

$$\ln \lambda_{syst}(\vec{f}) = -\frac{1}{2}(\vec{f} - \vec{f}_0)^T \mathbf{V}^{-1} (\vec{f} - \vec{f}_0), \quad (6.3)$$

where  $\vec{f}_0$  is a vector containing the nominal value of all the systematic parameters and  $\mathbf{V}$  is a covariance matrix containing the uncertainties of the systematic parameters [159].

In the limit of large statistics, quantities of the form  $-2 \ln \lambda$  have a  $\chi^2$  distribution, hence calculating the log-likelihood allows a goodness-of-fit test to be performed [160]. The total goodness-of-fit value is therefore given by,

$$\chi_{tot}^2 = -2(\ln \lambda_{d;b;s}(\vec{\theta}, \vec{f}) + \ln \lambda_{syst}(\vec{f})). \quad (6.4)$$

In order to create confidence regions, fits are performed between a certain *Asimov* dataset and  $n_{d;b;s}^{pred}$ . The Asimov dataset is a dataset where all systematic parameters are set to their nominal values and serves as a proxy for data in cases where only simulations are considered. It has been shown that in the same limit as the  $\chi^2$  approximation (in the limit of large statistics), the median of many toy MC experiments is equivalent to the Asimov dataset. This allows the significance of a given hypothesis to be compared to the median one whilst only requiring one *toy* experiment instead of needing to compute many toy MC experiments [161]. Two types of confidence regions may be constructed; an *exclusion* region and an *allowed* region. Both regions show the area where the chosen model is either

compatible or incompatible with the data. The difference is due to the input data which has either no oscillation signal (an exclusion region) or there is an injected signal (an allowed region). In the case of exclusion regions, the Asimov dataset corresponds to the case where no oscillations are observed which is the null-hypothesis and for allowed regions, the oscillation parameters are set to that of the injected signal.

## 6.2. Oscillation Channels Within SBN

As was discussed in Section 3.4, the BNB is  $\nu_\mu$  dominated with a small portion of  $\nu_e$ 's present. In the presence of mixing with a light sterile neutrino this would result in the disappearance of some percentage of the  $\nu_\mu$ 's due to oscillations. Additionally,  $\nu_\mu$  to  $\nu_e$  oscillations would result in the increase of the number of  $\nu_e$ 's present. Finally, the number of intrinsic  $\nu_e$ 's present in the BNB coupled with the large event rate SBN will detect means there are sufficient statistics to observe the disappearance of some  $\nu_e$ 's due to oscillations. This results in three possible oscillation channels,  $\nu_\mu$  disappearance,  $\nu_e$  appearance and  $\nu_e$  disappearance. The mixing angles which determine their respective oscillation probabilities are shown in Equations (2.50 – 2.52) which also imply that the oscillation channels are coupled (that is the presence of non-zero  $\nu_e$  appearance also requires non-zero  $\nu_\mu$  disappearance and  $\nu_e$  disappearance). Despite this, currently, the oscillation channels are treated completely independently. In principle oscillations involving  $\nu_\tau$  are also possible, but due to the high energy threshold required these are usually not expected to be observed with any significant statistics. The energy range of the BNB above the  $\nu_\tau$  threshold is of the order 1%, but since the statistics in SBND are large, this may be sufficient to observe  $\nu_\mu$  to  $\nu_\tau$  appearance. Currently, this channel is not considered in the analysis but may be explored in future work [162].

The  $\nu_\mu$  disappearance as well as both the  $\nu_e$  channels have already been explored by a number of different experiments, many of which have been discussed in Section 2.2.3.4. This has led to tension due to the conflict between null-results from some experiments and the hints of possible mixing with light sterile neutrinos seen by others. SBN will be particularly sensitive to the  $\nu_\mu$  disappearance and  $\nu_e$

appearance channels due to the high flux of  $\nu_\mu$ 's observed which will allow for the LSND and MiniBooNE anomalies to be investigated. Additionally, SBN will be simultaneously sensitive to  $\nu_\mu$  disappearance and  $\nu_e$  appearance.

The remainder of this chapter will focus on the  $\nu_e$  channels. Some of the key results for the  $\nu_\mu$  channel are shown in Appendix D and a detailed discussion can be found in [163].

## 6.3. Specifics of SBN Sensitivity Simulation Implementation in VALOR

### 6.3.1. Baseline and Binning Analysis Choices

Two other key analysis choices are the neutrino baseline parameterisation and the binning scheme used for the kinematic variable. As is shown in Equation 2.49, the baseline is one of the components that drives the oscillation probability and therefore any approximations to the true baseline must be chosen such that the impact to the oscillation probability is negligible. The kinematic variable used in this analysis is the energy of the neutrino for both true and reconstructed quantities.

#### 6.3.1.1. Baseline

For long baseline experiments, it is not uncommon for fitting frameworks to simply use some average value for the baseline since factors such as the interaction point in the detector or the position at which a particle decays into a neutrino would only change the average baseline for the experiment by a negligible amount. However, for short baseline experiments such as SBN, these factors may change the baseline significantly, up to around 20% in SBND.

In an attempt to minimise computing resources, the true baseline was not initially used, but instead, several approximations to the baseline were tried. To begin with, the average baseline of each SBN detector was used for all neutrino energies. This

was calculated from the true baseline distribution of  $\nu_\mu$  events in each detector which are shown in Figure 6.1. Secondly, a 4-knot spline (named spline V1) for each detector was defined in order to try and better approximate the baseline. This method was improved upon by producing a spline for each of the true energy bins (named spline V2) which are defined in Section 6.3.1.2. In order to establish the impact of any baseline approximations on the oscillation probability, the oscillation probability was plotted as a function of true neutrino energy with the oscillation parameters  $\sin^2 2\theta_{\mu\mu} = 0.01$  and  $\Delta m_{41}^2 = 50 \text{ eV}^2$ . This oscillation point was chosen to ensure that a region where rapid oscillations occur was being investigated, which would highlight the effect of any baseline choices. The oscillation probabilities as a function of energy are shown in Figure 6.2 for the four different baselines described. It was eventually decided that any approximation would be insufficient and that the true baseline should be used.

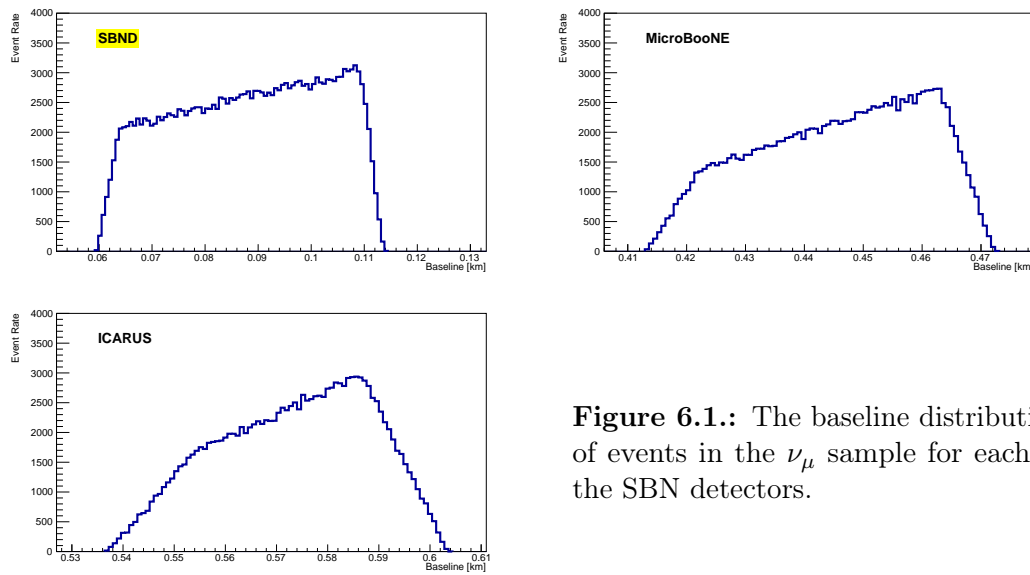


**Figure 6.1.:** The baseline distribution of events in the  $\nu_\mu$  sample for each of the SBN detectors.

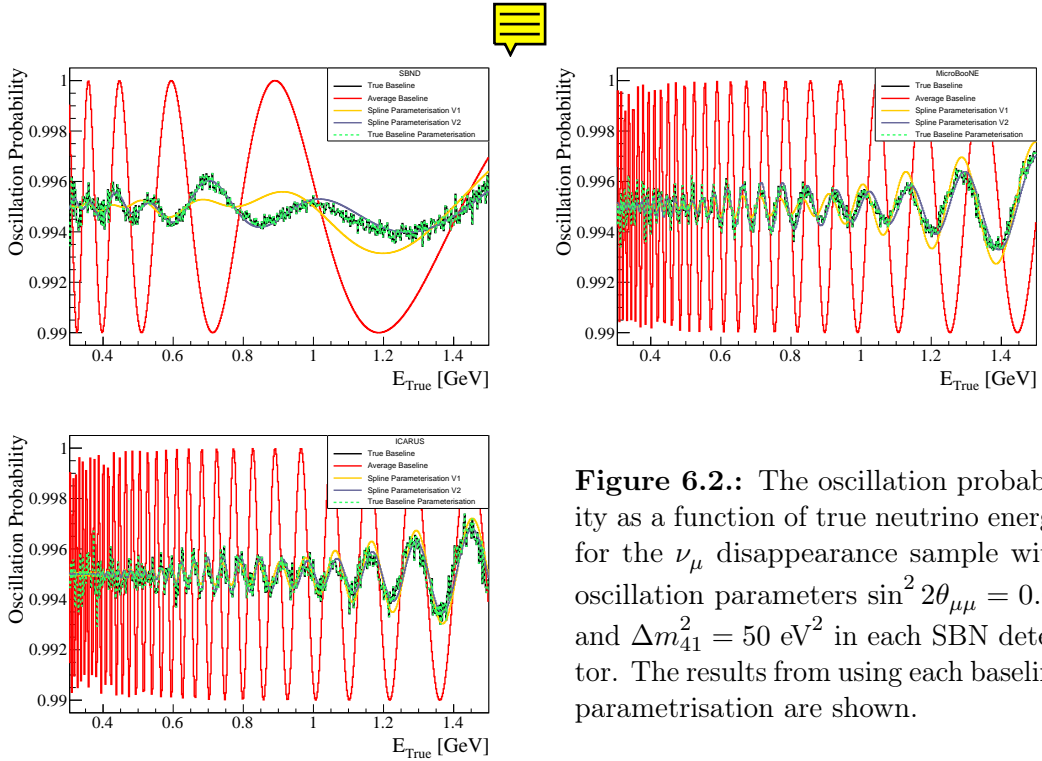


**Figure 6.2.:** The oscillation probability as a function of true neutrino energy for the  $\nu_\mu$  disappearance sample with oscillation parameters  $\sin^2 2\theta_{\mu\mu} = 0.01$  and  $\Delta m_{41}^2 = 50 \text{ eV}^2$  in each SBN detector. The results from using each baseline parametrisation are shown.

The studies of the baseline approximations were done in the context of the  $\nu_\mu$  disappearance channel. In principle, within the  $\nu_e$  sample, different approximations should be applied to the different sub-samples since the baseline distribution is not the same for all the sub-samples. For example, the  $\nu_\mu$ 's in the oscillated and  $\nu_\mu$  sub-samples will both mainly be the result of pion decays whereas the  $\nu_e$ 's in the intrinsic sub-sample will have a larger contribution from kaon and secondary muon decays. Pions and kaons have different lifetimes which coupled with the contribution from the decay of secondary particles means that the baseline distribution of the oscillated and  $\nu_\mu$  sub-sample will be different to that of the intrinsic  $\nu_e$  sub-sample. This was never done since it was decided that the true baseline should be used. The baseline distributions for the intrinsic  $\nu_e$ , oscillated  $\nu$  and the overall  $\nu_e$  sample from combining all the sub-samples together are shown in Figure 6.3, Figure 6.4 and Figure 6.5 respectively for each of the SBN detectors. It should be noted that the baseline distributions for oscillated  $\nu_e$  sample from Figure 6.4 and the  $\nu_\mu$  sample from Figure 6.1 are comparable. This is due to the initial parameters describing the oscillated sample being the same as for the  $\nu_\mu$

sample. The only difference being the neutrino oscillations from  $\nu_\mu$  to  $\nu_e$  which is not something that affects the baseline.

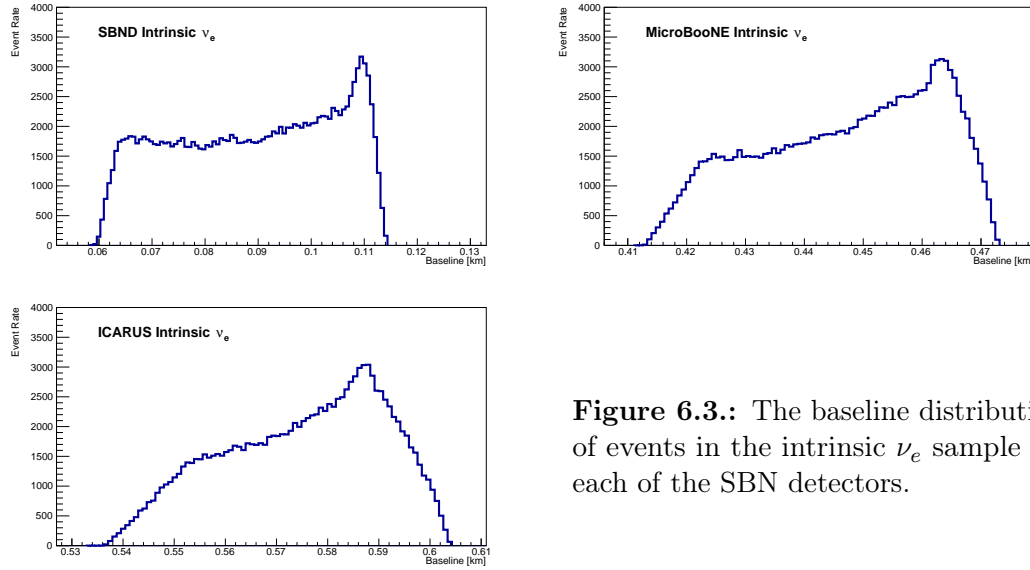


**Figure 6.3.:** The baseline distribution of events in the intrinsic  $\nu_e$  sample for each of the SBN detectors.

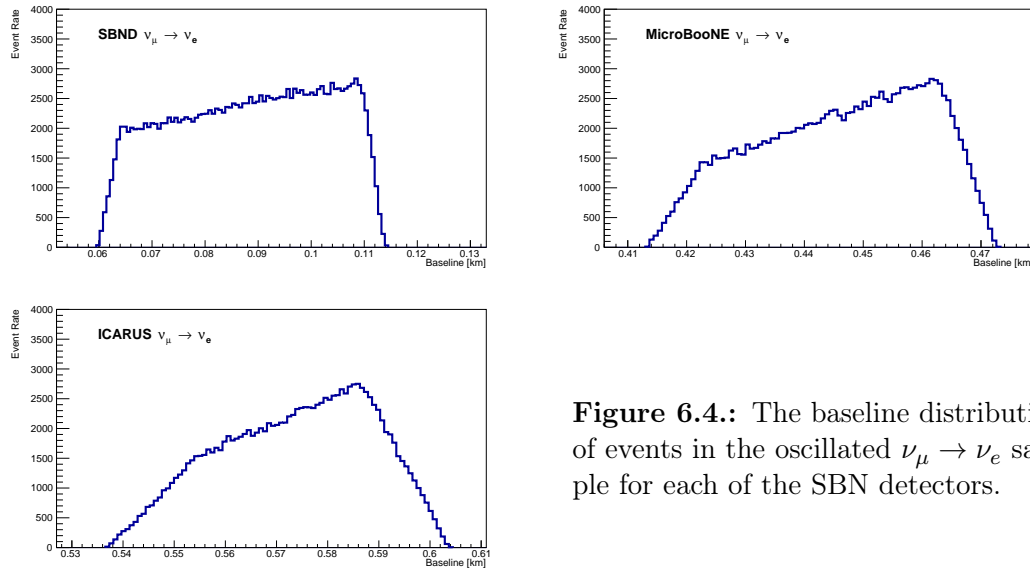


**Figure 6.4.:** The baseline distribution of events in the oscillated  $\nu_\mu \rightarrow \nu_e$  sample for each of the SBN detectors.

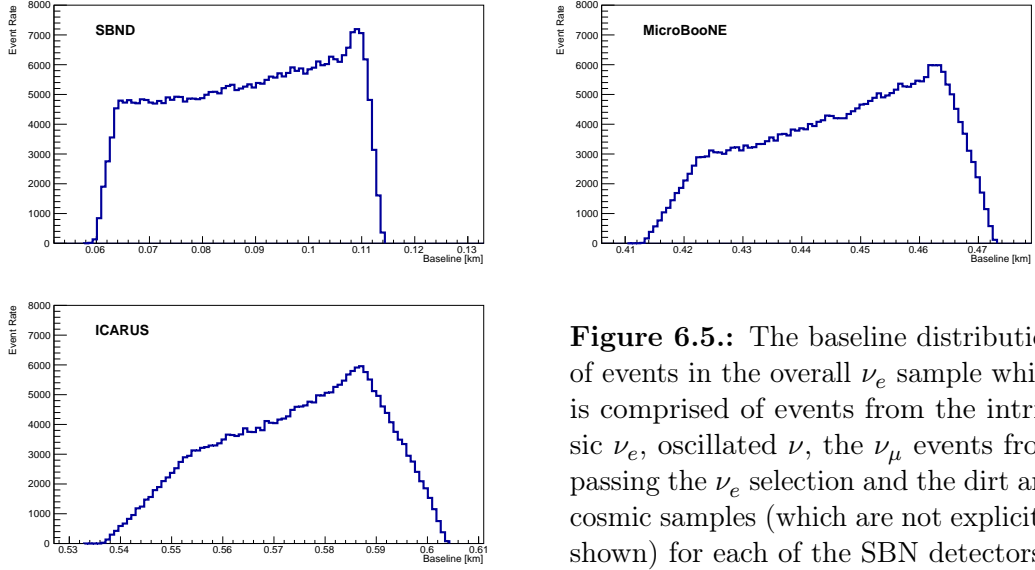


**Figure 6.5.:** The baseline distribution of events in the overall  $\nu_e$  sample which is comprised of events from the intrinsic  $\nu_e$ , oscillated  $\nu$ , the  $\nu_\mu$  events from passing the  $\nu_e$  selection and the dirt and cosmic samples (which are not explicitly shown) for each of the SBN detectors.

### 6.3.1.2. Binning

The energy binning schemes used are the same across each of the three detectors, however, the scheme used is different for the  $\nu_\mu$  and  $\nu_e$  analyses. Furthermore, there are separate schemes for both the true and reconstructed energies. Each of the binning schemes is outlined below.

The  $\nu_\mu$  edge-to-edge binning has 21 bins in reconstructed neutrino energy which are bounded as follows:

- 1 bin from 0.00-0.20 GeV,
- 2 0.10-GeV bins from 0.20-0.40 GeV,
- 12 0.05-GeV bins from 0.40-1.00 GeV,
- 2 0.25-GeV bins from 1.00-1.50 GeV,
- 3 0.50-GeV bins from 1.50-3.00 GeV and
- 1 bin from 3.00-10.00 GeV.

The  $\nu_\mu$  edge-to-edge binning has 22 bins in true neutrino energy which are bounded as follows:

- 1 bin from 0.00-0.30 GeV,
- 3 0.10-GeV bins from 0.30-0.60 GeV,
- 12 0.05-GeV bins from 0.60-1.20 GeV,
- 1 bin from 1.20-1.50 GeV,
- 3 0.50-GeV bins from 1.50-3.00 GeV,
- 1 bin from 3.00-5.00 GeV and
- 1 bin from 5.00-10.00 GeV.



The  $\nu_e$  edge-to-edge binning has 12 bins in reconstructed neutrino energy which are bounded as follows:

- 1 0.35-GeV bin from 0.00-0.35 GeV,
- 5 0.15-GeV bins from 0.35-1.10 GeV,
- 2 0.20-GeV bins from 1.10-1.50 GeV,
- 2 0.25-GeV bins from 1.50-2.00 GeV,
- 1 bin from 2.00-3.00 GeV and
- 1 bin from 3.00-10.00 GeV.

The  $\nu_e$  edge-to-edge binning has 33 bins in true neutrino energy which are bounded as follows:

- 2 0.25-GeV bin from 0.00-0.50 GeV,
- 15 0.05-GeV bins from 0.50-1.25 GeV,
- 15 0.25-GeV bins from 1.25-5.00 GeV and
- 1 bin from 5.00-10.00 GeV.

### 6.3.2. Reaction Modes

The reaction modes define the topology of neutrino interactions. Categorising neutrino events is a requirement for handling systematic uncertainties since these are reaction mode dependent. The reaction modes are grouped into two sets<sup>1</sup>: the *fine* reaction modes which outline the complete list of all possible reaction modes and the *coarse* reaction modes which define a broader class of interaction which encompass one or more fine reaction mode. The fine reaction modes are listed in Table 6.1 and are typically used at the analysis level. The coarse reaction modes used depend on the analysis channel and are listed in Table 6.2. They are usually only used when displaying data such as in a breakdown of event rate spectra since using the complete list of reaction modes would be impractical.

---

<sup>1</sup>The CC QE  $0\pi$  mode is sometimes simply written as CC QE.

<i>Fine Reaction Modes</i>		
$\nu_\mu, \bar{\nu}_\mu$	$\nu_e, \bar{\nu}_e$	$\nu_\mu \rightarrow \nu_e, \bar{\nu}_\mu \rightarrow \bar{\nu}_e$
CC QE $0\pi$	CC QE $0\pi$	CC QE $0\pi$
NC Elastic	NC Elastic	CC 2p2h
CC, NC 2p2h	CC, NC 2p2h	CC $1\pi^\pm$
CC, NC $1\pi^\pm$	CC, NC $1\pi^\pm$	CC $1\pi^0$
CC, NC $1\pi^0$	CC, NC $1\pi^0$	CC $2\pi^\pm$
CC, NC $2\pi^\pm$	CC, NC $2\pi^\pm$	CC $2\pi^0$
CC, NC $2\pi^0$	CC, NC $2\pi^0$	CC Coh
CC, NC $\pi^\pm \pi^0$	CC, NC $\pi^\pm \pi^0$	Elastic Scattering
CC, NC Coh	CC, NC Coh	CC Other
CC, NC Elastic Scattering	CC+NC Elastic Scattering	
NC $1\gamma$	NC $1\gamma$	
CC, NC Other	CC, NC Other	
<i>Cosmic &amp; Dirt</i>		

**Table 6.1.:** The complete list of reaction modes considered in an SBN analysis. The 2p2h mode is defined as having a charged lepton + 2 nucleon topology distinguishing it from the other topologies.

<i>Coarse Reaction Modes</i>	
$\nu_\mu, \bar{\nu}_\mu$	$\nu_e, \bar{\nu}_e$
$\nu_\mu$ CC QE $0\pi$	$\nu_e$ CC QE $0\pi$
$\nu_\mu$ CC 2p2h	$\nu_e$ CC 2p2h
$\nu_\mu$ CC $1\pi$	$\nu_e$ CC $1\pi$
$\nu_\mu$ CC $2\pi$	$\nu_e$ CC $2\pi$
$\nu_\mu$ CC Other	$\nu_e$ CC Other
$\bar{\nu}_\mu$ CC	$\bar{\nu}_e$ CC
$\nu_e$ & $\bar{\nu}_e$ CC	$\nu_\mu$ CC
NC	$\bar{\nu}_\mu$ CC
<i>Cosmic</i>	Oscillated $\nu_e$ CC
<i>Dirt</i>	NC $0\pi$
	NC Other
<i>Cosmic</i>	
<i>Dirt</i>	

**Table 6.2.:** The *coarse* reaction modes used for both the  $\nu_\mu$  and  $\nu_e$  channels. These are a broader definition of the reaction modes where one or more of the *fine* reaction modes listed in Table 6.1 would come under the umbrella of a given coarse reaction mode.

### 6.3.3. Implementing and Validating SBN Systematic Uncertainties in VALOR

The systematics that are considered as part of the current SBN analysis have been detailed in Section 5.4. Unless explicitly stated, efficiency uncertainties are not considered due to there currently not being a general consensus on their magnitude.

The systematics from the GENIE and MicroBooNE reweight packages are initially in the form of weights which correspond to variations of the parameter. Systematic uncertainties in this form can not be directly used in an oscillation analysis, but must instead first be processed internally, the details of which are described below.

#### 6.3.3.1. Processing Systematic Uncertainties

Many *universes* are simulated, each with different weights associated with each of the systematic parameters. This allows the impact of varying systematic parameters on the event rate of neutrino interactions to be observed. If the systematic parameters are uncorrelated, the weights are simply an  $n\sigma$  variation which is the value used in a given universe. For correlated parameters, the weights are due to a unique variation of all the correlated parameters of a given universe. Of the systematic uncertainties associated with either the GENIE or MicroBooNE reweight packages, only the neutrino production flux uncertainties which are listed in Table 5.4 are correlated. All other parameters are uncorrelated.

Depending on whether a given systematic parameter is correlated or not, the way that it is processed within VALOR is done in two different ways. For the uncorrelated parameters, a set of associated response functions which represent the impact on the event rate that tweaking a given systematic parameter will have are constructed. For each parameter, individual response functions are constructed for each combination of  $d$ ,  $b$ ,  $s$ ,  $m$ ,  $r$  and  $t$ . Each response function is a 13-knot spline which nominally represents the change in event rate from parameter variations ranging from  $[-3, +3]\sigma$  in  $0.5\sigma$  intervals. The response functions are constructed by first identifying the 12 universes which have a variation closest to each of the non-zero  $\sigma$  intervals and then taking the ratio of the event rate from the selected

universe in a 2D ( $r$ ,  $t$ ) bin to the nominal event rate in that bin. By definition there will be a knot at  $0\sigma$  with a response of 1, however, in most cases, the remaining 12 knots will not be exactly at  $0.5\sigma$  intervals.

For the case of correlated parameters, it is not straightforward to construct response functions as was done for the uncorrelated parameters because any variations will be due to multiple parameters. These parameters are instead represented by a covariance matrix. Matrices of this type,  $\mathbf{C}_{ij}$ , are constructed such that,

$$\mathbf{C}_{ij} = \frac{1}{U} \sum_{u=1}^U (N_i^u - N_i^{cv})(N_j^u - N_j^{cv}), \quad (6.5)$$

where  $U$  is the number of universes,  $N_{i,j}^u$  is the event rate in universe  $u$  in bin  $i$  or  $j$  and  $N_{i,j}^{cv}$  nominal event rate in bin  $i$  or  $j$ .

### 6.3.3.2. Validating Systematic Uncertainties

In order to establish that the systematic parameters are being correctly handled within VALOR, a comparison between the event rate variations as seen by VALOR and those obtained directly from the universes is performed. This is done in two different ways;

1. Tweak the nominal spectra using the response functions within VALOR for a single systematic parameter and then compare them with the spectra that were obtained directly from the universe files.
2. Generate  $N$  toy samples (typically 500 in order to match the total number of universes) with some set of systematic parameters randomly tweaked. The one sigma spread from all the toys is found. This is done for both VALOR and for the universe files and the results are compared.

As an example, the  $+1\sigma$  variation for the  $f_{HornCurrent}$ ,  $f_{M_A^{CCRes}}$  and  $f_{\Delta \rightarrow N\gamma}$  parameters from the  $\nu_e$  sample in SBND between the VALOR response functions and the universes are shown in Figure 6.6<sup>2</sup>. A complete list of the  $+3\sigma$  variation

---

<sup>2</sup>The terms *spline* and *response function* are used interchangeably.

comparisons for all the uncorrelated systematic parameters in SBND are shown for the  $\nu_e$  channel in Appendix A. In all cases, there is either perfect agreement or differences of only up to a few tens of events. It should be noted that the event rate shown in the spectra used for validating the systematic parameters for the  $\nu_e$  channel is several orders of magnitude greater than the nominal event rates as seen in for example Figure 6.9. This is due to manually setting the oscillation parameters to  $\sin^2 2\theta_{\mu e} = 1$  and  $\Delta m_{41}^2 = 100$  eV<sup>2</sup> which ensures that many of the events from the oscillated  $\nu_\mu \rightarrow \nu_e$  sub-sample are processed which is required because the response functions are indexed by mode and therefore contributions from all the sub-samples are needed. Since oscillation and systematic effects commute, this approach is sufficient to correctly produce a complete set of response functions. In the nominal event rate spectra, the assumption is that no oscillations occur, so no events from the oscillated sample are included hence the much lower event rate.

Figure 6.7 shows a double ratio comparison from VALOR and the universes for the flux, proposal interaction and modern interaction systematic parameters. These plots are constructed by first finding the ratio between the  $1\sigma$  variation and the nominal using VALOR and the analogous ratio using the universe files. The double ratio is then constructed by taking the ratio of both the previous  $1\sigma$  ratios. There are some minor differences between the variations in VALOR and the universes, however, event-perfect agreement is not expected since the  $1\sigma$  variations are found by taking the average from many toy samples. Nevertheless, the disagreement is for the most part < 1% with a maximum of just over 2%.

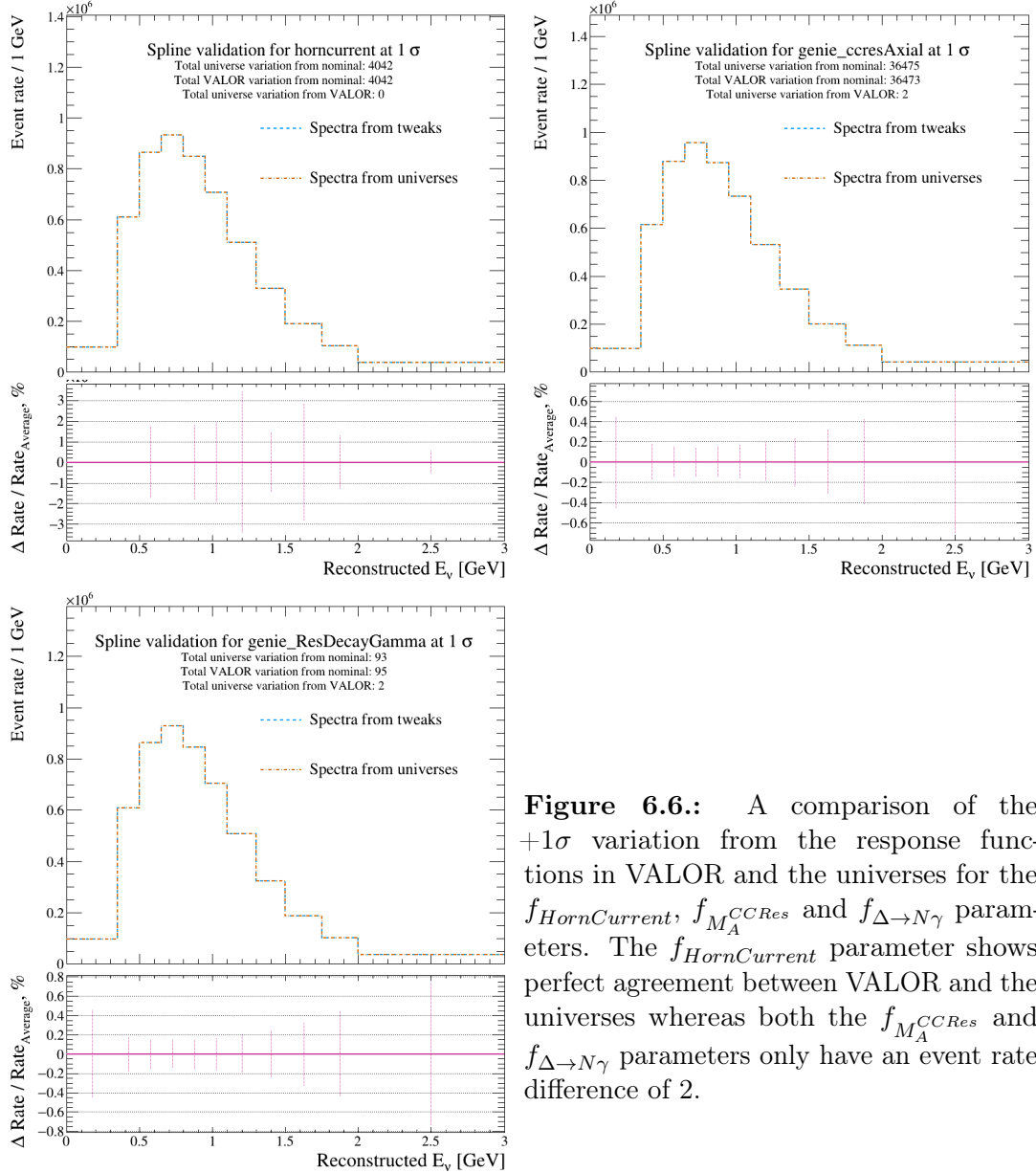


**Figure 6.6.:** A comparison of the  $+1\sigma$  variation from the response functions in VALOR and the universes for the  $f_{HornCurrent}$ ,  $f_{M_A^{CCRes}}$  and  $f_{\Delta \rightarrow N\gamma}$  parameters. The  $f_{HornCurrent}$  parameter shows perfect agreement between VALOR and the universes whereas both the  $f_{M_A^{CCRes}}$  and  $f_{\Delta \rightarrow N\gamma}$  parameters only have an event rate difference of 2.

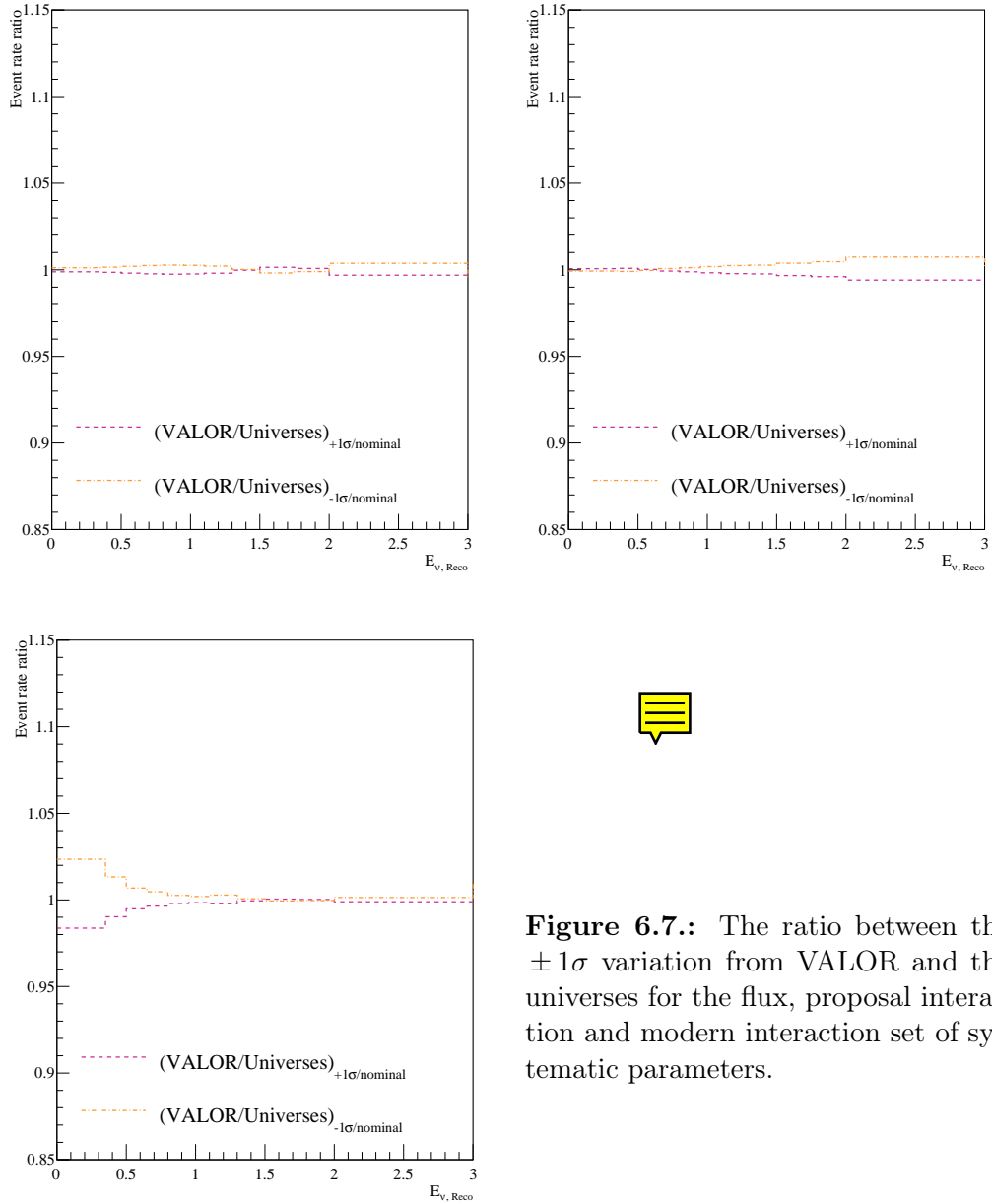


**Figure 6.7.:** The ratio between the  $\pm 1\sigma$  variation from VALOR and the universes for the flux, proposal interaction and modern interaction set of systematic parameters.

### 6.3.4. SBN Contour Construction

The relevant phase space for each of the three analysis channels considered is split into a  $40 \times 40$  grid. This number was chosen in order to find a balance between having sufficient granularity when constructing contours without having excessive computing times. The dimensions of the phase space considered are different for each analysis channel and are listed in Table 6.3. Fits are performed for each of the  $40 \times 40$  points where the oscillation parameters are fixed and the systematic parameters, if any, are allowed to float up to  $\pm 5\sigma$  from their nominal value. Once the fits have been produced, a contour of constant  $\chi^2$  is constructed. The  $\chi^2$  value is chosen such that it corresponds to a certain confidence level,  $CL$ , which for SBN analyses is typically  $5\sigma$ . The critical value of  $\chi^2$ ,  $\chi_{critical}^2$ , corresponding to a  $5\sigma$  confidence level along with a number of other  $\chi_{critical}^2$  values with their associated confidence levels which are commonly seen in literature are outlined in Table 6.4. An example of a 2D  $\chi^2$  surface with exclusion contours at 90%,  $3\sigma$  and  $5\sigma$  confidence levels for the  $\nu_e$  appearance channel is shown in Figure 6.8. The contours have been produced for the entire SBN program with the inclusion of flux and interaction systematics.

Analysis Channel	Phase Space Considered	
	$\sin^2 2\theta$	$\Delta m_{41}^2$
$\nu_\mu$ Disappearance	$\theta_{\mu\mu}$ : $[10^{-3} - 1]$	$[10^{-2} - 10^2]$ eV $^2$
$\nu_e$ Appearance	$\theta_{\mu e}$ : $[10^{-5} - 1]$	$[10^{-2} - 10^2]$ eV $^2$
$\nu_e$ Disappearance	$\theta_{ee}$ : $[10^{-2} - 1]$	$[10^{-2} - 10^2]$ eV $^2$

**Table 6.3.:** The phase space considered when constructing contours for each of the three oscillation channels within SBN.

Confidence level	68%	90%	95%	99%	$3\sigma$	$5\sigma$
$\chi^2_{critical}$	0.23	1.64	2.71	5.41	7.74	23.66

**Table 6.4.:** The  $\chi^2_{critical}$  values corresponding to various confidence levels which are commonly used when performing sensitivity studies. The confidence levels and  $\chi^2_{critical}$  are related via  $CL = \int_0^{\chi^2_{critical}} \frac{e^{-x/2} x^{u/2-1}}{2^{u/2} \Gamma(u/2)} dx$ , where  $u$  is the degrees of freedom (in this case 1) and  $\Gamma$  is the Gamma function [164].

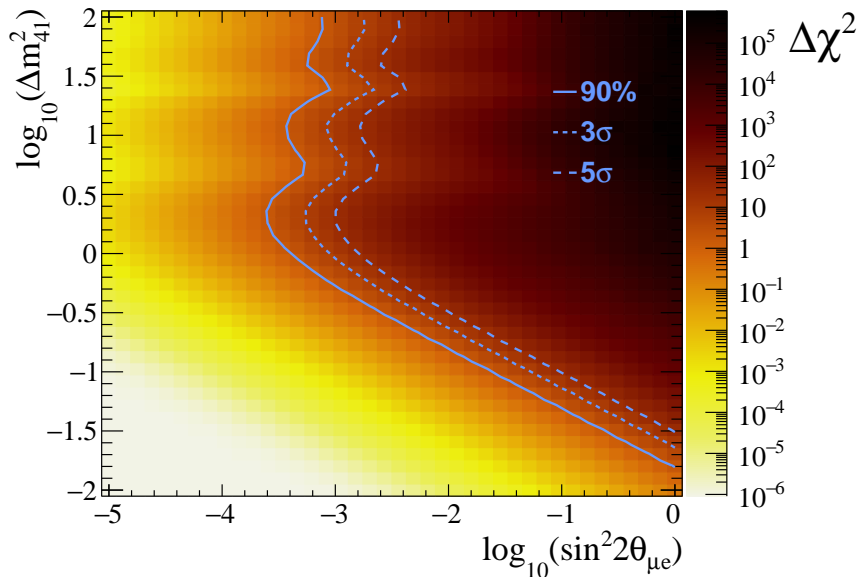


**Figure 6.8.:** The  $\nu_e$  appearance  $\chi^2$  surface from fits including flux and interaction systematics. Contours of constant  $\chi^2$  values which correspond to 90%,  $3\sigma$  and  $5\sigma$  confidence levels have been overlaid onto the surface.

## 6.4. Event Rate Predictions and the Expected Signal

In order to perform sensitivity calculations, the events are required to be binned in terms of a kinematical variable, which is chosen to be the **neutrino** energy.

The nominal event rates, event rates with an uncertainty envelope due to systematic uncertainties and the event rates due to an oscillation signal are discussed below

for each SBN detector. Additionally, the impact of the uncorrelated systematic parameters are quantified in terms of their effect on the oscillation parameters.

#### 6.4.1. Nominal Event Rate Predictions

It has been established that there are two oscillations channels associated with  $\nu_e$ :  $\nu_e$  appearance and  $\nu_e$  disappearance. Since the only difference between these channels is due to oscillations, the nominal event rates are common between the two.

The breakdown of the nominal number of events by interaction mode and channel are shown numerically in Table 6.5, Table 6.6 and Table 6.7 for SBND, MicroBooNE and ICARUS respectively. The same events rates are also shown in Figure 6.9 in the form of spectra. The spectra show the modal breakdown in terms of the coarse reaction modes where the events have been binned in reconstructed neutrino energy.

	$\nu_\mu \rightarrow \nu_\mu$	$\bar{\nu}_\mu \rightarrow \bar{\nu}_\mu$	$\nu_e \rightarrow \nu_e$	$\bar{\nu}_e \rightarrow \bar{\nu}_e$	$\nu_\mu \rightarrow \nu_e$	$\bar{\nu}_\mu \rightarrow \bar{\nu}_e$	Non-neutrino	Total
CCQE	17.0	0.0	5957.8	166.6	0.0	0.0	N/A	6141.5
CCMEC	1.1	0.0	1433.0	59.7	0.0	0.0	N/A	1493.8
CC $1\pi^\pm$	234.6	0.0	2859.9	112.4	0.0	0.0	N/A	3206.8
CC $1\pi^0$	230.7	0.0	513.8	14.6	0.0	0.0	N/A	759.2
CC $2\pi^\pm$	19.3	0.0	293.3	7.9	0.0	0.0	N/A	320.6
CC $2\pi^0$	5.2	0.0	24.1	0.6	0.0	0.0	N/A	29.9
CC $1\pi^0 1\pi^\pm$	37.1	0.0	187.0	7.0	0.0	0.0	N/A	231.1
CCcoherent	0.0	0.0	38.1	3.8	0.0	0.0	N/A	41.9
CC $\nu_e$ El	0.0	0.0	N/A	N/A	N/A	N/A	N/A	0.0
CCother	20.7	0.0	270.9	8.3	0.0	0.0	N/A	299.9
NCEL	3.4	0.0	0.0	0.0	N/A	N/A	N/A	3.5
NCMEC	0.6	0.0	0.0	0.0	N/A	N/A	N/A	0.6
NC $1\pi^\pm$	135.6	0.0	0.8	0.0	N/A	N/A	N/A	136.4
NC $1\pi^0$	772.6	0.0	5.5	0.2	N/A	N/A	N/A	778.4
NC $2\pi^\pm$	2.3	0.0	0.1	0.0	N/A	N/A	N/A	2.4
NC $2\pi^0$	6.9	0.0	0.1	0.0	N/A	N/A	N/A	7.0
NC $1\pi^0 1\pi^\pm$	16.1	0.0	0.4	0.0	N/A	N/A	N/A	16.5
NCcoherent	76.8	0.0	0.4	0.1	N/A	N/A	N/A	77.2
NC $1\gamma$	0.0	0.0	0.0	0.0	N/A	N/A	N/A	0.0
NC $\nu_e$ El	181.9	0.0	N/A	N/A	N/A	N/A	N/A	181.9
NCother	50.0	0.0	0.5	0.0	N/A	N/A	N/A	50.5
$\nu_e$ El	N/A	N/A	0.0	0.0	0.0	0.0	N/A	0.0
cosmic	N/A	N/A	N/A	N/A	N/A	N/A	0.3	0.3
dirt	N/A	N/A	N/A	N/A	N/A	N/A	33.9	33.9
Total	1812.0	0.0	11585.9	381.3	0.0	0.0	34.2	13813.5

**Table 6.5.:** Nominal  $\nu_e$  event rate breakdown in SBND.

	$\nu_\mu \rightarrow \nu_\mu$	$\bar{\nu}_\mu \rightarrow \bar{\nu}_\mu$	$\nu_e \rightarrow \nu_e$	$\bar{\nu}_e \rightarrow \bar{\nu}_e$	$\nu_\mu \rightarrow \nu_e$	$\bar{\nu}_\mu \rightarrow \bar{\nu}_e$	Non-neutrino	Total
CCQE	4.2	0.0	384.9	10.4	0.0	0.0	N/A	399.5
CCMEC	0.1	0.0	93.9	3.7	0.0	0.0	N/A	97.6
CC1 $\pi^\pm$	18.9	0.0	196.8	7.5	0.0	0.0	N/A	223.2
CC1 $\pi^0$	19.1	1.0	35.5	1.1	0.0	0.0	N/A	56.7
CC2 $\pi^\pm$	1.0	0.0	21.9	0.6	0.0	0.0	N/A	23.5
CC2 $\pi^0$	3.3	0.0	1.9	0.1	0.0	0.0	N/A	5.2
CC1 $\pi^0$ 1 $\pi^\pm$	7.2	0.0	13.6	0.6	0.0	0.0	N/A	21.4
CCcoherent	0.0	0.0	2.6	0.4	0.0	0.0	N/A	3.0
CC $\nu_e$ El	0.0	0.0	N/A	N/A	N/A	N/A	N/A	0.0
CCother	3.3	0.0	19.1	0.4	0.0	0.0	N/A	22.9
NCEL	0.3	0.0	0.0	0.0	N/A	N/A	N/A	0.3
NCMEC	0.0	0.0	0.0	0.0	N/A	N/A	N/A	0.0
NC1 $\pi^\pm$	13.9	0.0	0.1	0.0	N/A	N/A	N/A	14.0
NC1 $\pi^0$	59.3	1.0	0.4	0.0	N/A	N/A	N/A	60.7
NC2 $\pi^\pm$	0.7	0.0	0.0	0.0	N/A	N/A	N/A	0.7
NC2 $\pi^0$	0.7	0.1	0.0	0.0	N/A	N/A	N/A	0.7
NC1 $\pi^0$ 1 $\pi^\pm$	2.3	0.0	0.0	0.0	N/A	N/A	N/A	2.3
NCcoherent	5.5	0.2	0.0	0.0	N/A	N/A	N/A	5.8
NC1 $\gamma$	0.0	0.0	0.0	0.0	N/A	N/A	N/A	0.0
NC $\nu_e$ El	14.9	0.0	N/A	N/A	N/A	N/A	N/A	14.9
NCother	3.3	0.0	0.0	0.0	N/A	N/A	N/A	3.3
$\nu_e$ El	N/A	N/A	0.0	0.0	0.0	0.0	N/A	0.0
cosmic	N/A	N/A	N/A	N/A	N/A	N/A	0.0	0.0
dirt	N/A	N/A	N/A	N/A	N/A	N/A	14.8	14.8
Total	157.8	2.3	770.9	24.8	0.0	0.0	14.8	970.6

**Table 6.6.:** Nominal  $\nu_e$  event rate breakdown in MicroBooNE.

	$\nu_\mu \rightarrow \nu_\mu$	$\bar{\nu}_\mu \rightarrow \bar{\nu}_\mu$	$\nu_e \rightarrow \nu_e$	$\bar{\nu}_e \rightarrow \bar{\nu}_e$	$\nu_\mu \rightarrow \nu_e$	$\bar{\nu}_\mu \rightarrow \bar{\nu}_e$	Non-neutrino	Total
CCQE	4.6	0.0	727.9	19.3	0.0	0.0	N/A	751.9
CCMEC	0.2	0.0	176.5	7.1	0.0	0.0	N/A	183.8
CC1 $\pi^\pm$	37.4	0.2	372.3	12.9	0.0	0.0	N/A	422.8
CC1 $\pi^0$	25.8	0.1	64.8	2.2	0.0	0.0	N/A	92.9
CC2 $\pi^\pm$	4.9	0.1	39.4	1.0	0.0	0.0	N/A	45.4
CC2 $\pi^0$	2.9	0.1	3.6	0.1	0.0	0.0	N/A	6.6
CC1 $\pi^0$ 1 $\pi^\pm$	7.5	0.0	25.8	1.1	0.0	0.0	N/A	34.5
CCcoherent	0.0	0.0	5.0	0.5	0.0	0.0	N/A	5.4
CC $\nu_e$ El	0.0	0.0	N/A	N/A	N/A	N/A	N/A	0.0
CCother	2.8	0.0	36.9	0.8	0.0	0.0	N/A	40.5
NCEL	0.5	0.0	0.0	0.0	N/A	N/A	N/A	0.5
NCMEC	0.0	0.0	0.0	0.0	N/A	N/A	N/A	0.0
NC1 $\pi^\pm$	17.7	0.2	0.1	0.0	N/A	N/A	N/A	18.1
NC1 $\pi^0$	108.5	0.7	0.7	0.0	N/A	N/A	N/A	110.0
NC2 $\pi^\pm$	0.7	0.0	0.0	0.0	N/A	N/A	N/A	0.8
NC2 $\pi^0$	0.9	0.0	0.0	0.0	N/A	N/A	N/A	0.9
NC1 $\pi^0$ 1 $\pi^\pm$	3.4	0.1	0.1	0.0	N/A	N/A	N/A	3.6
NCcoherent	11.3	0.4	0.1	0.0	N/A	N/A	N/A	11.8
NC1 $\gamma$	0.0	0.0	0.0	0.0	N/A	N/A	N/A	0.0
NC $\nu_e$ El	17.9	0.0	N/A	N/A	N/A	N/A	N/A	17.9
NCother	8.0	0.0	0.1	0.0	N/A	N/A	N/A	8.1
$\nu_e$ El	N/A	N/A	0.0	0.0	0.0	0.0	N/A	0.0
cosmic	N/A	N/A	N/A	N/A	N/A	N/A	2.3	2.3
dirt	N/A	N/A	N/A	N/A	N/A	N/A	24.1	24.1
Total	255.0	2.0	1453.3	44.9	0.0	0.0	26.4	1781.6

**Table 6.7.:** Nominal  $\nu_e$  event rate breakdown in ICARUS.

Similar to Figure 6.9, Figure 6.10 again shows the nominal event rate in each SBN detector, but in an integrated form. Additionally,  $1\sigma$  prefit uncertainty envelopes are shown which are due to the flux and interaction systematics. The accuracy of say the ICARUS prediction can be improved by constraining the systematics from an SBND fit. This is shown in Figure 6.11 which shows the nominal integrated ICARUS spectrum along with the prefit uncertainty envelope as in Figure 6.10, but also a postfit uncertainty envelope based on an SBND fit is shown. The reduction in size from the prefit to postfit envelope highlights the impact of SBND on the ICARUS prediction.

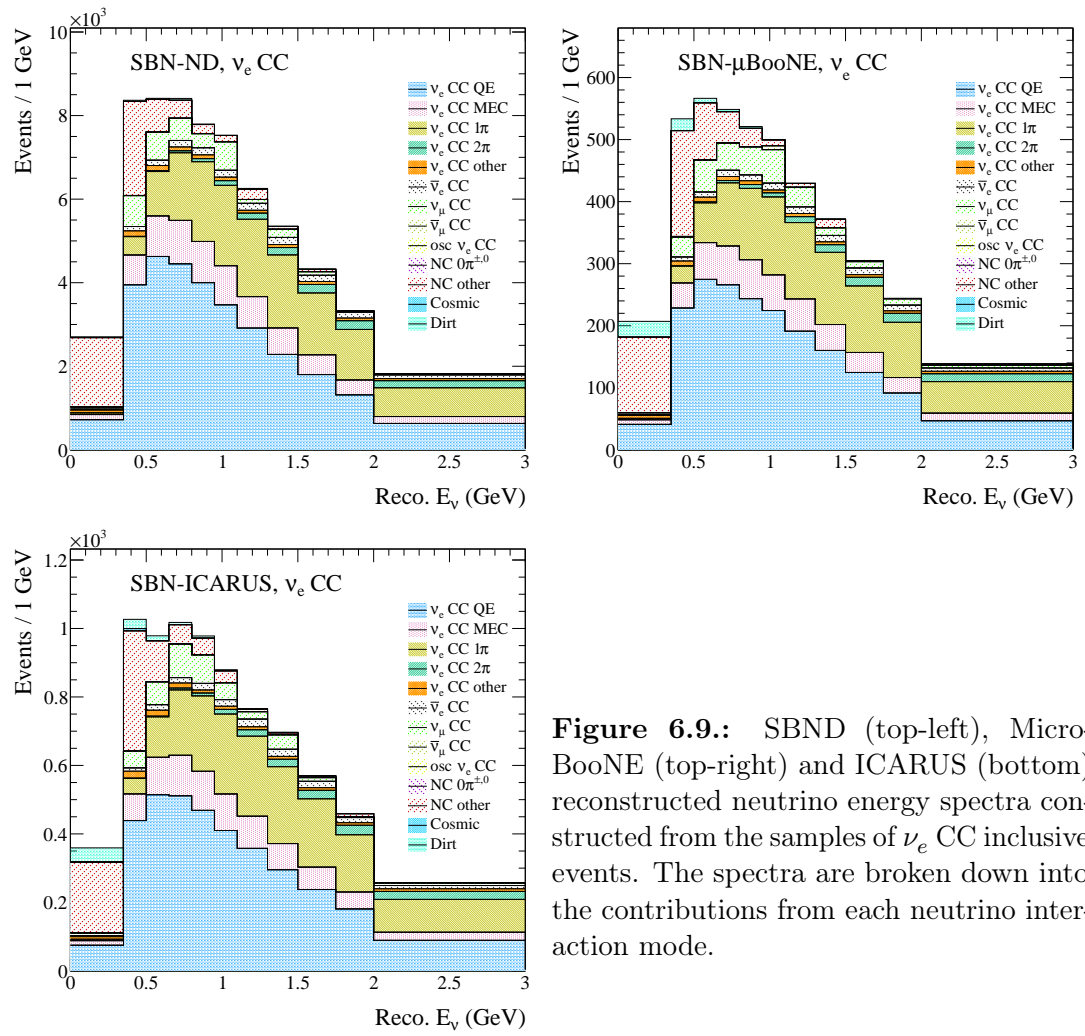


**Figure 6.9.:** SBND (top-left), Micro-BooNE (top-right) and ICARUS (bottom) reconstructed neutrino energy spectra constructed from the samples of  $\nu_e$  CC inclusive events. The spectra are broken down into the contributions from each neutrino interaction mode.

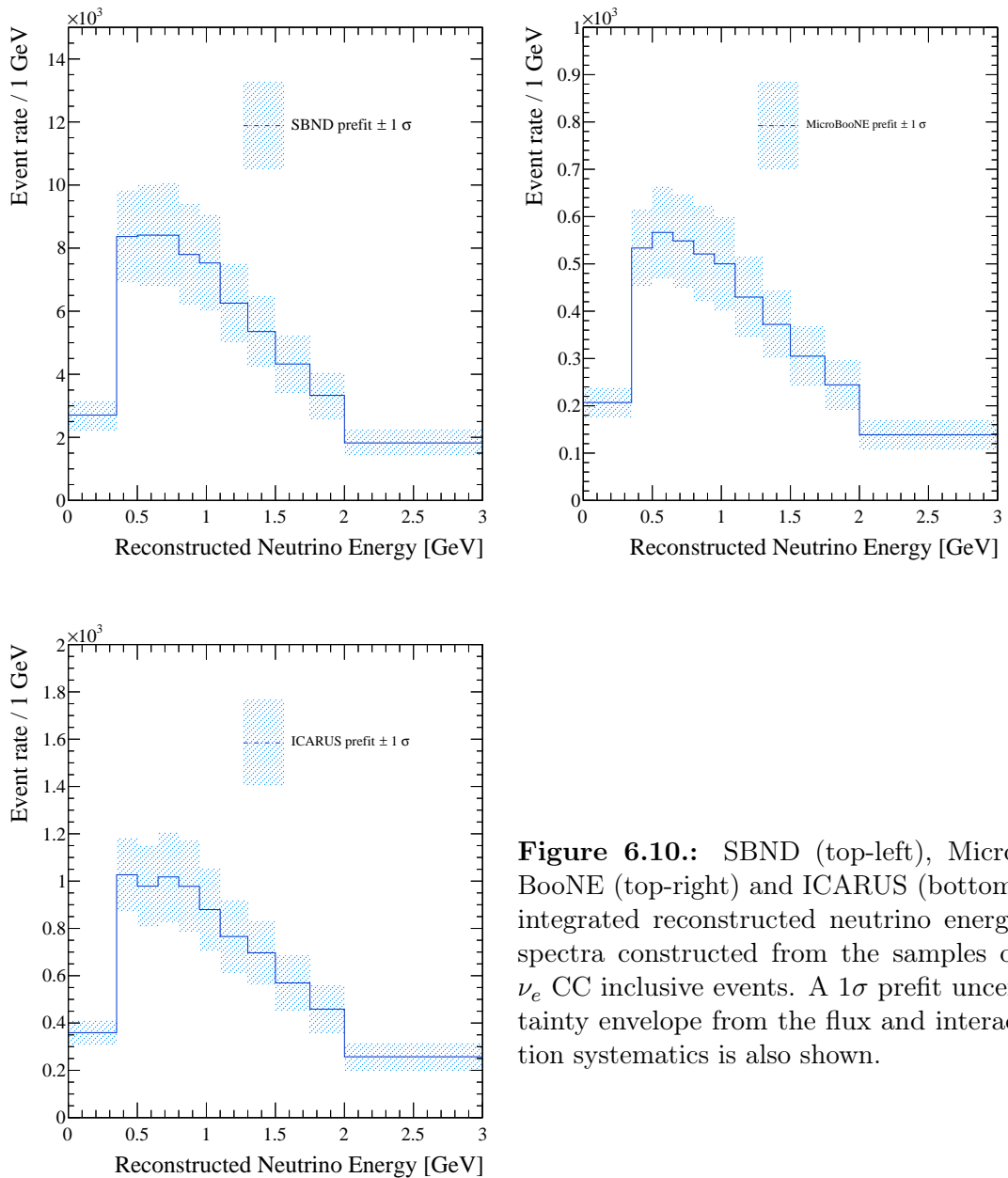


**Figure 6.10.:** SBND (top-left), MicroBooNE (top-right) and ICARUS (bottom) integrated reconstructed neutrino energy spectra constructed from the samples of  $\nu_e$  CC inclusive events. A  $1\sigma$  prefit uncertainty envelope from the flux and interaction systematics is also shown.

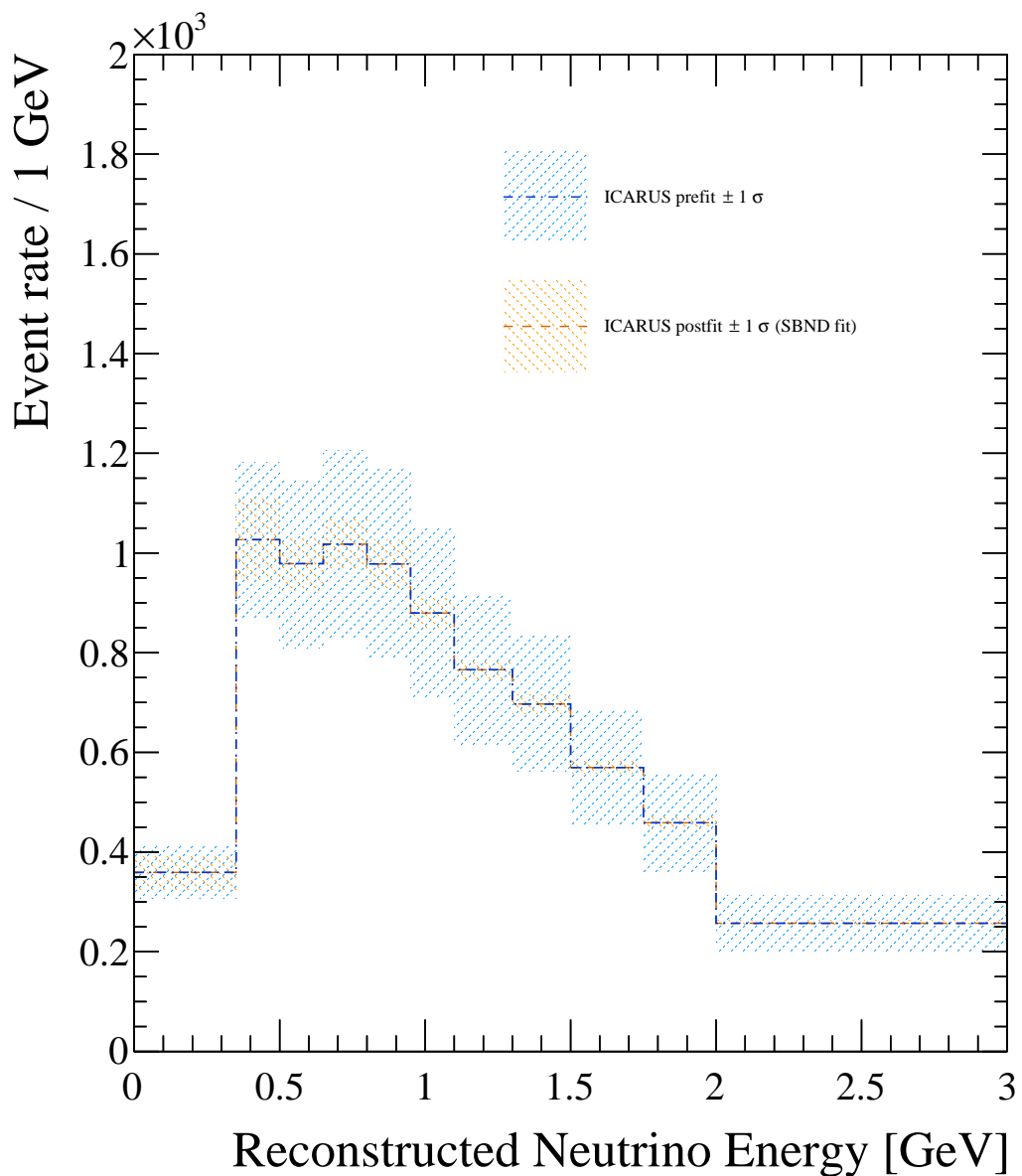


**Figure 6.11.:** ICARUS integrated reconstructed neutrino energy spectrum constructed from the samples of  $\nu_e$  CC inclusive events. The  $1\sigma$  prefit envelope is shown as well as a  $1\sigma$  postfit envelope based on an SBND fit. The reduction in size of the error envelope when going from prefit to postfit shows the impact of SBND on improving the accuracy of the ICARUS prediction.

## 6.4.2. Expected Oscillation Signal

Assuming that mixing with a light sterile neutrino occurs, a change to the nominal event rate will be observed. Since the oscillation channels are currently considered as stand-alone analyses, this will either result in an increase or decrease in the event rate depending on whether an appearance or disappearance channel is considered.

### 6.4.2.1. $\nu_e$ Appearance Analysis

The  $\nu_e$  appearance channel is concerned with oscillations from  $\nu_\mu$  to  $\nu_e$  meaning an increase in the event rate is expected. This is shown in Figure 6.12 where the nominal event rate breakdown is shown as in Figure 6.9 but overlaid with an integrated spectrum that was produced with oscillation parameters  $\sin^2 2\theta_{\mu e} = 0.003$  and  $\Delta m_{41}^2 = 1.32 \text{ eV}^2$ . The oscillation signal seen for these parameters in SBND is small whereas for MicroBooNE and ICARUS it is substantial which is consistent with what is seen in Figure 3.11. This highlights the fact that SBND will largely be used to constrain systematic parameters due to observing no or very few oscillated events with the oscillation signal being largely left to MicroBooNE and ICARUS.

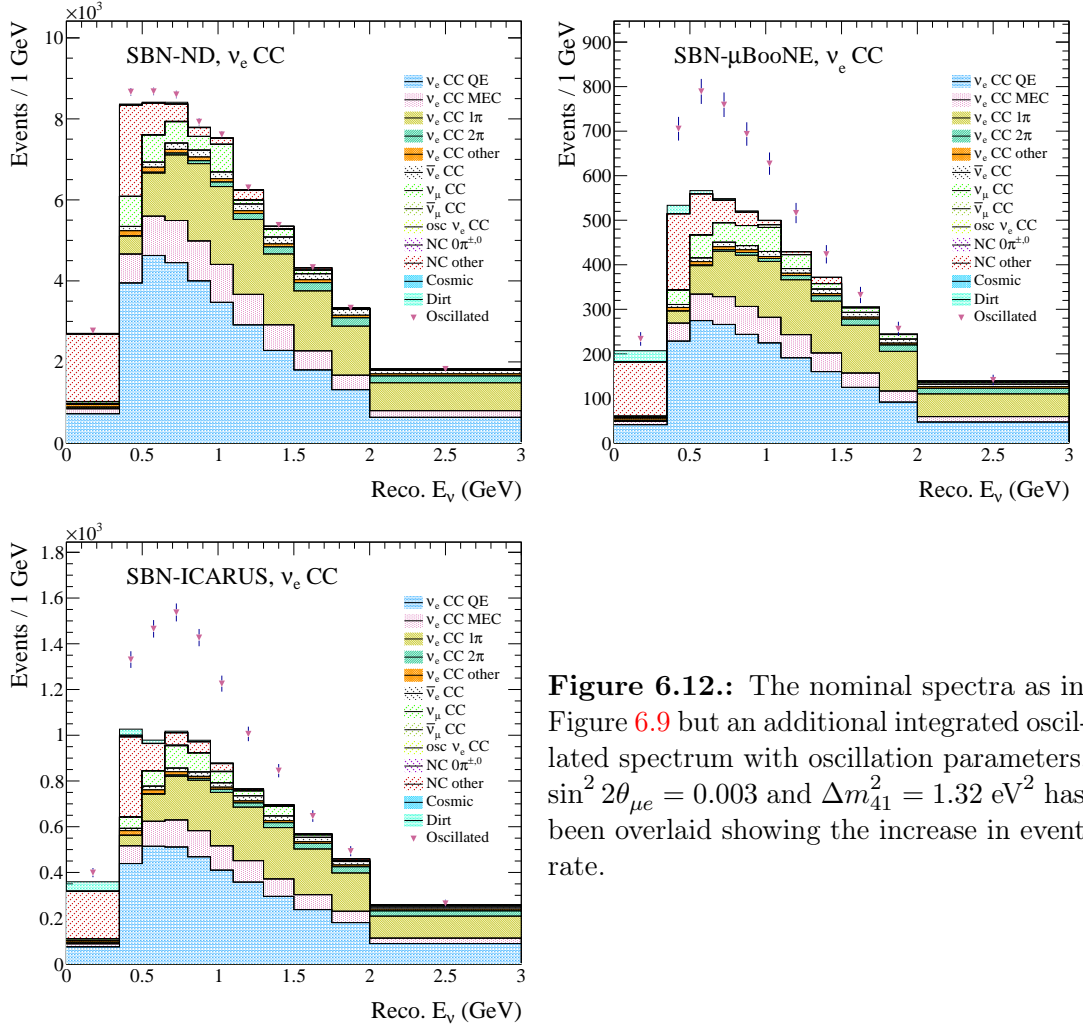


**Figure 6.12.:** The nominal spectra as in Figure 6.9 but an additional integrated oscillated spectrum with oscillation parameters,  $\sin^2 2\theta_{\mu e} = 0.003$  and  $\Delta m_{41}^2 = 1.32 \text{ eV}^2$  has been overlaid showing the increase in event rate.

The top left plot of Figure 6.13 shows the  $\nu_e$  appearance statistical only exclusion contour and allowed region from fits combining all three SBN detectors. The injected point  $\Delta m_{41}^2 = 1.32 \text{ eV}^2$ ,  $\sin^2 2\theta_{\mu e} = 0.003$ , used when producing the allowed region is shown along with two further points on the exclusion contour at  $\Delta m_{41}^2 = 1 \text{ eV}^2$ ,  $\sin^2 2\theta_{\mu e} = 0.0014$  and  $\Delta m_{41}^2 = 100 \text{ eV}^2$ ,  $\sin^2 2\theta_{\mu e} = 0.0005$ .  $\nu_e$  appearance spectra are produced using oscillation parameters corresponding to each of these three points for each of the three SBN detectors. The ratio of each of these oscillated spectra to the nominal for each detector are shown in the remaining plots in Figure 6.13 and highlight the expected oscillation signal.

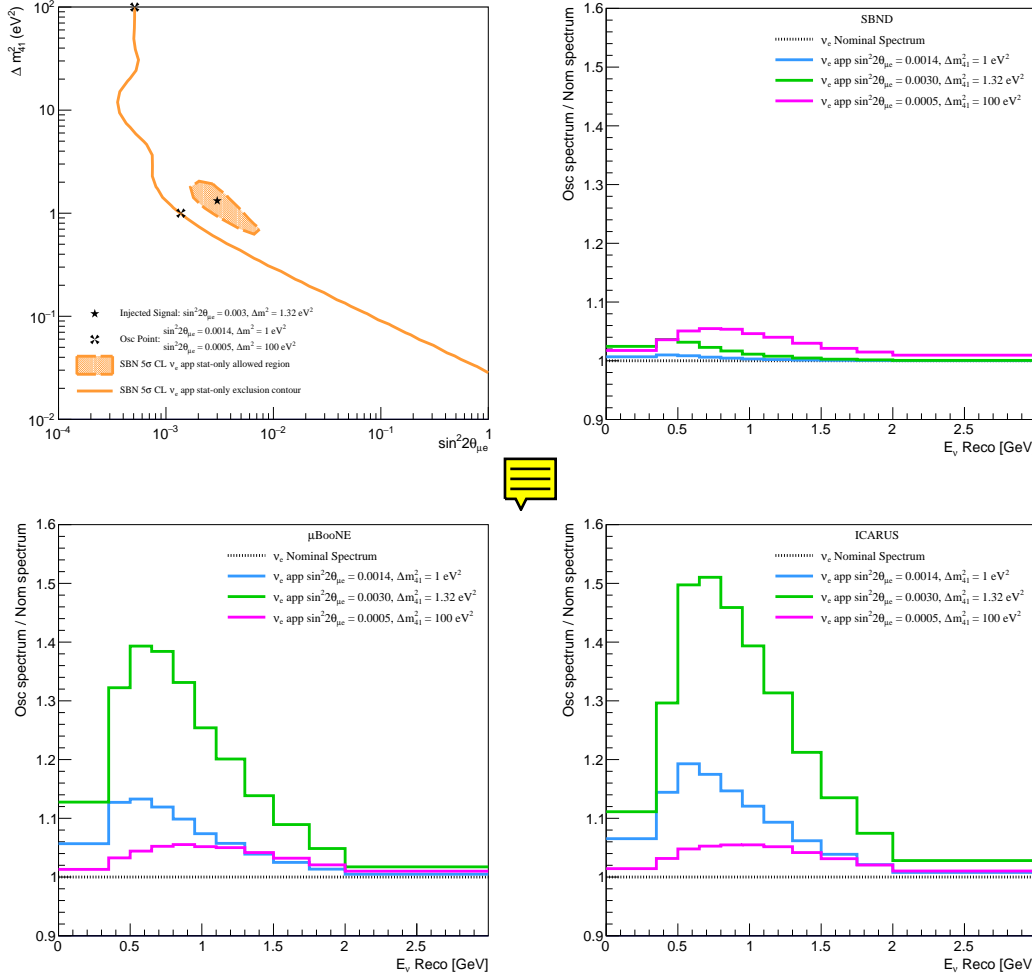


**Figure 6.13.:**  $\nu_e$  appearance stat-only exclusion contour and allowed region. The injected point at  $\sin^2 2\theta_{\mu e} = 0.003$ ,  $\Delta m_{41}^2 = 1.32 \text{ eV}^2$  used for the allowed region is shown along with two further points at  $\sin^2 2\theta_{\mu e} = 0.0014$ ,  $\Delta m_{41}^2 = 1 \text{ eV}^2$  and  $\sin^2 2\theta_{\mu e} = 0.0005$ ,  $\Delta m_{41}^2 = 100 \text{ eV}^2$  (top left). The ratio of spectra with oscillation parameters corresponding to the three points mentioned versus nominal are shown for SBND (top right), MicroBooNE (bottom left) and ICARUS (bottom right).

#### 6.4.2.2. $\nu_e$ Disappearance Analysis

Mirroring the  $\nu_e$  appearance channel, the  $\nu_e$  disappearance channel observes a reduction in the nominal  $\nu_e$  event rate. This is shown in Figure 6.14 where the integrated spectrum produced with oscillation parameters  $\sin^2 2\theta_{ee} = 0.4$  and

$\Delta m_{41}^2 = 3 \text{ eV}^2$  has been overlaid onto the breakdown of the nominal spectrum for each of the three detectors. As is the case for  $\nu_e$  appearance, the oscillation signal is relatively small in SBND whereas both MicroBooNE and ICARUS observe a much more significant signal.

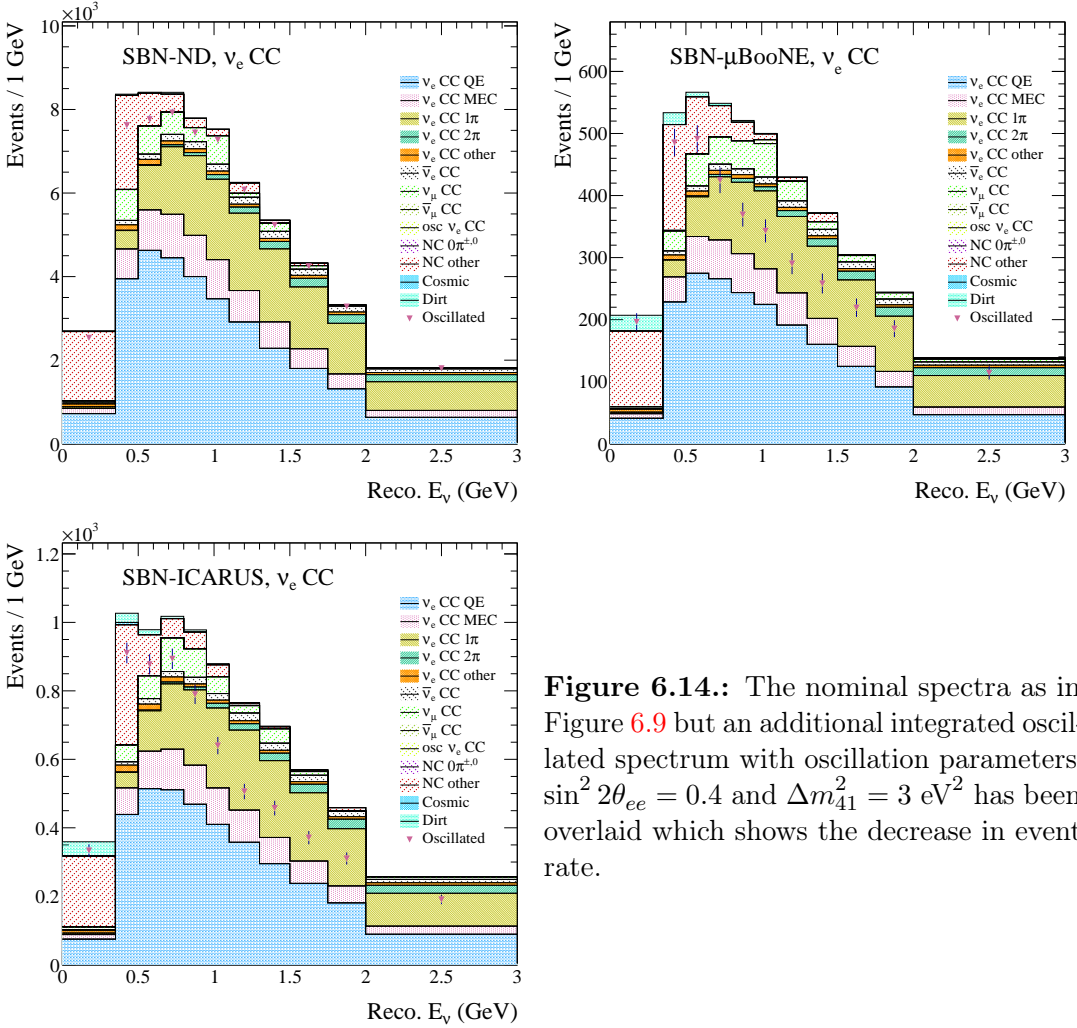


**Figure 6.14.:** The nominal spectra as in Figure 6.9 but an additional integrated oscillated spectrum with oscillation parameters,  $\sin^2 2\theta_{ee} = 0.4$  and  $\Delta m_{41}^2 = 3 \text{ eV}^2$  has been overlaid which shows the decrease in event rate.

The top left plot of Figure 6.15 shows the  $\nu_e$  disappearance statistical only exclusion contour and allowed region from fits combining all three SBN detectors. The injected point  $\Delta m_{41}^2 = 3 \text{ eV}^2$ ,  $\sin^2 2\theta_{\mu e} = 0.4$ , used when producing the allowed region is shown along with two further points on the exclusion contour at  $\Delta m_{41}^2 = 1 \text{ eV}^2$ ,  $\sin^2 2\theta_{\mu e} = 0.29$  and  $\Delta m_{41}^2 = 100 \text{ eV}^2$ ,  $\sin^2 2\theta_{\mu e} = 0.085$ .  $\nu_e$  disappearance spectra are produced using oscillation parameters corresponding

to each of these three points for each of the three SBN detectors. The ratio of each of these oscillated spectra to the nominal for each detector are shown in the remaining plots in Figure 6.15 and highlight the expected oscillation signal.

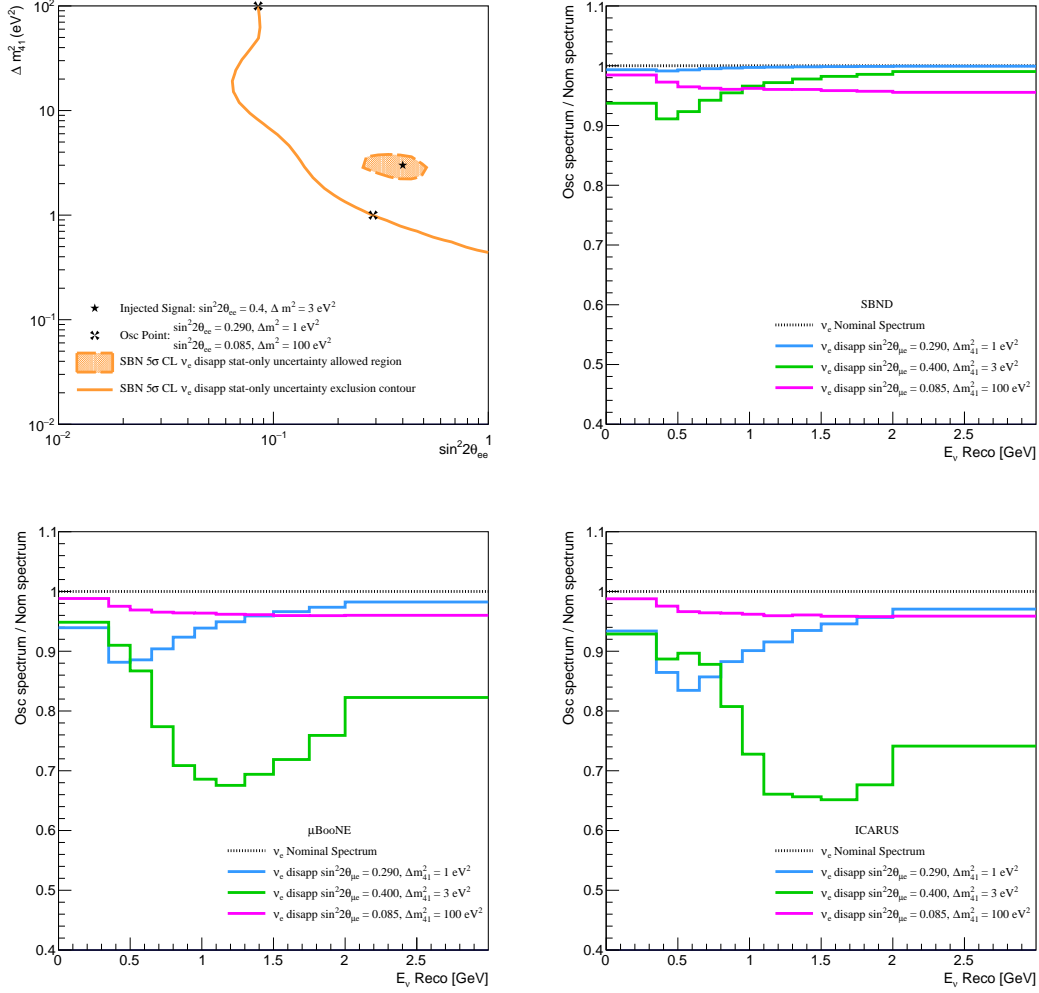


**Figure 6.15.:**  $\nu_e$  disappearance stat-only exclusion contour and allowed region. The injected point at  $\sin^2 2\theta_{ee} = 0.4$ ,  $\Delta m_{41}^2 = 3 \text{ eV}^2$  used for the allowed region is shown along with two further points at  $\sin^2 2\theta_{ee} = 0.29$ ,  $\Delta m_{41}^2 = 1 \text{ eV}^2$  and  $\sin^2 2\theta_{ee} = 0.085$ ,  $\Delta m_{41}^2 = 100 \text{ eV}^2$  (top left). The ratio of spectra with oscillation parameters corresponding to the three points mentioned versus nominal are shown for SBND (top right), MicroBooNE (bottom left) and ICARUS (bottom right).

## 6.5. Sensitivities Studies

Following the scheme outlined in Section 6.3.4, both allowed and exclusion sensitivity contours are produced for the entire SBN program. Additionally, the contribution from individual and combination of detectors on the contours is investigated as well as the impact of different sets of systematic parameters and certain individual parameters.

The sensitivity contours shown in Section 6.5.1 and Section 6.5.2 are produced using the well validated flux and interaction uncertainties, whereas Section 6.5.3 and Section 6.5.4 discuss the impact on the exclusion sensitivity contours from the inclusion of additional efficiency uncertainties as well as tweaking the energy smearing used in the event selection based on results from Chapter 4.

### 6.5.1. Evaluation of SBN Sensitivities for $\nu_e$ Appearance and Disappearance

The complete  $\nu_e$  appearance exclusion sensitivities and allowed regions for both the statistical-only case and with the inclusion of flux and interaction systematics are shown in Figure 6.16 for the entire SBN program alongside external limits from the LSND and KARMEN experiments [107]. For comparison purposes, it should be noted that the contours produced for the SBN program are at the  $5\sigma$  confidence level whereas the results from both LSND and KARMEN are at the 99% confidence level. The results from SBN shows an improvement over the KARMEN results for essentially all  $\Delta m_{41}^2$  values and the allowed region is largely consistent with the LSND result.

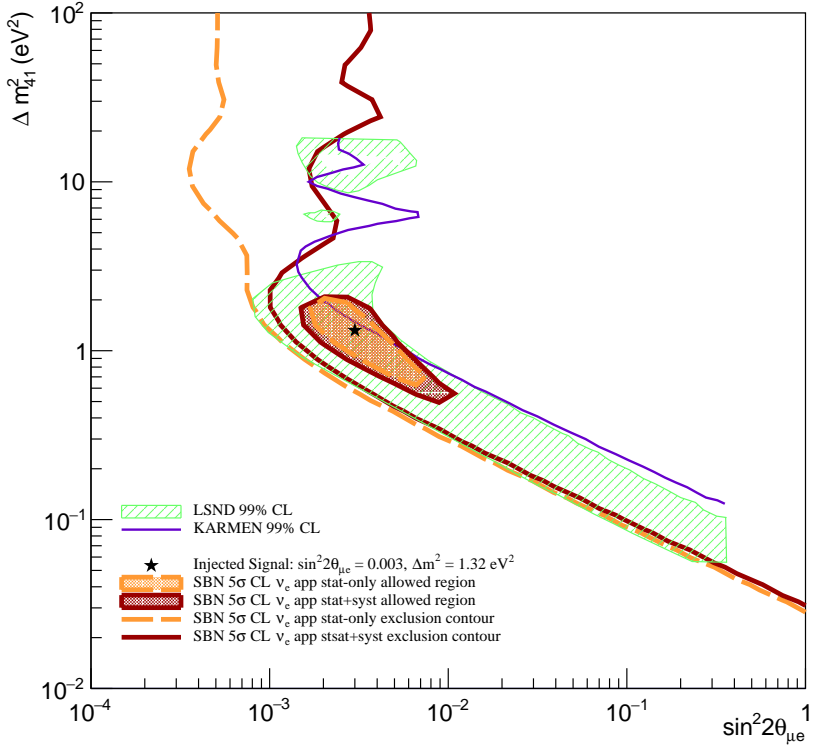


**Figure 6.16.:**  $\nu_e$  appearance exclusion contours and allowed regions for the stat only case and with flux and interaction systematic uncertainties included. External limits from the LSND and KARMEN experiments have been overlaid [107]. (The confidence intervals for each contour are shown in the legend and it should be noted that those from external limits are not the same as those from the contours produced for the SBN program.)

The complete  $\nu_e$  disappearance exclusion sensitivities and allowed regions for both the statistical-only case and with the inclusion of flux and interaction systematics are shown in Figure 6.17 for the entire SBN program alongside external limits from the ND280 detector which serves as one of the near detectors as part of the T2K experiment [165]. The results for the SBN program are shown at a  $5\sigma$  confidence level whereas the allowed region from the T2K experiment is shown at both 68% and 90% confidence level and the exclusion contour is at a 95% confidence level [98]. The results from SBN exclude a substantial portion of the

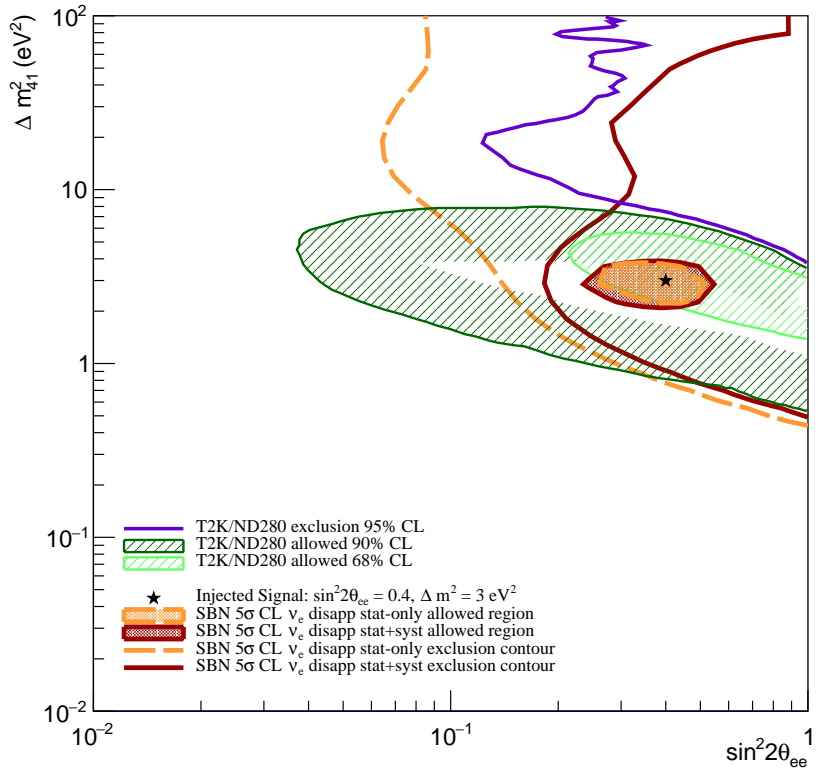


**Figure 6.17.:**  $\nu_e$  disappearance exclusion contours and allowed regions for the stat only case and with flux and interaction systematic uncertainties included. External limits from the T2K experiments have been overlaid [98]. (The confidence intervals for each contour are shown in the legend and it should be noted that those from external limits are not the same as those from the contours produced for the SBN program.)

T2K allowed region with the exclusion limits at high  $\Delta m^2_{41}$  not being as strong for the current comparison.

To see the impact that each detector has on the sensitivity contour, the left plot of Figure 6.18 shows the  $\nu_e$  appearance statistical-only sensitivity contours from each individual detector as well as all possible combinations (the black curve labelled “SBN” refers to a contour from combining all three detectors). It can be seen that for large  $\Delta m^2_{41}$  (greater than  $\sim 5 \text{ eV}^2$ ), that the SBND detector dominates the sensitivity whereas for small  $\Delta m^2_{41}$  (less than  $\sim 0.7 \text{ eV}^2$ ) the ICARUS detector dominates. It should also be noted that only by combining the fits from all three

detectors can the best sensitivities be obtained. Having this multi-detector design is one of the key advantages of the SBN program. The right plot of Figure 6.18 is akin to the left one, but with the inclusion of flux and interaction systematics in the fits. Again, the improvements to the sensitivity are highlighted by combining multiple detectors.

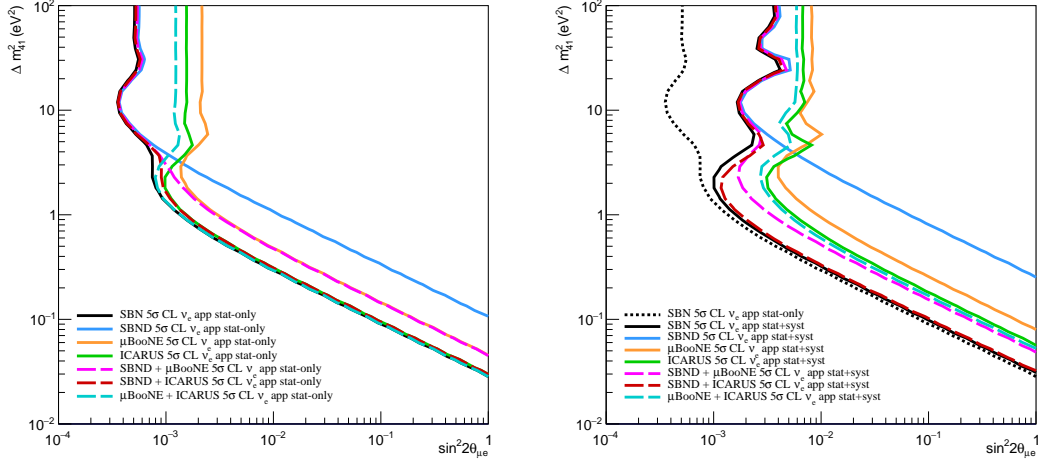


**Figure 6.18.:** Contributions to the SBN  $\nu_e$  appearance sterile oscillation sensitivity from each detector and combinations of detectors in the SBN program. The statistical-only plots in the left-hand figure show that SBND is most sensitive to the region  $\Delta m_{41}^2 > \sim 3$  eV<sup>2</sup> and ICARUS is most sensitive to  $\Delta m_{41}^2 < \sim 3$  eV<sup>2</sup>. The right-hand figure includes flux and interaction systematic parameters and highlights the considerable improvement in the oscillation sensitivity when including multiple detectors in the fits.

Similar to Figure 6.18, Figure 6.19 shows the  $\nu_e$  disappearance sensitivity from individual detectors and combinations of multiple detectors for both the statistical-only case (Left) and the case with flux and interaction systematics (Right). Again, SBND dominates the sensitivity at high mass splitting whereas ICARUS is dominant for low mass splitting with the emphasis being on the improvement to the overall sensitivity when fits from all three SBN detectors are combined.

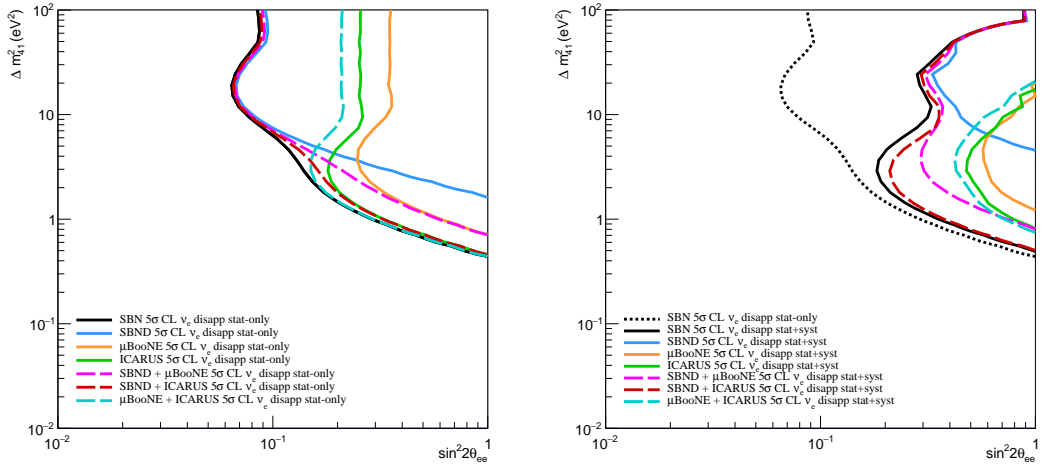


**Figure 6.19.:** Contributions to the SBN  $\nu_e$  disappearance sterile oscillation sensitivity from each detector and combinations of detectors in the SBN program produced. The statistical-only plots in the left-hand figure show that SBND is most sensitive to the region  $\Delta m_{41}^2 > 3 \text{ eV}^2$  and ICARUS is most sensitive below  $\Delta m_{41}^2 < 3 \text{ eV}^2$ . The right-hand figure includes flux and interaction systematic parameters and highlights the considerable improvement in the oscillation sensitivity when including multiple detectors in the fits.

### 6.5.2. Impact of Systematic Uncertainties

The impact of systematic sub-groups on the sensitivities are investigated by applying each group in isolation. Following this, the impact of individual systematic parameters on the oscillation parameters is investigated and the dominant uncertainties are identified. The impact of these dominant uncertainties on the sensitivities is then discussed.

#### 6.5.2.1. Impact of Systematic Uncertainty Sub-Groups

The results from applying the flux, proposal interaction, modern interaction and proposal + modern interaction systematic subgroups for the  $\nu_e$  appearance channel is shown in the left plot of Figure 6.20. This highlights the reduction in sensitivity when individually applying each systematic subgroup when compared to the statistical-only case. The right-hand plot of Figure 6.20 shows the ratio of the exclusion contours to the statistical-only case. This gives a clearer measure

of the impact on the sensitivity in  $\sin^2 2\theta_{\mu e}$  space. It follows that the interaction systematics have the biggest impact on the sensitivity which in turn are dominated by the modern set of interaction parameters. The proposal set of interaction parameters have the smallest impact with the magnitude of the impact from the flux parameters being somewhere in between the two sets of interaction parameters.

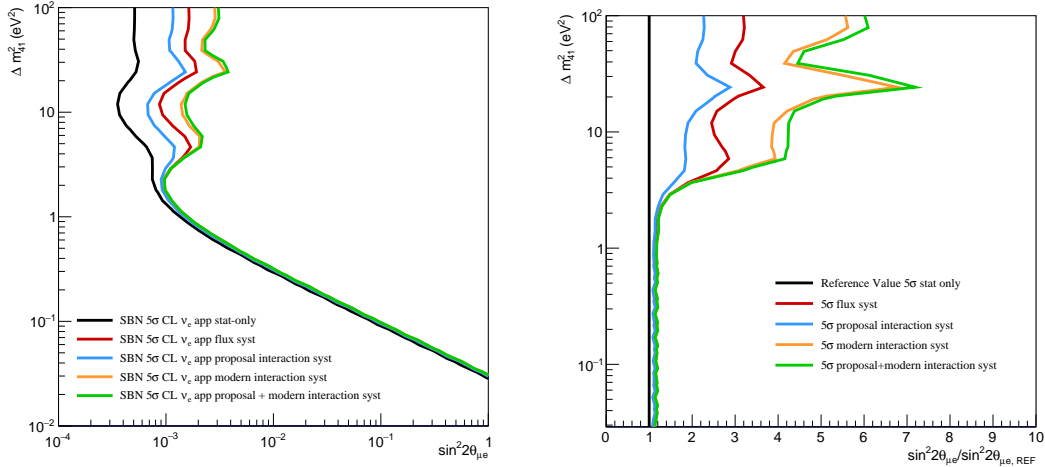


**Figure 6.20.:** The left plot shows the reduction in sensitivity from the stat-only contour when including each set of systematic parameters in the fits. The right plot shows the relative location of each systematic contour in  $\sin^2 2\theta_{\mu e}$  space, with respect to the statistical-only case for the active region of  $\Delta m_{41}^2$  phase space.

The relative contribution of the different systematic groups to the overall exclusion contour for  $\nu_e$  disappearance is shown in Figure 6.21 and is comparable to the  $\nu_e$  appearance case. The interaction systematics again have the largest impact, the majority of which is due to the modern set of parameters. The proposal set of parameters have the smallest impact with the magnitude of the impact from the flux parameters being somewhere in between the two sets of interaction parameters.

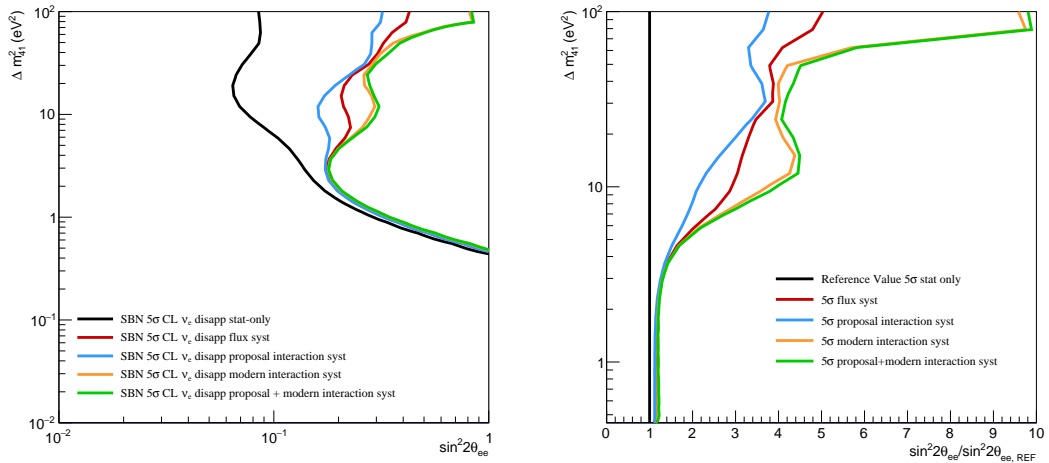


**Figure 6.21.:** The left plot shows the reduction in sensitivity from the stat-only contour when including each set of systematic parameters in the fits. The right plot shows the relative location of each systematic contour in  $\sin^2 2\theta_{ee}$  space, with respect to the statistical-only case for the active region of  $\Delta m_{41}^2$  phase space.

### 6.5.2.2. Impact of Individual Systematics

To assess the impact of the different systematic parameters on the oscillation parameters the following study is performed;

1. Generate a toy experiment with a given oscillation signal with a single systematic parameter,  $f_i$ , set to  $\pm 1\sigma$  from its nominal value and all other systematic parameters are set to their nominal value.
2. Perform a fit on the toy experiment with  $f_i$  fixed to its nominal value. Both the oscillation parameters and all the systematic parameters are initially set to their nominal value and are allowed to float with the exception of  $f_i$ . The other systematic parameters are allowed to float in order to obtain the best possible agreement between the fit and the toy experiment.
3. Steps 1. and 2. are then repeated for all  $i$  systematic parameters of interest. Both the  $+1\sigma$  and  $-1\sigma$  variations should be performed for each systematic parameter since the effect on the oscillation parameters is typically not symmetric.

If  $f_i$  were allowed to float it would be expected that the fit would be able to recover the same oscillation parameters used in the toy experiment since the same MC was used for the toy experiment and the fit. By fixing  $f_i$  to its nominal value in the fit, the fit is forced to make a mistake. This results in the fit remapping the changes in  $f_i$  to the oscillation parameters (and the other systematic parameters).

This study was performed for the  $\nu_e$  appearance and disappearance channels using oscillation parameters  $\sin^2 2\theta_{\mu e} = 0.003$ ,  $\Delta m_{41}^2 = 1.32 \text{ eV}^2$  and  $\sin^2 2\theta_{ee} = 0.4$ ,  $\Delta m_{41}^2 = 3 \text{ eV}^2$  respectively and includes the results from all uncorrelated systematic parameters. The results are shown in Figure 6.22 and Figure 6.23. For both oscillation parameters, the ratio of their value after performing the fit to their nominal value,  $\mathcal{R}$ , are shown after having varied  $f_i$  by  $\pm 1\sigma$ . The ratios shown in Figure 6.22 and Figure 6.23 are always  $\geq 1$  by construction since  $\mathcal{R}$  is defined as,

$$\mathcal{R} = \begin{cases} \frac{\zeta_{fit}}{\zeta_{nom}}, & \text{if } \zeta_{fit} > \zeta_{nom} \\ \frac{\zeta_{nom}}{\zeta_{fit}}, & \text{if } \zeta_{nom} > \zeta_{fit}, \end{cases} \quad (6.6)$$

where  $\zeta \in \{\sin^2 2\theta, \Delta m_{41}^2\}$  and the subscript *nom* and *fit* refer to the nominal value of the oscillation parameters and the values after performing the fit respectively. The arrows are colour coded such that black corresponds to the case where  $\zeta_{fit} > \zeta_{nom}$  and red corresponds to the case where  $\zeta_{nom} > \zeta_{fit}$ .

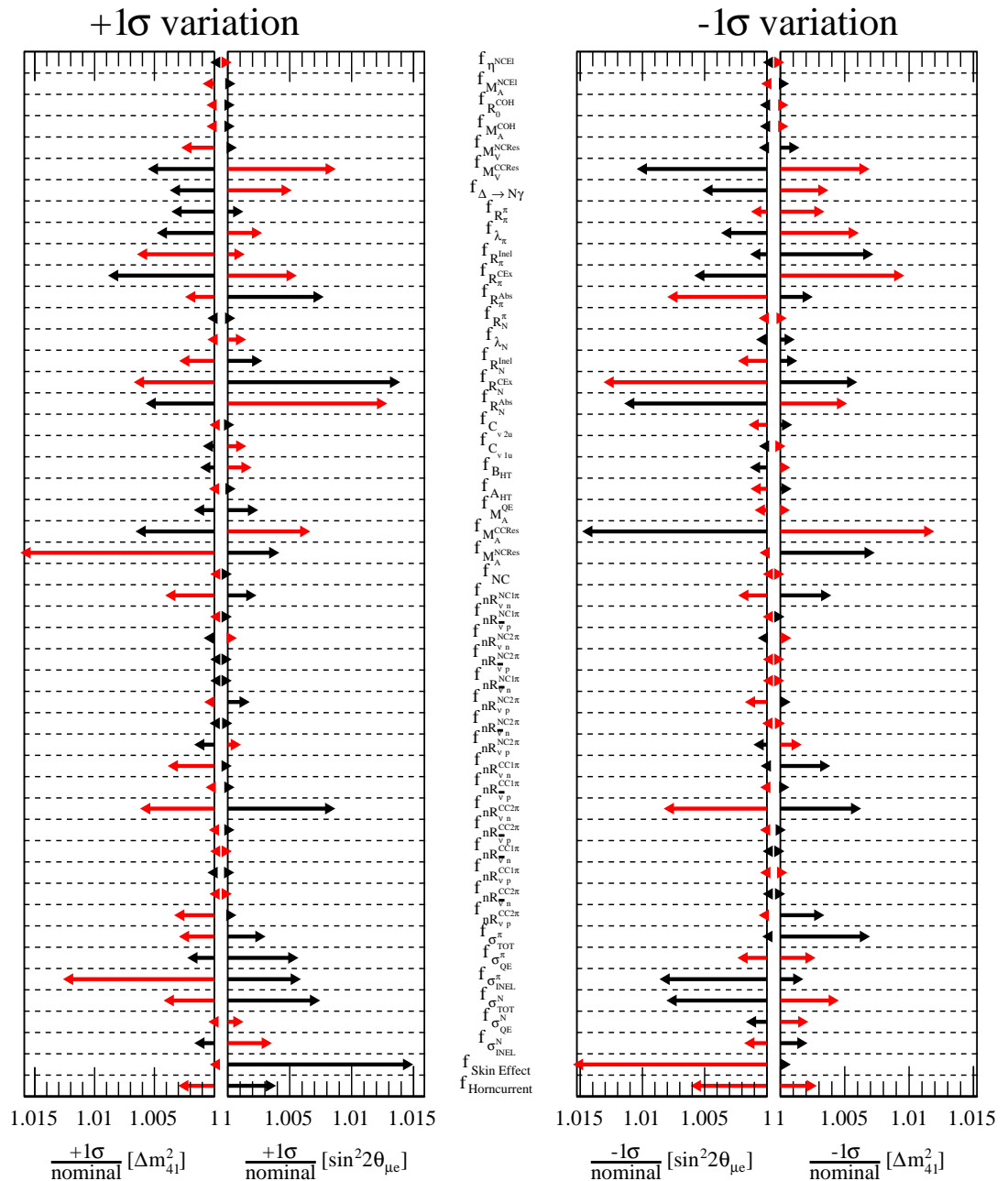
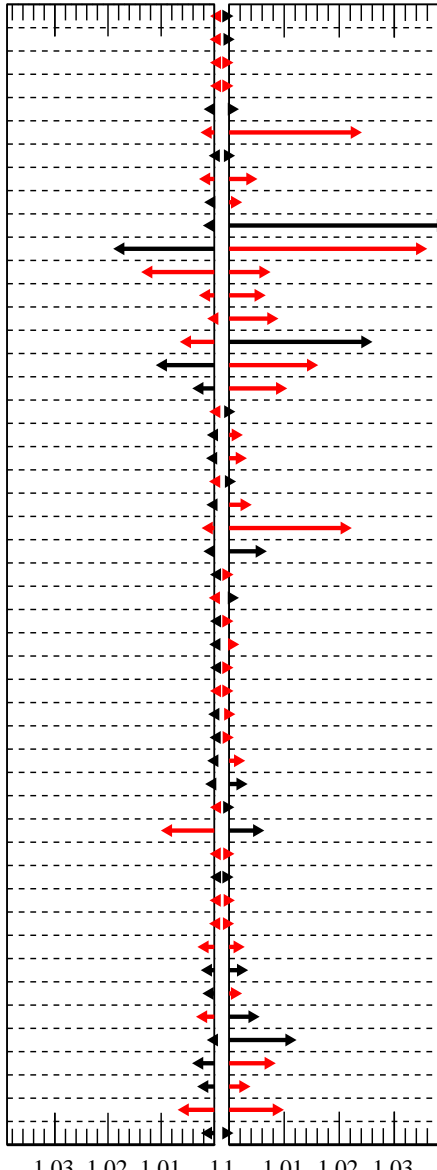


**Figure 6.22.:** The variation in the  $\nu_e$  appearance oscillation parameters due to varying a single systematic parameter at a time by  $\pm 1\sigma$ .

+1 $\sigma$  variation



$$\frac{\pm 1\sigma}{\text{nominal}} [\Delta m_{41}^2] \quad \frac{\pm 1\sigma}{\text{nominal}} [\sin^2 2\theta_{ee}]$$

-1 $\sigma$  variation

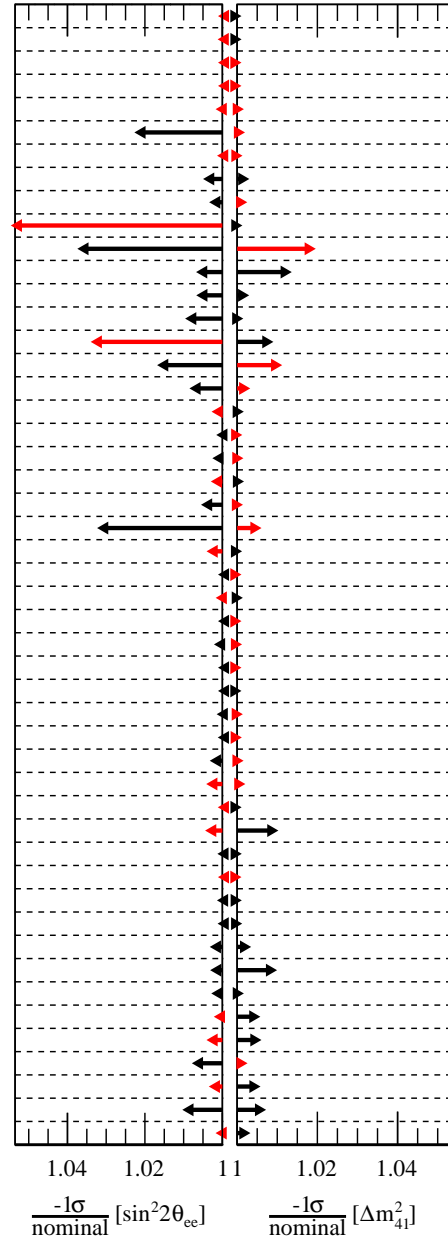


**Figure 6.23.:** The variation in the  $\nu_e$  disappearance oscillation parameters due to varying a single systematic parameter at a time by  $\pm 1\sigma$ .

The impact of the  $f_{M_V^{CCRes}}$ ,  $f_{M_A^{CCRes}}$ ,  $f_{R_N^{CEx}}$  and  $f_{\sigma_{INEL}^\pi}$  parameters on the  $\nu_e$  appearance exclusion sensitivities are shown in Figure 6.24. The parameters were applied one at a time and chosen as some that showed the largest variations in Figure 6.22, ensuring at least one parameter is from each systematic subgroup. Similarly, the  $f_{M_V^{CCRes}}$ ,  $f_{M_A^{CCRes}}$ ,  $f_{R_\pi^{CEx}}$  and  $f_{expskin}$  parameters were used for the  $\nu_e$  disappearance channel and the results are shown in Figure 6.25. Both the statistical-only contour and the one including all the flux and interaction systematics are shown for comparison. It should be noted that single parameters may contribute significantly to the total reduction in sensitivity from the inclusion of all systematic parameters. Additionally, the systematics considered were chosen based on a study which used an injected signal meaning the large impact seen there may not be directly mapped to an exclusion contour which gives a possible reason for the relatively minor impact seen due to  $f_{\sigma_{INEL}^\pi}$  and  $f_{R_\pi^{CEx}}$ .

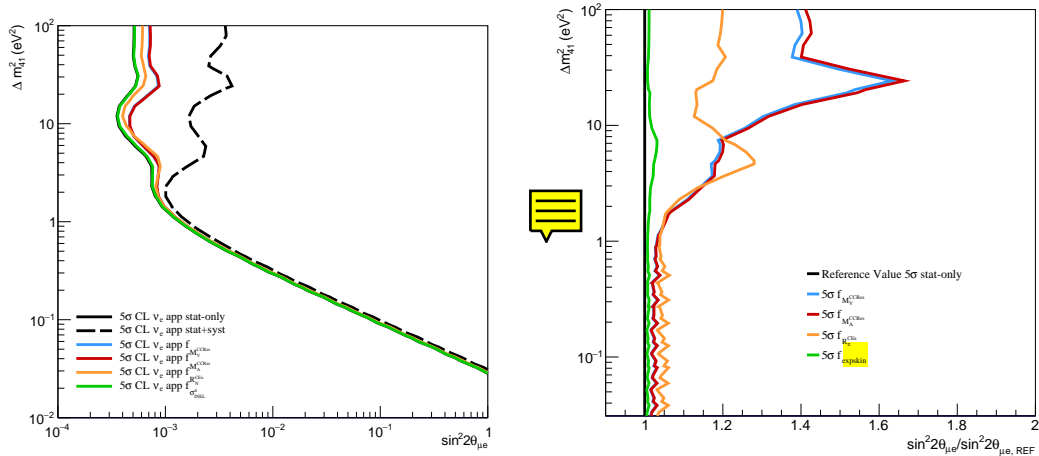


**Figure 6.24.:** Left:  $\nu_e$  appearance exclusion contours with the inclusion of a single systematic parameter at a time. The systematic parameters considered are  $f_{M_V^{CCRes}}$ ,  $f_{M_A^{CCRes}}$ ,  $f_{R_N^{CEx}}$  and  $f_{\sigma_{INEL}^\pi}$ . Right: The ratio of the exclusion contours with the inclusion of a single systematic parameter to the statistical-only contour.

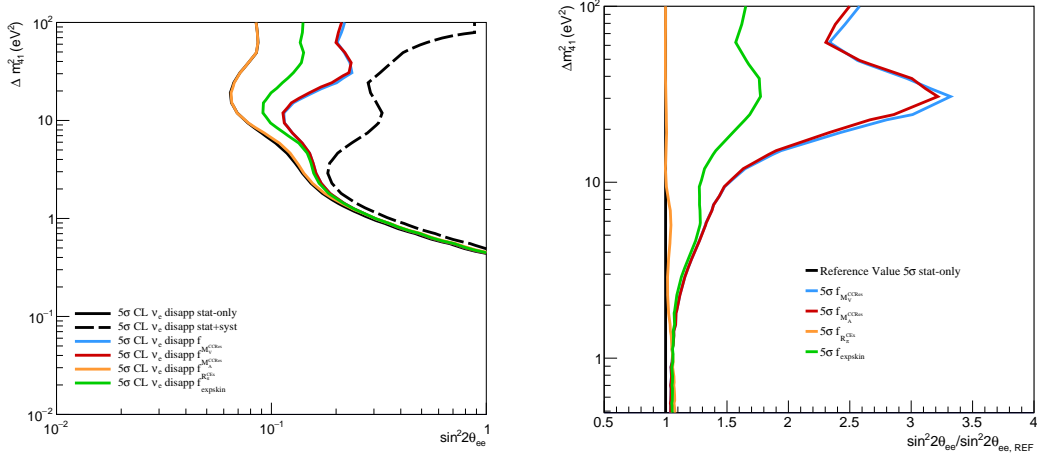


**Figure 6.25.:** Left:  $\nu_e$  disappearance exclusion contours with the inclusion of a single systematic parameter at a time. The systematic parameters considered are  $f_{M_V^{CCR_{Res}}}$ ,  $f_{M_A^{CCR_{Res}}}$ ,  $f_{R_\pi^{CEx}}$  and  $f_{expskin}$ . Right: The ratio of the exclusion contours with the inclusion of a single systematic parameter to the statistical-only contour.

To further assess the reduction in sensitivities due to specific parameters or parameter groups, allowed regions have been constructed using the same injected signal as was used for the study done to identify the dominant systematics. Figure 6.26 shows the change in allowed regions from applying the same set of single systematic parameters for both the  $\nu_e$  appearance and disappearance channels as was done for the exclusion contours. Both the statistical-only contour and the one including flux and interaction systematics have again been included for comparison.

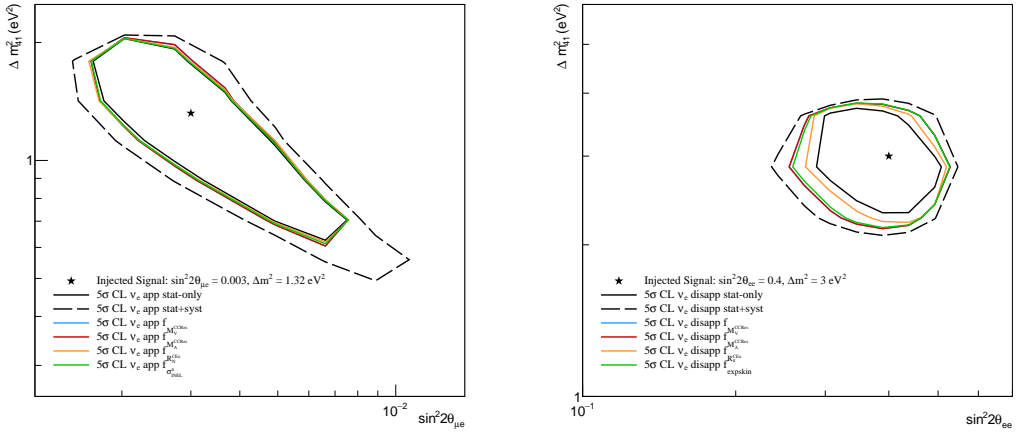


**Figure 6.26.:**  $\nu_e$  appearance and disappearance allowed regions with the inclusion of a single systematic parameter at a time. The injected signal for  $\nu_e$  appearance is  $\sin^2 2\theta_{\mu e} = 0.003$ ,  $\Delta m_{41}^2 = 1.32$  eV $^2$  whereas the injected signal for  $\nu_e$  disappearance is  $\sin^2 2\theta_{ee} = 0.4$ ,  $\Delta m_{41}^2 = 3$  eV $^2$ . The systematic parameters considered for the  $\nu_e$  appearance channel are  $f_{M_V^{CCRes}}$ ,  $f_{M_A^{CCRes}}$ ,  $f_{R_N^{CEx}}$  and  $f_{\sigma_{INEL}^\pi}$  (Left) and the systematic parameters considered for the  $\nu_e$  disappearance channel are  $f_{M_V^{CCRes}}$ ,  $f_{M_A^{CCRes}}$ ,  $f_{R_\pi^{CEx}}$  and  $f_{expskin}$  (Right).

In addition to the exclusion regions, the allowed region with the inclusion of a single parameter are shown along with the corresponding contour from the entire associated set of systematic parameters for the  $\nu_e$  appearance and  $\nu_e$  disappearance channels in Figure 6.27 and Figure 6.28 respectively. Unlike for the exclusion contours, the  $f_{\sigma_{INEL}^\pi}$  and  $f_{R_\pi^{CEx}}$  parameters don't show the smallest change across the entire parameter space. The change is comparable to the other parameters for at least some of the parameter space which is more consistent with the size of the impact seen in the initial study.

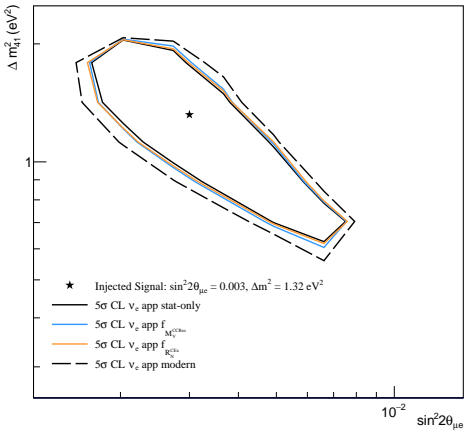
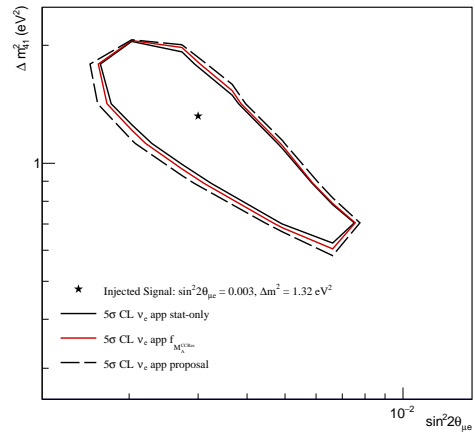
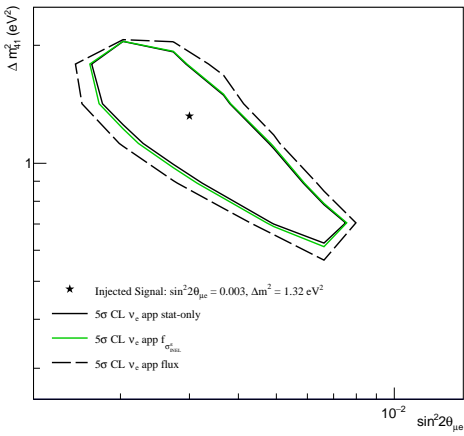


**Figure 6.27.:** The  $\nu_e$  appearance allowed region from an injected signal at  $\sin^2 2\theta_{\mu e} = 0.003$ ,  $\Delta m^2_{41} = 1.32 \text{ eV}^2$  showing the impact of the  $f_{\sigma_{INEL}^\pi}$  compared to the total flux systematics (Top Left), the impact of  $f_{M_A^{CCRes}}$  compared to the total proposal systematics (Top Right) and the impact of both  $f_{M_V^{CCRes}}$  and  $f_{R_\pi^{CEEx}}$  on the total modern systematics (Bottom Left). The stat only and total flux + interaction contours have been included for comparison.

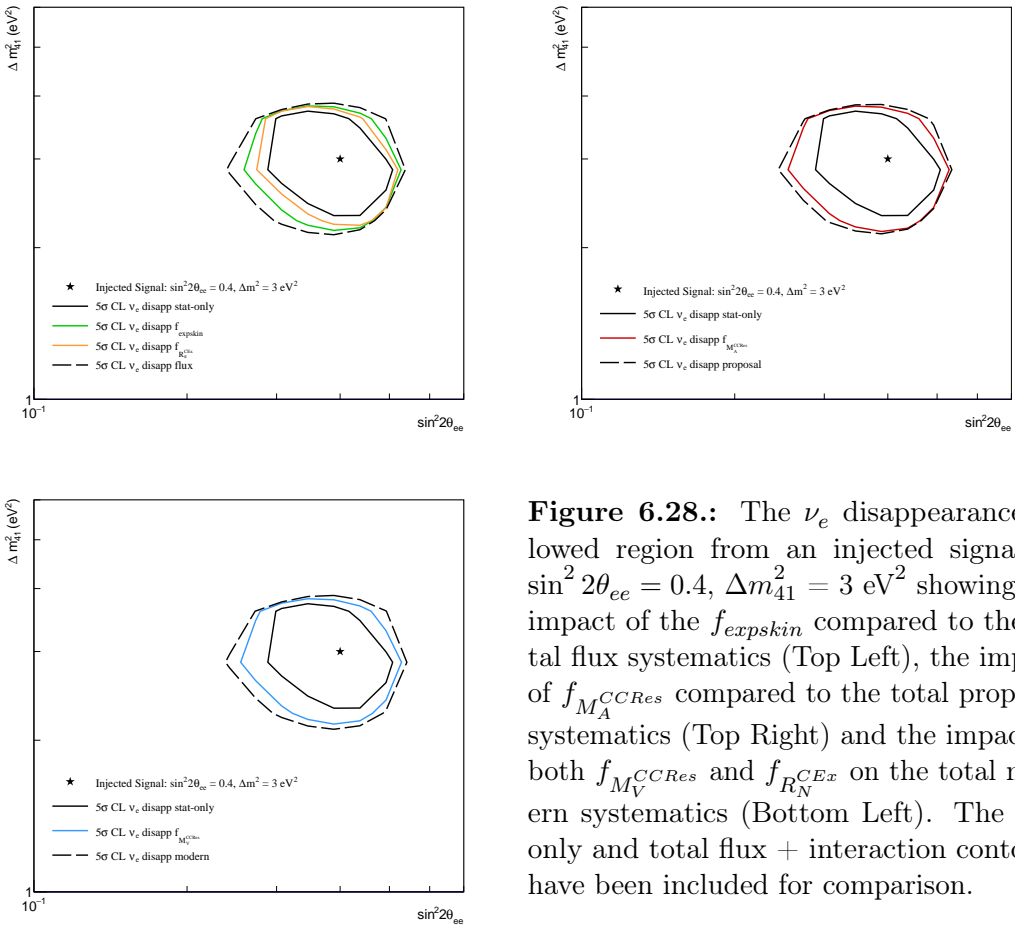


**Figure 6.28.:** The  $\nu_e$  disappearance allowed region from an injected signal at  $\sin^2 2\theta_{ee} = 0.4$ ,  $\Delta m_{41}^2 = 3 \text{ eV}^2$  showing the impact of the  $f_{expskin}$  compared to the total flux systematics (Top Left), the impact of  $f_{M_A^{CCRes}}$  compared to the total proposal systematics (Top Right) and the impact of both  $f_{M_V^{CCRes}}$  and  $f_{R_N^{CEx}}$  on the total modern systematics (Bottom Left). The stat only and total flux + interaction contours have been included for comparison.

### 6.5.2.3. Future Constraints on Systematic Uncertainties

To further constrain some of the dominant systematic uncertainties in future work a number of options are being considered, which include updated hadron production runs, improvements to GENIE fits and using SBND data.

The NA61/SHINE experiment has already collected data from proton interactions on carbon, beryllium and aluminium with proton momenta of 60 GeV/c and 120 GeV/c (only 60 GeV/c protons were used for the aluminium target) [166]. New runs are being considered using a BNB-like target to update the currently available dataset.

As GENIE continues to be developed, further improvements to interaction models and systematic uncertainty constraints are expected. These may arise from the release of new datasets which will allow for new fits to be performed with inclusion of additional or updated data points. Another possibility is for models to be tuned against exclusive data channels as well as joint exclusive channels in addition to inclusive ones [167].

Finally, SBND data may also be used to help constrain systematics. This may be achieved, for example, by measuring neutrino-argon interactions with unprecedented statistics or by utilising the *PRISM* concept. The large statistics will allow for the measurement of many different exclusive final state topologies, some of which remain largely unmeasured within argon. An example is the  $\nu e^- \rightarrow \nu e^-$  elastic scattering channel. The cross-section of this interaction is well known and the topological signature is easily identifiable in a LArTPC. For  $6.6 \times 10^{20}$  POT, SBND expects to observe  $\sim 400$  of these events which is sufficient to make a neutrino flux measurement [13] [168].

Due to the close proximity of SBND to the neutrino beam source, it is possible to exploit the PRISM effect by considering neutrino interactions as a function of their off-axis angle. As the off-axis angle increases, the peak of the energy spectrum decreases and the overall spectrum becomes narrower. SBND-PRISM may, therefore, measure neutrino interactions at different off-axis angles and deduce the energy dependence on the cross-section over a range of  $\sim 200$  MeV. The narrowing of the energy spectrum at larger off-axis angles may also allow

certain effects (typically non quasi-elastic) which start to dominate in the  $\gtrsim 1$  GeV region to be disentangled from other contributions.

### 6.5.3. Evaluation of Impact of Efficiency Uncertainties

Efficiency systematics are not implemented in the *standard* analyses because there currently is not a good handle on how to correctly quantify them. A rigorous scheme akin to those described in Section 5.4.1 and Section 5.4.2 does not exist, so instead in-house methods have been developed which are described below.

The current scheme for implementing efficiency (detector) systematics into a fit is by use of a covariance matrix where each element is defined by the systematics outlined in Table 6.8. This allows for the lack of associated event reweighting schemes to be bypassed whilst still being able to capture varying uncertainties being applied to different kinematic ranges, detectors and signal or background processes in each sample. In general, it is assumed that a covariance matrix  $\mathcal{M}_{ij}$  is comprised of both correlated and uncorrelated uncertainties such that

$$\mathcal{M}_{ij} = \mathcal{M}_{ij}^{corr} + \mathcal{M}_{ij}^{uncorr}, \quad (6.7)$$

where  $\mathcal{M}_{ij}^{corr}$  is the correlated component and  $\mathcal{M}_{ij}^{uncorr}$  is the uncorrelated component. For correlated uncertainties,

$$\mathcal{M}_{ij}^{corr} = \begin{cases} \sigma_i^2, & i = j \\ C_{ij}\sigma_i\sigma_j, & i \neq j, \end{cases} \quad (6.8)$$

where  $C_{ij}$  represents the correlation between the off-diagonal elements and  $\sigma_{i,j}$  is some percentage error associated with each systematic. In the case of fully correlated uncertainties,  $C_{ij}$  reduces to one and  $\sigma_i = \sigma_j$ . For uncorrelated uncertainties,

$$\mathcal{M}_{ij}^{uncorr} = \begin{cases} \sigma_i'^2, & i = j \\ 0, & i \neq j, \end{cases} \quad (6.9)$$

with  $\sigma'_i$  again being a percentage error. If any correlated errors are assumed to be fully correlated,  $\mathcal{M}_{ij}$  will then have diagonal elements given by  $\sigma_i^2 + \sigma'^2_i$  and off-diagonal elements given by  $\sigma_i^2$ .

Applies to					
Systematic	Beam	Detector	Sample	Mode	Reco. energy bin edges
$f_0 - f_7$	FHC	SBND	$\nu_\mu$ CC-like	signal/ $\nu_\mu$ CC	{0, 0.2, 0.4, 0.6, 0.8, 1.0, 1.5, 2.0, $\infty$ }
$f_8 - f_{13}$	FHC	SBND	$\nu_\mu$ CC-like	bkg/NC	{0, 0.2, 0.4, 0.6, 0.8, 1.0, $\infty$ }
$f_{14}$	FHC	SBND	$\nu_\mu$ CC-like	bkg/Dirt	{0, $\infty$ }
$f_{15}$	FHC	SBND	$\nu_\mu$ CC-like	bkg/Cosmics	{0, $\infty$ }
$f_{16} - f_{24}$	FHC	SBND	$\nu_e$ CC-like	signal/ $\nu_e$ CC	{0, 0.2, 0.4, 0.6, 0.8, 1.0, 1.5, 2.0, 3.0, $\infty$ }
$f_{25} - f_{33}$	FHC	SBND	$\nu_e$ CC-like	bkg/ $\nu_\mu$ CC	{0, 0.2, 0.4, 0.6, 0.8, 1.0, 1.5, 2.0, 3.0, $\infty$ }
$f_{34} - f_{42}$	FHC	SBND	$\nu_e$ CC-like	bkg/NC1 $\gamma$	{0, 0.2, 0.4, 0.6, 0.8, 1.0, 1.5, 2.0, 3.0, $\infty$ }
$f_{43} - f_{51}$	FHC	SBND	$\nu_e$ CC-like	bkg/NC1 $\pi^0$	{0, 0.2, 0.4, 0.6, 0.8, 1.0, 1.5, 2.0, 3.0, $\infty$ }
$f_{52} - f_{60}$	FHC	SBND	$\nu_e$ CC-like	bkg/NCother	{0, 0.2, 0.4, 0.6, 0.8, 1.0, 1.5, 2.0, 3.0, $\infty$ }
$f_{61} - f_{66}$	FHC	SBND	$\nu_e$ CC-like	bkg/Dirt	{0, 0.2, 0.4, 0.6, 0.8, 1.0, $\infty$ }
$f_{67} - f_{72}$	FHC	SBND	$\nu_e$ CC-like	bkg/Cosmics	{0, 0.2, 0.4, 0.6, 0.8, 1.0, $\infty$ }
$f_{73} - f_{145}$	As above, but for $\mu$ B				
$f_{146} - f_{218}$	As above, but for ICARUS				

**Table 6.8.:** The binning scheme used to produce the efficiency uncertainty covariance matrices.

All future discussion involving correlated uncertainties should from here on be assumed to be fully correlated even if not explicitly stated. A set of example covariance matrices are shown in Figure 6.29. The top left plot corresponds to a 10% correlated error only. The remaining three plots all have a correlated error of 2%, with some varying amounts of an uncorrelated error associated with each systematic.

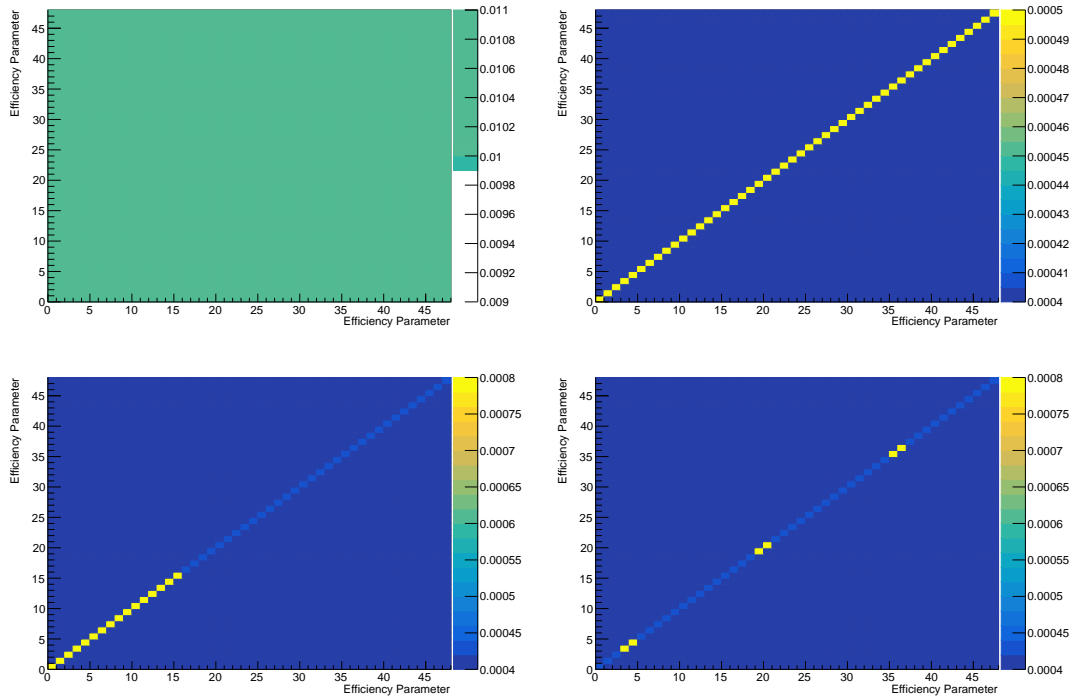


**Figure 6.29.:** Covariance matrices produced to investigate the effects of efficiency systematics for the  $\nu_\mu$  disappearance channel. Top left: A 10% fully correlated error only. Top right: A 2% fully correlated error with an additional 1% uncorrelated error across all bins. Bottom left: A 2% fully correlated error with an additional 2% uncorrelated error for all SBND bins and a 0.5% uncorrelated error for all MicroBooNE and ICARUS bins. Bottom right: A 2% fully correlated error with an additional 2% uncorrelated error for the peak energy bins (0.6 - 1.0 GeV) in each detector and a 0.5% uncorrelated error for all other bins.

In order to get a measure of the possible impact of efficiency systematics on the sensitivity, various covariance matrices were produced to investigate the impact of:

1. Fully correlated errors only.
2. Various combinations of uncorrelated errors with a fixed correlated error.
3. Uncorrelated errors only applied to a single detector at a time.
4. A poorly constrained uncorrelated error on a single set of bins.

Unless otherwise stated, the uncertainties from efficiency covariance matrices are applied in addition to the flux and interaction systematics.

The study on the impact of different efficiency uncertainties was first done for the  $\nu_\mu$  disappearance channel because it was expected that there would be a greater impact than for either of the  $\nu_e$  channels. This is because the typical event rate for the  $\nu_\mu$  channel is several orders of magnitude greater than that of  $\nu_e$  meaning that the  $\nu_\mu$  channel is systematics limited whereas the  $\nu_e$  channels may tend towards being statistics limited. Once a contour becomes statistics limited, continuing to apply additional systematic uncertainties will begin to have diminishing impacts.

Sensitivities including efficiency uncertainties for the  $\nu_\mu$  disappearance channel are shown alongside the other figures in Appendix D. The impact of the efficiency uncertainties on both  $\nu_e$  channels is discussed below.

### Impact of Efficiency Systematics on $\nu_e$ Appearance Sensitivities

In order to gauge the contribution of some typical efficiency uncertainty, Figure 6.30 shows the impact on the  $\nu_e$  appearance sensitivity from individual sets of systematic parameters as in Figure 6.20 but with the additional case where only a 2% correlated + 2% uncorrelated efficiency uncertainty has been applied. The impact of the efficiency uncertainty is comparable to the proposal interaction systematics having the smallest contribution to the sensitivity.

The reduction in sensitivity from applying a 10% correlated uncertainty and a 2% correlated + 2% uncorrelated uncertainty on top of the standard flux and interaction systematics are shown in Figure 6.31. Since a correlated error of 10% has a close to negligible impact, the results from applying correlated uncertainties less than 10% as was done for the  $\nu_\mu$  channel have been omitted. Similarly, applying smaller uncorrelated uncertainties would again only have a minor impact so these have also been omitted.

Figure 6.32 assess the impact of a 2% uncorrelated uncertainty which is applied to each detector one at a time. Applying the uncertainty to MicroBooNE and ICARUS appears to have a negligible impact across all  $\Delta m_{41}^2$  values. SBND has a

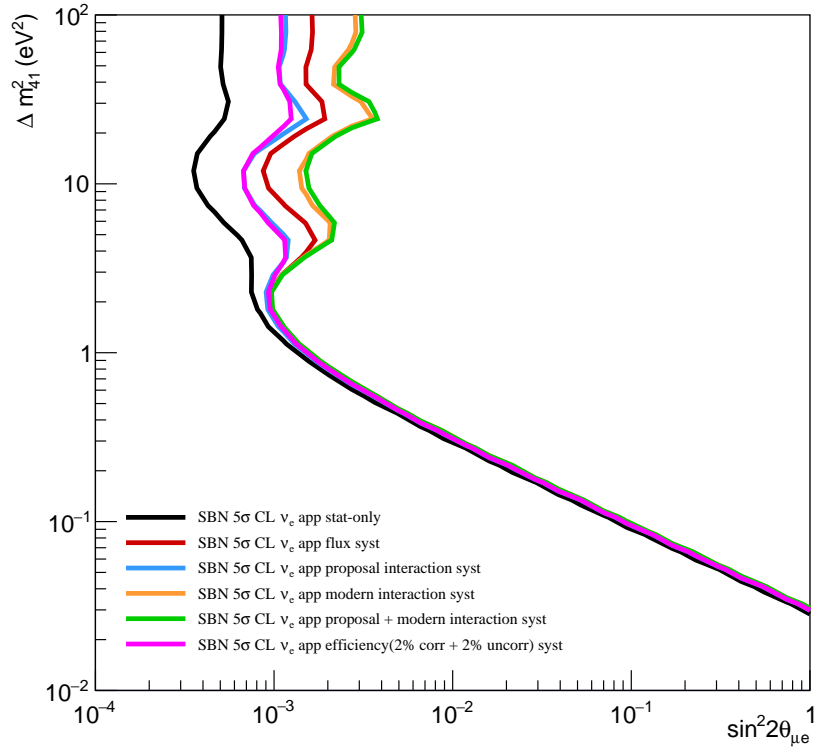


**Figure 6.30.:** The reduction in the  $\nu_e$  appearance sensitivity from the stat-only contour when including each set of systematic parameters in the fits. Similar to Figure 6.20 but with the addition of a 2% correlated and 2% uncorrelated efficiency uncertainty.

relatively small impact at high  $\Delta m_{41}^2$  values which resembles the loss in sensitivity that was seen by applying a 2% correlated + 2% uncorrelated uncertainty across all bins in Figure 6.31. It follows that any reduction in sensitivity due to efficiency uncertainties is driven by SBND. Since SBND is most sensitive to large  $\Delta m_{41}^2$  values and has higher statistics than MicroBooNE and ICARUS, the results are consistent with the idea that  $\nu_e$  channel is close to becoming statistics limited.

Instead of exploring the impact from fully correlated uncertainties or a constant uncorrelated uncertainty across all bins in a detector, Figure 6.33 considers the case where a single set of bins are poorly constrained. The sets of bins considered are,

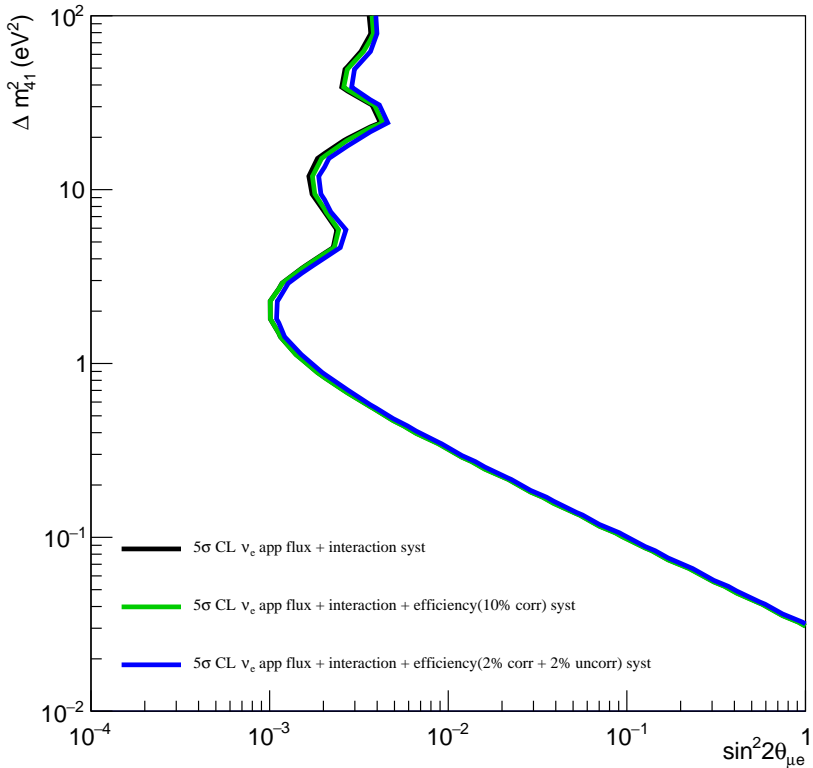


**Figure 6.31.:** The impact on the  $\nu_e$  appearance exclusion sensitivity by applying a 10% fully correlated efficiency uncertainty to all bins and by applying 2% fully correlated + 2% uncorrelated efficiency uncertainty.

- CC signal below the peak energy ( $< 0.6$  GeV),
- CC signal at the peak energy ( $[0.6 - 1.0]$  GeV),
- CC signal above the peak energy ( $> 1.0$  GeV),
- Background.

In each case, the uncorrelated uncertainty for the bins of interest are set to 2% in each of the SBN detectors, whilst the rest of the uncorrelated uncertainties are set to 0.5% and the fully correlated uncertainty is fixed at 2%. The background and low energy bins have the smallest impact with almost no visible difference whereas

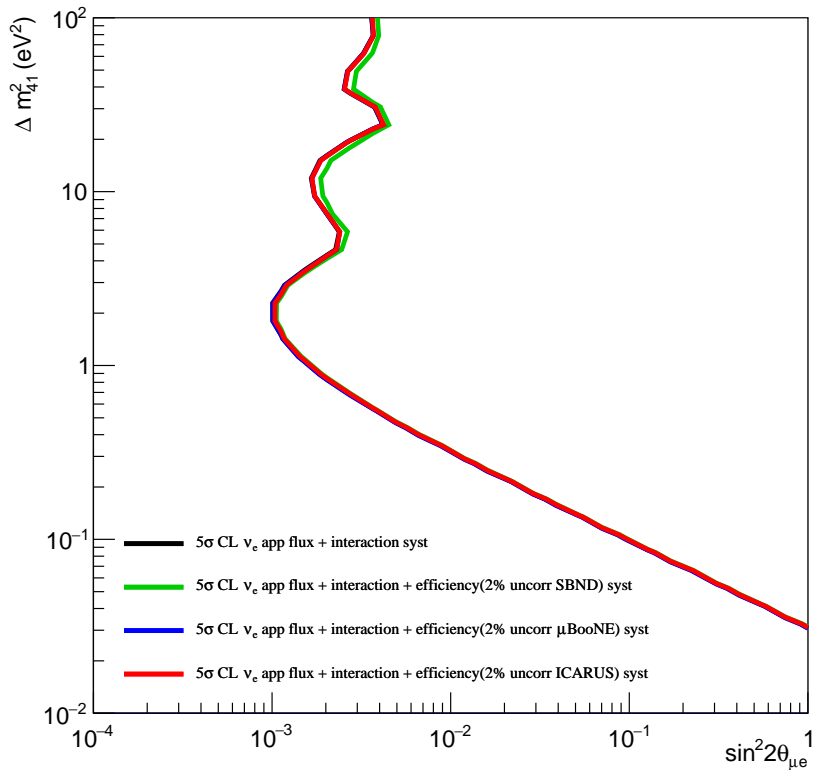


**Figure 6.32.:** The impact on the  $\nu_e$  appearance exclusion sensitivity by applying a 2% uncorrelated efficiency uncertainty to a single one of the three SBN detectors.

the peak and high energy bins do show some small reduction in the sensitivity at  $\Delta m_{41}^2$  greater than 1 eV<sup>2</sup>.

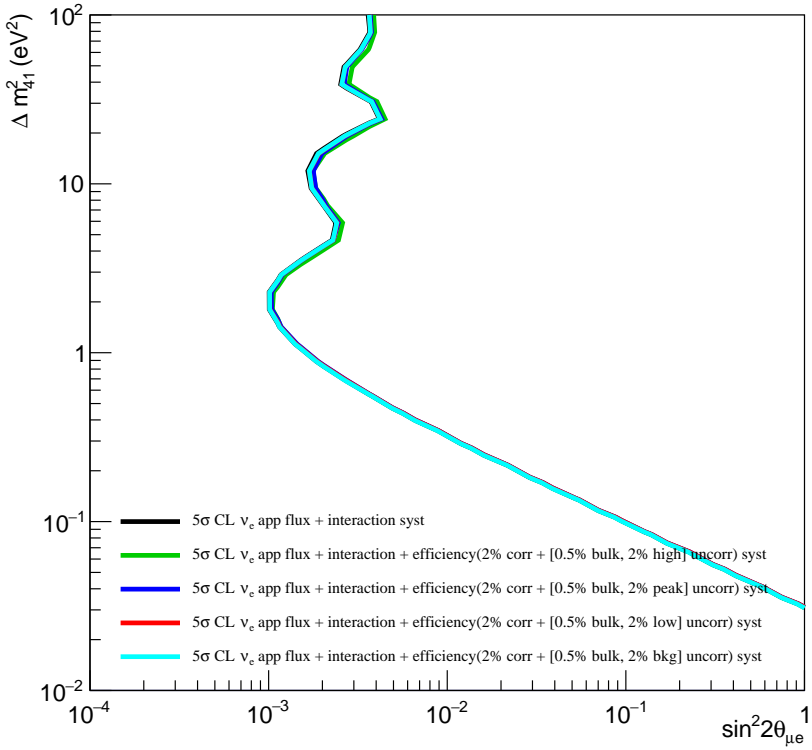


**Figure 6.33.:** The impact on the  $\nu_e$  appearance exclusion sensitivity by applying a 2% fully correlated efficiency uncertainty for each of the SBN detectors and a 0.5% uncorrelated uncertainty for all but a single set of bins where the uncorrelated uncertainty is set to 2%. The 'peak' energy bins are defined as those covering an energy range of [0.6, 1.0] GeV. The 'high' and 'low' energy bins are defined as those covering energies above and below the peak energy respectively and the 'bkg' bins are all the bins associated with background events. The set of bins of interest are applied to each of the three detectors.

### Impact of Efficiency Systematics on $\nu_e$ Disappearance Sensitivities

As was done for  $\nu_e$  appearance, Figure 6.34 shows the impact from  $\nu_e$  disappearance sensitivity from individual sets of systematic parameters as in Figure 6.21 but with the addition of a 2% correlated + 2% uncorrelated efficiency uncertainty. The efficiency uncertainty shows the smallest reduction in sensitivity across all ranges of  $\Delta m_{41}^2 \gtrsim 3$  and is comparable to the other systematic sets at  $\Delta m_{41}^2$  values below  $\sim 3$ .

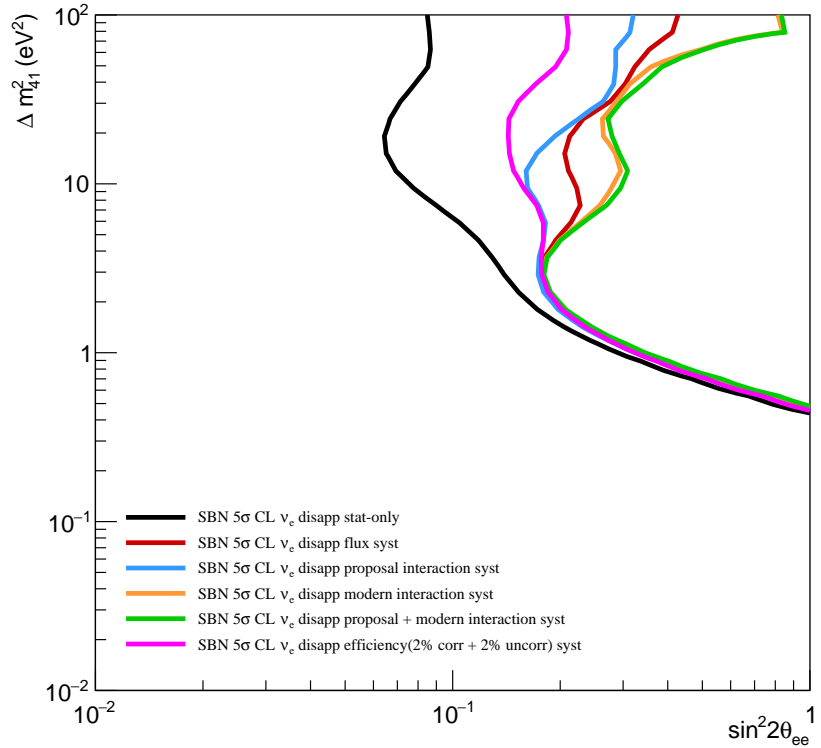


**Figure 6.34.:** The reduction in the  $\nu_e$  disappearance sensitivity from the stat-only contour when including each set of systematic parameters in the fits. Similar to Figure 6.21 but with the addition of a 2% correlated and 2% uncorrelated efficiency uncertainty.

Mirroring what was done for  $\nu_e$  appearance, Figure 6.35 shows the impact of applying a 10% correlated error and a 2% correlated + 2% uncorrelated error. The correlated error again has an almost negligible impact and whilst the uncorrelated error has a larger impact it is still relatively small.

A 2% uncorrelated uncertainty is then applied to each detector one at a time. Figure 6.36 shows that majority of the reduction is due to SBND at above  $\Delta m^2_{41} \sim 10$  (where SBND is dominant). Both MicroBooNE and ICARUS only have a minimal impact for any  $\Delta m^2_{41}$  values. This is consistent with what is shown in Figure 6.35.

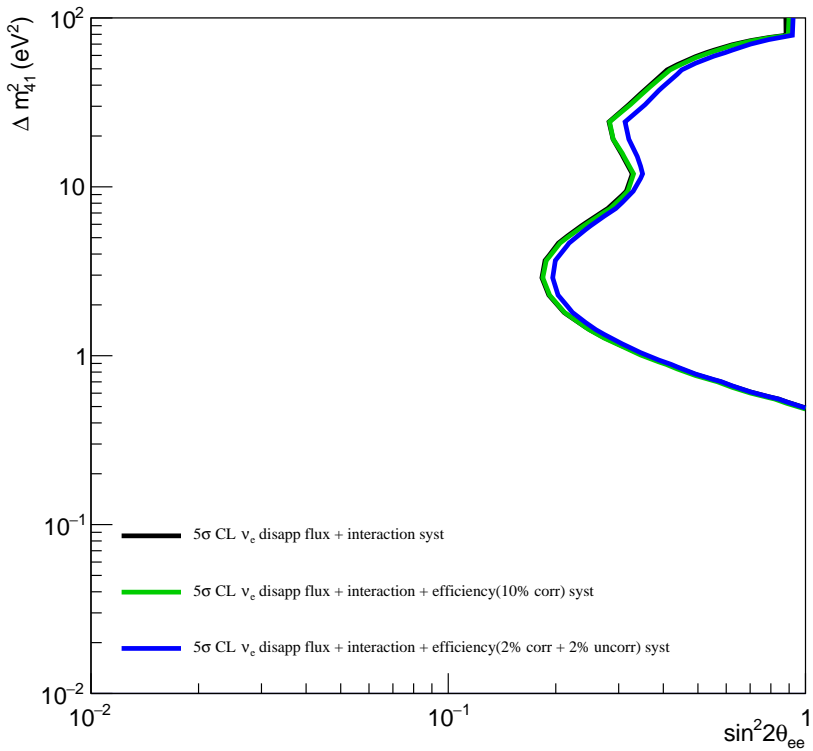


**Figure 6.35.:** The impact on the  $\nu_e$  disappearance exclusion sensitivity by applying a 10% fully correlated efficiency uncertainty to all bins and by applying 2% fully correlated + 2% uncorrelated efficiency uncertainty.

Finally, the impact of having a set of poorly constrained bins is investigated in Figure 6.37. Similar to the  $\nu_e$  appearance case, the low energy and background bins only have a minimal impact, whereas the peak and high energy bins show a slightly larger impact but are far less prominent than for the  $\nu_\mu$  channel.

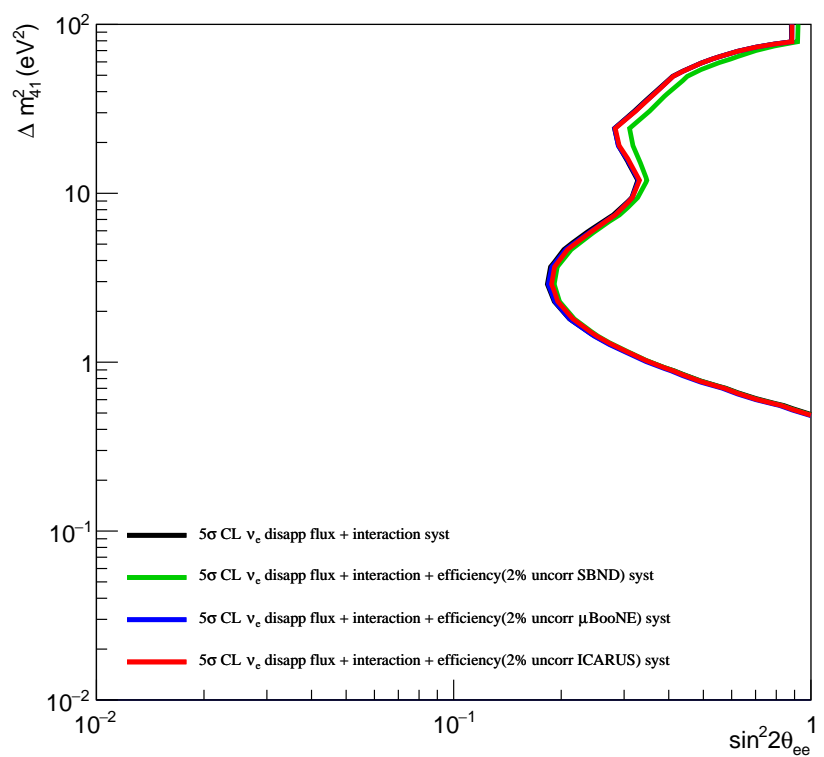


**Figure 6.36.:** The impact on the  $\nu_e$  disappearance exclusion sensitivity by applying a 2% uncorrelated efficiency uncertainty to a single one of the three SBN detectors.

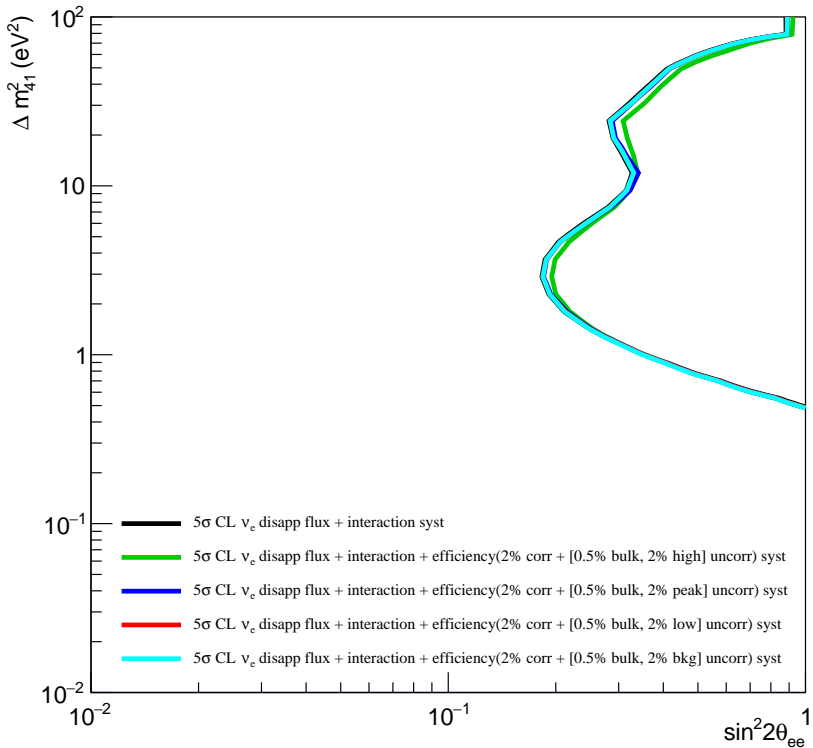


**Figure 6.37.:** The impact on the  $\nu_e$  disappearance exclusion sensitivity by applying a 2% fully correlated efficiency uncertainty for each of the SBN detectors and a 0.5% uncorrelated uncertainty for all but a single set of bins where the uncorrelated uncertainty is set to 2%. The 'peak' energy bins are defined as those covering an energy range of  $[0.6, 1.0]$  GeV. The 'high' and 'low' energy bins are defined as those covering energies above and below the peak energy respectively and the 'bkg' bins are all the bins associated with background events. The set of bins of interest are applied to each of the three detectors.

### 6.5.4. Evaluation of Impact of Shower Energy Reconstruction Performance

The reconstructed neutrino energy used in the analyses shown so far is based on truth information where smearing has been applied to emulate a reconstructed value.

To better motivate the reconstructed energy used, the results from Chapter 4 have been used to tweak the true energy of the showering particles (electrons or photons) to emulate a reconstructed energy based on the reconstruction performance that has been observed with the currently available tools. Since only the reconstructed shower energy was actively investigated here, any non-showering particles continue to have their reconstructed energy estimated by directly smearing the true energy.

The two cases considered for estimating the reconstructed energy of the showering particle are,

- A flat negative bias of 20% is applied to the true energy for all particles.
- A flat negative bias is applied to the true energy along with an additional variation to emulate the resolution of the reconstruction performance. The magnitude of the bias and the width of the resolution are functions of the true energy. The resolution was emulated by randomly choosing a number based on a Gaussian with a given standard deviation. The three categories used depending on the true energy are shown in Table 6.9.

E [MeV]	Bias	$\sigma$
$E < 100$	40%	0.15
$100 \leq E < 200$	30%	0.125
$E > 200$	20%	0.1

**Table 6.9.:** The variable bias and resolution used to emulate reconstructed energy.

The simplistic approach of applying a flat 20% bias was motivated by the conservative results from Figure 4.6 which shows that the typical bias is of order 20%. The more involved process of applying an energy-dependent bias and resolution

are motivated by Figure 4.15. It can be seen that above energies of  $\sim 200$  MeV, the bias and standard deviation remain fairly constant, but at energies below this, the bias and resolution increase as the energy decreases.

The full  $\nu_e$  event selection as described in Section 5.3.2 was repeated but with the above changes applied. The events from these selections were then used to produce exclusion contours using the same systematic uncertainties as previously described. The overall event rate from the selections using the reconstructed information motivated by Chapter 4 is lower than the traditional method which relied on energy smearing.

The exclusion contours comparing the three selections are shown on the left of Figure 6.38 and Figure 6.39 for  $\nu_e$  appearance and disappearance respectively. The difference between the three exclusion contours is relatively minor and therefore the ratios of the contours to the contour from the original selection are shown on the right of their respective figures. Since the event rate is reduced in the updated selections, it is expected that the overall exclusion sensitivity would also be reduced. This is indeed the case for most values of  $\Delta m_{41}^2$  with only a couple of areas where the selection with the flat 20% bias appears to improve the sensitivity.

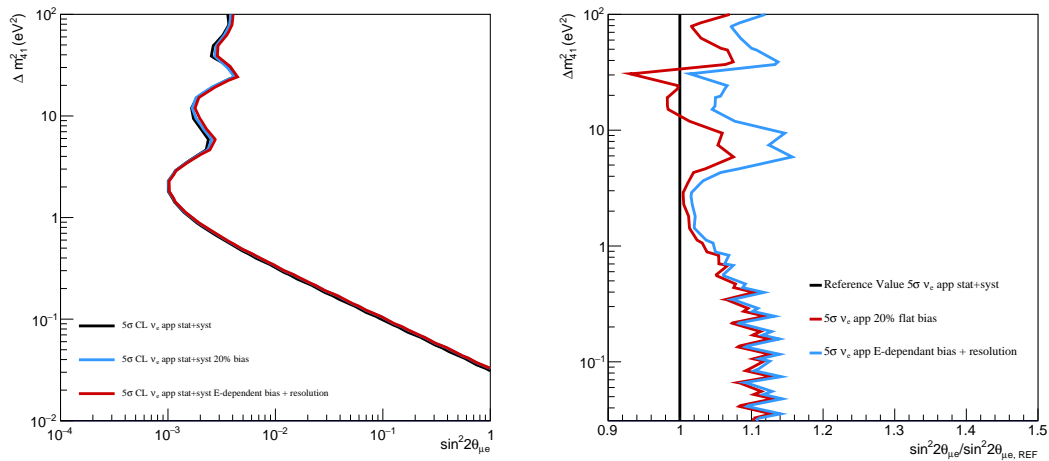


**Figure 6.38.:** Left:  $\nu_e$  appearance exclusion contours with flux and interaction uncertainties using events from the original selection and the ones motivated by results from EM shower reconstruction. Right: The ratio of the exclusion contours to the contour from the original selection.

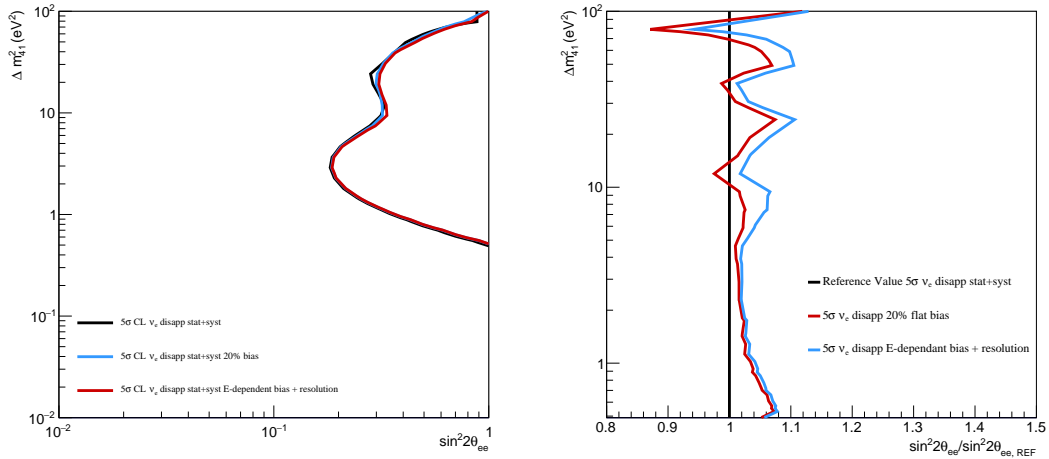


**Figure 6.39.:** Left:  $\nu_e$  disappearance exclusion contours with flux and interaction uncertainties using events from the original selection and the ones motivated by results from EM shower reconstruction. Right: The ratio of the exclusion contours to the contour from the original selection.

## 6.6. Summary of $\nu_e$ sensitivities within SBN

The sensitivities that have been produced for the SBN analysis were constructed using the VALOR fitting framework. The oscillation channels, namely  $\nu_e$  appearance and  $\nu_e$  disappearance, have been considered as stand-alone analyses as part of a  $\nu_e$  CC inclusive sample with both exclusion and allowed regions being investigated for both.

The flux and interaction systematics considered are initially provided by the MicroBooNE and GENIE reweight packages respectively before being processed internally by VALOR. The impact of some possible variations of efficiency systematics have been investigated by the use of covariance matrices within VALOR. It has been demonstrated that the inclusion of flux and interaction systematics significantly reduce the expected sensitivities, however, since they are already well constrained it is unlikely that their impact may be significantly decreased. The efficiency systematics are currently largely unconstrained, but the impact from various combinations of correlated and uncorrelated uncertainties have been shown

to only be relatively minor when included in addition to the flux and interaction systematics.

The exclusion sensitivities have been produced for each individual detector within SBN and all combinations of multi-detector fits including for the full SBN program (combining all three detectors). For both oscillation channels, the SBND detector dominates the sensitivity at large values of  $\Delta m_{41}^2$  ( $> 3 \text{ eV}^2$ ) and ICARUS dominates for small values of  $\Delta m_{41}^2$  ( $< 3 \text{ eV}^2$ ). One of the key features of the SBN program is the three-detector design. This is highlighted by the fact the best sensitivity can only be obtained by combining data from all three detectors.

The current SBN  $\nu_e$  appearance exclusion sensitivity supersedes that of KARMEN for essentially the entire parameters space, whereas the allowed region is much smaller than that obtained from LSND, but is nevertheless consistent with the result. The  $\nu_e$  disappearance exclusion sensitivity improves on that of ND280 for  $\Delta m_{41}^2$  values less than  $10 \text{ eV}^2$  and excludes much of the 90% allowed region from ND280. Most of the SBN allowed region is again still consistent with what was obtained by ND280.

It is expected that the SBN sensitivities may be further improved in the future by considering exclusive samples and not just the  $\nu_e$  CC inclusive one. Additionally, the possibility of producing joint fits which allow the mixing angles to be over-constrained would allow for an improvement in the sensitivity by profiling over one of the mixing angles. Finally, the POT of  $6.6 \times 10^{20}$  used for SBND and ICARUS and the POT of  $13.2 \times 10^{20}$  used for MicroBooNE are nominal values estimated for three years of data taking at the time of the SBN proposal. Current BNB projections estimate that the actual POT may be close to two or three times this nominal POT value. This increased event rate will also provide a noticeable improvement to the sensitivities.

# Chapter 7.

## Conclusion

The three SBN detectors are expected to provide a rich physics programme, with the main aims being to confirm or refute the possible existence of light sterile neutrinos, investigate neutrino-argon interactions and to develop large scale LArTPC technologies. Both the MicroBooNE and ICARUS detectors are currently taking data and the full SBN program is expected to come online in early 2024 once SBND is ready to also take data.

In this thesis, the development of two new EM shower reconstruction algorithms have been presented along with the necessary inputs and results from an oscillation analysis within SBN. The oscillation analysis focuses on the  $\nu_e$  appearance and disappearance channels and uses a modern set of inputs that better reflect the actual SBN program and the relevant physics than what was used in the SBN proposal.

Both the *Shower Num Electrons Energy tool* and the *Shower ESTAR Energy tool* have been newly developed to work within SBND. The *Shower Num Electrons Energy tool* uses a nominal recombination factor and the pre-existing calibration within SBND that allows for the conversion of charge in ADC units to the number of electrons. This approach is much more flexible to physics changes than the previous algorithm, the *Shower Linear Energy tool*, which relied on in-house calibration curves produced from MIP muons. The *Shower ESTAR Energy tool* combines the modified box recombination model with the ESTAR database provided by NIST. This allows for the creation of a lookup curve relating the

number of electrons to energy. In both tools, the charge associated with the hits is found and converted to energy using the respective method and the energy of all the hits is summed to find the total energy of the shower. All the reconstruction algorithms have been validated against truth information using events across the energy spectrum of the BNB. Assuming a  $1\sigma$  hit width when calculating the true energy of the hits, it has been demonstrated that the *Shower ESTAR Energy tool* shows minimal bias in the reconstructed energy. The *Shower Num Electrons Energy tool* systematically applies a larger energy to all of the hits and therefore tends to overestimate the reconstructed hit energy. When comparing with the true energy of the showering particle, all methods underestimate the energy due to hit reconstruction inefficiencies and the expectation of an overall bias. The bias observed by *Shower ESTAR Energy tool* is of the order  $-20\%$  and since the *Shower Num Electrons Energy tool* applies higher energies to the hits, the bias is a little smaller at around the  $-10\%$  level.

The oscillation analysis was initially performed in order to recreate the work done in the SBN proposal with an updated and better motivated set of inputs. The focus was on using a  $\nu_e$  CC inclusive sample as part of a (3+1) neutrino framework where both the  $\nu_e$  appearance and disappearance channels were considered independently. Exclusion contours as well as allowed regions from an injected signal at  $\sin^2 2\theta_{\mu e} = 0.003$ ,  $\Delta m_{41}^2 = 1.32 \text{ eV}^2$  for the appearance channel and  $\sin^2 2\theta_{ee} = 0.4$ ,  $\Delta m_{41}^2 = 3 \text{ eV}^2$  for the disappearance channel have been created at the  $5\sigma$  confidence level. The degradation in the sensitivities due to the inclusion of various efficiency uncertainties on top of the flux and interaction systematics have been investigated. It was shown that any uncorrelated efficiencies dominate the correlated component. On the whole, the impact from efficiency uncertainties on the sensitivity from either  $\nu_e$  channel is relatively minor with the most significant contribution occurring for large  $\Delta m_{41}^2$  values where SBND is dominant.

Going forward, the oscillation analysis will be performed using a fully reconstructed MC sample (once it has been sufficiently completed) instead of using the current pseudo-reconstruction. The option to produce joint fits is also currently being developed which should provide an improvement to the sensitivities. Finally, the

possibility of using exclusive samples instead of the CC-inclusive one are being investigated.



## Appendix A.

### Single Parameter Variations

The  $+3\sigma$  variations between the values obtained directly from the universes and those due to the response function in VALOR have been evaluated for all the systematic parameters that are modelled by response functions. The uncorrelated flux variations are shown in Figure A.1 whereas the proposal and modern interaction parameters are shown in Figure A.2 and Figure A.3 respectively. All the uncorrelated flux parameters show perfect agreement between the response functions and the universes. Some of the interaction parameters do show some minor differences, however, the differences are small ( $< 10$  events) which is negligible when compared with the total event rate.

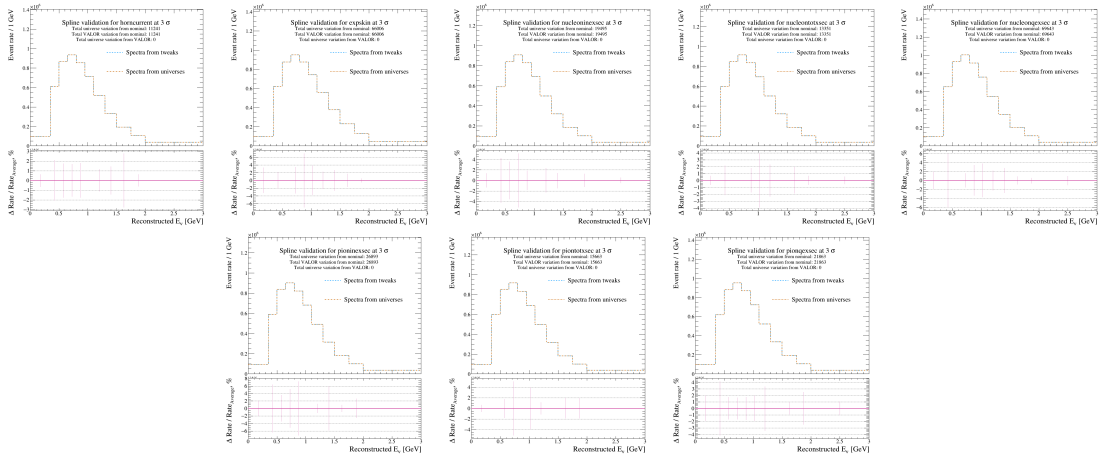


**Figure A.1.:** A comparison of the  $+3\sigma$  variations from the response functions used by VALOR and the universes for the complete set of uncorrelated flux systematic parameters.

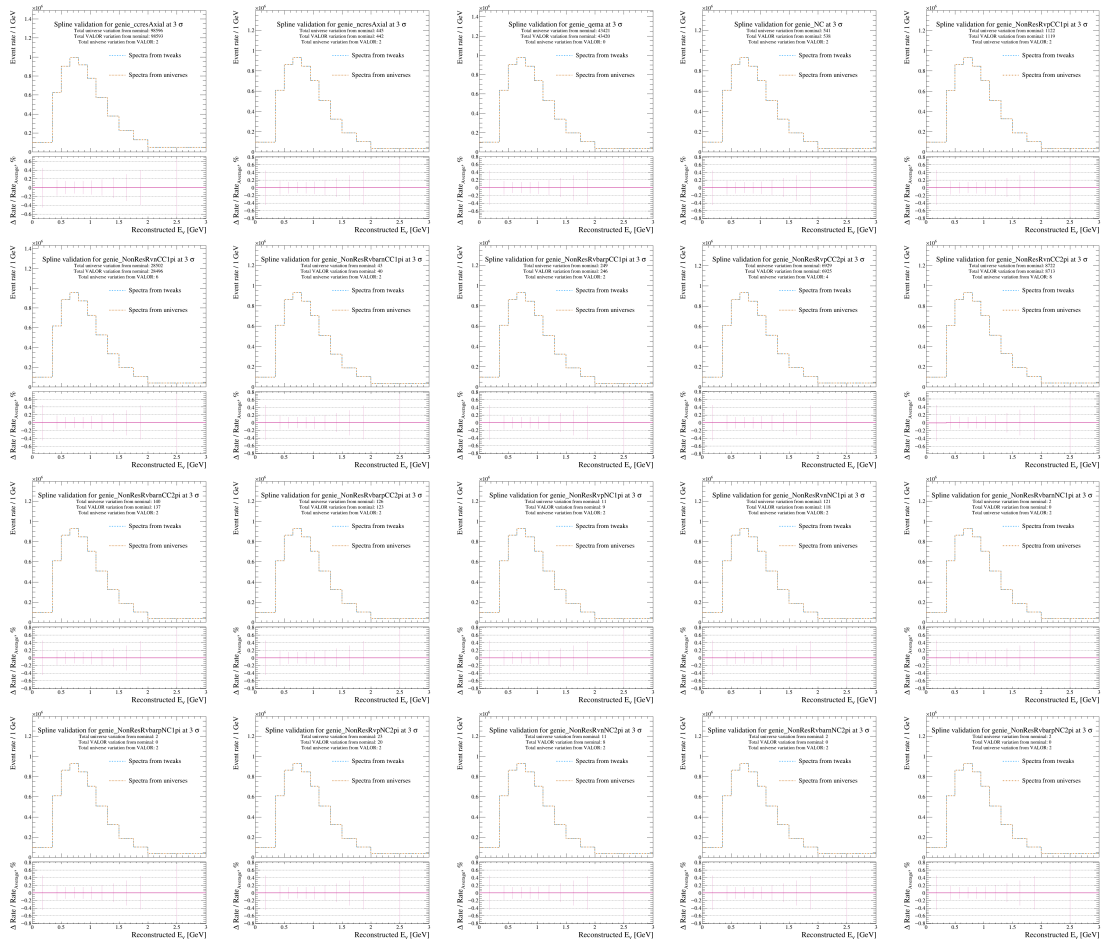


**Figure A.2.:** A comparison of the  $+3\sigma$  variations from the response functions used by VALOR and the universes for the complete set of proposal interaction systematic parameters.

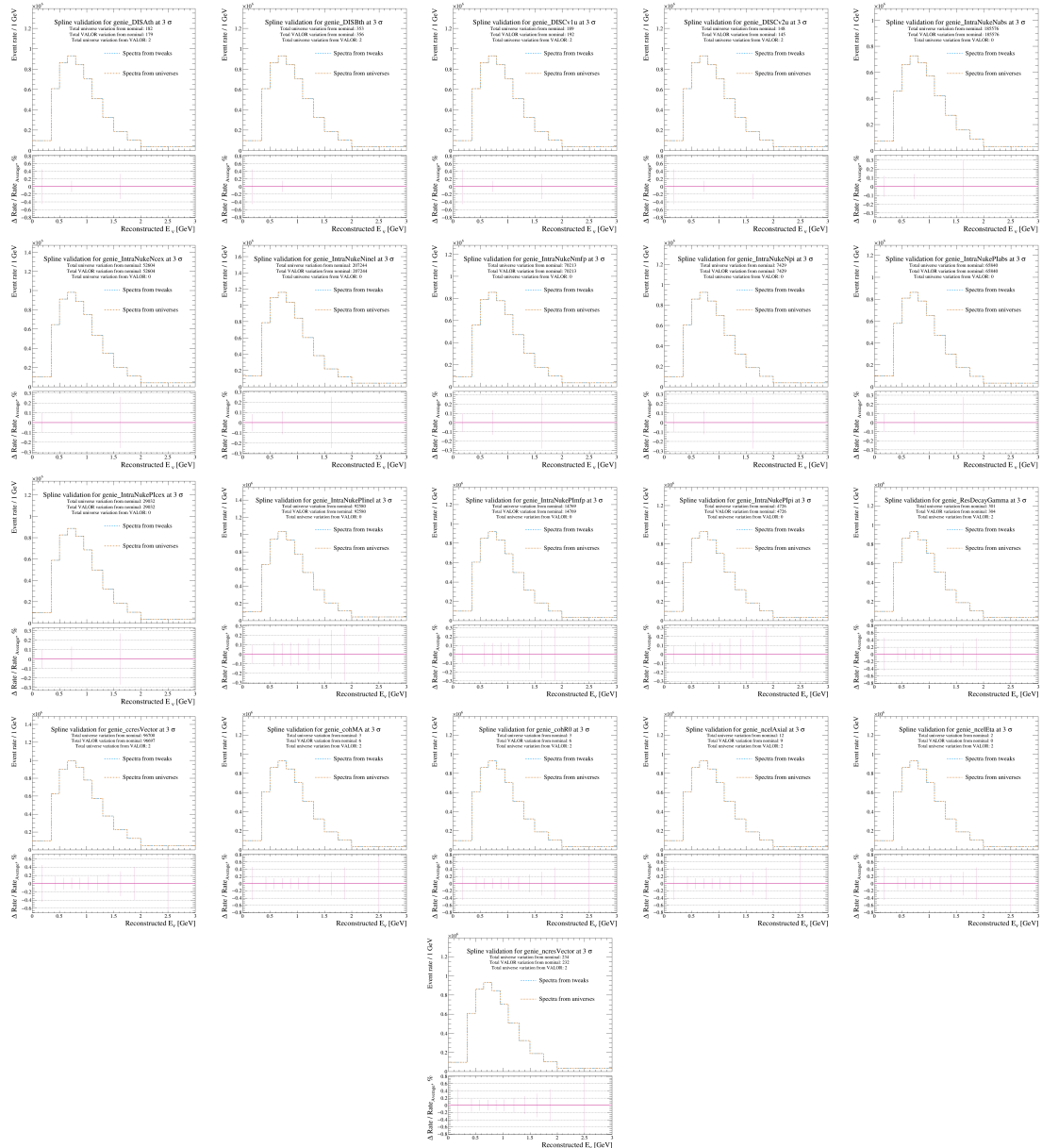


**Figure A.3.:** A comparison of the  $+3\sigma$  variations from the response functions used by VALOR and the universes for the complete set of modern cross-section systematic parameters.

## Appendix B.

### Detector Volumes

The (X, Y, Z) coordinates that define the active and fiducial volumes of each module or TPC are shown in Table B.1 for SBND, MicroBooNE, and ICARUS.

	X [cm]		Y [cm]		Z [cm]
Active Volume					
SBND	-199.15 –	199.15	-200.00 – 200.00	0.00 –	500.00
MicroBooNE	-1.55 –	254.80	-115.53 – 117.47	0.10 –	1036.90
ICARUS Module 1	-364.49 –	-67.94	-173.41 – 143.41	-909.95 –	879.95
ICARUS Module 2	67.94 –	364.49	-173.41 – 143.41	-909.95 –	879.95
Fiducial Volume					
SBND TPC 1	-190.90 –	5.60	-185.00 – 185.00	15.00 –	415.00
SBND TPC 2	10.90 –	190.90	-185.00 – 185.00	15.00 –	415.00
MicroBooNE	-1.55 –	229.80	-90.53 – 92.47	30.10 –	986.90
ICARUS TPC 1	-339.49 –	-221.04	-148.41 – 118.41	-879.95 –	829.95
ICARUS TPC 2	-218.89 –	-92.94	-148.41 – 118.41	-879.95 –	829.95
ICARUS TPC 3	92.94 –	211.39	-148.41 – 118.41	-879.95 –	829.95
ICARUS TPC 4	214.39 –	339.39	-148.41 – 118.41	-879.95 –	829.95

**Table B.1.:** The dimensions defining the active and fiducial volumes for each SBN detector using their respective coordinate systems.



## Appendix C.

# Reconstruction Performance

The figures in Chapter 4 showing the reconstruction performance were produced whilst running Pandora in cheating mode in order to decouple the reconstruction methods from inefficiencies within the pattern recognition. If Pandora is instead used without cheating mode enabled, the resolution of the reconstruction algorithms is expected to worsen owing to the fact that the number of hits associated with true and reconstructed information is no longer in perfect agreement.

With cheating mode no longer enabled in Pandora, the true vs reconstructed energy is shown for all three planes using the ESTAR method in Figure C.1. The fractional energy separation from the collection plane is shown in Figure C.2 for all three reconstruction methods.

Comparing Figure C.1 to the ESTAR plot in Figure 4.4 and Figure 4.9, it can be seen that the energy separation has degraded by disabling cheating mode in Pandora. Similarly, in Figure C.2, each of the distributions has a noticeable tail in the negative x-direction which isn't present in the distributions shown in Figure 4.6.

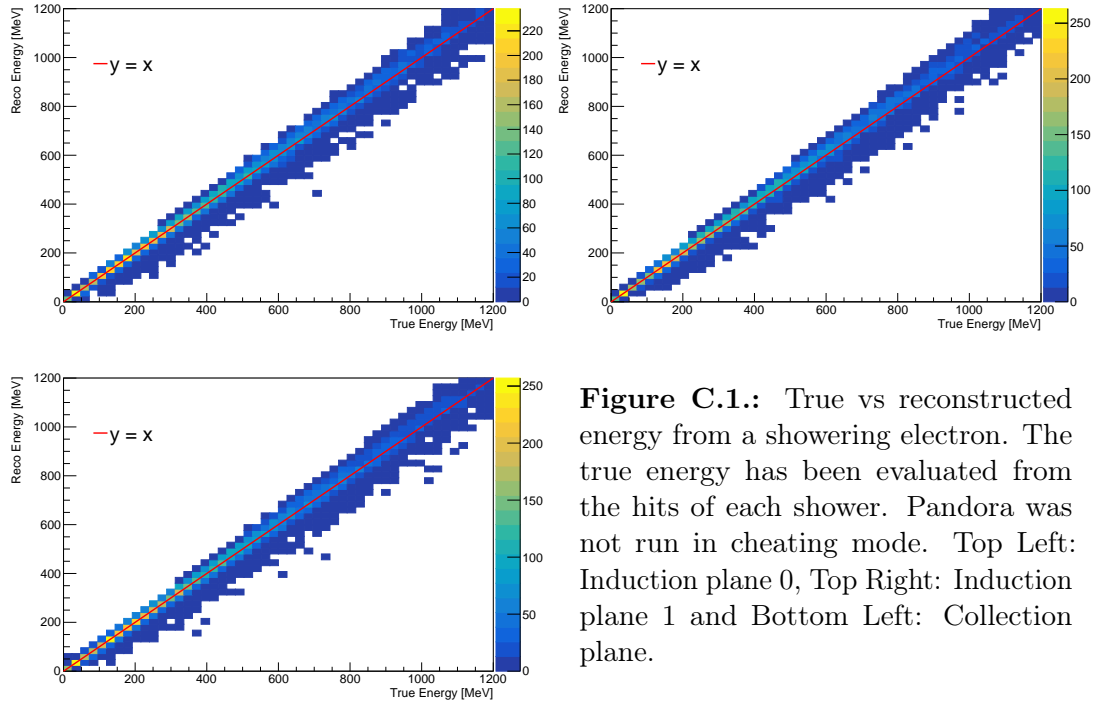


**Figure C.1.:** True vs reconstructed energy from a showering electron. The true energy has been evaluated from the hits of each shower. Pandora was not run in cheating mode. Top Left: Induction plane 0, Top Right: Induction plane 1 and Bottom Left: Collection plane.

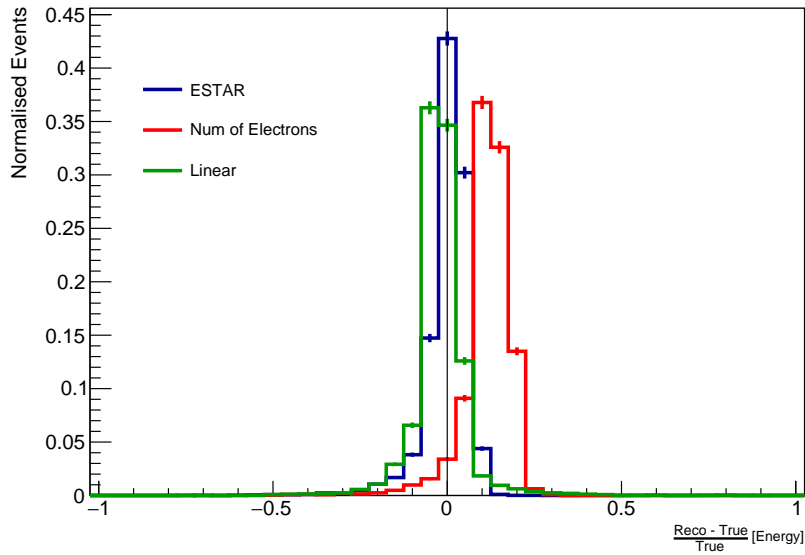


**Figure C.2.:** Comparison of the fractional energy separation from a showering electron for the *Shower Linear Energy tool*, the *Shower Num Electrons Energy tool* and the *Shower ESTAR Energy tool*. The true energy is taken to be the true energy of the available hits and for the reconstruction, Pandora was run whilst not in cheating mode.

## Appendix D.

### $\nu_\mu$ Disappearance Analysis

A similar analysis and validation to that described in Chapter 6 that was performed for the two  $\nu_e$  channels was also done for the  $\nu_\mu$  disappearance channel.

The nominal event rate breakdown for each of the detectors is shown in Figure D.1 where an integrated spectrum with oscillation parameters  $\sin^2 2\theta_{\mu\mu} = 0.072$ ,  $\Delta m_{41}^2 = 1.32 \text{ eV}^2$  has been overlayed. The overall magnitude of the event rate is several orders of magnitude greater than that for  $\nu_e$  owing to the fact that the BNB consists predominantly of  $\nu_\mu$ . As was the case for  $\nu_e$  disappearance, the reduction in events for SBND is relatively small whereas for MicroBooNE and ICARUS it is much more significant.

The complete  $\nu_\mu$  disappearance exclusion sensitivities and allowed regions for both the statistical only case and with the inclusion of flux and interaction systematics are shown in Figure D.2 for the entire SBN program alongside external limits from the combined results from SciBooNE and MiniBooNE, IceCube, MINOS and its successor MINOS+ [87] [99] [94] [169]. The results for the SBN program are shown at a  $5\sigma$  confidence level whereas the exclusion region from the SciBooNE/MiniBooNE, IceCube and MINOS/MINOS+ experiments are shown at the 90% confidence level. The IceCube experiment also shows an allowed region at the 99% confidence level. The results from SBN show a stronger sensitivity than that obtained by MiniBooNE/SciBooNE for all mass splitting values. The exclusion contour is also comparable to that from MINOS/MINOS+ for  $\Delta m_{41}^2 \gtrsim 1 \text{ eV}^2$ , however, below this value MINOS/MINOS+ provides a stronger

limit. The exclusion contour from IceCube again provides a stronger limit at  $\Delta m_{41}^2 \lesssim 1$  eV<sup>2</sup>, but for higher values, SBN expects to improve on the results from IceCube. The allowed region from IceCube intersects the one from SBN so they aren't fully compatible.

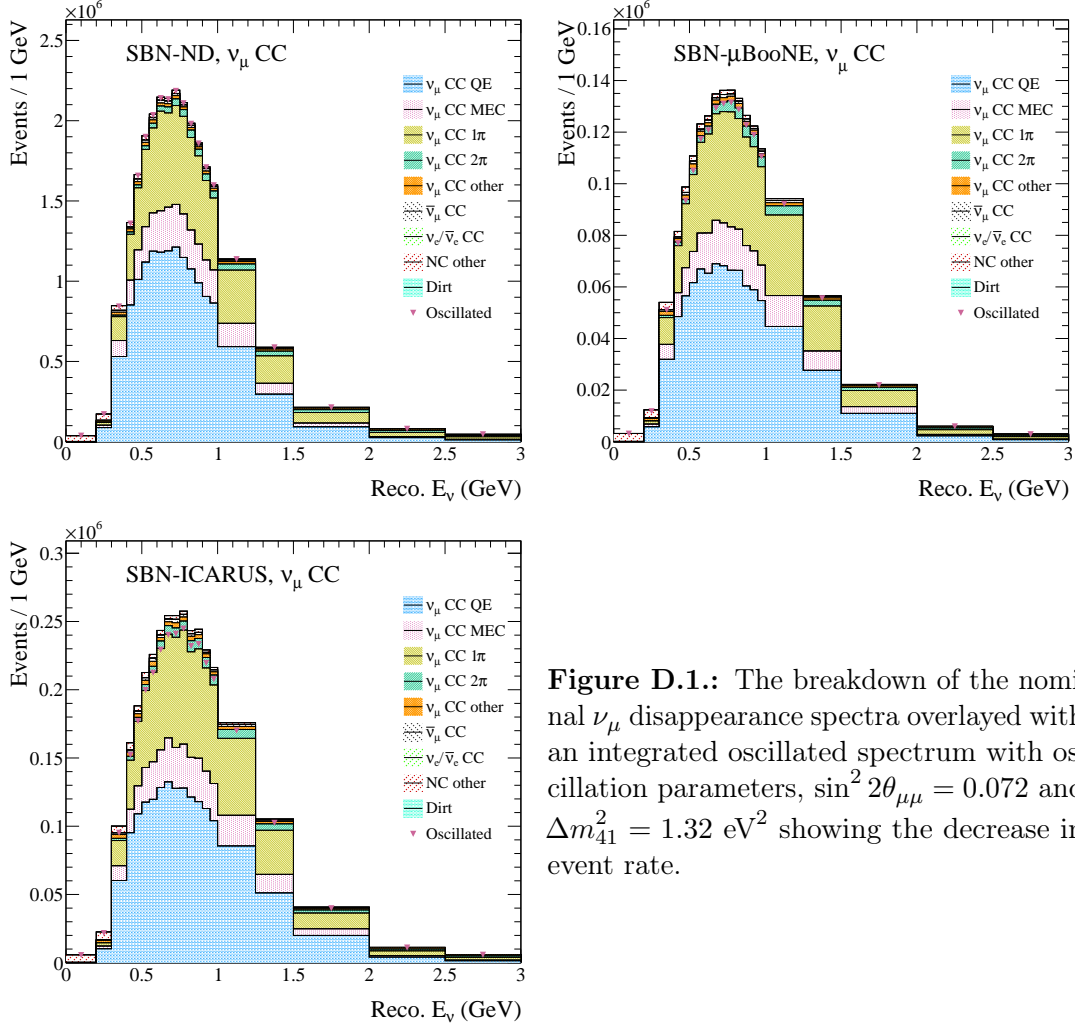


**Figure D.1.:** The breakdown of the nominal  $\nu_\mu$  disappearance spectra overlayed with an integrated oscillated spectrum with oscillation parameters,  $\sin^2 2\theta_{\mu\mu} = 0.072$  and  $\Delta m_{41}^2 = 1.32$  eV<sup>2</sup> showing the decrease in event rate.

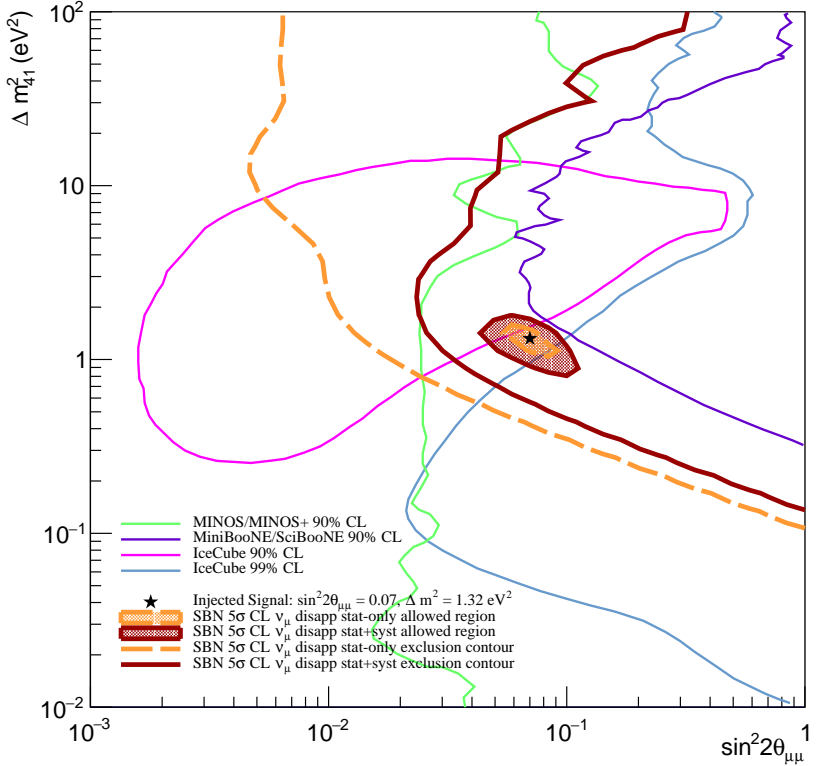
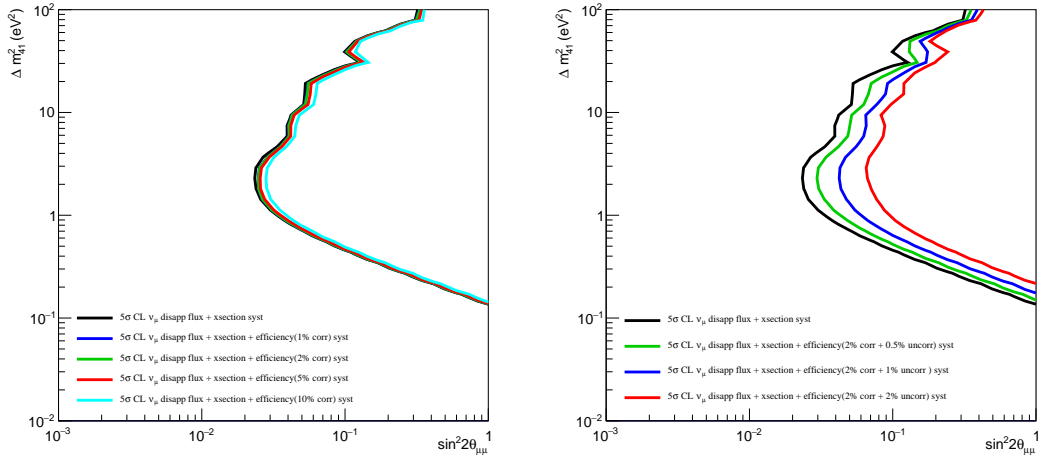


**Figure D.2.:**  $\nu_\mu$  disappearance exclusion contours and allowed regions for the stat only case and with flux and interaction systematic uncertainties included. External limits from the MiniBooNE/SciBooNE, MINOS/MINOS+ and IceCube experiments have been overlayed [87] [95] [99]. (The confidence intervals for each contour are shown in the legend and it should be noted that those from external limits are not the same as those from the contours produced for the SBN program.)

## Impact of Efficiency Systematics on $\nu_\mu$ Disappearance Sensitivities

The impact of fully correlated uncertainties up to 10% are shown on the left of Figure D.3 whilst keeping the uncorrelated uncertainty at 0%. The right plot shows the impact of increasing the uncorrelated uncertainties uniformly across all bins with a fixed correlated uncertainty of 2%. It follows that for even relatively

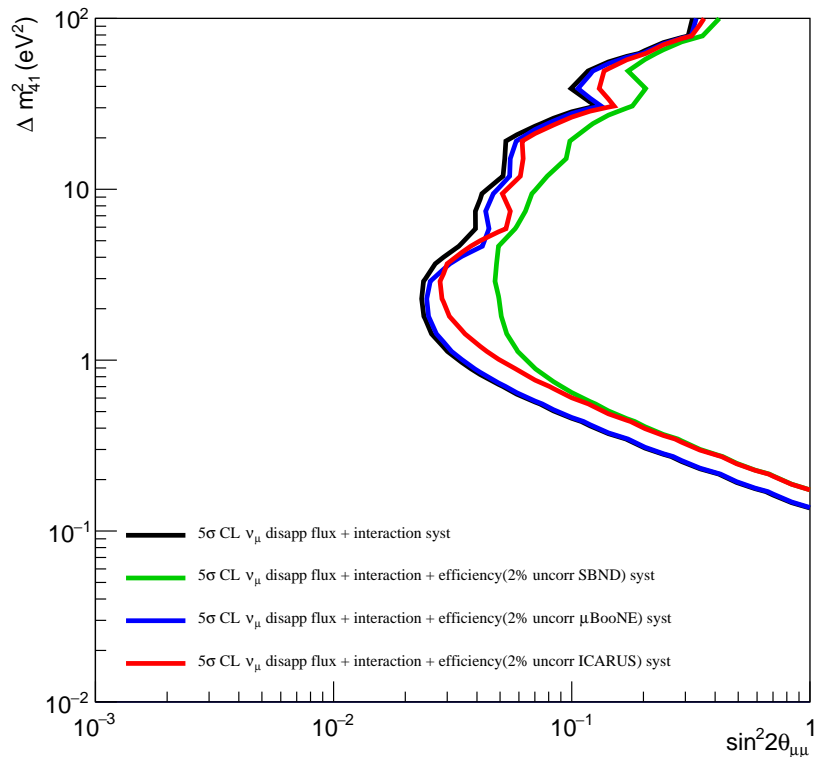
large correlated uncertainties the impact on the sensitivity is minor and that any reduction in sensitivities will be largely dominated by the uncorrelated uncertainty.



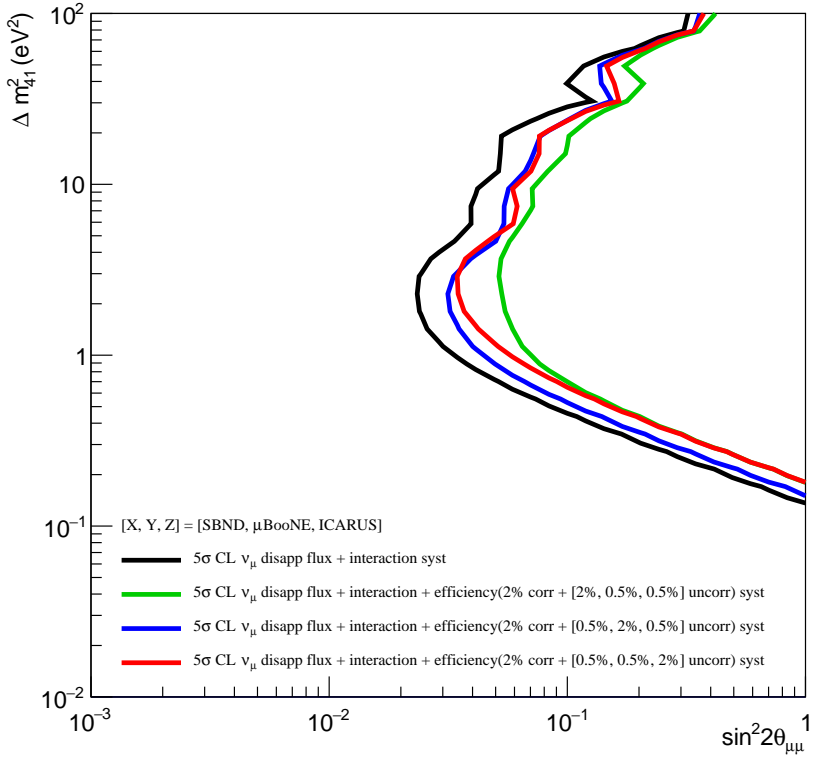
**Figure D.3.:** The impact on the  $\nu_\mu$  disappearance exclusion sensitivity by applying fully correlated uncertainties ranging from 1% to 10% to all bins (Left) and by applying a fixed 2% fully correlated uncertainty with additional uncorrelated uncertainty ranging from 0.5% to 2% across all bins (Right).

Figure D.4 shows the impact of applying a 2% uncorrelated uncertainty only to each of the SBN detectors one at a time. The MicroBooNE detector has a minor impact at around  $\Delta m_{41}^2 = 10 \text{ eV}^2$  and close to no impact at small and large  $\Delta m_{41}^2$  values. The ICARUS detector has a larger impact for most  $\Delta m_{41}^2$  values but again only has a minor contribution at very large  $\Delta m_{41}^2$  values. Across most  $\Delta m_{41}^2$  values greater than  $\sim 0.5 \text{ eV}^2$ , SBND dominates the sensitivity. At values below  $0.5 \text{ eV}^2$ , the reduction in sensitivity due to SBND and ICARUS are comparable. This point is emphasised in Figure D.5 where the fully correlated uncertainty is fixed at 2% and the uncorrelated uncertainty is set to 2% for one of the three SBN detectors whilst being set to 0.5% for the other two detectors. The contour where SBNDs uncorrelated uncertainty is set to 2% looks similar to the corresponding contour in Figure D.4. It has been shown that the uncorrelated component of the uncertainty has a large impact when compared to the correlated component and that any efficiency uncertainties impact SBND more than the other two detectors so this result ought to be expected. Similarly, the two contours

where uncorrelated uncertainty is set to 2% for MicroBooNE and ICARUS are pulled towards the SBND contour since despite it having a smaller associated uncorrelated uncertainty, it will still contribute significantly.



**Figure D.4.:** The impact on the  $\nu_\mu$  disappearance exclusion sensitivity by applying a 2% uncorrelated efficiency uncertainty to a single one of the three SBN detectors.



**Figure D.5.:** The impact on the  $\nu_\mu$  disappearance exclusion sensitivity by applying a 2% fully correlated efficiency uncertainty for each of the SBN detectors and a 2% uncorrelated uncertainty for one of the detectors and a 0.5% uncorrelated uncertainty for the other two detectors. This is repeated for each of the detectors. The associated covariance matrix used for the case where SBNDs uncorrelated uncertainty was set to 2% is shown in the bottom left plot of Figure 6.29.

Figure D.6 considers the case where a single set of bins are poorly constrained using the same scheme outlined in Section 6.5.3. In each case, the uncorrelated uncertainty for the bins of interest are again set to 2% in each of the SBN detectors, whilst the rest of the uncorrelated uncertainties are set to 0.5% and the fully correlated uncertainty is fixed at 2%. Increasing the uncertainty associated with the background bins has the smallest impact whereas increasing the uncertainty for the high and low energy bins has the largest impact at large and small  $\Delta m_{41}^2$  respectively. The peak energy bins also contribute significantly around  $\Delta m_{41}^2$  equal to 1 eV<sup>2</sup> and 10 eV<sup>2</sup>.

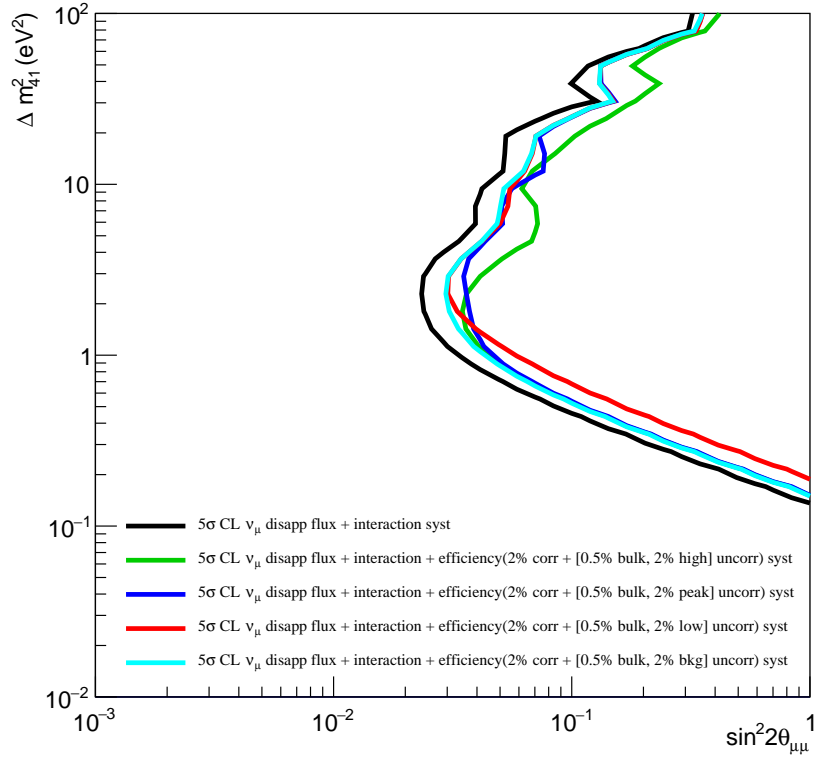


**Figure D.6.:** The impact on the  $\nu_\mu$  disappearance exclusion sensitivity by applying a 2% fully correlated efficiency uncertainty for each of the SBN detectors and a 0.5% uncorrelated uncertainty for all but a single set of bins where the uncorrelated uncertainty is set to 2%. The 'peak' energy bins are defined as those covering an energy range of [0.6, 1.0] GeV. The 'high' and 'low' energy bins are defined as those covering energies above and below the peak energy respectively and the 'bkg' bins are all the bins associated with background events. The set of bins of interest are applied to each of the three detectors and the covariance matrix for where the peak energy bins are the ones in question is shown in the bottom right plot of Figure 6.29.



# Colophon

This thesis was made in L<sup>A</sup>T<sub>E</sub>X 2 <sub>$\varepsilon$</sub>  using the “hepthesis” class.



# Bibliography

- [1] S. Braibant, G. Giacomelli, and M. Spurio, *Particles and Fundamental Interactions: An Introduction to Particle Physics* Undergraduate Lecture Notes in Physics (Springer Netherlands, 2011).
- [2] W. Pauli, Pauli letter collection: letter to Lise Meitner, <https://cds.cern.ch/record/83282>, Typed copy, [Accessed September 2021].
- [3] C. L. Cowan, Jr., F. Reines, F. B. Harrison, H. W. Kruse, and A. D. McGuire, Detection of the Free Neutrino: A Confirmation, [doi:10.1126/science.124.3212.103](https://doi.org/10.1126/science.124.3212.103), Science **124**, 103 (1956).
- [4] G. Danby *et al.*, Observation of High-Energy Neutrino Reactions and the Existence of Two Kinds of Neutrinos, [doi:10.1103/PhysRevLett.9.36](https://doi.org/10.1103/PhysRevLett.9.36), Physical Review Letters **9**, 36 (1962).
- [5] DONUT, K. Kodama *et al.*, Observation of tau neutrino interactions, FERMILAB-PUB-00-335-E, [doi:10.1016/S0370-2693\(01\)00307-0](https://doi.org/10.1016/S0370-2693(01)00307-0), Phys. Lett. **B504**, 218 (2001), hep-ex/0012035.
- [6] Y. Fukuda *et al.*, Evidence for Oscillation of Atmospheric Neutrinos, [doi:10.1103/physrevlett.81.1562](https://doi.org/10.1103/physrevlett.81.1562), Physical Review Letters **81**, 1562–1567 (1998).
- [7] K. Lande *et al.*, Results from the Homestake solar neutrino observatory, Conf. Proc. **C900802**, 867 (1990), [Conf. Proc.C900802V1,C900802V1:667(1990)].
- [8] Super-Kamiokande, J. G. Learned, The Atmospheric neutrino anomaly: Muon neutrino disappearance, p. 89 (2000), hep-ex/0007056.

- [9] W. Rodejohann, Neutrino-less Double Beta Decay and Particle Physics, [doi:10.1142/s0218301311020186](https://doi.org/10.1142/s0218301311020186), International Journal of Modern Physics E **20**, 1833 (2011).
- [10] K. N. Abazajian *et al.*, Light Sterile Neutrinos: A White Paper, FERMILAB-PUB-12-881-PPD, [arXiv:1204.5379](https://arxiv.org/abs/1204.5379), 2012, 1204.5379.
- [11] LAr1-ND, ICARUS-WA104, MicroBooNE, M. Antonello *et al.*, A Proposal for a Three Detector Short-Baseline Neutrino Oscillation Program in the Fermilab Booster Neutrino Beam, [arXiv:1503.01520](https://arxiv.org/abs/1503.01520), 2015, 1503.01520.
- [12] A. Schukraft, SBND Project Overview: progress, schedule and resources, <https://sbn-docdb.fnal.gov/cgi-bin/sso>ShowDocument?docid=26247>, 2022, [Accessed: Aug, 2022].
- [13] P. A. Machado, O. Palamara, and D. W. Schmitz, The Short-Baseline Neutrino Program at Fermilab, [doi:10.1146/annurev-nucl-101917-020949](https://doi.org/10.1146/annurev-nucl-101917-020949), Annual Review of Nuclear and Particle Science **69**, 363–387 (2019).
- [14] M. L. Perl *et al.*, Evidence for Anomalous Lepton Production in  $e^+ - e^-$  Annihilation, [doi:10.1103/PhysRevLett.35.1489](https://doi.org/10.1103/PhysRevLett.35.1489), Phys. Rev. Lett. **35**, 1489 (1975).
- [15] B. R. Martin and G. Shaw, *Particle Physics, Third Edition* (John Wiley and Sons, Ltd, Publication, 2008).
- [16] C. S. Wu, E. Ambler, R. W. Hayward, D. D. Hoppes, and R. P. Hudson, Experimental Test of Parity Conservation in Beta Decay, [doi:10.1103/PhysRev.105.1413](https://doi.org/10.1103/PhysRev.105.1413), Physical Review **105**, 1413 (1957).
- [17] E. Majorana, A Symmetric Theory of Electrons and Positrons, in *Scientific Papers of Ettore Majorana: A New Expanded Edition*, edited by L. Cifarelli, pp. 113–128, Springer International Publishing, Cham, 2020.
- [18] M. Goldhaber, L. Grodzins, and A. W. Sunyar, Helicity of Neutrinos, [doi:10.1103/PhysRev.109.1015](https://doi.org/10.1103/PhysRev.109.1015), Phys. Rev. **109**, 1015 (1958).
- [19] A. Blondel, The Number of Neutrinos and the Z Line Shape, [doi:10.1142/9789814733519\\\_0008](https://doi.org/10.1142/9789814733519\_0008), (2016).

- [20] ALEPH, D. Decamp *et al.*, Determination of the Number of Light Neutrino Species, CERN EP 89-132, [doi:10.1016/0370-2693\(89\)90704-1](https://doi.org/10.1016/0370-2693(89)90704-1), Phys. Lett. B **231**, 519 (1989).
- [21] LSND Collaboration, A. Aguilar *et al.*, Evidence for neutrino oscillations from the observation of  $\bar{\nu}_e$  appearance in a  $\bar{\nu}_\mu$  beam, [doi:10.1103/PhysRevD.64.112007](https://doi.org/10.1103/PhysRevD.64.112007), Phys. Rev. D **64**, 112007 (2001).
- [22] MiniBooNE Collaboration, A. A. Aguilar-Arevalo *et al.*, Significant Excess of Electron like Events in the MiniBooNE Short-Baseline Neutrino Experiment, [doi:10.1103/PhysRevLett.121.221801](https://doi.org/10.1103/PhysRevLett.121.221801), Phys. Rev. Lett. **121**, 221801 (2018).
- [23] GALLEX, W. Hampel *et al.*, Final results of the Cr-51 neutrino source experiments in GALLEX, DAPNIA-SPP-97-26, MPI-H-V41-1997, BNL-64864, ROM2F-97-45, TUM-SFB-375-221, [doi:10.1016/S0370-2693\(97\)01562-1](https://doi.org/10.1016/S0370-2693(97)01562-1), Phys. Lett. B **420**, 114 (1998).
- [24] F. Kaether, W. Hampel, G. Heusser, J. Kiko, and T. Kirsten, Reanalysis of the Gallex solar neutrino flux and source experiments, [doi:<https://doi.org/10.1016/j.physletb.2010.01.030>](https://doi.org/10.1016/j.physletb.2010.01.030), Physics Letters B **685**, 47 (2010).
- [25] J. N. Abdurashitov *et al.*, Measurement of the response of a Ga solar neutrino experiment to neutrinos from a  $^{37}\text{Ar}$  source, [doi:10.1103/PhysRevC.73.045805](https://doi.org/10.1103/PhysRevC.73.045805), Phys. Rev. C **73**, 045805 (2006).
- [26] G. Mention *et al.*, Reactor antineutrino anomaly, [doi:10.1103/physrevd.83.073006](https://doi.org/10.1103/physrevd.83.073006), Physical Review D **83** (2011).
- [27] T. Morii , C. S. Lim , S. N. Mukherjee, *The Physics Of The Standard Model And Beyond* (World Scientific Publishing Co. Pte. Ltd., 2004).
- [28] W. H. Furry, On Transition Probabilities in Double Beta-Disintegration, [doi:10.1103/PhysRev.56.1184](https://doi.org/10.1103/PhysRev.56.1184), Phys. Rev. **56**, 1184 (1939).
- [29] V. Barger, D. Marfatia, and K. Whisnant, *The Physics of Neutrinos* (Princeton University Press, 2012).

- [30] Alessandro De Angelis, Mário Pimenta, *Introduction to Particle and Astroparticle Physics: Multimessenger Astronomy and its Particle Physics Foundations*, second ed. (Springer International Publishing AG, 2018).
- [31] C. Giunti and C. W. Kim, *Fundamentals of Neutrino Physics and Astrophysics*. (Oxford: Oxford University Press, 2007).
- [32] Particle Data Group, R. L. Workman and Others, Review of Particle Physics: Particle Detectors for Non-Accelerator Physics, [doi:10.1093/ptep/ptac097](https://doi.org/10.1093/ptep/ptac097), PTEP **2022**, 083C01 (2022).
- [33] F. Halzen and A. Martin, *Quarks and Leptons: An Introductory Course in Modern Particle Physics* (John Wiley, New York, 1984).
- [34] C. E. Patrick, *Measurement of the Antineutrino Double-Differential Charged-Current Quasi-Elastic Scattering Cross Section at MINERvA* (Springer International Publishing, Cham, 2018).
- [35] E. Scantamburlo, *Measurement of the Water to Scintillator Charged-Current Cross-Section Ratio for Muon Neutrinos at the T2K Near Detector*, PhD thesis, UNIVERSITÉ DE GENÈVE, 2017, Presented 06 Jun 2017.
- [36] M. Acero *et al.*, Adjusting neutrino interaction models and evaluating uncertainties using NOvA near detector data, [doi:10.1140/epjc/s10052-020-08577-5](https://doi.org/10.1140/epjc/s10052-020-08577-5), The European Physical Journal C **80** (2020).
- [37] T. Van Cuyck, N. Jachowicz, R. González-Jiménez, J. Ryckebusch, and N. Van Dessel, Seagull and pion-in-flight currents in neutrino-induced  $1n$  and  $2n$  knockout, [doi:10.1103/PhysRevC.95.054611](https://doi.org/10.1103/PhysRevC.95.054611), Phys. Rev. C **95**, 054611 (2017).
- [38] J. H. Christenson, J. W. Cronin, V. L. Fitch, and R. Turlay, Evidence for the  $2\pi$  Decay of the  $K_2^0$  Meson, [doi:10.1103/PhysRevLett.13.138](https://doi.org/10.1103/PhysRevLett.13.138), Phys. Rev. Lett. **13**, 138 (1964).
- [39] A. D. Sakharov, Violation of  $CP$  invariance,  $C$  asymmetry, and baryon asymmetry of the universe, [doi:10.1070/pu1991v034n05abeh002497](https://doi.org/10.1070/pu1991v034n05abeh002497), Soviet Physics Uspekhi **34**, 392 (1991).

- [40] G. C. Branco, R. G. Felipe, and F. R. Joaquim, Leptonic CP Violation, CERN-PH-TH-2011-289, CFTP-11-020, [doi:10.1103/RevModPhys.84.515](https://doi.org/10.1103/RevModPhys.84.515), Rev. Mod. Phys. **84**, 515 (2012), 1111.5332.
- [41] M. Kobayashi and T. Maskawa, CP-Violation in the Renormalizable Theory of Weak Interaction, [doi:10.1143/PTP.49.652](https://doi.org/10.1143/PTP.49.652), Progress of Theoretical Physics **49**, 652 (1973).
- [42] S. W. Herb *et al.*, Observation of a dimuon resonance at 9.5 gev in 400-gев proton-nucleus collisions, [doi:10.1103/PhysRevLett.39.252](https://doi.org/10.1103/PhysRevLett.39.252), Phys. Rev. Lett. **39**, 252 (1977).
- [43] T. Mannel, Theory and phenomenology of cp violation, [doi:<https://doi.org/10.1016/j.nuclphysbps.2006.12.083>](https://doi.org/10.1016/j.nuclphysbps.2006.12.083), Nuclear Physics B - Proceedings Supplements **167**, 170 (2007), Proceedings of the 7th International Conference on Hyperons, Charm and Beauty Hadrons.
- [44] NuFit, v5.2: Three-neutrino fit based on data available in November 2022, <http://www.nu-fit.org/>.
- [45] Hyper-Kamiokande, K. Abe *et al.*, Hyper-Kamiokande Design Report, (2018), 1805.04163.
- [46] R. Acciarri *et al.*, Long-Baseline Neutrino Facility (LBNF) and Deep Underground Neutrino Experiment (DUNE) Conceptual Design Report Volume 1: The LBNF and DUNE Projects, [doi:10.48550/ARXIV.1601.05471](https://doi.org/10.48550/ARXIV.1601.05471), (2016).
- [47] E. Akhmedov, *Majorana neutrinos and other Majorana particles: Theory and experiment* (, 2014), , 1412.3320.
- [48] Micheal E. Peskin and Daniel V. Schroeder, *An Introduction to Quantum Field Theory* (Perseus Books Publishing, 1995).
- [49] M. Aker *et al.*, First direct neutrino-mass measurement with sub-ev sensitivity, [doi:10.48550/ARXIV.2105.08533](https://doi.org/10.48550/ARXIV.2105.08533), (2021).
- [50] Y. Wang, Neutrino Detectors: Present and Future, [doi:10.1016/j.phpro.2012.03.703](https://doi.org/10.1016/j.phpro.2012.03.703), Physics Procedia **37**, 22 (2012).

- [51] Zen Collaboration, First search for the majorana nature of neutrinos in the inverted mass ordering region with kamland-zen, [doi:10.48550/ARXIV.2203.02139](https://arxiv.org/abs/2203.02139), (2022).
- [52] N. Aghanim *et al.*, Planck 2018 results. VI. Cosmological parameters, [doi:10.1051/0004-6361/201833910](https://doi.org/10.1051/0004-6361/201833910), *Astronomy & Astrophysics* **641**, A6 (2020).
- [53] B. Pontecorvo, Neutrino Experiments and the Problem of Conservation of Leptonic Charge, *Zh. Eksp. Teor. Fiz.* **53**, 1717 (1967).
- [54] Z. Maki, M. Nakagawa, and S. Sakata, Remarks on the Unified Model of Elementary Particles, [doi:10.1143/PTP.28.870](https://doi.org/10.1143/PTP.28.870), *Progress of Theoretical Physics* **28**, 870 (1962).
- [55] L. Wolfenstein, Neutrino oscillations in matter, [doi:10.1103/PhysRevD.17.2369](https://doi.org/10.1103/PhysRevD.17.2369), *Phys. Rev. D* **17**, 2369 (1978).
- [56] Y. Chan, RESULTS FROM SNO, <https://www.osti.gov/servlets/purl/822831>, 2001, DOE Contract No. DE-AC03-76SF00098.
- [57] SNO Collaboration, Q. R. Ahmad *et al.*, Measurement of the Rate of  $\nu_e + d \rightarrow p + p + e^-$  Interactions Produced by  $^8B$  Solar Neutrinos at the Sudbury Neutrino Observatory, [doi:10.1103/PhysRevLett.87.071301](https://doi.org/10.1103/PhysRevLett.87.071301), *Phys. Rev. Lett.* **87**, 071301 (2001).
- [58] X. Qian and P. Vogel, Neutrino mass hierarchy, [doi:10.1016/j.ppnp.2015.05.002](https://doi.org/10.1016/j.ppnp.2015.05.002), *Progress in Particle and Nuclear Physics* **83**, 1–30 (2015).
- [59] Son Cao, Recent neutrino oscillation results from T2K, <https://www-he.scphys.kyoto-u.ac.jp/member/nuICISE/Neutrino.html>, 2016.
- [60] Particle Data Group, P. Zyla *et al.*, Review of Particle Physics, [doi:10.1093/ptep/ptaa104](https://doi.org/10.1093/ptep/ptaa104), *PTEP* **2020**, 083C01 (2020).
- [61] B. T. Cleveland *et al.*, Measurement of the solar electron neutrino flux with the homestake chlorine detector, [doi:10.1086/305343](https://doi.org/10.1086/305343), *The Astrophysical Journal* **496**, 505 (1998).

- [62] J. N. Abdurashitov *et al.*, Measurement of the solar neutrino capture rate with gallium metal. III. results for the 2002–2007 data-taking period, [doi:10.1103/physrevc.80.015807](https://doi.org/10.1103/physrevc.80.015807), Physical Review C **80** (2009).
- [63] G. Bellini *et al.*, Precision measurement of the  ${}^7\text{Be}$  solar neutrino interaction rate in borexino, [doi:10.1103/physrevlett.107.141302](https://doi.org/10.1103/physrevlett.107.141302), Physical Review Letters **107** (2011).
- [64] G. Bellini *et al.*, Final results of borexino phase-i on low-energy solar neutrino spectroscopy, [doi:10.1103/physrevd.89.112007](https://doi.org/10.1103/physrevd.89.112007), Physical Review D **89** (2014).
- [65] J. Hosaka *et al.*, Solar neutrino measurements in super-kamiokande-i, [doi:10.1103/physrevd.73.112001](https://doi.org/10.1103/physrevd.73.112001), Physical Review D **73** (2006).
- [66] J. P. Cravens *et al.*, Solar neutrino measurements in super-kamiokande-II, [doi:10.1103/physrevd.78.032002](https://doi.org/10.1103/physrevd.78.032002), Physical Review D **78** (2008).
- [67] K. Abe *et al.*, Solar neutrino results in super-kamiokande-III, [doi:10.1103/physrevd.83.052010](https://doi.org/10.1103/physrevd.83.052010), Physical Review D **83** (2011).
- [68] Y. Nakano, *8B solar neutrino spectrum measurement using Super-Kamiokande IV*, PhD thesis, University of Tokyo, 2016.
- [69] B. Aharmim *et al.*, Combined analysis of all three phases of solar neutrino data from the sudbury neutrino observatory, [doi:10.1103/physrevc.88.025501](https://doi.org/10.1103/physrevc.88.025501), Physical Review C **88** (2013).
- [70] N. Vinyoles *et al.*, A new generation of standard solar models, [doi:10.3847/1538-4357/835/2/202](https://doi.org/10.3847/1538-4357/835/2/202), The Astrophysical Journal **835**, 202 (2017).
- [71] S. Abe *et al.*, Precision measurement of neutrino oscillation parameters with KamLAND, [doi:10.1103/physrevlett.100.221803](https://doi.org/10.1103/physrevlett.100.221803), Physical Review Letters **100** (2008).
- [72] A. Gando *et al.*, Constraints on  $\theta_{13}$  from a three-flavor oscillation analysis of reactor antineutrinos at KamLAND, [doi:10.1103/physrevd.83.052002](https://doi.org/10.1103/physrevd.83.052002), Physical Review D **83** (2011).

- [73] The KamLAND Collaboration, Reactor on-off antineutrino measurement with kamland, [doi:10.48550/ARXIV.1303.4667](https://doi.org/10.48550/ARXIV.1303.4667), (2013).
- [74] P. F. de Salas *et al.*, 2020 global reassessment of the neutrino oscillation picture, [doi:10.1007/JHEP02\(2021\)071](https://doi.org/10.1007/JHEP02(2021)071), JHEP **02**, 071 (2021), 2006.11237.
- [75] G. Bak *et al.*, Measurement of reactor antineutrino oscillation amplitude and frequency at RENO, [doi:10.1103/physrevlett.121.201801](https://doi.org/10.1103/physrevlett.121.201801), Physical Review Letters **121** (2018).
- [76] J. Yoo, RENO, [doi:10.5281/zenodo.4123573](https://doi.org/10.5281/zenodo.4123573), (2020).
- [77] D. Adey *et al.*, Measurement of the electron antineutrino oscillation with 1958 days of operation at daya bay, [doi:10.1103/physrevlett.121.241805](https://doi.org/10.1103/physrevlett.121.241805), Physical Review Letters **121** (2018).
- [78] M. Jiang *et al.*, Atmospheric neutrino oscillation analysis with improved event reconstruction in super-kamiokande IV, [doi:10.1093/ptep/ptz015](https://doi.org/10.1093/ptep/ptz015), Progress of Theoretical and Experimental Physics **2019** (2019).
- [79] M. Aartsen *et al.*, Determining neutrino oscillation parameters from atmospheric muon neutrino disappearance with three years of IceCube DeepCore data, [doi:10.1103/physrevd.91.072004](https://doi.org/10.1103/physrevd.91.072004), Physical Review D **91** (2015).
- [80] P. Dunne, Latest neutrino oscillation results from t2k, [doi:10.5281/zenodo.3959558](https://doi.org/10.5281/zenodo.3959558), (2020).
- [81] M. Acero *et al.*, New constraints on oscillation parameters from  $\nu_e$  and  $\nu_\mu$  disappearance in the NOvA experiment, [doi:10.1103/physrevd.98.032012](https://doi.org/10.1103/physrevd.98.032012), Physical Review D **98** (2018).
- [82] M. Acero *et al.*, First measurement of neutrino oscillation parameters using neutrinos and antineutrinos by NOvA, [doi:10.1103/physrevlett.123.151803](https://doi.org/10.1103/physrevlett.123.151803), Physical Review Letters **123** (2019).
- [83] P. Adamson *et al.*, Measurement of neutrino and antineutrino oscillations using beam and atmospheric data in MINOS, [doi:10.1103/physrevlett.110.251801](https://doi.org/10.1103/physrevlett.110.251801), Physical Review Letters **110** (2013).

- [84] P. Adamson *et al.*, Electron neutrino and antineutrino appearance in the full MINOS data sample, [doi:10.1103/physrevlett.110.171801](https://doi.org/10.1103/physrevlett.110.171801), Physical Review Letters **110** (2013).
- [85] E. Aliu *et al.*, Evidence for muon neutrino oscillation in an accelerator-based experiment, [doi:10.1103/physrevlett.94.081802](https://doi.org/10.1103/physrevlett.94.081802), Physical Review Letters **94** (2005).
- [86] A. Diaz, C. Argüelles, G. Collin, J. Conrad, and M. Shaevitz, Where are we with light sterile neutrinos?, [doi:10.1016/j.physrep.2020.08.005](https://doi.org/10.1016/j.physrep.2020.08.005), Physics Reports **884**, 1 (2020).
- [87] K. B. M. Mahn *et al.*, Dual baseline search for muon neutrino disappearance at  $0.5 \text{ eV}^2 < \Delta m^2 < 40 \text{ eV}^2$ , [doi:10.1103/physrevd.85.032007](https://doi.org/10.1103/physrevd.85.032007), Physical Review D **85** (2012).
- [88] J. Kostensalo, J. Suhonen, C. Giunti, and P. Srivastava, The gallium anomaly revisited, [doi:<https://doi.org/10.1016/j.physletb.2019.06.057>](https://doi.org/10.1016/j.physletb.2019.06.057), Physics Letters B **795**, 542 (2019).
- [89] M. A. Acero *et al.*, White Paper on Light Sterile Neutrino Searches and Related Phenomenology, [doi:10.48550/ARXIV.2203.07323](https://doi.org/10.48550/ARXIV.2203.07323), (2022).
- [90] KARMEN Collaboration, B. Armbruster *et al.*, Upper limits for neutrino oscillations  $\bar{\nu}_\mu \rightarrow \bar{\nu}_e$  from muon decay at rest, [doi:10.1103/PhysRevD.65.112001](https://doi.org/10.1103/PhysRevD.65.112001), Phys. Rev. D **65**, 112001 (2002).
- [91] B. Armbruster *et al.*, Limits on neutrino oscillations in the appearance channels  $\nu_\mu \rightarrow \nu_e$  and  $\bar{\nu}_\mu \rightarrow \bar{\nu}_e$ , [doi:\[https://doi.org/10.1016/0920-5632\\(94\\)00752-H\]\(https://doi.org/10.1016/0920-5632\(94\)00752-H\)](https://doi.org/10.1016/0920-5632(94)00752-H), Nuclear Physics B - Proceedings Supplements **38**, 235 (1995), Neutrino 94.
- [92] B. Achkar *et al.*, Search for neutrino oscillations at 15, 40 and 95 meters from a nuclear power reactor at bugey, [doi:\[https://doi.org/10.1016/0550-3213\\(94\\)00513-E\]\(https://doi.org/10.1016/0550-3213\(94\)00513-E\)](https://doi.org/10.1016/0550-3213(94)00513-E), Nuclear Physics B **434**, 503 (1995).

- [93] A. Romosan *et al.*, High statistics search for  $\nu_\mu(\bar{\nu}_\mu) \rightarrow \nu_e(\bar{\nu}_e)$  oscillations in the small mixing angle regime, [doi:10.1103/PhysRevLett.78.2912](https://doi.org/10.1103/PhysRevLett.78.2912), Phys. Rev. Lett. **78**, 2912 (1997).
- [94] MINOS Collaboration, P. Adamson *et al.*, Search for Sterile Neutrinos Mixing with Muon Neutrinos in MINOS, [doi:10.1103/PhysRevLett.117.151803](https://doi.org/10.1103/PhysRevLett.117.151803), Phys. Rev. Lett. **117**, 151803 (2016).
- [95] P. Adamson *et al.*, Search for Sterile Neutrinos in MINOS and MINOS+ Using a Two-Detector Fit, [doi:10.1103/physrevlett.122.091803](https://doi.org/10.1103/physrevlett.122.091803), Physical Review Letters **122** (2019).
- [96] S. Mertens *et al.*, A novel detector system for KATRIN to search for keV-scale sterile neutrinos, [doi:10.1088/1361-6471/ab12fe](https://doi.org/10.1088/1361-6471/ab12fe), Journal of Physics G: Nuclear and Particle Physics **46**, 065203 (2019).
- [97] M. Aker *et al.*, Improved eV-scale sterile-neutrino constraints from the second KATRIN measurement campaign, [doi:10.1103/physrevd.105.072004](https://doi.org/10.1103/physrevd.105.072004), Physical Review D **105** (2022).
- [98] K. Abe *et al.*, Search for short baseline  $\nu_e$  disappearance with the T2K near detector, [doi:10.1103/physrevd.91.051102](https://doi.org/10.1103/physrevd.91.051102), Physical Review D **91** (2015).
- [99] M. Aartsen *et al.*, Searching for eV-scale sterile neutrinos with eight years of atmospheric neutrinos at the IceCube Neutrino Telescope, [doi:10.1103/physrevd.102.052009](https://doi.org/10.1103/physrevd.102.052009), Physical Review D **102** (2020).
- [100] P. Abratenko *et al.*, Search for neutrino-induced neutral-current  $\delta$  radiative decay in MicroBooNE and a first test of the MiniBooNE low energy excess under a single-photon hypothesis, [doi:10.1103/physrevlett.128.111801](https://doi.org/10.1103/physrevlett.128.111801), Physical Review Letters **128** (2022).
- [101] MicroBooNE Collaboration *et al.*, Search for an excess of electron neutrino interactions in microboone using multiple final state topologies, [doi:10.48550/ARXIV.2110.14054](https://doi.org/10.48550/ARXIV.2110.14054), (2021).

- [102] P. Abratenko *et al.*, Search for an anomalous excess of charged-current quasielastic  $\nu_e$  interactions with the MicroBooNE experiment using Deep-Learning-based reconstruction, [doi:10.1103/physrevd.105.112003](https://doi.org/10.1103/physrevd.105.112003), Physical Review D **105** (2022).
- [103] MicroBooNE Collaboration *et al.*, Search for an anomalous excess of charged-current  $\nu_e$  interactions without pions in the final state with the MicroBooNE experiment, [doi:10.48550/ARXIV.2110.14065](https://doi.org/10.48550/ARXIV.2110.14065), (2021).
- [104] C. Argüelles *et al.*, MicroBooNE and the  $\nu_e$  Interpretation of the MiniBooNE Low-Energy Excess, [doi:10.1103/physrevlett.128.241802](https://doi.org/10.1103/physrevlett.128.241802), Physical Review Letters **128** (2022).
- [105] H. Almazán *et al.*, STEREO neutrino spectrum of  $^{235}U$  fission rejects sterile neutrino hypothesis, [doi:10.1038/s41586-022-05568-2](https://doi.org/10.1038/s41586-022-05568-2), Nature **613**, 257 (2023).
- [106] S. S. Wilks, The Large-Sample Distribution of the Likelihood Ratio for Testing Composite Hypotheses, [doi:10.1214/aoms/1177732360](https://doi.org/10.1214/aoms/1177732360), The Annals of Mathematical Statistics **9**, 60 (1938).
- [107] M. Dentler *et al.*, Updated global analysis of neutrino oscillations in the presence of eV-scale sterile neutrinos, [doi:10.1007/jhep08\(2018\)010](https://doi.org/10.1007/jhep08(2018)010), Journal of High Energy Physics **2018** (2018).
- [108] C. Rubbia, The Liquid Argon Time Projection Chamber: A New Concept for Neutrino Detectors, CERN-EP-INT-77-08, CERN-EP-77-08, (1977).
- [109] R. Acciarri *et al.*, Design and Construction of the MicroBooNE Detector, [doi:10.1088/1748-0221/12/02/P02017](https://doi.org/10.1088/1748-0221/12/02/P02017), Journal of Instrumentation **12** (2016).
- [110] W. Walkowiak, Drift velocity of free electrons in liquid argon, [doi:\[https://doi.org/10.1016/S0168-9002\\(99\\)01301-7\]\(https://doi.org/10.1016/S0168-9002\(99\)01301-7\)](https://doi.org/10.1016/S0168-9002(99)01301-7), Nuclear Instruments and Methods in Physics Research Section A: Accelerators, Spectrometers, Detectors and Associated Equipment **449**, 288 (2000).

- [111] M. Schenk, *Studies with a Liquid Argon Time Projection Chamber: Addressing Technological Challenges of Large-Scale Detectors* BestMaster, 1 ed. (Springer Specktrum, 2015).
- [112] Y. Li *et al.*, Measurement of longitudinal electron diffusion in liquid argon, [doi:10.1016/j.nima.2016.01.094](https://doi.org/10.1016/j.nima.2016.01.094), Nuclear Instruments and Methods in Physics Research Section A: Accelerators, Spectrometers, Detectors and Associated Equipment **816**, 160–170 (2016).
- [113] C. Anderson *et al.*, The ArgoNeUT detector in the NuMI low-energy beam line at Fermilab, [doi:10.1088/1748-0221/7/10/p10019](https://doi.org/10.1088/1748-0221/7/10/p10019), Journal of Instrumentation **7**, P10019–P10019 (2012).
- [114] MicroBooNE, A Measurement of the Attenuation of Drifting Electrons in the MicroBooNE LArTPC, [doi:10.2172/1573054](https://doi.org/10.2172/1573054), (2017).
- [115] G. Jaffé, Zur Theorie der Ionisation in Kolonnen, [doi:<https://doi.org/10.1002/andp.19133471205>](https://doi.org/10.1002/andp.19133471205), Annalen der Physik **347**, 303 (1913), <https://onlinelibrary.wiley.com/doi/pdf/10.1002/andp.19133471205>.
- [116] J. Thomas and D. A. Imel, Recombination of electron-ion pairs in liquid argon and liquid xenon, [doi:10.1103/PhysRevA.36.614](https://doi.org/10.1103/PhysRevA.36.614), Phys. Rev. A **36**, 614 (1987).
- [117] M. Mooney, The MicroBooNE Experiment and the Impact of Space Charge Effects, <https://arxiv.org/abs/1511.01563>, [doi:10.48550/ARXIV.1511.01563](https://doi.org/10.48550/ARXIV.1511.01563), 2015.
- [118] S. Palestini and K. McDonald, Space charge in ionization detectors, <https://physics.princeton.edu/examples/spacecharge.pdf>, 2016, [Accessed: August, 2022].
- [119] P. Cennini *et al.*, Detection of scintillation light in coincidence with ionizing tracks in a liquid argon time projection chamber, [doi:10.1016/S0168-9002\(99\)00519-7](https://doi.org/10.1016/S0168-9002(99)00519-7), Nuclear Instruments and Methods in Physics Research Section A: Accelerators, Spectrometers, Detectors and Associated Equipment **432**, 240 (1999).

- [120] M. Antonello *et al.*, Detection of cherenkov light emission in liquid argon, [doi:`https://doi.org/10.1016/j.nima.2003.08.177`](https://doi.org/10.1016/j.nima.2003.08.177), Nuclear Instruments and Methods in Physics Research Section A: Accelerators, Spectrometers, Detectors and Associated Equipment **516**, 348 (2004).
- [121] C. Adams *et al.*, Ionization electron signal processing in single phase larptcs. part ii. data/simulation comparison and performance in microboone, [doi:`10.1088/1748-0221/13/07/P07007`](https://doi.org/10.1088/1748-0221/13/07/P07007), Journal of Instrumentation **13**, P07007 (2018).
- [122] V. Shiltsev, Fermilab Proton Accelerator Complex Status and Improvement Plans, FERMILAB-PUB-17-129-APC, [doi:`10.1142/S0217732317300129`](https://doi.org/10.1142/S0217732317300129), Mod. Phys. Lett. A **32**, 1730012 (2017), 1705.03075.
- [123] SciBooNE, A. A. Aguilar-Arevalo *et al.*, Bringing the SciBar detector to the booster neutrino beam, FERMILAB-PROPOSAL-0954, (2006), hep-ex/0601022.
- [124] MiniBooNE Collaboration, A. A. Aguilar-Arevalo *et al.*, Neutrino flux prediction at MiniBooNE, [doi:`10.1103/PhysRevD.79.072002`](https://doi.org/10.1103/PhysRevD.79.072002), Phys. Rev. D **79**, 072002 (2009).
- [125] D. Schmitz, SBND POT and Event Estimates, <https://sbn-docdb.fnal.gov/cgi-bin/sso>ShowDocument?docid=27405>, 2022, [Accessed: Aug, 2022].
- [126] K. Majumdar and K. Mavrokoridis, Review of Liquid Argon Detector Technologies in the Neutrino Sector, [doi:`10.3390/app11062455`](https://doi.org/10.3390/app11062455), Applied Sciences **11**, 2455 (2021).
- [127] M. Auger *et al.*, A novel cosmic ray tagger system for liquid argon tpc neutrino detectors, <https://arxiv.org/abs/1612.04614>, [doi:`10.48550/ARXIV.1612.04614`](https://doi.org/10.48550/ARXIV.1612.04614), 2016.
- [128] C. Adams *et al.*, Design and construction of the MicroBooNE Cosmic Ray Tagger system, [doi:`10.1088/1748-0221/14/04/p04004`](https://doi.org/10.1088/1748-0221/14/04/p04004), Journal of Instrumentation **14**, P04004–P04004 (2019).

- [129] A. Machado and E. Segreto, ARAPUCA a new device for liquid argon scintillation light detection, [doi:10.1088/1748-0221/11/02/c02004](https://doi.org/10.1088/1748-0221/11/02/c02004), Journal of Instrumentation **11**, C02004 (2016).
- [130] A. Machado *et al.*, The X-ARAPUCA: an improvement of the ARAPUCA device, [doi:10.1088/1748-0221/13/04/c04026](https://doi.org/10.1088/1748-0221/13/04/c04026), Journal of Instrumentation **13**, C04026–C04026 (2018).
- [131] R. Acciarri *et al.*, Design and construction of the MicroBooNE detector, [doi:10.1088/1748-0221/12/02/p02017](https://doi.org/10.1088/1748-0221/12/02/p02017), Journal of Instrumentation **12**, P02017–P02017 (2017).
- [132] Sandbox Studio, Chicago, Schematic of the ICARUS detector., <https://www.symmetrymagazine.org/article/sterile-neutrino-sleuths>, [Accessed: January, 2022].
- [133] ICARUS Collaboration, C. Rubbia and C. S. Montanari, Status and plans of WA104/ICARUS, CERN-SPSC-2017-012, SPSC-SR-207, <https://cds.cern.ch/record/2256748>, 2017.
- [134] C. Frugueule, Probing sub-GeV dark sectors via high energy proton beams at LBNF/DUNE and MiniBooNE, [doi:10.1103/PhysRevD.96.015029](https://doi.org/10.1103/PhysRevD.96.015029), Phys. Rev. D **96**, 015029 (2017).
- [135] P. Ballett, S. Pascoli, and M. Ross-Lonergan, MeV-scale sterile neutrino decays at the Fermilab Short-Baseline Neutrino program, [doi:10.1007/jhep04\(2017\)102](https://doi.org/10.1007/jhep04(2017)102), Journal of High Energy Physics **2017** (2017).
- [136] E. Bertuzzo, S. Jana, P. A. N. Machado, and R. Zukanovich Funchal, Dark Neutrino Portal to Explain MiniBooNE Excess, [doi:10.1103/PhysRevLett.121.241801](https://doi.org/10.1103/PhysRevLett.121.241801), Phys. Rev. Lett. **121**, 241801 (2018).
- [137] A. P. Furmanski and C. Hilgenberg, Neutrino energy estimation in neutral current interactions and prospects for sterile neutrino searches, [doi:10.1103/PhysRevD.103.112011](https://doi.org/10.1103/PhysRevD.103.112011), Phys. Rev. D **103**, 112011 (2021).

- [138] C. Andreopoulos *et al.*, The GENIE Neutrino Monte Carlo Generator, FERMILAB-PUB-09-418-CD, [doi:10.1016/j.nima.2009.12.009](https://doi.org/10.1016/j.nima.2009.12.009), Nucl. Instrum. Meth. A **614**, 87 (2010), 0905.2517.
- [139] GEANT4 A Simulation Toolkit, <https://geant4.web.cern.ch/>, [Accessed August, 2022].
- [140] S. Agostinelli *et al.*, Geant4—a simulation toolkit, [doi:\[https://doi.org/10.1016/S0168-9002\\(03\\)01368-8\]\(https://doi.org/10.1016/S0168-9002\(03\)01368-8\)](https://doi.org/10.1016/S0168-9002(03)01368-8), Nuclear Instruments and Methods in Physics Research Section A: Accelerators, Spectrometers, Detectors and Associated Equipment **506**, 250 (2003).
- [141] MicroBooNE, R. Acciarri *et al.*, The Pandora multi-algorithm approach to automated pattern recognition of cosmic-ray muon and neutrino events in the MicroBooNE detector, FERMILAB-PUB-17-306-ND, [doi:10.1140/epjc/s10052-017-5481-6](https://doi.org/10.1140/epjc/s10052-017-5481-6), Eur. Phys. J. C **78**, 82 (2018), 1708.03135.
- [142] LArSoft, <https://larsoft.org/>, [Accessed: July, 2022].
- [143] E. L. Snider and G. Petrillo, LArSoft: Toolkit for Simulation, Reconstruction and Analysis of Liquid Argon TPC Neutrino Detectors, FERMILAB-CONF-17-052-CD, [doi:10.1088/1742-6596/898/4/042057](https://doi.org/10.1088/1742-6596/898/4/042057), J. Phys. Conf. Ser. **898**, 042057 (2017).
- [144] T. Usher, GausHitFinder Hit Finding and Fitting, <https://indico.fnal.gov/event/18523/contributions/47921/attachments/29850/36753/GaussHitFinder121118.pdf>, 2018, [Accessed: July, 2022].
- [145] R. Acciarri *et al.*, A study of electron recombination using highly ionizing particles in the ArgoNeuT Liquid Argon TPC, [doi:10.1088/1748-0221/8/08/p08005](https://doi.org/10.1088/1748-0221/8/08/p08005), Journal of Instrumentation **8**, P08005–P08005 (2013).
- [146] C. Adams *et al.*, Reconstruction and measurement of  $\mathcal{O}(100)$  MeV energy electromagnetic activity from  $\pi^0 \rightarrow \gamma\gamma$  decays in the MicroBooNE LArTPC, [doi:10.1088/1748-0221/15/02/p02007](https://doi.org/10.1088/1748-0221/15/02/p02007), Journal of Instrumentation **15**, P02007–P02007 (2020).

- [147] E. Tyley, SBND Recombination Study for Shower Calorimetry, <https://sbn-docdb.fnal.gov/cgi-bin/sso>ShowDocument?docid=12033>, 2019, [Accessed: July, 2022].
- [148] R. Acciarri *et al.*, Demonstration of MeV-scale physics in liquid argon time projection chambers using ArgoNeuT, [doi:10.1103/PhysRevD.99.012002](https://doi.org/10.1103/PhysRevD.99.012002), Phys. Rev. D **99**, 012002 (2019).
- [149] M. Berger, J. Coursey, M. Zucker, and J. Chang, ESTAR, PSTAR, and ASTAR: Computer Programs for Calculating Stopping-Power and Range Tables for Electrons, Protons, and Helium Ions (version 2.0.1)., <http://physics.nist.gov/Star>, National Institute of Standards and Technology, Gaithersburg, MD., [Accessed: September, 2021].
- [150] GENIE, L. Alvarez-Ruso *et al.*, Recent highlights from GENIE v3, FERMILAB-PUB-21-266-SCD-T, [doi:10.1140/epjs/s11734-021-00295-7](https://doi.org/10.1140/epjs/s11734-021-00295-7), Eur. Phys. J. ST **230**, 4449 (2021), 2106.09381.
- [151] GENIE, J. Tena-Vidal *et al.*, Neutrino-nucleon cross-section model tuning in GENIE v3, FERMILAB-PUB-20-531-SCD-T, [doi:10.1103/PhysRevD.104.072009](https://doi.org/10.1103/PhysRevD.104.072009), Phys. Rev. D **104**, 072009 (2021), 2104.09179.
- [152] A. Ankowski *et al.*, Measurement of through-going particle momentum by means of multiple scattering with the ICARUS T600 TPC, [doi:10.1140/epjc/s10052-006-0051-3](https://doi.org/10.1140/epjc/s10052-006-0051-3), The European Physical Journal C - Particles and Fields **48**, 667 (2006).
- [153] D. Barker, *Developments Towards a  $\nu_e$  CC Sterile Appearance Sensitivity in the Short-Baseline Neutrino Programme*, PhD thesis, [uk.bl.ethos.832514](https://uk.bl.ethos.ac.uk/832514), University of Sheffield, 2020.
- [154] C. Andreopoulos *et al.*, The GENIE Neutrino Monte Carlo Generator: Physics and User Manual, 2015, 1510.05494.
- [155] MicroBooNE Collaboration, Booster Neutrino Flux Prediction at MicroBooNE, [doi:10.2172/1573216](https://doi.org/10.2172/1573216), (2018).

- [156] GENIE, J. Tena-Vidal *et al.*, Neutrino-nucleus CC $\bar{\nu}\pi$  cross-section tuning in GENIE v3, FERMILAB-PUB-22-296-ND-QIS-SCD, [doi:10.1103/PhysRevD.106.112001](https://doi.org/10.1103/PhysRevD.106.112001), Phys. Rev. D **106**, 112001 (2022), 2206.11050.
- [157] S. Dytman *et al.*, Comparison of validation methods of simulations for final state interactions in hadron production experiments, [doi:10.1103/PhysRevD.104.053006](https://doi.org/10.1103/PhysRevD.104.053006), Phys. Rev. D **104**, 053006 (2021).
- [158] C. Andreopoulos *et al.*, The VALOR Group, <https://valor.pp.rl.ac.uk>.
- [159] C. Andreopoulos *et al.*, VALOR DUNE Joint Oscillation and Systematics Constraint Fit (Version 2016a v2), [DUNEDocID1291](#), 2016.
- [160] P. G. Hoel, *Introduction to Mathematical Statistics*, Fourth ed. (John Wiley & Sons, 1971).
- [161] G. Cowan, K. Cranmer, E. Gross, and O. Vitells, Asymptotic formulae for likelihood-based tests of new physics, [doi:10.1140/epjc/s10052-011-1554-0](https://doi.org/10.1140/epjc/s10052-011-1554-0), The European Physical Journal C **71** (2011).
- [162] G. Karagiorgi and J. Zennamo, SBND Oscillations Working Group Kick-off, <https://sbn-docdb.fnal.gov/cgi-bin/sso>ShowDocument?docid=27844>, 2022, [Accessed: Oct, 2022].
- [163] R. Jones, *Muon-neutrino disappearance with multiple liquid argon time projection chambers in the Fermilab Booster neutrino beam*, PhD thesis, [doi:10.17638/03143192](https://doi.org/10.17638/03143192), University of Liverpool, 2021.
- [164] A. G. Frodesen, O. Skjeggestad, H. Tøfte, *PROBABILITY AND STATISTICS IN PARTICLE PHYSICS* (Columbia University Press, 1979).
- [165] K. Abe *et al.*, The T2K experiment, [doi:<https://doi.org/10.1016/j.nima.2011.06.067>](https://doi.org/10.1016/j.nima.2011.06.067), Nuclear Instruments and Methods in Physics Research Section A: Accelerators, Spectrometers, Detectors and Associated Equipment **659**, 106 (2011).
- [166] NA61/SHINE, A. Aduszkiewicz *et al.*, Measurements of production and inelastic cross sections for p+C , p+Be , and p+Al at 60 GeV/c and p+C

and p+Be at 120 GeV/c, CERN-EP-2019-193, [doi:10.1103/PhysRevD.100.112001](https://doi.org/10.1103/PhysRevD.100.112001), Phys. Rev. D **100**, 112001 (2019), 1909.03351.

- [167] J. T. Vidal, *Global Analysis of Muon-Neutrino Charged-Current Data for the Characterization and Tuning of Cross-Section and Hadronization Models in the GENIE Neutrino EventGenerator*, PhD thesis, University of Liverpool, 2022.
- [168] MINER $\nu$ A Collaboration, J. Park *et al.*, Measurement of neutrino flux from neutrino-electron elastic scattering, [doi:10.1103/PhysRevD.93.112007](https://doi.org/10.1103/PhysRevD.93.112007), Phys. Rev. D **93**, 112007 (2016).
- [169] MINOS+, G. Tzanankos *et al.*, MINOS+: a Proposal to FNAL to run MINOS with the medium energy NuMI beam, FERMILAB-PROPOSAL-1016, [doi:10.2172/1028838](https://doi.org/10.2172/1028838), (2011).